

**Reconstruction of deglacial N- and O- cycling  
in the intermediate Pacific**

Dissertation

with the aim of achieving a doctoral degree

at the Faculty of Mathematics, Informatics and Natural Sciences

Department of Earth System Sciences

at University of Hamburg

submitted by

**Anjaly Govindankutty Menon**

from Kerala, India

Hamburg, 2024



---

Department of Earth Sciences

Date of Oral Defense:

27.01.2025

Reviewers:

Dr. Nicolaas Glock

Prof. Dr. Gerhard Schmiedl

Members of examination commission:

Dr. Nicolaas Glock

Prof. Dr. Gerhard Schmiedl

Prof. Dr. Christian Möllmann

Prof. Dr. Annette Eschenbach

Dr. Birgit Gaye

Chair of the Subject Doctoral Committee

Earth System Sciences:

Prof. Dr. Hermann Held

Dean of Faculty MIN:

Prof. Dr.-Ing. Norbert Ritter

---

**Don't blindly believe what I say. Don't believe me because others convince you of my words. Don't believe anything you see, read, or hear from others, whether of authority, religious teachers or texts**

**Guatama Buddha**



## Table of Contents

<b>Acknowledgements</b> .....	<b>i</b>
<b>Abstract (English)</b> .....	<b>iv</b>
<b>Zusammenfassung (Deutsch)</b> .....	<b>vii</b>
<b>List of figures</b> .....	<b>x</b>
<b>List of tables</b> .....	<b>xv</b>
<b>Abbreviations</b> .....	<b>xvi</b>
<b>List of publications</b> .....	<b>xviii</b>
<b>Objectives of the project</b> .....	<b>1</b>
<b>1 Introduction</b> .....	<b>3</b>
1.1 The marine nitrogen cycle .....	3
1.2 Nitrogen isotopes in biogeochemistry .....	5
1.3 The perturbation of nitrogen cycle .....	6
1.4 Oxygen Minimum/Deficient Zones .....	8
1.4.1 Ocean deoxygenation and expansion of ODZs .....	10
1.4.2 Nitrogen cycle in the ODZs .....	11
1.5 Foraminifera .....	11
1.5.1 Pore density as a proxy for bottom-water nitrate ( $[\text{NO}_3^-]_{\text{BW}}$ ) reconstruction ...	13
1.6 Importance of reconstructing redox conditions in the ODZs .....	16
1.6.1 Benthic foraminiferal manganese as a proxy for bottom-water redox conditions .....	17
<b>2 Study area</b> .....	<b>20</b>
2.1 Sea of Okhotsk .....	20
2.2 Gulf of California (Guaymas Basin) .....	22
2.3 Mexican Margin .....	24
2.4 Gulf of Guayaquil .....	25
<b>3 A deep-learning automated image recognition method for measuring pore patterns in closely related bolivinids and calibration for quantitative nitrate paleo-reconstructions</b> .....	<b>28</b>
3.1 Introduction .....	29
3.2 Methods .....	32
3.2.1 Sampling of sediment cores .....	32
3.2.2 Sample processing .....	34
3.2.3 Bottom-water nitrate analyses at core-top locations .....	34
3.2.4 Bottom-water salinity, temperature and oxygen at core-top locations .....	34
3.2.5 Image acquisition .....	35
3.2.6 Size normalization .....	35
3.2.7 Automated image analysis .....	36
3.2.8 Comparison of manual vs. automatic pore density determination .....	36
3.2.9 Automated pore measurements with and without manual corrections .....	36
3.3 Results .....	37
3.3.1 Comparison between manual and automated pore density analyses .....	37
3.3.2 Automated pore measurements with and without manual corrections .....	37
3.3.3 Interdependence between pore parameters of <i>B. spissa</i> .....	37
3.3.4 Inter-species comparison of pore parameters and pore density vs $[\text{NO}_3^-]_{\text{BW}}$ calibration in the core-top samples .....	41

3.4	Discussion .....	43
3.4.1	Evaluation of the automatic image recognition technique .....	43
3.4.2	Variation of pore patterns in <i>B. spissa</i> from different environments .....	44
3.4.3	Biogeochemical controls on the pore patterns in the Gulf of Guayaquil .....	45
3.4.4	Genetic controls on the pore patterns in the Gulf of Guayaquil .....	46
3.4.5	An extended modern pore density vs. nitrate calibration .....	46
3.5	Conclusions .....	48
<b>4</b>	<b>Quantitative reconstruction of deglacial bottom-water nitrate in marginal Pacific seas using the pore density of denitrifying benthic foraminifera .....</b>	<b>51</b>
4.1	Introduction .....	52
4.2	Materials and methods .....	57
4.2.1	Study area and sampling of sediment cores .....	57
4.2.2	Sampling of foraminiferal specimens for the quantitative nitrate record .....	57
4.2.3	Automated image analysis .....	58
4.2.4	Optimization of age models .....	59
4.2.5	Sedimentary nitrogen isotope ( $\delta^{15}\text{N}_{\text{bulk}}$ ) measurements .....	60
4.2.6	Nitrate offset to present conditions .....	61
4.3	Results .....	62
4.3.1	Sea of Okhotsk (MD01-2415) .....	62
4.3.2	Gulf of California (DSDP-480) .....	63
4.3.3	Mexican Margin (MAZ-1E-04) .....	63
4.3.4	Gulf of Guayaquil (M77/2-59-01) .....	64
4.3.5	Comparison of nitrate offset ( $\Delta[\text{NO}_3^-]$ ) between the cores .....	66
4.4	Discussion .....	67
4.4.1	Sea of Okhotsk .....	67
4.4.2	Gulf of California .....	68
4.4.3	Mexican Margin .....	70
4.4.4	Gulf of Guayaquil .....	71
4.4.5	Comparison of past and present $[\text{NO}_3^-]_{\text{BW}}$ at the studied locations .....	72
4.5	Conclusion .....	74
<b>5</b>	<b>Reconstruction of redox conditions in the Oxygen Deficient Zones in the marginal seas of the Pacific Ocean using benthic foraminiferal Mn/Ca .....</b>	<b>77</b>
5.1	Introduction .....	78
5.2	Materials and methods .....	81
5.2.1	Study area and sampling of sediment cores .....	81
5.2.2	Cleaning protocol for bulk foraminiferal tests for Quadrupole ICP-MS .....	82
5.2.3	Cleaning protocol for single foraminiferal tests for laser ablation .....	83
5.2.4	Operating conditions and instrument calibration for LA-ICP-MS .....	83
5.2.5	Data treatment of laser ablation profiles .....	85
5.3	Results .....	86
5.3.1	Effect of oxidative cleaning on laser ablated benthic foraminiferal Mn/Ca ratios .....	86
5.3.2	Comparison of laser ablation Mn/Ca ratios of cleaned specimens and bulk ICP-MS data .....	89
5.3.3	Trends in laser ablation-derived Mn/Ca ratios in the studied ODZs .....	91
5.4	Discussion .....	93

---

5.4.1	Laser ablation of single specimens .....	93
5.4.2	Comparison of Mn/Ca ratios from Q-ICP-MS and LA-ICP-MS .....	95
5.4.3	Comparison of Mn/Ca ratios from cleaned and uncleaned specimens using LA-ICP-MS .....	96
5.4.4	Variation in Mn/Ca over the past 20,000 years ago in the studied ODZs .....	97
5.5	Conclusion .....	99
<b>6</b>	<b>Conclusion .....</b>	<b>102</b>
<b>7</b>	<b>Limitations and implications for future research .....</b>	<b>105</b>
	<b>References .....</b>	<b>107</b>
	<b>Appendix A .....</b>	<b>142</b>
	<b>Appendix B .....</b>	<b>183</b>
	<b>Appendix C .....</b>	<b>195</b>
	<b>Appendix D .....</b>	<b>199</b>
	<b>Contribution to publications .....</b>	<b>201</b>
	<b>Declaration on oath .....</b>	<b>202</b>

---



### **Acknowledgements**

I would like to thank my supervisor Dr. Nicolaas Glock for trusting me and giving me this job. Nico, the help and support you have given me over the last three years cannot be expressed in words. I am grateful for everything you have shown me, and you are the “best mentor” in my life so far. Apart from guiding me through the project, you taught me scientific integrity and the etiquette that a scientist, and an educator should follow for a better society. I will forever keep those ethics and values in my life; and I will cherish them in my life, no matter where I am and where I work. I am so happy and proud to say that I am your first PhD student. From the bottom of my heart, thank you, Nico.

To Prof. Dr. Gerhard Schmiedl, to the amazing human being, the educator and to the great scientist. Gerhard, I still remember the first time I met you in person in your office. Thank you for welcoming me into your group, and introducing me to everything. More than being a great scientist; Gerhard, your patience and kindness impressed me multiple times. I learnt a big lesson from you that no matter what your situation is, do your job, stay kind and helpful to others. I am grateful to have had this wonderful opportunity to be your student. Thank you, Gerhard for always being so supportive, and helpful.

To the love of my life Sreedhar Puliyakote, Sree, your patience and kindness have always encouraged me to go forward. Thank you for the immense encouragement and support you have given me and continue to give me. I love you Sree, thank you so much for being in my life.

To my mother Kala G. Menon, my father Govindankutty Menon, my brother Aswin G. Menon: Though it has been two years since we have seen each other, you all have always encouraged me to be patient and resilient. Thank you for all your support and encouragement. To my late grandmother, Radha: thank you for always encouraging me to be independent and persistent towards my life goals.

To my flatmate Cora: Thank you for always creating a friendly and nice atmosphere at home, introducing me to your parents, and house, and teaching me how to ride a horse. The atmosphere in our home immensely helped me to focus and work on my PhD thesis.

To all my friends in Hamburg: Chathu, Malu, Vivienne (Vivi), Chevaly, Tian, Sreevidya, Sakshi Singh for bringing moments of joy into my life in Hamburg. A special thank you to my friend Ya-

Qing (Hanna) for all our fun cooking times, and long conversations. I would have gone crazy without your company.

Special thanks to my friends Jofin Joykutty, Akshay A. Kumar, Thuc, Pham Duy Nghia, Aleena Elsa Mani for being so helpful whenever I needed it. I would like to thank Devika Varma for sharing your PhD experience and encouraging me.

Thanks to my fellow colleagues and staff at the micropaleontology group: Dr. Ulrich Kotthoff, Dr. Yvonne Milker, Benjamin, technician Jutta, master students Manja and Hanna Firrincielli, and secretary Jutta for all the help and support you provided me throughout these years. I would like to thank my fellow PhD peers: Daniela Eichner and Raphael Hubert-Huard for being friendly and helpful, especially Dani; thank you for all the help. A special thanks to Dr. Sha Ni for helping me whenever I am in trouble with data processing, and Prof. Dr. Dirk Nürnberg for being my biggest support system at Geomar.

To the teachers at my Indian university: Kerala University of Fisheries and Ocean Studies, India, especially Dr. Ranjeet K Sir, Dr. Ambili Kumar Sir, Dr. M. S. Raju Sir, and Dr. Rajeev Raghavan Sir for the great support that paved the way for my studies in Europe. I am grateful to have met great educators like you.

I would like to thank my school teachers especially Mariamma Miss (Kinder Garden), Latha Miss (Mathematics), Bindu Miss (History), Lins Miss (History), Nirmala Miss (Economics), Prof. Jose Sir (Physics), Sijo Sir (Zoology), Prof. Cherian Sir (Organic Chemistry) for encouraging me to develop a willingness to learn new things and to be open minded to new techniques. I would like to specially mention Rev. Father. Dr. Shaji Behanan (School Principal) for motivating me to aim for higher levels and never take “no” as an answer.

During my PhD, I read books such as “Atomic habits” by James Clear, “Planet Earth” by David Attenborough, “Nineteen-Eighty-Four” by George Orwell, “I want to eat Taekboki, but I want to die” by Baek Sehee, “Climate Change” by Mark Maslin, “Women Who Run with the Wolves” by Clarissa Pinkola Estes, “Desert Flower” by Waris Dirie, “Leap of Faith” by Queen Noor. All these books have strengthened my inner sense, resilience and improved my diplomacy and negotiating skills. I would like to thank all the above authors for writing about their experiences with brutal honesty.



### Abstract (English)

Global warming, together with increased anthropogenic activities such as the large-scale production and use of chemical nitrogen-fertilizers, and fossil fuels is accelerating the ongoing ocean deoxygenation and the expansion of Oxygen deficient zones (ODZs). The marine nitrogen cycle in the ODZs is of scientific interest because ODZs contribute to 30-50% of global reactive nitrogen loss through denitrification. Nitrate ( $\text{NO}_3^-$ ) is the most abundant form of reactive inorganic nitrogen in the ocean, and an important macronutrient that can be limiting in several ecosystems. Given the perturbation of the marine nitrogen cycle in the ODZs, it is important to understand past changes in oceanic nitrate concentrations ( $\text{NO}_3^-$ ) and redox conditions.

The shallow infaunal benthic foraminifera species *Bolivina spissa* and *Bolivina subadvena* are abundant in ODZs all around the Pacific. These species can denitrify and take up  $\text{NO}_3^-$  as an electron acceptor most likely through their pores, making their pore density an empirical proxy for  $\text{NO}_3^-$  in the bottom water ( $[\text{NO}_3^-]_{\text{BW}}$ ). In Chapter 3, a novel automated image analysis technique is developed that uses the software Amira 3D™ to detect pores in *B. spissa* and *B. subadvena* tests (i.e., shells). The interdependence between pore parameters such as pore density (number of pores per unit area), porosity (% of test-area occupied by the pores) and mean pore size (average pore size of an individual) of *B. spissa* and *B. subadvena* is investigated. The fully automated image analysis technique allows an efficient measurement of pore parameters, producing large datasets with statistically robust results. The pore densities of four different closely related *Bolivina* species are compared as a potential  $\text{NO}_3^-$  proxy. *Bolivina spissa* and *B. subadvena* showed the same correlation between pore density and  $[\text{NO}_3^-]_{\text{BW}}$ , while the pore density of *Bolivina argentea* and *Bolivina subadvena accumeata* is much higher and did not fit into this correlation. The results indicate a stronger correlation of  $[\text{NO}_3^-]_{\text{BW}}$  with pore density than with porosity.

In chapter 4, the method developed in chapter 3 is applied. The pore density of *B. spissa* and *B. subadvena* is used as a  $\text{NO}_3^-$  proxy to quantitatively reconstruct  $[\text{NO}_3^-]_{\text{BW}}$  in intermediate to deep water depths of the Sea of Okhotsk (MD01-2415), the Gulf of California (DSDP-480), the Mexican Margin (MAZ-1E-04) and the Gulf of Guayaquil (M77/2-059-1) over the last ~20 ka BP. Reconstructed  $[\text{NO}_3^-]_{\text{BW}}$  in the Sea of Okhotsk range from 32.5  $\mu\text{mol/kg}$  to 44.08  $\mu\text{mol/kg}$ , with  $[\text{NO}_3^-]_{\text{BW}}$  levels gradually increasing through time and reaching modern concentrations during the Middle-Holocene. Reconstructed  $[\text{NO}_3^-]_{\text{BW}}$  in the Gulf of California range from 41.4  $\mu\text{mol/kg}$  to

49.1  $\mu\text{mol/kg}$ , with elevated  $[\text{NO}_3^-]_{\text{BW}}$  during the glacial period compared to deglacial and modern conditions. Reconstructed  $[\text{NO}_3^-]_{\text{BW}}$  in the Gulf of Guayaquil range from 40.5  $\mu\text{mol/kg}$  to 46.5  $\mu\text{mol/kg}$ , with elevated  $[\text{NO}_3^-]_{\text{BW}}$  during the glacial period. Given, the intermediate water depths of the sites from the Sea of Okhotsk, the Gulf of California and the Gulf of Guayaquil, the  $[\text{NO}_3^-]_{\text{BW}}$  could be influenced by the changes in the intermediate water masses. The Mexican Margin  $[\text{NO}_3^-]_{\text{BW}}$  record range from 37.7  $\mu\text{mol/kg}$  to 43.5  $\mu\text{mol/kg}$  and show high  $[\text{NO}_3^-]_{\text{BW}}$  during the Younger Dryas, which could be related to the release of nutrient- and dissolved inorganic carbon-rich Pacific deep waters to intermediate depths during the deglacial period. However, changes in water-column denitrification, dissolved oxygen concentration, temperature difference, and primary productivity may also influence the  $[\text{NO}_3^-]_{\text{BW}}$  in these ODZs. The comparison of reconstructed past  $[\text{NO}_3^-]_{\text{BW}}$  and modern  $[\text{NO}_3^-]_{\text{BW}}$  suggests that the Gulf of California and the Gulf of Guayaquil have stronger ODZs today (higher denitrification). The higher modern  $[\text{NO}_3^-]_{\text{BW}}$  at the Mexican Margin and the Sea of Okhotsk suggests higher oxygen concentrations and thus less denitrification under modern conditions.

Finally, the redox conditions in these ODZs (Chapter 5) are investigated using redox-sensitive Mn/Ca of *B. spissa* and *B. subadvena*. The influence of chemical cleaning methods on individual foraminifera analyses using laser ablation is tested and appears to have a minor impact on the results of the microanalyses. Subsequently, the results of solution-based quadrupole inductively coupled plasma mass spectrometry (Q-ICP-MS) using bulk samples of *B. spissa* and *B. subadvena* are compared with the results of individual foraminifera analyses using laser ablation Q-ICP-MS. The Mn/Ca in the Sea of Okhotsk range from 1288.3 to 6188.8  $\mu\text{mol/mol}$ , and is  $\sim 100$  times higher than in the other studied ODZs, which could be related to a continuous and strong terrestrial supply of Mn. The Mn/Ca in the Gulf of Guayaquil range from 30.5 to 131  $\mu\text{mol/mol}$ , and indicate a transition from glacial hypoxic to Holocene suboxic conditions. The Mn/Ca in the Gulf of California range from 50 to 75.6  $\mu\text{mol/mol}$ , and indicate a long-time continuous preservation of organic matter in the foraminiferal tests at this site. This might be caused by a continuous oxygen depletion to the extent of anoxia over the last deglaciation in the Gulf of California. The Mn/Ca in the Mexican Margin range from 97.3 to 538.5  $\mu\text{mol/mol}$ , and may be influenced by a shift of the ODZ towards deeper water depths due to low sea level during the glacial period. This might have

caused a shift of the primary productivity center towards the continental margin, as a large part of shelf sediments were exposed during the last glacial maximum in this region.

Overall, the quantitative reconstruction of  $[\text{NO}_3^-]_{\text{BW}}$  and redox conditions in the Pacific ODZs provides a better understanding that different processes, and factors could influence these sites, and is not just limited to one single factor or process. As we monitor, predict and respond to the impacts of climate change and its effects on marine ecosystems, an improved ability to understand the functioning of ODZs will provide information about future risks to marine ecosystems.

### Zusammenfassung (Deutsch)

Die globale Erwärmung und zunehmende anthropogene Aktivitäten, wie die großflächige Produktion und Nutzung von chemischen Stickstoffdüngern und fossilen Brennstoffen, beschleunigen die fortschreitende Desoxygenierung der Ozeane und die Ausbreitung sauerstoffarmer Zonen (ODZs). Der marine Stickstoffkreislauf in ODZs ist von wissenschaftlichem Interesse, da ODZs zu 30-50% des globalen reaktiven Stickstoffverlusts durch Denitrifikation beitragen. Nitrat ( $\text{NO}_3^-$ ) ist die häufigste Form von reaktivem anorganischem Stickstoff im Meer und ein wichtiger Makronährstoff, der in verschiedenen Ökosystemen limitierend wirken kann. Da der marine Stickstoffkreislauf in den ODZs gestört ist, ist es wichtig, die vergangenen Veränderungen von marinen Nitratkonzentrationen ( $[\text{NO}_3^-]$ ) und Redoxbedingungen zu verstehen.

Kapitel 3 beschäftigt sich mit der Weiterentwicklung eines quantitativen  $[\text{NO}_3^-]$  Proxies. Die benthischen Foraminiferen-Arten *Bolivina spissa* und *Bolivina subadvena* sind in den ODZs im gesamten Pazifik weit verbreitet. Diese Arten können denitrifizieren und nehmen wahrscheinlich  $\text{NO}_3^-$  als Elektronenakzeptor durch ihre Poren auf, was ihre Porendichte zu einem empirischen Indikator für  $\text{NO}_3^-$ -konzentrationen im Bodenwasser ( $[\text{NO}_3^-]_{\text{BW}}$ ) macht. Eine automatisierte Bildanalysetechnik mit der Software Amira 3D™ (Kapitel 3) wurde entwickelt, um Poren in den Gehäusen von *B. spissa* und *B. subadvena* zu erkennen. Die Interdependenz zwischen Porenparametern wie Porendichte (Anzahl der Poren pro Flächeneinheit), Porosität (prozentualer Anteil der Gehäusefläche, der von Poren eingenommen wird) und durchschnittliche Porengröße (durchschnittliche Porengröße eines Individuums) von *B. spissa* und *B. subadvena* wird untersucht. Die automatische Bildanalysetechnik ermöglicht eine effiziente Messung der Porenparameter und liefert große Datensätze mit statistisch zuverlässigen Ergebnissen. Die Porendichte und Porosität von vier verschiedenen, eng verwandten *Bolivina*-Arten werden als potenzieller  $\text{NO}_3^-$  Proxy verglichen. *Bolivina spissa* und *B. subadvena* zeigen die gleiche Korrelation zwischen Porendichte und  $[\text{NO}_3^-]_{\text{BW}}$ , während die Porendichte von *Bolivina argentea* und *Bolivina subadvena accumeata* viel höher ist und nicht in diese Korrelation passt. Die Ergebnisse zeigen eine stärkere Korrelation von  $[\text{NO}_3^-]_{\text{BW}}$  mit der Porendichte als mit der Porosität.

In Kapitel 4 wird nach der in Kapitel 3 verfeinerten Methode die Porendichte von *B. spissa* und *B. subadvena* als  $[\text{NO}_3^-]_{\text{BW}}$  Proxy verwendet (Kapitel 4), um die  $[\text{NO}_3^-]_{\text{BW}}$  in den mittleren bis tiefen Wassertiefen des Ochotskischen Meeres (MD01-2415), des Golfs von Kalifornien (DSDP-480), des mexikanischen Kontinentalhanges (MAZ-1E-04) und des Golfs von Guayaquil (M77/2-059-1) über die letzten ~20.000 Jahre quantitativ zu rekonstruieren. Die rekonstruierten  $[\text{NO}_3^-]_{\text{BW}}$ -Werte im Ochotskischen Meer reichen von 32,5  $\mu\text{mol/kg}$  bis 44,08  $\mu\text{mol/kg}$ , wobei die  $[\text{NO}_3^-]_{\text{BW}}$ -Werte im Laufe mit der Zeit allmählich ansteigen und im mittleren Holozän nahezu moderne Konzentrationen erreichen. Die rekonstruierten  $[\text{NO}_3^-]_{\text{BW}}$  im Golf von Kalifornien reichen von 41,4  $\mu\text{mol/kg}$  bis 49,1  $\mu\text{mol/kg}$ , wobei die  $[\text{NO}_3^-]_{\text{BW}}$  während der Eiszeit im Vergleich zu deglazialen und modernen Bedingungen erhöht waren. Die rekonstruierte  $[\text{NO}_3^-]_{\text{BW}}$  im Golf von Guayaquil reicht von 40,5  $\mu\text{mol/kg}$  bis 46,5  $\mu\text{mol/kg}$ , mit erhöhter  $[\text{NO}_3^-]_{\text{BW}}$  während der Eiszeit. In den aus mittleren Wassertiefen entnommenen Bohrkernen aus dem Ochotskischen Meer, dem Golf von Kalifornien und dem Golf von Guayaquil könnte die  $[\text{NO}_3^-]_{\text{BW}}$  durch die Veränderungen in den Zwischenwassermassen beeinflusst sein. Die  $[\text{NO}_3^-]_{\text{BW}}$  am mexikanischen Kontinentalhang reichen von 37,7  $\mu\text{mol/kg}$  bis 43,5  $\mu\text{mol/kg}$  und zeigen besonders hohe  $[\text{NO}_3^-]_{\text{BW}}$  während der Jüngeren Dryas, was mit der Freisetzung von nährstoff- und kohlenstoffreichem pazifischen Tiefenwasser während der Deglaziation zusammenhängen könnte. Verschiedene Faktoren und Prozesse wie Änderungen der Denitrifikation in der Wassersäule, des gelösten Sauerstoffs, Temperaturunterschiede und die Primärproduktivität können jedoch auch die  $[\text{NO}_3^-]_{\text{BW}}$  in diesen ODZs beeinflussen. Ein Vergleich der rekonstruierten  $[\text{NO}_3^-]_{\text{BW}}$  in der Vergangenheit mit der heutigen  $[\text{NO}_3^-]_{\text{BW}}$  deutet darauf hin, dass der Golf von Kalifornien und der Golf von Guayaquil heute stärkere ODZs haben und höhere Denitrifikation aufweisen. Der höhere moderne  $[\text{NO}_3^-]_{\text{BW}}$  am mexikanischen Kontinentalhang und im Ochotskischen Meer deutet auf eine heute erhöhte Sauerstoffkonzentration und damit eine geringere Denitrifikation hin.

Schließlich werden die Redoxbedingungen in den ODZs (Kapitel 5) anhand des Mn/Ca-Verhältnisses in den Gehäusen von *B. spissa* und *B. subadvena* untersucht. Dafür werden zuerst der Einfluss chemischer Reinigungsmethoden auf die Ergebnisse von Mikroanalysen mittels Laserablation untersucht. Zusätzlich werden die Ergebnisse von lösungsbasierter Quadrupol-Induktiv Gekoppelter Massenspektrometrie (Q-ICP-MS) mit ca. 20 Individuen pro Probe und Laserablations Q-ICP-MS an individuellen Foraminiferen verglichen. Die Mn/Ca im

Ochotskischen Meer reichen von 1288,3 bis 6188,8  $\mu\text{mol/mol}$  und sind  $\sim 100$  mal höher als in den anderen untersuchten ODZs, was auf eine kontinuierliche und starke terrestrische Mn-Zufuhr in diesem Gebiet zurückzuführen sein könnte. Die Mn/Ca im Golf von Guayaquil reichen von 30,5 bis 131  $\mu\text{mol/mol}$  und deuten auf einen Übergang von glazialen hypoxischen zu holozänen suboxischen Bedingungen hin. Die Mn/Ca im Golf von Kalifornien reichen von 50 bis 75,6  $\mu\text{mol/mol}$ , und es erscheint, dass organisches Material in den Foraminiferenproben über einen langen Zeitraum gut erhalten ist. Dies deutet auf eine kontinuierliche Sauerstoffverarmung bis hin zur Anoxie im Golf von Kalifornien hin. Das Mn/Ca-Verhältnis am mexikanischen Kontinentalhang reicht von 97,3 bis 538,5  $\mu\text{mol/mol}$  und könnte durch die Verlagerung der ODZ aufgrund des niedrigen Meeresspiegels während der Eiszeit beeinflusst worden sein.

Insgesamt bietet die quantitative Rekonstruktion von  $[\text{NO}_3^-]_{\text{BW}}$  und Redox-Bedingungen in den pazifischen ODZ ein umfassendes Verständnis dafür, dass verschiedene Prozesse und Faktoren diese Standorte beeinflussen können und nicht nur auf einen einzigen Faktor/Prozess beschränkt sind. In dem Maße, wie wir die Auswirkungen des Klimawandels und seine Folgen für die Meeresökosysteme überwachen, vorhersagen und darauf reagieren, wird eine verbesserte Fähigkeit, die Funktionsweise der ODZ zu verstehen, Informationen über zukünftige Risiken für die Meeresökosysteme liefern.

## List of figures

### Chapter 1

- Figure.1.1 Schematic diagram of the marine nitrogen cycle, and the major processes involved, such as the nitrogen fixation, assimilation, nitrification, anammox and denitrification. Modified after Sollai et al. (2015). The processes responsible for the gain of nitrogen to the ocean are in green, and the loss of nitrogen in red .....4
- Figure.1.2 The overall world population trend in relation to the production of artificial nitrogen fertilizers. The source of the image is from Erisman et al. (2008).....7
- Figure.1.3 The dissolved oxygen concentrations at the major ODZs such as the Eastern Tropical North Pacific (ETNP), Eastern Tropical South Pacific (ETSP), Arabian Sea (AS), Bay of Bengal (BB), Black Sea, Cariaco Basin, Baltic Sea, Northwest Africa Upwelling (NWAU), and Eastern Tropical South Atlantic (ETSA) are shown in the map. The source of the image is from the ODZ review by Wakeham, (2020).....9
- Figure.1.4 Schematic view of uptake of  $\text{NO}_3^-$  and the excretion of  $\text{N}_2$  by benthic foraminifera *Bolivina spissa* and the step-wise denitrification pathway.....12
- Figure.1.5 Scanning Electron Microscopic (SEM) images of the benthic foraminiferal species *Bolivina spissa* and *Bolivina subadvena* from different sampling locations used for the PhD work. ....15

### Chapter 2

- Figure.2.1 Map of the Sea of Okhotsk along with main surface currents and bathymetry. Surface currents such as East Sakhalin Current (ESC), North Okhotsk Current (NOC), West Kamchatka Current (WKC), Compensation Kamchatka Current (CKC), Soya Current (SC) are shown on the map. The Amur River is shown in light blue color. The red cross depicts the location from which the core MD01-2415 is collected. Ocean Data View is used for the map (Schlitzer, R., 2023).....21
- Figure.2.2 Map of Gulf of California. The major ocean currents such as the California Current and California Undercurrent are shown in the map. Entrance Zone is in open connection with the Eastern Tropical Pacific Ocean, SGC is the Southern Gulf of California, and NGC is the Northern Gulf of California which has shelf sea characteristics (Lavín and Marinone, 2003). The red cross depicts the location from which the sediment core DSDP – 480 has been collected. Ocean Data View is used for the map (Schlitzer, R., 2023).....23

Figure.2.3 The study area Mazatlán coast in the Northwest Mexican Margin. The circulation of water masses such as the North Pacific Intermediate Water (NPIW), Subtropical Surface Water (StSW), Equatorial Pacific Intermediate Water (EqPIW), and Tropical Surface Water (TSW) are shown in the map. The red cross depicts the location from which the sediment core MAZ-1E-04 has been collected. The Ocean Data View software has been used for the map (Schlitzer, R., 2023).....24

Figure.2.4 Sample location off Peru and environmental setting at the Gulf of Guayaquil. Surface currents such as South Equatorial Current (SEC), Peru Chile Current (PCC) are shown. Subsurface currents such as the Equatorial Under Current (EUC), Southern Subsurface Counter Current (SSCC), Peru Chile Under Current (PCUC) are shown in the map. The red cross depicts the location from where the sediment core M77/2-59-01 has been retrieved. The prominent surface and subsurface water masses are indicated as Tropical Surface Water (TSW), Equatorial Surface Water (ESW), Subtropical Surface Water (SSW) and Subantarctic Mode Water (SAMW). The TSW and ESW are separated by the Equatorial Front (EF). The Ocean Data View software has been used to create this map (Schlitzer, R., 2023). .....26

**Chapter 3**

Figure.3.1 a) Scanning Electron Microscopic images of *B. spissa* collected from the Mexican Margin (MAZ-1E-04), (water depth: 1463m) and b) their total area relative to first (oldest) ~ten chambers within 50,000 – 70,000  $\mu\text{m}^2$  measured using ZEN lite software.....31

Figure.3.2 Map showing site locations studied: Gulf of Guayaquil (M77/2-59-01, depth: 997 m), Mexican Margin (MAZ-1E-04, depth: 1463 m), Sea of Okhotsk (MD01-2415, depth: 822 m), core-top samples from Costa Rica (Quepos Slide, SO206-43-MUC, depth: 568 m), and Sagami Bay (Japan, depth: 1410). The map was produced using Ocean Data View (Schlitzer, R., 2023) .....32

Figure.3.3 Relationship between a) porosity vs. mean pore size b) porosity vs. pore density, and c) pore density vs. mean pore size of *B. spissa* specimens from the Gulf of Guayaquil (M77/2-59-01), the Mexican Margin (MAZ-1E-04), the Sea of Okhotsk (MD01-2415), and the core-top samples (Sagami Bay and Costa Rica). Total number of specimens utilized, n = 1344.....40

Figure.3.4 Correlation between the mean pore density of different closely related *Bolivina* species from core-top samples and  $[\text{NO}_3^-]_{\text{BW}}$ . If no species name is indicated, the analysed species was *B. spissa*. The specimens of *B. subadvena*, *B. subadvena accumeata* and *B. argentea* are all from location SO206-43-MUC off Costa Rica, except the one specimen of *B. subadvena* at  $\sim 42 \mu\text{mol/kg}$   $[\text{NO}_3^-]_{\text{BW}}$  that was collected at Sagami Bay (Japan). The linear fit (all data) has been applied to all available data for *B. spissa* and *B. subadvena*, except *B. subadvena accumeata* and *B. argentea*. **a)** Pore density vs  $[\text{NO}_3^-]_{\text{BW}}$  plot including all analysed *Bolivina* species. **b)** Pore density vs  $[\text{NO}_3^-]_{\text{BW}}$  plot only including *B. spissa* and *B. argentea*. The linear fit (Peru) alone was the published correlation from Glock et al. (2011 & 2018) and only included *B. spissa* collected off Peru. Error bars are the standard error of the mean (1SE) .....42

Figure.3.5 Scanning Electron Microscopic images of bolivinids a) *B. spissa*, b) *B. subadvena* c) *B. subadvena accumeata*, and d) *B. argentea* .....47

#### **Chapter 4**

Figure.4.1 Scanning electron microscope images of a) *Bolivina spissa* (Mexican Margin) and b) *Bolivina subadvena* (Gulf of California) used for the current study.....54

Figure.4.2 Location of sediment cores used in the current study and mean annual oxygen concentrations at 300 m depth (Garcia et al., 2019). The core sites of this study are in yellow triangles, and cores are taken from the Sea of Okhotsk (core MD01-2415; water depth: 822 m), the Gulf of California (core DSDP- 480; water depth: 747 m), the Mexican Margin (core MAZ-1E-04; water depth: 1468 m), and the Gulf of Guayaquil (Peru, core M77/2-59-01; water depth: 997 m). Ocean Data View software has been used to create the map (Schlitzer, R., 2023). .....55

Figure.4.3 Modern oceanographic a) salinity and b) nitrate distribution of sediment cores used for  $[\text{NO}_3^-]_{\text{BW}}$  reconstruction. Overview of major deeper ocean currents in the Pacific Ocean. Formation areas of North Pacific Intermediate Water (NPIW) and Southern Ocean Intermediate Water (SOIW) are shown here. The blue arrows show the major subsurface to deep water masses such as Equatorial Pacific Intermediate Water (EqPIW), Equatorial Undercurrent (EUC), NPIW, SOIW, Pacific Deep Water (PDW), Antarctic Bottom Water (AABW), and Circumpolar Deep Water (CDW). The red crosses show the location of the studied cores MD01-2415, DSDP- 480, MAZ-1E-04, and M77/2-59-01 projected to the N

- S salinity transect. Map was generated using Ocean Data View (Schlitzer, R., 2023) using the data from World Ocean Atlas 2018 (Garcia et al., 2019) .....56

Figure.4.4 Quantitative  $[\text{NO}_3^-]_{\text{BW}}$  reconstruction using the pore density of 1541 fossil specimens of *B. spissa*, *B. subadvena* in comparison to the sedimentary nitrogen isotope ( $\delta^{15}\text{N}_{\text{bulk}}$ ) records of sediment cores from a) the Sea of Okhotsk (MD01-2415), b) the Gulf of California (DSDP-480), c) the Mexican Margin (MAZ-1E-04), and foraminifera-bound (Studer et al 2021)  $\delta^{15}\text{N}_{\text{FB}}$  data from core ME-24 (violet line) and d) the Gulf of Guayaquil (M77/2-59-01). The  $\delta^{15}\text{N}_{\text{bulk}}$  data was not available for the Mexican Margin. The error bars represent 1 SE including a complete error propagation (using equation Eq 4.2 and 4.3). Total Organic Carbon, TOC (%) data taken from published literature (Bubenshchikova et al., 2015; Leclaire & Kerry, 1982; Mollier-Vogel et al., 2019) is shown in blue dashed lines for the Sea of Okhotsk, the Gulf of California and the Gulf of Guayaquil cores respectively. The TOC data was not available for the Mexican Margin core. Time intervals such as Middle to Late Holocene (MLH), Early Holocene (EH), Younger Dryas (YD), Bølling-Allerød (BA), Heinrich Stadial 1 (H1), and Last Glacial Maximum (LGM) are shown in the figure.....65

Figure.4.5 The relative changes of  $[\text{NO}_3^-]_{\text{BW}}$  calculated from the pore density of benthic foraminifera *B. spissa* and *B. subadvena* from all studied cores compared to modern  $\text{NO}_3^-$  at each location. This provides the nitrate offset ( $\Delta[\text{NO}_3^-]$  ( $\mu\text{M}$ )). The modern nitrate at the different locations has been taken from the World Ocean Atlas, 2018 (Garcia et al., 2019). Error bars represent 1 SE.....66

**Chapter 5**

Figure.5.1 Schematic diagram of shallow infaunal benthic foraminifera and their relationship with the sediment redox boundaries and calcification depth. Image modified from Ní Fhlaithearta et al. (2018) .....80

Figure.5.2 Study area of the Pacific Ocean with oxygen concentration at 300 m water depth and locations of study sites in the Sea of Okhotsk (MD01-2415), Gulf of California (DSDP-480), Mexican margin (MAZ-1E-04), and Gulf of Guayaquil (M77/2-59-01). Ocean Data View (Schlitzer, R., 2023) has been used for the construction of the map using the data from World Ocean Atlas, 2008 .....81

Figure.5.3 Scanning electron microscope (SEM) images of a) *Bolivina spissa* b) *Bolivina subadvena* specimens after laser ablation analysis of multiple chambers including the proloculus. ....85

Figure.5.4 Comparison of Mn/Ca ratios of cleaned and uncleaned specimens of *B. spissa* and *B. subadvena* using LA-ICP-MS from the a) Gulf of Guayaquil, b) the Mexican margin c) the Gulf of California. The specimens indicated by black squares represents the average Mn/Ca value of uncleaned specimen while the orange triangles are the chemically cleaned specimens. SN depicts the Sample Number. Error bars show 1SE.....88

Figure.5.5 The Mn/Ca ratios of cleaned single specimens of *B. spissa* and *B. subadvena* and bulk Q-ICP-MS data from a) the Gulf of Guayaquil b) the Mexican margin, and c) the Gulf of California. The error bars show heterogeneity (2SD). ....90

Figure.5.6 The Mn/Ca of benthic foraminiferal specimens *B. spissa* and *B. subadvena* from the a) Sea of Okhotsk b) Gulf of California c) Mexican margin and d) the Gulf of Guayaquil over the last 20, 000 years ago. The red lines represent the average Mn/Ca ratios from single foraminiferal specimens using LA-ICP-MS. The dashed red lines represent the bulk Mn/Ca ratios, except for the Sea of Okhotsk. The bulk Mn/Ca was not measured for the Sea of Okhotsk core, due to lack of *B. spissa* specimens. The black lines represent the reconstructed  $[\text{NO}_3^-]_{\text{BW}}$  data using the pore density of *B. spissa* and *B. subadvena* from the same study sites. Error bars represent 1SD.....92

**List of tables**

Table.1.1 Oxygen conditions in the ODZs taken from Levin (2018), Erdem et al. (2020) .....9

Table.3.1 Site location information and distribution of specimens (*B. spissa*) from different sampling locations used in the study.....33

Table.3.2 Bottom-water conditions at the sampling locations that have been used for the core-top calibration. Sampling locations in italic letters have been taken from Glock et al. (2011) ....35

Table.4.1 Site location information of modern  $[\text{NO}_3^-]_{\text{BW}}$  taken for the nitrate offset from World Ocean Atlas 2018.....61

Table.5.1 Laser controls for the standards.....84

Table.5.2 Absolute elemental values and external reproducibility for the duration of this study (relative standard deviation (r.s.d)) of NIST 610 silicate glass standard in comparison to absolute values from Jochum et al. (2011). NFHS is the calibration standard for Mn/Ca of the foraminiferal samples, using the recommended values for Jochum et al. (2011) .....86

Table.5.3 Mean ( $\pm$ SD) of Mn/Ca ratios of cleaned and uncleaned benthic foraminiferal specimens of *B. spissa* and *B. subadvena* from different study locations. N is the number of laser ablations.....87

**Abbreviations**

$[\text{NO}_3^-]_{\text{BW}}$	Bottom-water nitrate
$[\text{O}_2]_{\text{BW}}$	Bottom-water oxygen
AABW	Antarctic Bottom Water
AMS	Accelerator Mass Spectrometry
AS	Arabian Sea
BA	Bølling-Allerød Event
BB	Bay of Bengal
BNF	Biological Nitrogen Fixation
BSE	Back-Scattered Electron
CDW	Circumpolar Deep Water
CKC	Compensation Kamchatka Current
CNN	Convolutional Neural Network
DSDP	Deep-Sea Drilling Project
EEP	Eastern Equatorial Pacific
EF	Equatorial Front
EH	Early Holocene
EqPIW	Equatorial Pacific Intermediate Water
ESC	East Sakhalin Current
ETNP	Eastern Tropical North Pacific
ETSA	Eastern Tropical South Atlantic
ETSP	Eastern Tropical South Pacific
EUC	Equatorial Under Current
H1	Heinrich Stadial
ICN	Intracellular Nitrate
IRMS	Isotope Ratio Mass Spectrometer
ITCZ	Intertropical Convergence Zone
LA-ICP-MS	Laser Ablation Inductively Coupled Plasma Mass Spectrometry
LGM	Last Glacial Maximum
MLH	Middle to Late Holocene
MRA	Marine Reservoir Age
NGC	Northern Gulf of California
NOC	North Okhotsk Current
NPDW	North Pacific Deep Water
NPIW	North Pacific Intermediate Water
NWAU	Northwest Africa Upwelling
ODZs	Oxygen Deficient Zones
OMZs	Oxygen Minimum Zones
OSIW	Okhotsk Sea Intermediate Water
PCC	Peru Chile Current
PCUC	Peru Chile Under Current
PD	Pore density
PDW	Pacific Deep Water
Q-ICP-MS	Quadrupole Inductively Coupled Plasma Mass Spectrometry

ROW	Reverse Osmosis Water
SAMW	Subantarctic Mode Water
SC	Soya Current
SD	Standard Deviation
SE	Standard Error of the Mean
SEC	South Equatorial Current
SEM	Scanning Electron Microscope
SGC	Southern Gulf of California
SOIW	Southern Ocean Intermediate Water
SSCC	Southern Subsurface Counter Current
SST	Sea Surface Temperature
StSW	Subtropical Surface Water
TN	Total Nitrogen
TOC	Total Organic Carbon
TSW	Tropical Surface Water
WKC	West Kamchatka Current
YD	Younger Dryas

### **List of publications**

The PhD thesis is based on three scientific publications.

The first research article is published in an international journal, and is included as chapter 3.

- Govindankutty Menon, A., Davis, C. V., Nürnberg, D., Nomaki, H., Salonen, I., Schmiedl, G., & Glock, N. A deep-learning automated image recognition method for measuring pore patterns in closely related bolivinids and calibration for quantitative nitrate paleo-reconstructions. *Scientific Reports*, 13(1), 19628 (2023).

<https://www.nature.com/articles/s41598-023-46605-y#Sec24>

The second research article is prepared and is ready to be submitted to an international journal, and is included as chapter 4.

- Govindankutty Menon, A., Bieler, A.L., Firrincieli, H., Lahajnar, N., Alcorn, R., Davis, C.V., Martinez-Garcia, A., Schiebel, R., Nürnberg, D., Schmiedl, G., Glock, N. Quantitative reconstruction of deglacial bottom-water nitrate in marginal Pacific seas using the pore density of denitrifying benthic foraminifera.

The third research article is prepared and is ready to be submitted to an international journal, and is included as chapter 5.

- Govindankutty Menon, A., Barras, C., Hathorne, E., Nürnberg, D., Davis, C.V., Schmiedl, G., Glock, N. Reconstruction of redox conditions in the Oxygen Deficient Zones in the marginal seas of the Pacific Ocean using benthic foraminiferal Mn/Ca.

### **Objectives of the project**

The PhD work focuses on the paleo-reconstruction of bottom-water nitrate ( $[\text{NO}_3^-]_{\text{BW}}$ ) and redox conditions using sediment cores from four different oxygen deficient zones (ODZs) around the Pacific, including the Sea of Okhotsk, the Gulf of California (Guaymas Basin), the Mexican Margin, and the Gulf of Guayaquil (Peru).

**Objective 1:** The development of a fully automated image analysis technique for pore recognition in benthic foraminifera, *Bolivina spissa* and *Bolivina subadvena*.

**Objective 2:** The calibration of the pore density of *B. spissa* and *B. subadvena* as an empirical proxy for  $[\text{NO}_3^-]_{\text{BW}}$ .

#### **Research questions:**

1. How to develop a fully automated image analysis technique for foraminiferal pore detection that is non-destructive, fast, and can produce large statistically robust data sets?
2. Which pore parameters can be utilized as a better proxy for  $[\text{NO}_3^-]_{\text{BW}}$  reconstructions, and why?

**Objective 3:** The application of the fully automated image analysis technique to quantitatively reconstruct  $[\text{NO}_3^-]_{\text{BW}}$  in four different oxygen deficient zones (ODZs) in the Pacific and its marginal sea basins during the last deglaciation.

**Objective 4:** The reconstructed  $[\text{NO}_3^-]_{\text{BW}}$  is compared with nitrogen isotope signatures of sedimentary organic matter ( $\delta^{15}\text{N}_{\text{bulk}}$ ) to constrain changes in the balance of different  $\text{NO}_3^-$  sources and sinks within the past nitrogen cycle.

**Objective 5:** The present and the past  $[\text{NO}_3^-]_{\text{BW}}$  in the four different ODZs are compared to quantify the changes.

#### **Research questions:**

1. What are the potential processes and/or factors that could have influenced the  $[\text{NO}_3^-]_{\text{BW}}$  in the different ODZs during the last deglaciation?
2. How does pore density reconstructed  $[\text{NO}_3^-]_{\text{BW}}$  data from benthic foraminifera correlate to sedimentary  $\delta^{15}\text{N}$  signatures?

**Objective 6:** The application of Manganese to Calcium ratios (Mn/Ca) from the tests of *B. spissa* and *B. subadvena* as an independent redox proxy for changes in redox conditions to uncouple the changes in nutrient concentrations from local oxygen (O<sub>2</sub>) fluctuations.

**Objective 7:** The comparison of Mn/Ca ratios obtained by laser ablation of chemically cleaned foraminifera specimens with uncleaned specimens to see the effect of chemical cleaning.

**Objective 8:** The comparison of Mn/Ca from bulk samples of foraminifera measured with solution-based quadrupole inductively coupled plasma mass spectrometry (Q-ICP-MS) and individual foraminifera specimens measured with laser ablation Q-ICP-MS.

**Research questions:**

1. How does Mn/Ca determined by laser ablation Q-ICP-MS of chemically cleaned foraminifera specimens differ from uncleaned specimens?
2. How similar and comparable is the Mn/Ca of bulk samples of foraminifera from the Mn/Ca of laser ablated individual foraminifera specimens?
3. What are the changes in redox conditions in the different ODZs from the glacial period to the Holocene, and what processes or factors could have influenced the Mn/Ca signatures in the tests of *B. spissa* and *B. subadvena*?

## Chapter 1 Introduction

### 1.1 The marine nitrogen cycle

Nitrogen is an abundant element (atomic mass = 14.0067) in Earth's atmosphere, biosphere and hydrosphere (Henry et al., 2000; Stüeken et al., 2016) and an important building block of amino acids, proteins and nucleic acids (DNA, RNA) (Smil, 2004). Although it is abundant, nitrogen exists almost entirely in the form of molecular nitrogen ( $N_2$ ) with a strong triple chemical bond (Galloway et al., 2004). This chemical state of  $N_2$  cannot be used for energy needs for 99% of living organisms as a large amount of energy is needed to break this triple bond (Galloway et al., 2003). The nitrogen compounds in nature can be divided into two groups: nonreactive and reactive (or bioavailable) (Galloway et al., 2003). The nonreactive nitrogen is molecular nitrogen,  $N_2$ . All nitrogen compounds which are biologically, photochemically, and radioactively active in the Earth's atmosphere and biosphere includes the bioavailable nitrogen (Galloway et al., 2003, 2004). Nitrogen has many different reactive forms as nitrogen is redox sensitive (Li et al., 2021; Johnson et al., 2022), and exists in oxidation state ranging from +5 (in  $NO_3^-$ ) to -3 (in  $NH_4^+$ ). The bioavailable nitrogen includes inorganic reduced forms of nitrogen such as ammonia [ $NH_3$ ] and ammonium [ $NH_4^+$ ], inorganic oxidized forms (e.g., nitrogen oxide [ $NO_x$ ], nitric acid [ $HNO_3$ ], nitrous oxide [ $N_2O$ ], nitrite ( $NO_2^-$ ) and nitrate [ $NO_3^-$ ]), and organic compounds (e.g., urea, amines, proteins, and nucleic acids) (Galloway et al., 2003). These bioavailable nitrogen compounds are considered as "fixed" nitrogen (Gruber and Galloway, 2008; Casciotti et al., 2024).

The marine nitrogen cycle (**Fig.1.1**) is a complex web of microbially mediated processes that control the inventory and distribution of reactive nitrogen in marine environments (Voss et al., 2013; Casciotti, 2016a), and is linked to the availability of carbon (Gruber and Galloway, 2008; Ader et al., 2016), phosphorus (Deutsch et al., 2007), and trace elements. Nitrogen is very redox sensitive, and therefore nitrogen cycle is closely related to the redox state of the ocean, and the atmosphere (Li et al., 2021). Microbial transformations (see **Fig. 1.1**) such as nitrogen fixation, assimilation, nitrification, anammox and denitrification are important processes involved in the marine nitrogen cycle (Voss et al., 2013). Nitrate ( $NO_3^-$ ) is the most abundant form of reactive inorganic nitrogen and can be a main limiting nutrient for phytoplankton in most of the tropical and subtropical oceans (Arrigo, 2005; Lam et al., 2009; Moore et al., 2013). Nitrate also directly influences the productivity and carbon sequestration in the ocean via the biological pump (Karl et

al., 2002; Gruber, 2004). The  $\text{NO}_3^-$  concentrations in the tropics and subtropics vary from zero in the surface waters up to several tens of micromoles per liter in the temperate and Arctic and Antarctic Oceans (Voss et al., 2013). Through denitrification, a bacterial mediated process occurring only in low oxygen ( $<5 \mu\text{mol/kg}$ ) environments (Codispoti et al., 2001; Levin, 2018),  $\text{NO}_3^-$  is converted into dinitrogen gas (Korom, 1992) which is lost to the atmosphere (Richter and Markewitz, 2001). Thus, denitrification creates a  $\text{NO}_3^-$  deficit in global oceans in relation to other macronutrients such as phosphate,  $\text{PO}_4^{3-}$  (Tyrrell, 1999; Codispoti et al., 1995; Codispoti et al., 2001; Gruber, 2004). Denitrification occurs both in the water column and in the sediments (Christensen et al., 1987). Of these, the largest sink of bioavailable nitrogen in the ocean occurs in the sediments; approx. 100 to 200 Tg N/yr (Dale et al., 2016 and references therein). The global ocean nitrogen inventory is a balance between nitrogen fixation (gain of bioavailable nitrogen) at the ocean's surface and the removal of nitrogen (loss of bioavailable nitrogen) by water-column and sediments (Karl et al., 2002). However, the estimates of nitrogen loss range widely and are a major uncertainty in the marine nitrogen budget (Gruber and Sarmiento, 1997; Brandes and Devol, 2002; Wang et al., 2019). The Last Glacial Maximum (LGM) ~22,000 years ago, observed reduced nitrogen loss processes due to lower temperatures, higher oxygen solubility and improved oxygen supply to the upper ocean ODZs (Jaccard and Galbraith, 2012).

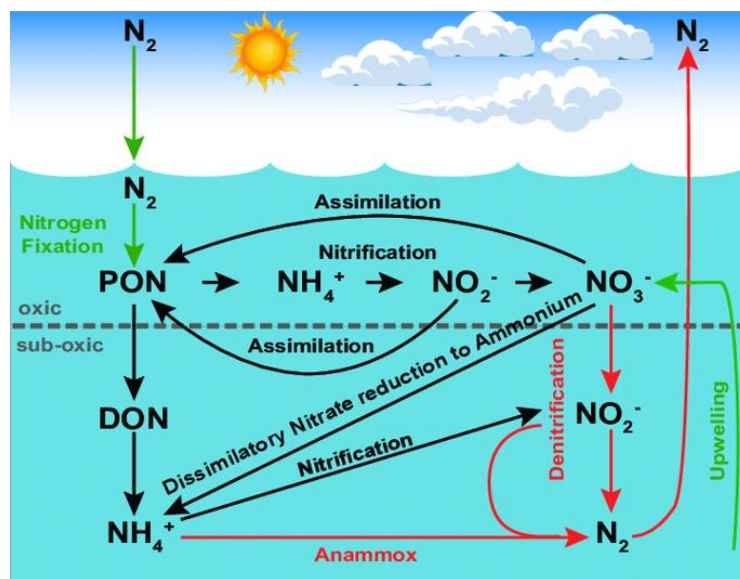


**Figure 1.1.** Schematic diagram of the marine nitrogen cycle, and the major processes involved, such as the nitrogen fixation, assimilation, nitrification, anammox and denitrification. Modified after Sollai et al. (2015). The processes responsible for the gain of nitrogen to the ocean are in green, and the loss of nitrogen in red.

## 1.2 Nitrogen isotopes in biogeochemistry

Nitrogen has two stable isotopes,  $^{14}\text{N}$  (~99.632%) and  $^{15}\text{N}$  (~0.368%) (Stüeken et al., 2016). The reactions within the nitrogen cycle are often accompanied by isotopic fractionation between the two stable isotopes,  $^{14}\text{N}$  and  $^{15}\text{N}$  (Falkowski and Godfrey, 2008; Casciotti, 2009). The isotope values are often expressed as delta (“ $\delta$ ”) notation expressing the ratio of heavy isotope compared to light isotope relative to an international standard (Fry, 2006). The international reference standard for  $\delta^{15}\text{N}$  is atmospheric  $\text{N}_2$  (Mariotti, 1983), and therefore has a  $\delta^{15}\text{N}$  value of 0‰ (Stüeken et al., 2016), where  $\delta^{15}\text{N} = [({}^{15}\text{N}:{}^{14}\text{N}_{\text{sample}} / {}^{15}\text{N}:{}^{14}\text{N}_{\text{air}}) - 1] \times 1,000$  (Mariotti, 1983; Stüeken et al., 2016). In sediments, nitrogen is mostly carried by the organic matter sinking from the surface ocean (Sollai et al., 2015). Thus, the stable nitrogen isotope ( $\delta^{15}\text{N}$ ) of organic nitrogen provides an important tool for studying the nitrogen budget in the ocean (Altabet et al., 1995).

When bioavailable nitrogen enters the ocean through nitrogen fixation, nitrogen ( $\text{N}_2$ ) is reduced to  $\text{NH}_4^+$ , and is assimilated with minimal isotope fractionation (-2‰ to 1‰) (Wada et al., 1975). When oxygen is present,  $\text{NH}_4^+$  is oxidized to  $\text{NO}_2^-$  and then to  $\text{NO}_3^-$  by nitrification (Casciotti et al., 2013) in a two-step process, which is associated with >20‰ nitrogen isotope fractionation (Sigman et al., 2009; Stüeken et al., 2016). This  $\text{NO}_3^-$  becomes a major source of nitrogen for aerobic organisms (Stüeken et al., 2016). This transformation of  $\text{NH}_4^+$  to  $\text{NO}_3^-$  is generally a complete process (Altabet and Francois, 1994; Thunell et al., 2004), and thus this fractionation is rarely expressed in modern marine environments. Thus, under oxic conditions, the marine sediments approach the isotopic composition of  $\text{NO}_3^-$  in the overlying water column (Thunell et al., 2004), which is mainly from subsurface nitrate augmented by in situ  $\text{N}_2$  fixation, atmospheric nitrogen deposition, and terrestrial input of organic and inorganic nitrogen.

The  $\text{NO}_3^-$  with  $\delta^{15}\text{N}_{\text{NO}_3^-}$  is denitrified (or reduced) back to  $\text{N}_2$  in locally suboxic regions (**Fig. 1.1**) in the water column (25% denitrification) and in sediments (75% denitrification) (Sigman et al., 2009; Stüeken et al., 2016). A higher degree of (incomplete) denitrification can result in heavier  $\delta^{15}\text{N}$  values (Stüeken et al., 2016). During denitrification,  $^{14}\text{N}$  is preferentially removed relative to  $^{15}\text{N}$ , leaving residual marine  $\text{NO}_3^-$  enriched in heavy isotope  $^{15}\text{N}$  (average ocean  $\delta^{15}\text{N}_{\text{NO}_3^-} \sim +5\%$ ‰) (Sigman et al., 2000; Ader et al., 2016). When this heavy isotope signature of  $\text{NO}_3^-$  is upwelled into the photic zone, it can be assimilated by organisms (**Fig.1.1**) living in the water column and then after settling down the water column recorded in organic matter in the sediments (Altabet and

Francois, 1994; Ganeshram et al., 2002; Deutsch et al., 2004). When oxygen supply is reduced either due to global warming or greater availability of organic matter for remineralization, the sedimentary  $\delta^{15}\text{N}$  increases alongside intensified water column denitrification (Wang et al., 2019). The  $\delta^{15}\text{N}$  signature of bulk sedimentary organic matter is widely accepted and used as a proxy for water column denitrification (Altabet et al., 1995; Ganeshram et al., 2000; Thunell et al., 2004; Martinez and Robinson, 2010; Dubois et al., 2011). However, the interpretation of sedimentary  $\delta^{15}\text{N}$  records is complex as different nitrogen sources (Kienast et al., 2005; Schubert and Calvert, 2001) and sedimentary diagenesis can potentially influence (Altabet and Francois, 1994; Lourey et al., 2003; Studer et al., 2021) the  $\delta^{15}\text{N}$  signatures. This has been challenged recently due to the different signal in organic matter in planktic foraminifera (Studer et al., 2021) due to the preservation of bulk organic matter.

### 1.3 The perturbation of nitrogen cycle

Population growth and the increased demand for food supply, fossil fuel combustion and the industrial Haber-Bosch process (**Fig. 1.2**) have all potentially contributed to a rise in reactive nitrogen in most environmental reservoirs including oceans in the last few decades (Galloway et al., 2004; 2008). Today, global food production is being sustained through reactive nitrogen from artificial nitrogen fertilizers (Gruber and Galloway, 2008) and cultivation induced Biological Nitrogen Fixation (BNF) (Smil, 2004). All these caused massive acceleration of the nitrogen cycle which is both beneficial and detrimental to the welfare of people and ecosystems (Erisman et al., 2008; Fowler et al., 2013). Reactive nitrogen pollution can affect ecosystem function and services, alter marine food webs, and decrease the fish production and also affect biogeochemical processes (Voss et al., 2013; Limburg et al 2020).

Earth system models are uncertain about the evolution of nitrogen fixation under the scenario of increased global warming (Wrightson and Tagliabue, 2020). During the Last Glacial Maximum (LGM) ~22,000 years ago, some studies observed reduced nitrogen loss processes due to lower temperatures, higher oxygen solubility and improved oxygen supply to the upper ocean ODZs (Jaccard and Galbraith, 2012).

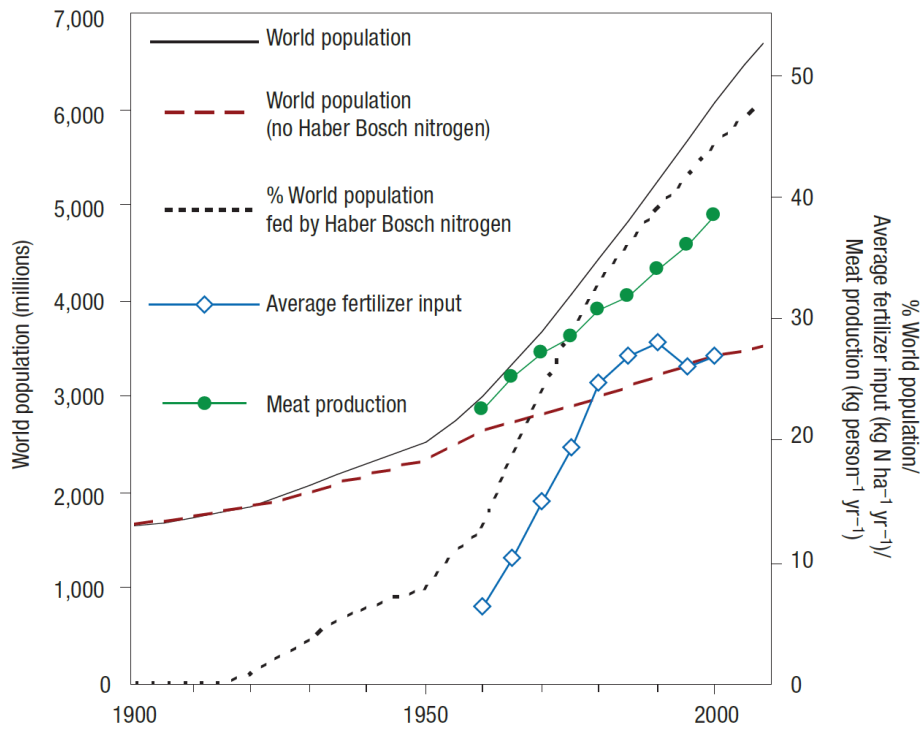


**Figure 1.2.** The overall world population trend in relation to the production of artificial nitrogen fertilizers. The source of the image is from Erisman et al. (2008).

A modeling study by Somes et al. (2017) predicted a decrease in nitrogen loss processes during the last glacial maximum (LGM) due to higher thermocline oxygen concentrations. They have observed that the enhanced atmospheric iron (Fe) deposition increased the export production in the Southern Ocean. They proposed that increased deep ocean nutrient storage reduced the transport of preformed nutrients to the tropics via the Subantarctic Mode Water (SAMW). Furthermore, their study concluded that the global  $\text{NO}_3^-$  inventory play an important role in the biological carbon pump, which contributed to a reduction in atmospheric  $\text{CO}_2$  during the LGM. Therefore, the quantification of sources and sinks of fixed nitrogen is relevant for predicting the evolution of Earth's climate (Galbraith et al., 2004).

In addition to warming, ocean acidification, nutrient enrichment and ocean stratification have also major consequences on the marine nitrogen cycle (Karl et al., 2002; Hutchins and Capone, 2022). However, ocean deoxygenation has the most noticeable impact on the nitrogen cycle (Keeling et al., 2010; Hutchins and Capone, 2022). The high primary production and elevated flux of organic matter can result in extensive bottom-water hypoxia (Turner and Rabalais, 1994; Parsons et al.,

2002; Turner and Rabalais, 2013; Rabalais et al., 2014). Several biological and geochemical transitions can occur in the benthic community (Middelburg and Levin, 2009) with changes in bottom-water oxygen levels. Therefore, oceanic oxygen concentration has a direct relation to which organic matter is produced and distributed in the ocean (Keeling et al., 2010). When oxygen levels drop below 5  $\mu\text{mol/kg}$ ,  $\text{NO}_3^-$  becomes the major electron acceptor, and denitrification occurs. Thus, the extent of ocean deoxygenation can control the rate of denitrification in world's oceans (Keeling et al., 2010), and thereby control the supply of  $\text{NO}_3^-$  (Codispoti et al., 2001; Keeling et al., 2010). The marine biogeochemical nitrogen and oxygen cycles are strongly linked to each other (Lam et al., 2009), especially in regions such as the Oxygen Minimum/Deficient Zones (OMZs or ODZs).

#### 1.4 Oxygen Minimum/Deficient Zones

Oxygen is fundamental to the biological, chemical and geological processes in ocean (Levin, 2018) as well as for all organisms. Oxygen minimum/deficient zones (OMZs or ODZs) are large mid-water (intermediate) regions of very low oxygen ( $\text{O}_2$ ) where the  $\text{O}_2$  concentration is  $<22 \mu\text{mol kg}^{-1}$ , usually within depths of 100 – 1,200 m (Levin, 2003; 2018), and are major sites of carbon burial along the continental margins (Levin et al., 2003; Wakeham, 2020). Here,  $\text{NO}_3^-$  act as the dominant electron acceptor at very low oxygen ( $<5 \mu\text{mol/kg}$ ) concentrations (Keeling et al., 2010). Thus, the nitrogen cycling in ODZs is of special scientific interest (Devol and Hartnett, 2001; Keeling et al., 2010; Voss et al., 2013).

The high primary production along with the increased organic matter remineralization, and reduced ventilation of intermediate waters results in the formation of oxygen depleted zones with a thickness of several hundred meters (e.g., Arabian Sea) (Levin, 2003; Karstensen et al., 2008; Voss et al., 2013; Wakeham 2020). In the ODZ off Chile, remineralisation up to 5 times higher than in the oxygenated zone is estimated to maintain the ODZ (Paulmier et al., 2006). Nitrogen fixation in tropical and subtropical oceans plays a key role in the global marine nitrogen budget (Karl et al., 2002). Globally, the largest ODZs are found in the tropical and subtropical oceans under high upwelling productivity (Helly and Levin, 2004; Karstensen et al., 2008; Rabalais et al., 2010; Wakeham 2020). The largest permanent open ocean ODZs are found in the Eastern Tropical North Pacific (ETNP), Eastern Tropical South Pacific (ETSP), and in the Arabian Sea (Lam and Kuypers, 2011) (Fig. 1.3).

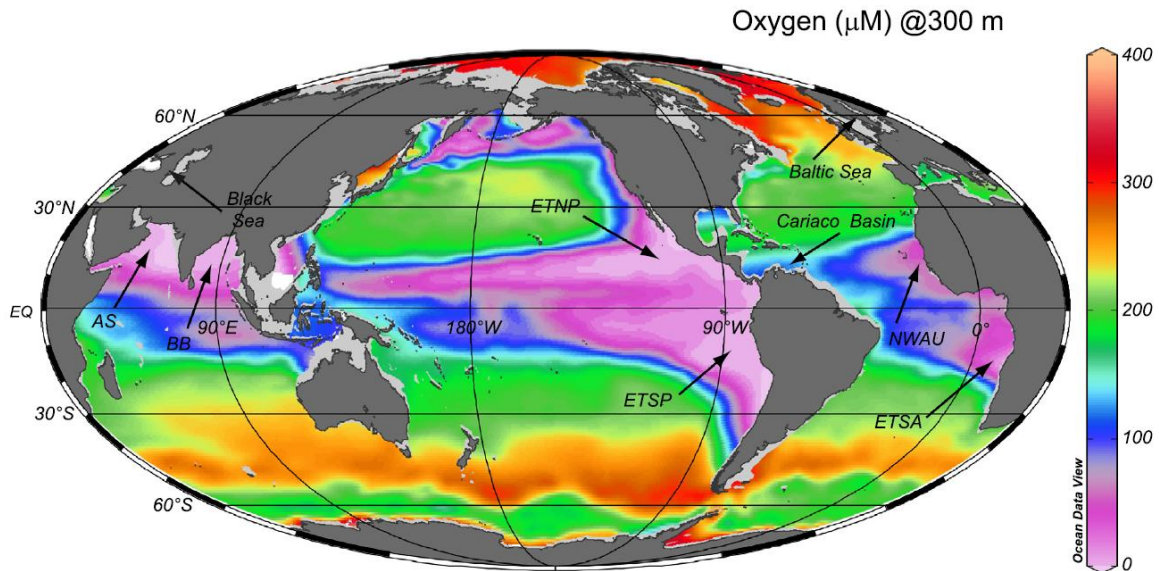


**Figure 1.3.** The dissolved oxygen concentrations at the major ODZs such as the Eastern Tropical North Pacific (ETNP), Eastern Tropical South Pacific (ETSP), Arabian Sea (AS), Bay of Bengal (BB), Black Sea, Cariaco Basin, Baltic Sea, Northwest Africa Upwelling (NWAU), and Eastern Tropical South Atlantic (ETSA) are shown in the map. The source of the image is from the ODZ review by Wakeham (2020).

Globally, the ODZs make up less than 1% of the ocean's total volume (Codispoti et al., 2001). The intermediate depth waters of the eastern Pacific have a high ventilation age and, thus, have lower oxygen concentration than other water masses leading to an extensive development of ODZs (Wyrski, 1967). The thickness of ODZs is strongly regulated by the water circulation and oxygen content of the ocean (Levin, 2003). A range of terms such as hypoxic, dysoxic, suboxic and anoxic have been used to define the dissolved oxygen concentrations in the ODZs (see Table 1.1). In modern ocean, anoxia is rare in the water column, however; suboxic and hypoxic conditions can occur at middepths in the North Pacific and in the South Pacific (Keeling et al., 2010).

**Table 1.1.** Oxygen conditions in the ODZs taken from Levin (2018), Erdem et al. (2020).

Redox condition	Oxygen concentration
Hypoxic	<63 $\mu\text{mol/kg}$
Dysoxic	5 – 45 $\mu\text{mol/kg}$
Suboxic	<5 $\mu\text{mol/kg}$
Anoxic	Absence of measurable oxygen

### 1.4.1 Ocean deoxygenation and expansion of ODZs

Dissolved oxygen concentrations declined since the middle of the 20<sup>th</sup> century, in the open ocean and coastal waters (IPCC, 2007; Helm et al., 2011; Keeling et al., 2010; Stramma et al., 2008; Schmidtko et al., 2017). Nearly 1-2% of the oceanic oxygen inventory has been lost (Schmidtko et al., 2017; Limburg et al., 2020) due to increased global warming and altered ocean circulation (Oschlies et al., 2018). Increased global warming causes a decrease in oxygen solubility (Levin, 2018) and an increase in oxygen consumption via microbial respiration (Breitburg et al., 2018; Limburg et al., 2020). Rising global temperatures could reduce the introduction of oxygen from the atmosphere and surface waters into ocean's interior (Glecker et al., 2016), as warmer ocean waters can hold less dissolved oxygen. Studies (Helm et al., 2011; Talley et al., 2016) have attributed a large fraction of deoxygenation at intermediate-depths due to altered ocean stratification. The highest oxygen loss in the last half century has been recorded in the equatorial Pacific (21.9% of total, Schmidtko et al., 2017; Levin, 2018). It is also the largest area of naturally occurring oxygen depletion at mid-water (intermediate) depths (Paulmier et al., 2008).

The ODZs expanded globally during the past decades (Stramma et al., 2008; Keeling et al., 2010; Levin, 2018; Breitburg et al., 2018) mainly related to increased global warming, change in ocean circulation along with decline in oxygen levels (Keeling et al., 2010; Schmidtko et al., 2017; Limburg et al., 2020). Climate models predict an overall decline in dissolved oxygen concentrations (Matear et al., 2000; Long et al., 2016) of 1% to 7%, with potentially the largest decline in tropical oceans (Stramma et al., 2008). Consequently, ODZs will intensify and expand (Evans et al., 2023), due to a combination of warming induced oxygen decline (Keeling et al., 2010) and reduced ventilation of the deep ocean (Long et al., 2016). Ocean circulation plays a big role in regulating oxygen dynamics of the Eastern Tropical Pacific (Montes et al., 2014). There is still debate on the timescale in which the ODZs will expand in the future (Yamamoto et al., 2015; Takano et al., 2018; Frölicher et al., 2020). Some studies even predicted that the modern ocean deoxygenation trends might reverse in the future (Hess et al., 2023), suggesting the need for further scientific investigations. Although, global warming promotes ocean deoxygenation due to lower solubility of oxygen at the surface, the exact reason for the ocean deoxygenation is still under debate especially for the tropical oceans (Watson, 2016).

### 1.4.2 Nitrogen cycle in the ODZs

ODZs play a key role in regulating the global marine nitrogen cycle (Gruber and Galloway, 2008; Lam and Kuypers, 2011; Evans et al., 2023). This is because globally ~30 - 50% of fixed nitrogen loss from the world's oceans occurs in the ODZs (Gruber, 2004, 2008; Lam and Kuypers, 2011; Voss et al., 2013). Furthermore, oxygen plays an important role in nitrogen cycle processes as some microbial reactions require oxygen and others are inhibited by it (Voss et al., 2013). Although, ODZ sediments cover only 1% of the global seafloor, globally 10% of the benthic denitrification occur in the ODZs (Bohlen et al., 2012) which makes ODZs globally key regions of scientific interest. Benthic denitrification plays a huge role in shaping global nitrogen fixation and net primary production (Li et al., 2024). Sediments contribute to nearly 60 - 75% of global ocean denitrification (Somes et al., 2013; DeVries et al., 2013; Eugster and Gruber, 2012; Brandes and Devol, 2002), and are a major sink for fixed nitrogen. Moreover, with ongoing expansion of the ODZs, the benthic denitrification rates are likely to increase in the future.

### 1.5 Foraminifera

Foraminifera (Kingdom: Chromista; Order: Foraminiferida) are a group of amoeboid protists (unicellular eukaryotes) that are abundant in marine environments (Goldstein, 1999). These organisms are typically <1 mm in diameter (Levin, 2003) and are characterized by a cytoplasmic body covered by a test of one or more interconnected chambers (reviewed in Hoogakker et al., 2024). The foraminiferal tests can be made of agglutinated particles, organic material, or biomineralized crystals of calcite, aragonite, or rarely silica (Loeblich and Tappan, 1988). Foraminifera first appeared in the Cambrian (Goldstein, 1999), and extend into the present (Sen Gupta, 2003; Debenay, 2012). They are abundant, and colonized diverse marine environments where they occur from coastal settings to both planktic and benthic habitats of the ocean (Goldstein, 1999; Sen Gupta, 1999; Gooday, 2003).

Many calcareous foraminiferal tests are porous (Goldstein, 1999). The pores in benthic foraminiferal tests play an important role in facilitating gas exchange and osmoregulation between foraminifera and the environment. This is because mitochondria (involved in respiration) are more abundant near the pores in foraminifer's species from low-oxygen environments (Leutenegger & Hansen 1979).

Some species of benthic foraminifera from oxygen depleted environments are able to use  $\text{NO}_3^-$  as an electron acceptor (Risgaard-Petersen 2006; Piña-Ochoa et al., 2010a; 2010b) for respiration. This  $\text{NO}_3^-$  is completely denitrified to dinitrogen gas ( $\text{N}_2$ ) either by the foraminifera themselves (Risgaard-Petersen 2006; Glock et al., 2019a) or by using prokaryotic endobionts (Bernhard et al., 2012a). The step-wise denitrification pathway from  $\text{NO}_3^-$  to  $\text{N}_2$  involving enzymes such as nitrate reductase (Nr Nar), nitrite reductase (Nir), nitric-oxide reductase (Nor), and nitrous oxide reductase (Nos) is shown in **Fig. 1.4**. So far, benthic foraminifera are the only eukaryotes known to perform complete denitrification (Risgaard-Petersen 2006; Kamp et al., 2015; Glock et al., 2019a). The uptake of  $\text{NO}_3^-$  in denitrifying benthic foraminifera is most likely facilitated by the test pores (Leutenegger & Hansen 1979; Glock et al., 2011; 2012a).

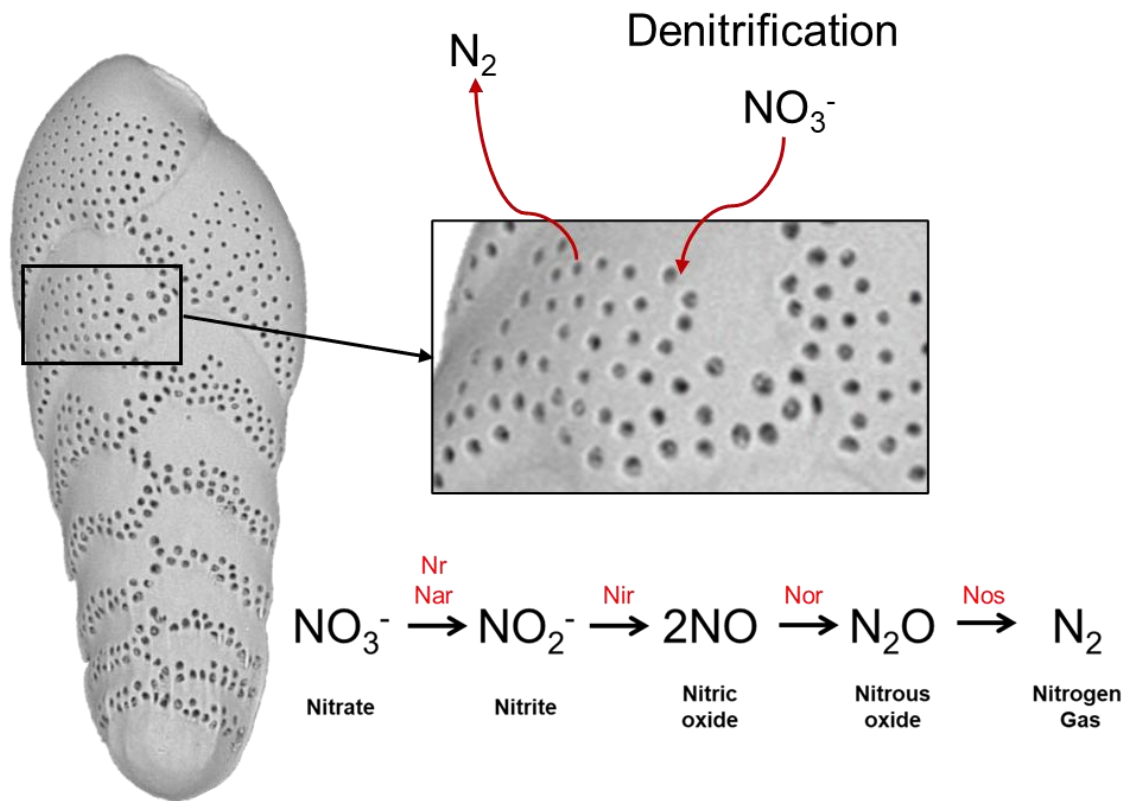


**Figure 1.4.** Schematic view of uptake of  $\text{NO}_3^-$  and the excretion of  $\text{N}_2$  by benthic foraminifera *Bolivina spissa* and the step-wise denitrification pathway.

Foraminifera account for a major part of benthic denitrification in the ODZs partly due to their high abundance in these environments (Piña-Ochoa et al., 2010a; 2010b; Glock et al., 2013; Dale

et al., 2016). Dale et al. (2016) showed that denitrification by foraminifera can account for nearly 90% of  $N_2$  production at the lower edge of the Peruvian ODZ. Therefore, benthic foraminifera play an important role in global nitrogen cycle (Risgaard-Petersen 2006; Glock et al., 2013; Glock et al., 2019a).

The foraminiferal morphometrics such as porosity (% of test area occupied by pores), pore density (number of pores per unit area) varies in pore size, density and shape between different foraminiferal taxa (Kuhnt et al., 2013; Richirt et al., 2019a; Schönfeld et al., 2021). Some species of benthic foraminifera living in oxygen-or  $NO_3^-$ - depleted environments have higher pore density and porosity than those living in environments with higher oxygen or  $NO_3^-$  concentrations, most likely to optimize the electron acceptor uptake through the pores (Glock et al., 2011; Kuhnt et al., 2013; Rathburn et al., 2018). Hence, pore parameters of these benthic foraminifera are potential proxies for past oxygen and  $NO_3^-$  concentrations.

### **1.5.1 Pore density as a proxy for bottom-water nitrate ( $[NO_3^-]_{BW}$ ) reconstruction**

Many bolivinid foraminiferal species have an affinity for low-oxygen environments (Harman, 1964). *Bolivina spissa* (Cushman, 1926) is a shallow infaunal benthic foraminifera, which is found in the top few centimeters of the sediment and is abundant in the ODZs (Glock et al., 2011; Fontanier et al., 2014). This species is lanceolate with a relatively flat surface (Glock et al., 2011). The life cycle of *B. spissa* is related to phytoplankton blooms (Nomaki et al., 2006; Glock et al., 2011), as it selectively feeds on fresh phytodetritus (Nomaki et al., 2006) transported from the surface ocean. Thus, *B. spissa* is considered to be a phytophagous species (Nomaki et al., 2005; 2006).

The pore density of *B. spissa* is significantly correlated to  $NO_3^-$  in their habitats as the pores facilitate the uptake of  $NO_3^-$  for respiration (Glock et al., 2011). In  $NO_3^-$ - depleted habitats, *B. spissa* optimizes its  $NO_3^-$  accumulation by building more pores resulting in higher pore density (Glock et al., 2011). Every *Bolivina* species tested so far (including *Bolivina seminuda*, Cardich et al., 2015), has the ability to denitrify (Piña-Ochoa et al., 2010a; Bernhard et al., 2012b). This suggests that denitrification is a common survival strategy of Bolivinidae under oxygen depleted conditions (Glock et al., 2019a). Therefore, the pore characteristics like pore density of *B. spissa* is suitable as an empirical proxy for paleo- $NO_3^-$  reconstruction (Glock et al., 2018).

Previous work on marine nitrogen cycling (Thunell et al., 2004; Martinez and Robinson, 2010; Dubois et al., 2011) is mainly based on the reconstruction of sedimentary nitrogen isotopes ( $\delta^{15}\text{N}_{\text{bulk}}$ ). The  $\delta^{15}\text{N}_{\text{bulk}}$  proxy is influenced by the complex interplay of the diverse processes that control the marine nitrogen cycle (e.g., denitrification, nitrogen fixation, nutrient utilization, anammox, etc.). Thus, quantitative statements are hardly to achieve from  $\delta^{15}\text{N}_{\text{bulk}}$  data alone. Through this PhD work,  $[\text{NO}_3^-]_{\text{BW}}$  is quantitatively reconstructed in different ODZs in the Pacific Ocean using the pore density of Bolivinids such as *B. spissa* and *B. subadvena* (see **Fig. 1.5**). *Bolivina spissa* was originally classified as a variant of *B. subadvena* with the name *B. subadvena* var. *spissa* (Cushman, 1926). Previously, Glock et al. (2018) made the first attempt to reconstruct the  $[\text{NO}_3^-]_{\text{BW}}$  in the Peruvian continental margin using the pore density of benthic foraminifera *B. spissa*. Reconstruction of past  $[\text{NO}_3^-]_{\text{BW}}$  in the ODZs can provide important insights on the marine nitrogen budget and the process involved in it, which will be helpful in predicting future changes in the marine nitrogen cycle.

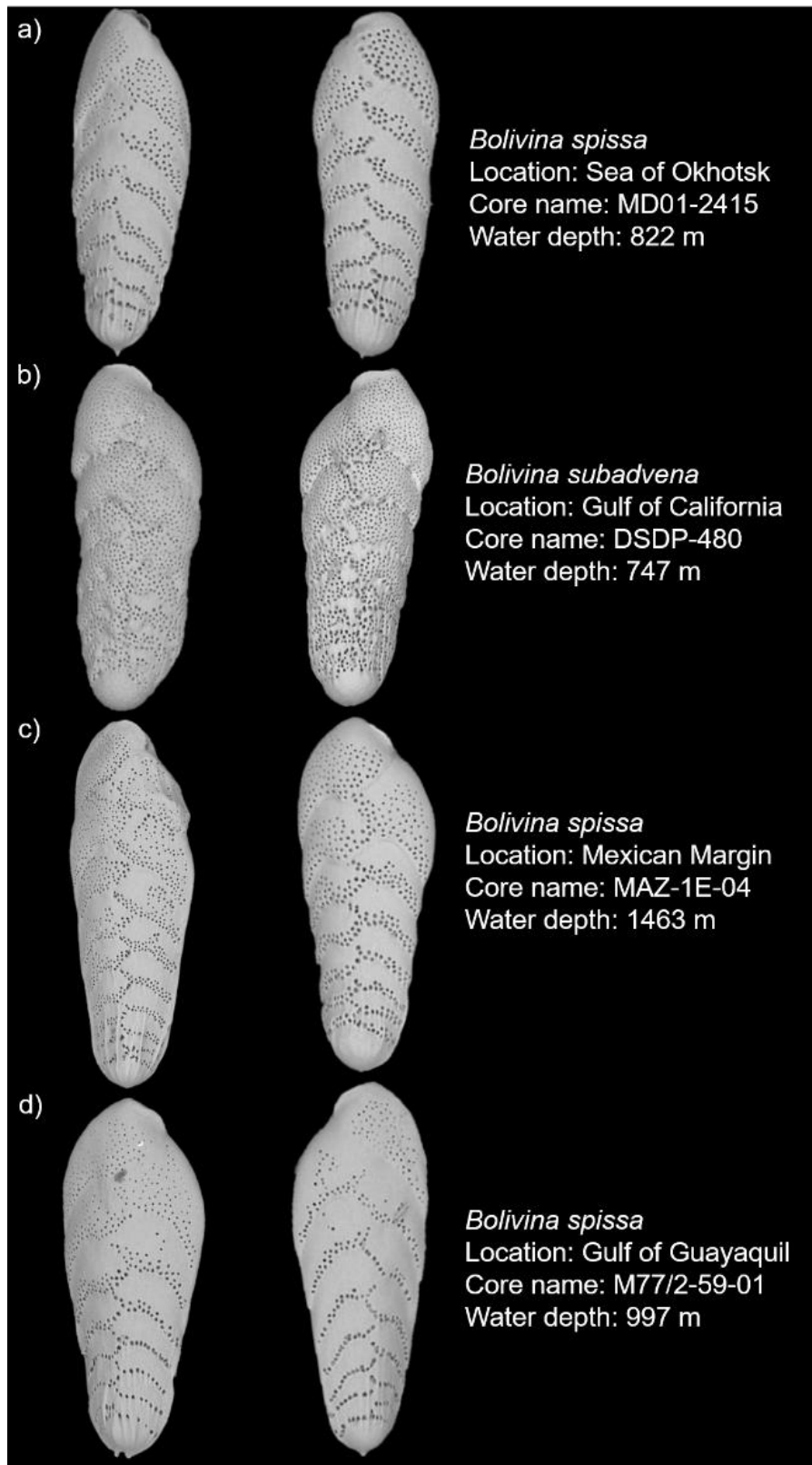


**Figure 1.5.** Scanning Electron Microscopic (SEM) images of the benthic foraminiferal species *Bolivina spissa* and *Bolivina subadvena* from different sampling locations used for the PhD work.

## 1.6 Importance of reconstructing redox conditions in the ODZs

Many of the regions that have experienced deoxygenation are highly productive and important for commercial fisheries, e.g., Peru (Limburg et al., 2020). Oxygen loss or deoxygenation can cause major changes in the productivity, biodiversity, and functioning of different ecosystems (Levin, 2018) and can affect global food security (Limburg et al., 2020). A study by Wishner et al. (2018) in the eastern tropical North Pacific showed that some zooplankton species live close to their physiological limits, despite being hypoxia-tolerant. Their findings suggest that zooplankton in the eastern tropical Pacific ODZ have virtually no capacity to tolerate further ocean oxygen loss. Some species might be able to shift depth to waters with higher oxygen levels in response to decreasing oxygen (Wishner et al., 2018). However, this is nearly impossible for many other species due to associated changes in food, light, temperature, predation pressure, and other environmental factors (Wishner et al., 2018). Therefore, oxygen depletion or deoxygenation could lead to large unanticipated changes in the structure and function of ODZ ecosystems (Wishner et al., 2018; Limburg et al., 2020).

Both modern and paleo studies (reviewed in Hoogakker et al., 2024) show that even small differences in oxygen concentrations can have huge consequences if they carry a system across key thresholds (Vaquer-Sunyer & Duarte 2008). The increased productivity, and subsurface oxygen decline are high in the tropical Pacific Ocean (Ito et al., 2016). Many habitats between 500 and 1000 meters in the East Pacific are vulnerable to macrofaunal biodiversity loss due to ocean warming and deoxygenation (Sperling et al., 2016). The Earth System Model 2.1 predicts that decreased ventilation in the North Pacific will increase the supply of  $\text{NO}_3^-$  in source waters to the California Current System leading to deoxygenation by 18% in 2100 (Rykaczewski & Dunne, 2010).

The direct measurement of dissolved oxygen over large areas and long time periods is challenging due to technical and resource limitations (Guo et al., 2021). Hence, a suitable proxy that could provide a quantitative estimate of past and present dissolved oxygen concentration is highly desirable. Redox-sensitive elemental concentrations in benthic foraminiferal tests have been suggested as a potential proxy for bottom-water oxygen (Glock et al., 2012b; Groeneveld and Filipsson, 2013; Koho et al., 2017; Guo et al., 2019; Brinkmann et al., 2023). Bottom-water oxygenation is important due to its key role in regulating various biogeochemical cycles and

benthic ecosystem diversity (Levin et al., 2009; Koho et al., 2013), and its reconstruction provides important constraints on past redox conditions (Koho et al., 2015).

### **1.6.1 Benthic foraminiferal manganese as a proxy for bottom-water redox conditions**

Manganese (Mn) is a redox sensitive element which exists in three oxidation states Mn (II), Mn (III) and Mn (IV) in naturally occurring minerals and in surface waters (Calvert and Pedersen, 1993). The distribution and state of matter of Mn can reflect dissolved oxygen concentrations (Calvert and Pedersen, 1993; Groeneveld et al., 2018; Algeo and Li, 2020; Koho et al., 2017) and, thus can be a potential proxy to reconstruct past redox conditions (Schenau et al., 2002). Manganese is delivered to the ocean as oxide coatings on particulate matter transported by wind or rivers and by diffusion from shelf sediments (Finney et al., 1988; Calvert and Pedersen, 1993). Manganese maxima are observed in intermediate water depths wherever oxygen concentrations fall below 100  $\mu\text{M}$  (Johnson et al., 1992).

The Mn incorporation into the benthic foraminiferal tests varies with oxygen conditions. Under oxic conditions, Mn exists in the form of solid Mn (oxyhydr) oxides, i.e.,  $\text{MnO}_2$  or  $\text{MnOOH}$  (Burdige and Gieskes, 1983; Glasby 2006; Koho et al., 2017), and thus benthic foraminiferal tests have low Mn/Ca ratio. However, when oxygen concentration in the sediment decreases due to increased organic matter remineralization,  $\text{MnO}_2$  or  $\text{MnOOH}$  are reduced to aqueous  $\text{Mn}^{2+}$  in the upper part of the sediment (Froelich et al., 1979; Slomp et al., 1997). The released  $\text{Mn}^{2+}$  into the pore waters diffuses upwards and reprecipitates in the oxic zone in the sediment, resulting in high subsurface  $\text{MnO}_2$  or  $\text{MnOOH}$  concentrations (Burdige and Gieskes, 1983; De Lange et al., 1989). Thus, there is a continuous cycling of solid and aqueous  $\text{Mn}^{2+}$  in sediments (Slomp et al., 1997). This will build up the pore water  $\text{Mn}^{2+}$  concentration in the suboxic part of the sediment until a Mn carbonate phase starts to precipitate (De Lange, 1986; Middelburg et al., 1987; Calvert and Pedersen, 1993). The Mn flux across the sediment–water interface is controlled by the reductive dissolution of reactive  $\text{MnO}_2$  or  $\text{MnOOH}$  (Froelich et al., 1979). In permanently oxic bottom water conditions, most of the Mn initially deposited as  $\text{MnO}_2$  or  $\text{MnOOH}$ , is ultimately buried as Mn carbonates (Schenau et al., 2002). Under hypoxic conditions ( $<63 \mu\text{mol/kg}$ ), Mn (existing as solid  $\text{MnO}_2$  or  $\text{MnOOH}$ ) cannot escape to the overlying hypoxic bottom water. Hence, it accumulates on the sediment surface, increasing the  $\text{Mn}^{2+}$  concentration in the porewater (Middelburg et al., 1987; Koho et al., 2015; 2017). Contrary to this, under anoxic (absence of measurable oxygen) or

suboxic (<5  $\mu\text{mol/kg}$ ) bottom water conditions, dissolved  $\text{Mn}^{2+}$  in pore waters is low because  $\text{MnO}_2$  or  $\text{MnOOH}$  are reduced either in the water column or at the sediment-water interface (Schenau et al., 2002).

Benthic foraminifera precipitate their tests in the upper sediment layer, and dissolved  $\text{Mn}^{2+}$  can be incorporated into their calcium carbonate tests during calcification (Koho et al., 2015; 2017). Therefore, the chemical composition of benthic foraminiferal test reflects the environmental conditions in the upper sediment column. When benthic foraminifera calcify under hypoxic conditions, their calcitic tests is expected to have high Mn/Calcium ratios (Mn/Ca), and low during anoxic or suboxic conditions as dissolved  $\text{Mn}^{2+}$  in pore waters is low (Groeneveld and Filipsson, 2013; McKay et al., 2015; Koho et al., 2015; Petersen et al., 2018; Brinkmann et al., 2023). Previously, Mn was considered as an indicator of contamination by Mn carbonate or  $\text{MnO}_2$  or  $\text{MnOOH}$  (Barker et al., 2003; Leduc et al., 2014). However, new chemical cleaning techniques and high-resolution laser ablation inductively coupled plasma mass spectrometry (LA-ICP-MS) now allow reliable analysis of foraminiferal test-associated Mn (Reichert et al., 2003; Petersen et al., 2018; Mojtahid et al., 2019; Brinkmann et al., 2023).

The Mn/Ca of some benthic foraminiferal species have already been suggested as a proxy for bottom-water oxygen (Groeneveld and Filipsson, 2013; Petersen et al., 2018; Ní Fhlaithearta et al., 2018; Guo et al., 2021; Brinkmann et al., 2023). A study by Ni et al. (2020) applied benthic foraminiferal Mn/Ca to reconstruct bottom water conditions in the Baltic Sea over the past 7.7 kyr. In this PhD work, redox conditions in different ODZs are investigated using Mn/Ca ratios from the tests of *B. spissa* and *B. subadvena*. The microhabitat of these shallow infaunal foraminifera (Glock et al., 2011) close to the sediment-water interface exposes them to higher variability in porewater Mn, leading to higher sensitivity for recording changes in redox conditions. Moreover, the Mn concentration in the foraminiferal tests is not subjected to diagenetic processes (Koho et al., 2015; Petersen et al., 2018) in comparison to Mn in bulk sediments (Schenau et al., 2002). However, it is not straightforward to infer the Mn/Ca ratios from benthic foraminifera. Various factors such as productivity, foraminiferal ecology and habitat preferences, and species-specific responses to oxygen availability (Jorissen et al., 1995; Koho et al., 2015, 2017; Ní Fhlaithearta et al., 2018) and the supply of Mn (Morton et al., 2019; Nakaguchi et al., 2022) needs to be considered for the data interpretation. Changes in redox conditions in the ODZs due to ocean warming or

anthropogenic pressures can cause perturbations in the marine nitrogen cycle. Thus, reconstruction of past bottom-water conditions can improve knowledge of the potential mechanisms involved in these ecosystems, which can provide valuable insights into future resilience of marine ecosystems (Schmiedl, 2019).

## Chapter 2

### Study area

This study is based on sediment samples collected from four different ODZs around the Pacific Ocean such as the Sea of Okhotsk, Gulf of California (Guaymas Basin), Mexican Margin, and the Gulf of Guayaquil (Peru). This chapter deals with each of these study areas and their physical settings.

#### 2.1 Sea of Okhotsk

The Sea of Okhotsk (also called Okhotsk Sea) is a subpolar marginal sea in the northwestern Pacific (**Fig. 2.1**) and is connected to the Pacific Ocean via the Kuril Straits ([Nishioka et al., 2014](#)). It is surrounded by the Kamchatka Peninsula, Siberia, and Sakhalin, Hokkaido, and Kuril Islands ([Nakaguchi et al., 2022](#)). It is also the southernmost seasonal sea ice production region in the northern hemisphere ([Kimura and Wakatsuchi, 1999](#)), and plays an important role in the hydrology of North Pacific ([Gorbarenko et al., 2014](#)). Most of the sea ice is formed in the northern continental shelf region ([Martin et al., 1998](#)). The densest water which originates over the northwestern continental shelf of the Sea of the Okhotsk ( $<-1^{\circ}\text{C}$ ) ventilates the North Pacific ([Kitani, 1973](#)). This dense shelf water from the Sea of Okhotsk is produced by brine rejection during sea ice formation ([Kitani, 1973](#)), and has a potential density of 26.7 – 27.0 ([Nakatsuka et al. 2002, 2004](#)). This dense shelf water penetrates into intermediate depths and mixes horizontally to form the Okhotsk Sea Intermediate Water (OSIW, potential density = 26.8 – 27.4, [Yamamoto et al., 2002; Yamamoto-Kawai et al., 2004](#)), which is generally distributed between 250 m to 1000 m depths ([Yamamoto-Kawai et al., 2004](#)). This water is further transported to the North Pacific intermediate layer through the Bussol strait and form the North Pacific Intermediate Water (NPIW). Thus, the Sea of Okhotsk serves as the source region of NPIW ([Talley, 1991; Wong et al., 1998; Seki et al., 2012](#)). The NPIW which is widely distributed in the North Pacific has a noticeable influence on the climate of the North Pacific ([Ito et al., 2014](#)). The Sea of Okhotsk has lower water temperature and salinity, and higher dissolved oxygen than the North Pacific water ([Talley, 1991; Itoh et al., 2003](#)). Thus, the outflow of intermediate waters from the Sea of Okhotsk ventilates the NPIW ([Talley, 1991; Kobayashi, 2000](#)).

The sediment core MD01-2415, for the PhD work is collected from the central part of the Sea of Okhotsk at a water depth of 822 m (**Fig. 2.1**). Primary production in the northwestern shelf region

in the Sea of Okhotsk is high throughout the year except during the sea ice period (Saitoh et al., 1996; Sorokin and Sorokin, 1999). The benthic flux of organic matter is possibly high in this shelf region since the particulate organic matter produced on the shelf is exported efficiently to the pelagic intermediate water (Nakatsuka et al., 2002). Studies by Yoshikawa et al (2006) found that benthic denitrification is high at the continental margin of Sea of Okhotsk. The contribution of denitrification over the Sea of Okhotsk shelf region to the  $N^*$  tracer has been estimated to be  $5.6 \pm 2.4 \mu\text{mol/kg}$  (Ito et al., 2014).

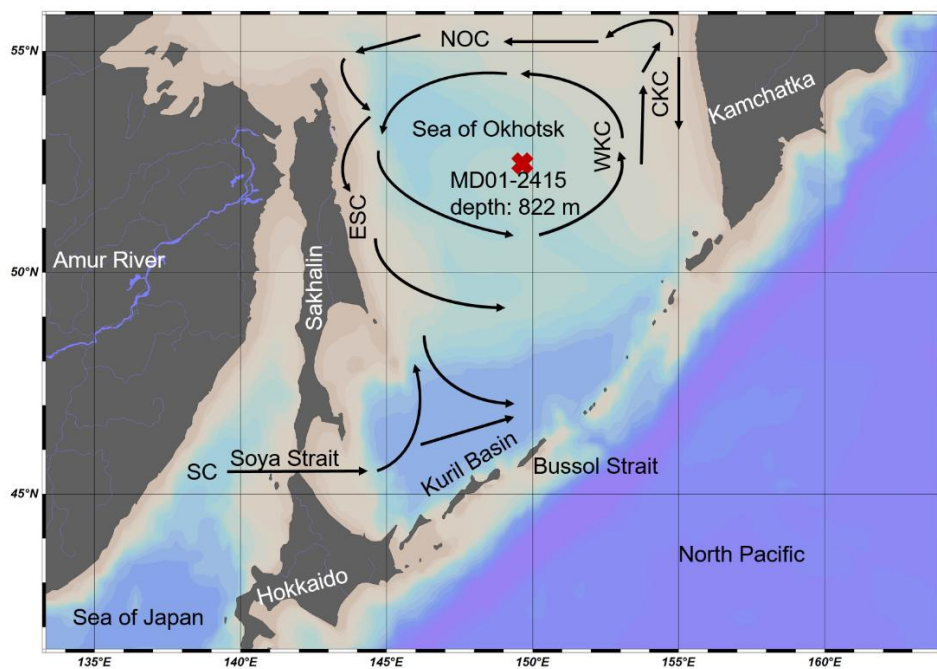


**Figure 2.1.** Map of the Sea of Okhotsk along with main surface currents and bathymetry. Surface currents such as East Sakhalin Current (ESC), North Okhotsk Current (NOC), West Kamchatka Current (WKC), Compensation Kamchatka Current (CKC), Soya Current (SC) are shown on the map. The Amur River is shown in light blue color. The red cross depicts the location from which the core MD01-2415 is collected. Ocean Data View is used for the map (Schlitzer, R., 2023).

The Sea of Okhotsk has an anticlockwise cyclonic current system (see **Fig. 2.1**). The West Kamchatka Current (northward water transport) dominates to the west of the Kamchatka Peninsula, whereas East Sakhalin Current (southward transport) does so to the east of Sakhalin (Seki et al., 2012). The Amur River is the major source of terrestrial organic matter (Seki et al., 2012) to the Sea of Okhotsk. Annually, the Amur River exports  $5653 \times 10^3$  t organic matter (Levshina, 2008), which is comparable to that of the largest rivers in the world (Spitzky and Leenheer, 1991; Telang et al., 1991). A large amount of terrestrial organic matter supplied by

Amur River to the northwestern area of the sea is transported to the southern region through the intermediate waters which flow along the east coast of Sakhalin Island (Seki et al., 2012).

## 2.2 Gulf of California (Guaymas Basin)

The Gulf of California is a semi-enclosed, evaporitic marginal sea which is connected to the Pacific Ocean (Chang et al., 2015) through the southern end (Fig. 2.2). The Gulf is located between the Mexican mainland and the Baja California peninsula (Bray, 1988a&b; Campbell et al., 1988). The seasonal dynamics of the Gulf of California are dominated by the Pacific Ocean, not by the local wind or buoyancy flux. The modern thermohaline circulation in the Gulf includes a surface layer driven by seasonal winds, outflow of subsurface waters (50 – 250 m depth), and inflow of NPIW (500 -1000 m), and Pacific Deep Water, PDW (> 1000 m) (Bray, 1988a and b; Chang et al., 2015).

The sediment core (DSDP-480) for the PhD work is collected from the Guaymas Basin from a water depth of 747 m (Fig. 2.2). A strong ODZ is situated at depths of 500 – 1000 m within the basin having a minimum dissolved oxygen concentration of 5.63  $\mu\text{M}$  (Garcia et al., 2006). This ODZ is modulated by high primary productivity (Kahru et al., 2004) of  $>450 \text{ g C/m}^2/\text{yr}$  and the oxygen concentration of NPIW and Subtropical Surface Water (Wyrki, 1962). It has narrow shelves except in the north with strong tides and little freshwater inflow (Chen et al., 2004). The Gulf of California has a monsoon climate (Thunell, 1998). The surface circulation and primary productivity in Gulf of California are modulated by the atmospheric Monsoon circulation over southwestern North America (Thunell, 1998). Atmospheric pressure systems like North Pacific High, North America Low, and Intertropical Convergence Zone (ITCZ) can influence the climate in the Gulf of California (Thunell, 1998; Chang et al., 2015 and ref therein). The basin sediments of Gulf of California are strongly enriched in Mn (Campbell et al., 1988) as well as in reactive Fe. The deep-water is separated from the neighboring basins and the open ocean by a sill. The Eastern Equatorial Pacific (EEP) ODZ impinges the seafloor at intermediate depths. The Guaymas Basin has similar characteristics with predominantly oxic ocean basins like the Pacific but is relatively small and semi-restricted similar to the euxinic Black Sea. Compared to the EEP, oxygen concentrations increase again below the ODZ (Scholz et al., 2019). Underneath the ODZ, the lack of bioturbation within sediments leads to the formation of laminated sediments (Keigwin and Jones, 1990, Thunell, 1998), which reflect the climatic conditions in the Gulf of California (Calvert, 1966; Pride et al., 1999). There are high sedimentation rates (up to  $2.8 \text{ m kyr}^{-1}$ ) within

the Guaymas Basin (Calvert, 1966). Thus, the lack of bioturbation along with high rates of sedimentation made sediments of the Guaymas Basin ideal for climate reconstructions.

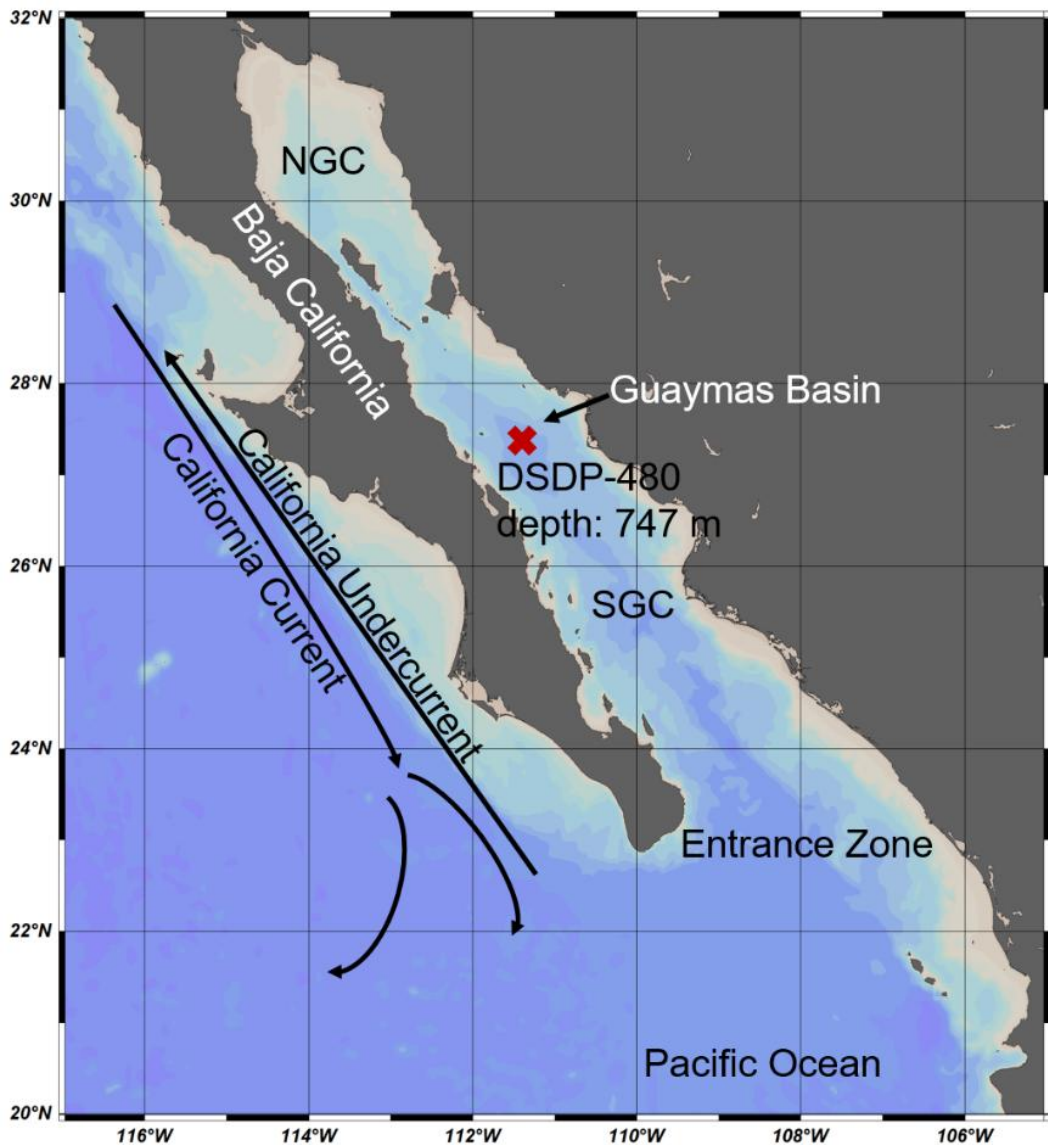


**Figure 2.2.** Map of Gulf of California. The major ocean currents such as the California Current and California Undercurrent are shown in the map. Entrance Zone is in open connection with the Eastern Tropical Pacific Ocean, SGC is the Southern Gulf of California, and NGC is the Northern Gulf of California which has shelf sea characteristics (Lavín and Marinone, 2003). The red cross depicts the location from which the sediment core DSDP – 480 has been collected. Ocean Data View is used for the map (Schlitzer, R., 2023).

### 2.3 Mexican Margin

The Mexican Margin (**Fig. 2.3**) is a region lying between the Gulf of Tehuantepec and Cabo San Lucas and extends seaward between the California Current and the North Equatorial Current (Roden, 1964). The Mexican Margin has a narrow continental shelf with a shelf break at ~200 m, and the continental slope deepens to ~3000 m. The primary production is between 48 and 150 g C m<sup>-2</sup> yr<sup>-1</sup> during spring and summer seasons (Longhurst et al., 1995).

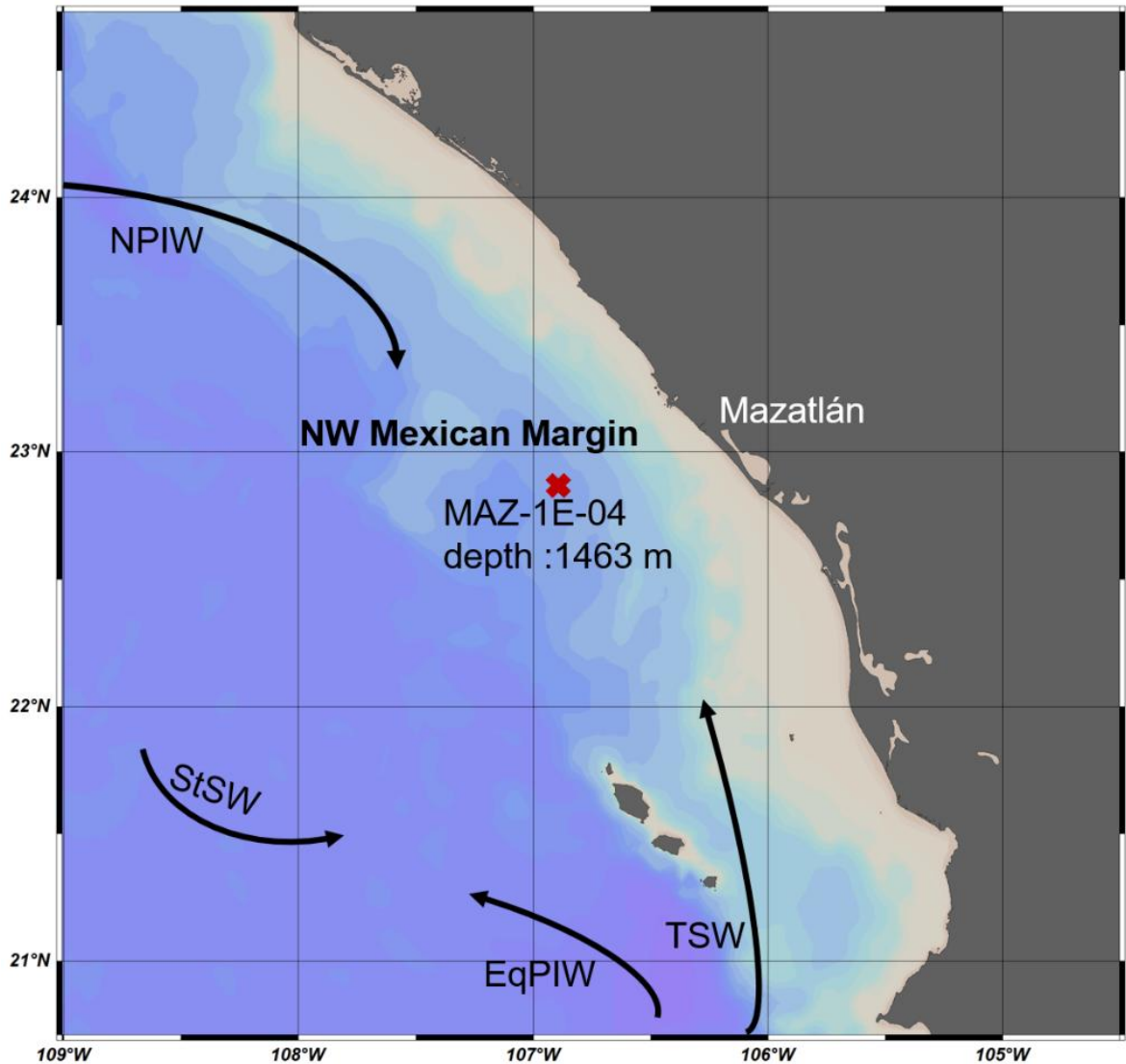


**Figure 2.3.** The study area Mazatlán coast in the Northwest Mexican Margin. The circulation of water masses such as the North Pacific Intermediate Water (NPIW), Subtropical Surface Water (StSW), Equatorial Pacific Intermediate Water (EqPIW), and Tropical Surface Water (TSW) are shown in the map. The red cross depicts the location from which the sediment core MAZ-1E-04 has been collected. The Ocean Data View software has been used for the map (Schlitzer, R., 2023).

The Mexican Margin is distinguished by the presence of a strong ODZ in the ETNP, and oxygen-deficient conditions are linked to enhanced carbon preservation (Hartnett and Devol, 2003). The ODZ impinges on the upper slope and shelf between water depths of ~ 100 m to 1000 m (Roden, 1964). Studies have shown that the ODZ in the Mexican Margin contracted and weakened during the last century (Ontiveros-Cuadras et al., 2019), and the sediments are not bioturbated (Hartnett and Devol, 2003).

The sediment core (MAZ-1E-04) for the PhD work is collected from the Northwest Mexican Margin (southwest of Mazatlán) from a water depth of 1463 m (Fig. 2.3). This region is influenced, a) at the surface by the equatorward California Current, b) tropical surface waters of the Costa Rica Coastal Current from the south, as well as c) poleward flowing subsurface California Undercurrent (Codispoti, 1989). The northwesterly winds in this region results in offshore Ekman transport and upwelling of nutrient-rich subsurface waters (Roden, 1972; Kessler, 2006). This wind driven coastal upwelling is most intense during the winter and the early spring (Ontiveros-Cuadras et al., 2019). As a result, high primary production occurs and large quantities of organic material are exported (Codispoti, 1989; Kamykowski and Zentara, 1990) to the water column which consumes oxygen as it moves down. Therefore, oxygen deficient subsurface and intermediate water masses of the Eastern Tropical North Pacific impinge on the upper slope of the Mexican Margin (Ganeshram et al., 2002). This results in an intense ODZ ( $O_2 < 10 \mu M$ ) at the Mexican Margin near the Mazatlán coast (Ontiveros-Cuadras et al., 2019). The sediment core, MAZ-1E-04 is collected from a deep-water depth which is strongly influenced by the PDW. The Mexican Margin water column has high rates of water column denitrification ( $NO_3^-$  deficit) within the ODZ (Brandes et al., 1998; Hartnett and Devol, 2003; Davis et al., 2019).

## 2.4 Gulf of Guayaquil

The Gulf of Guayaquil (Fig. 2.4) is the largest estuary on the Pacific coast of South America (Twilley et al., 2001; Navarrete-Forero et al., 2019), and is part of the ETSP. This region provides livelihoods for the fishing communities and to the local people (Twilley et al., 2001). The Gulf of Guayaquil is located on the banks of Guayaquil River, formed by the union of rivers such as Daule, Vinces and Babahoyo (Twilley et al., 2001). The major sources of contamination in the Guayaquil estuary includes mining and agriculture (Navarrete-Forero et al., 2019) and thus, this region is under strong pressure from human activities (Twilley et al., 2001). A strong and shallow ODZ is

maintained at intermediate depths due to immense biological production, and weak ocean ventilation (Pennington et al., 2006; Karstensen et al., 2008). The ODZ in the ETSP is defined by an oxygen concentration of  $<20 \mu\text{mol/kg}$  (Helly and Levin, 2004).

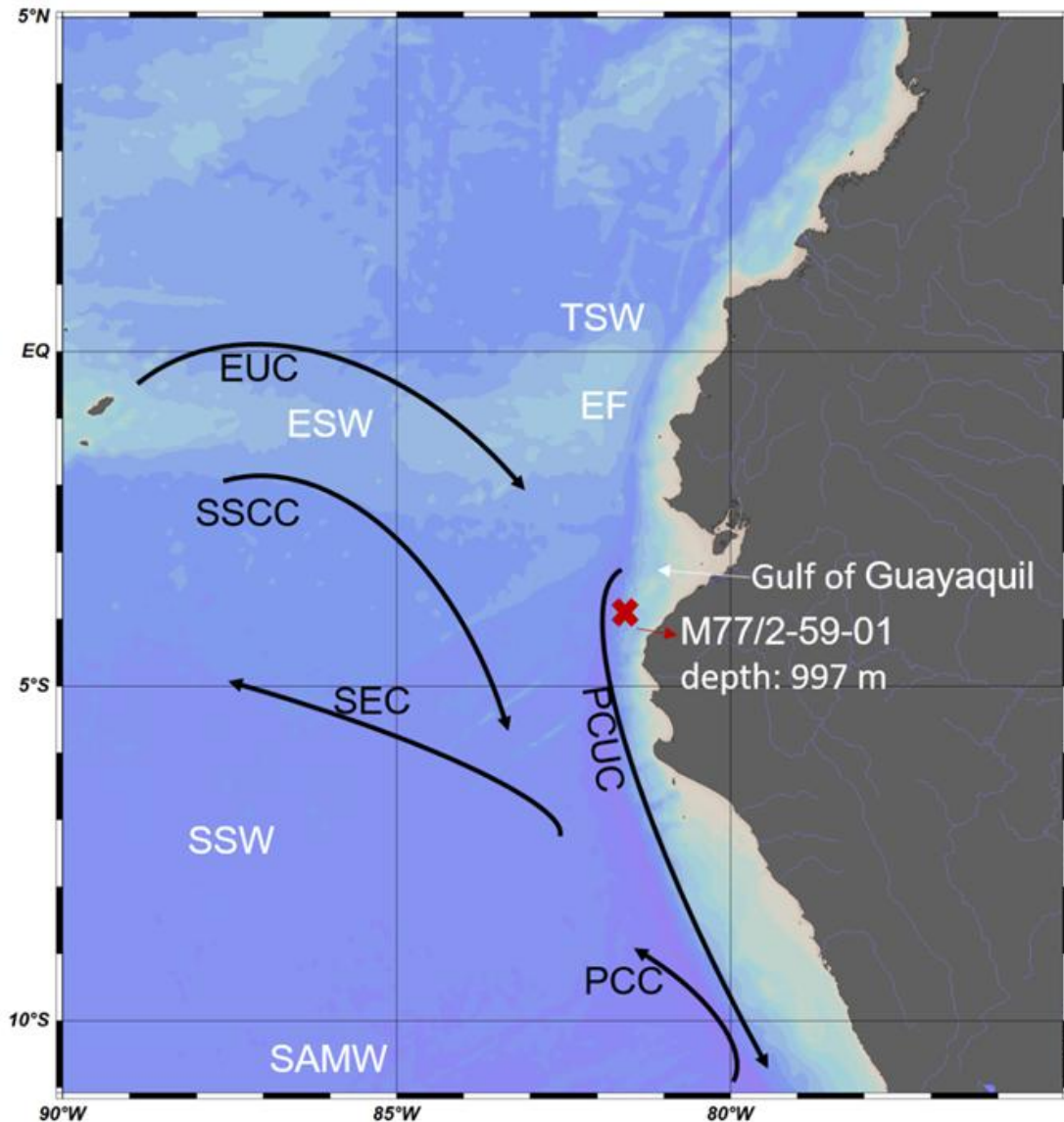


**Figure 2.4.** Sample location off Peru and environmental setting at the Gulf of Guayaquil. Surface currents such as South Equatorial Current (SEC), Peru Chile Current (PCC) are shown. Subsurface currents such as the Equatorial Under Current (EUC), Southern Subsurface Counter Current (SSCC), Peru Chile Under Current (PCUC) are shown in the map. The red cross depicts the location from where the sediment core M77/2-59-01 has been retrieved. The prominent surface and subsurface water masses are indicated as Tropical Surface Water (TSW), Equatorial Surface Water (ESW), Subtropical Surface Water (SSW) and Subantarctic Mode Water (SAMW). The TSW and ESW are separated by the Equatorial Front (EF). The Ocean Data View software has been used to create this map (Schlitzer, R., 2023).

The Gulf of Guayaquil is in the EEP and is under the influence of Equatorial Surface Water, Tropical Surface Water, and Cold Coastal Water (Nurnberg et al., 2015). The Tropical Surface Water and Equatorial Surface Water are separated (**Fig. 2.4**) by the Equatorial Front, EF (Nurnberg et al., 2015). The EF is a steep thermal gradient limited to the upper ~100 m of the water column (Rincón-Martínez et al., 2010). The position of the EF is controlled by the ITCZ (Twilley et al., 2001; Nurnberg et al., 2015). The southeast trade winds result in an offshore Ekman transport along the Peruvian margin (Nurnberg et al., 2015). This brings cold, nutrient-rich waters from below through coastal upwelling (Kessler, 2006). Surface currents such as the South Equatorial Current, Peru Chile Current, Ecuador-Peru Coastal Current, and subsurface currents such as the Equatorial Undercurrent, Southern Subsurface Counter Current, Peru Chile Under Current, and Peru Chile Counter Current (Kessler, 2006; Nurnberg et al., 2015) are the major currents which influence the hydrology and climate of Gulf of Guayaquil. The sediment core (M772-59-01) for the PhD work has been collected from the northern margin of the Peruvian ODZ (**Fig. 2.4**) at a water depth of 997 m. This region has higher oxygen concentrations which allows benthic life, and prevent the formation of laminations (Mollier-Vogel et al., 2019).

### Chapter 3

#### **A deep-learning automated image recognition method for measuring pore patterns in closely related bolivinids and calibration for quantitative nitrate paleo-reconstructions**

Anjaly Govindankutty Menon, Catherine V. Davis, Dirk Nürnberg, Hidetaka Nomaki, Iines Salonen, Gerhard Schmiedl, Nicolaas Glock

#### **Abstract**

Eutrophication is accelerating the recent expansion of oxygen-depleted coastal marine environments. Several bolivinid foraminifera are abundant in these oxygen-depleted settings and take up nitrate through the pores in their shells for denitrification. This makes their pore density a possible nitrate proxy. This study documents three aspects related to the porosity of bolivinids. 1) A new automated image analysis technique to determine the number of pores in bolivinids is tested. 2) The pore patterns of *Bolivina spissa* from five different ocean settings are analysed. The relationship between porosity, pore density and mean pore size significantly differs between the studied locations. Their porosity is mainly controlled by the size of the pores at the Gulf of Guayaquil (Peru), but by the number of pores at other studied locations. This might be related to the presence of a different cryptic *Bolivina* species in the Gulf of Guayaquil. 3) The pore densities of closely related bolivinids in core-top samples are calibrated as a bottom water nitrate proxy. *Bolivina spissa* and *Bolivina subadvena* showed the same correlation between pore density and bottom-water nitrate concentrations, while the pore density of *Bolivina argentea* and *Bolivina subadvena accumeata* is much higher.

*Keywords: Bolivinids, Pore density, Automation, Image analysis, Bottom-water nitrate*

### 3.1 Introduction

Oceanic oxygen concentrations are predicted to decrease globally affecting the stability of marine ecosystems (Stramma et al., 2008; Schmidtko et al., 2017; Salvattecchi et al., 2022; Moffitt et al., 2015). Global warming accelerates ongoing ocean deoxygenation (IPCC, 2018: Global warming of 1.5°C; Keeling et al., 2010), and expansion of oxygen minimum zones (OMZs) (Stramma et al., 2008 & 2010; Schmidtko et al., 2017). Increased ocean warming enhances upper-ocean stratification (Voss et al., 2013), reduces ventilation, and has implications for biological productivity (Stramma et al., 2010) as well as carbon, nitrogen, (Gruber & Galloway, 2008) and phosphorus cycling (Wallmann, 2003) in the oceans. These processes are amplified by the large-scale use of chemical nitrogenous fertilizers to satisfy global demand for food production which drastically disrupts the nitrogen cycle (Canfield et al., 2010; Sutton et al., 2019). Oxygen is a major influence on the marine nitrogen cycle in the global oceans (Keeling et al., 2010) as some microbial processes require oxygen while others are inhibited by it (Voss et al., 2013). When oxygen concentrations drop below  $\sim 4.5 \mu\text{mol/kg}$ , nitrate becomes the major electron acceptor for respiration replacing oxygen, a condition called suboxic (Karstensen et al., 2008; Codispoti et al., 2001; Lam & Kuypers, 2011). The continued expansion of suboxia results in the loss of fixed nitrogen via denitrification (Codispoti et al., 2001; Gruber, 2004), a dissimilatory process in which nitrate ( $\text{NO}_3^-$ ) is ultimately converted into dinitrogen gas (Korom, 1992). Therefore, denitrification reduces the supply of  $\text{NO}_3^-$  in global oceans (Codispoti et al., 2001; Gruber, 2004). Nitrogen fixation, nitrification, and denitrification are major processes in the nitrogen cycle that are mainly facilitated by bacteria (Klotz & Stein, 2008), while lower oxygen concentrations can either enhance or inhibit these processes (Codispoti et al., 2001). Therefore, the nitrogen cycling in OMZs is different from the rest of the open ocean (Lam & Kuypers, 2011). Approximately 30-50% of fixed nitrogen loss in the world's oceans occurs in oxygen minimum and deficient zones (Codispoti et al., 2001). Quantitative paleoreconstruction of nitrate levels could provide a comprehensive understanding of how the different processes mentioned above interacted in the past. This will help us to predict future changes in marine nutrient budgets and possible impacts of eutrophication.

Foraminifera are a group of amoeboid protists that are abundant in marine environments (Goldstein, 1999), and account for a major part of benthic denitrification in the OMZs (Glock et al., 2013; Piña-Ochoa et al., 2010; Dale et al., 2016). Many calcareous foraminiferal tests (shells)

are porous. The pores in benthic foraminiferal tests play an important role in facilitating gas exchange and osmoregulation between the foraminifera and the environment (Leutenegger & Hansen, 1979). The pore density (number of pores per unit area), mean pore size (average pore sizes of one individual), and shape of pores are important morphological features that vary among different taxa (Kuhnt et al., 2013; Richirt et al., 2019a; Schönfeld et al., 2021). The porosity (% of area of the tests occupied by the pores), and pore density of foraminifera are likely driven by environmental factors. Factors that have been suggested include latitude, water density (Bé, 1968; Frerichs et al. 1972; Bé et al. 1973; Frerichs and Ely, 1978), temperature, salinity (Bijma et al. 1990), oxygen, and nitrate concentrations (Glock et al., 2011; Kuhnt et al., 2013; Rathburn et al., 2018; Richirt et al., 2019b). Porosity might also be genetically encoded (Richirt et al., 2019a; Quillevere et al., 2013). Porosity is a species-specific trait that can be used to distinguish certain pseudocryptic species such as *Ammonia* spp. (Richirt et al., 2019a). Nevertheless, within a single species phenotypic plasticity exists. Thus, porosity can be influenced by environmental conditions, and hence used as a paleoproxy.

Porosity in benthic foraminifera plays an important role in adaptation strategies by facilitating gas exchange through larger pore areas in low oxic conditions (Perez-Cruz & Machain-Castillo, 1990; Glock et al., 2011; Kuhnt et al., 2013). Cell organelles involved in respiration (i.e., mitochondria) are more abundant around the inner pore surfaces of species living in oxygen-depleted conditions than in well-oxygenated conditions (Leutenegger & Hansen, 1979). In some foraminiferal species, increased gas exchange can be attained by either increasing the number of pores or by increasing the surface area of the test (or shell) (Gary et al., 1989). However, the function of pores may vary among species because of their difference in evolutionary history (Glock et al., 2012a).

The shallow oxygen minimum zones of the Eastern Pacific have large standing stocks of benthic foraminiferal species (Phleger & Soutar, 1973). Several benthic foraminiferal species living in oxygen-depleted environments perform complete denitrification, which is rare amongst eukaryotes (Risgaard-Petersen et al., 2006). Denitrification is the preferred respiration pathway in several foraminiferal species from oxygen-depleted environments, making these eukaryotes an important part of benthic nitrogen cycling in some environments (Glock et al., 2019). Previously, it has been found that benthic foraminifera living in oxygen- or nitrate-depleted environments have higher pore density and porosity than those living under well-oxygenated conditions or high ambient

nitrate concentrations (Glock et al., 2011; Kuhnt et al., 2013; Rathburn et al., 2018). Therefore, pore parameters of fossil shells are promising proxies for paleo oxygen and nitrate concentrations. We determined pore parameters mean pore size, pore density, and porosity of the shallow infaunal species *Bolivina spissa* (see Fig. 3.1). Many bolivinids have an affinity for low-oxygen environments (Harman, 1964). *Bolivina spissa* is well adapted to low oxygen conditions (Glock et al., 2011; Fontanier et al., 2014), and has the ability to denitrify (Glock et al., 2019a), which makes it a promising species that might facilitate quantitative  $\text{NO}_3^-$  reconstructions.

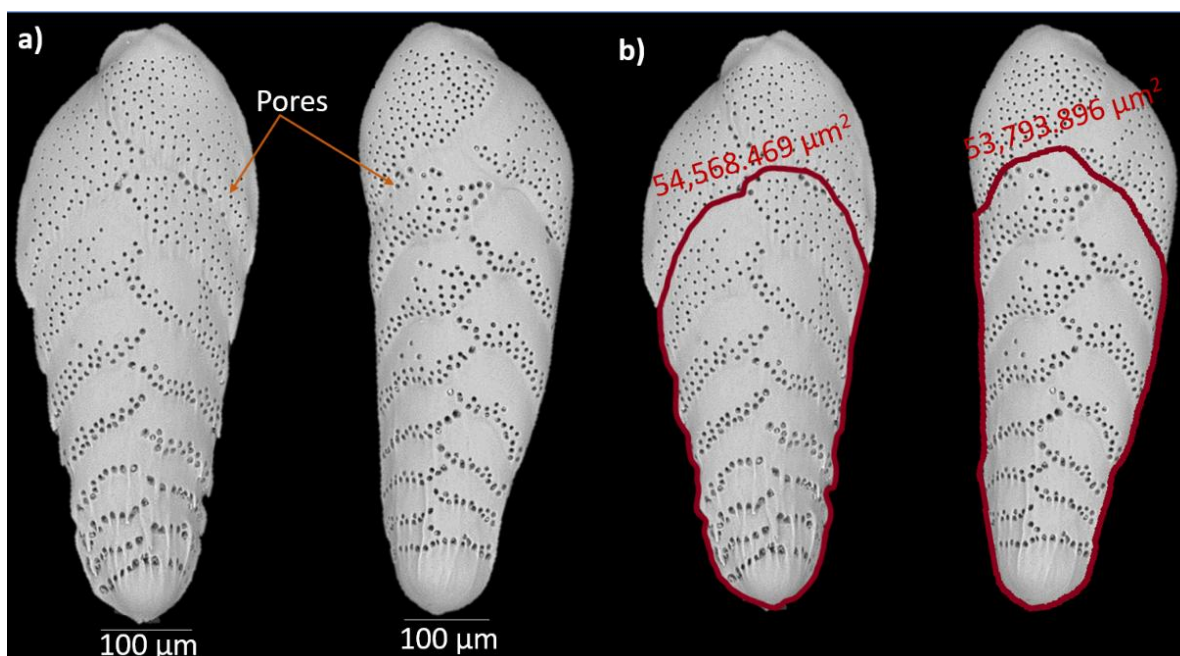


**Figure 3.1.** a) Scanning Electron Microscopic images of *B. spissa* collected from the Mexican Margin (MAZ-1E-04), (water depth: 1463m) and b) their total area relative to first (oldest) ~ten chambers within 50,000 – 70,000  $\mu\text{m}^2$  measured using ZEN lite software.

We used foraminiferal specimens retrieved from five oxygen-depleted locations around the Pacific: The Gulf of Guayaquil (core M77/2-59-01), the Mexican Margin (core MAZ-1E-04), the Sea of Okhotsk (core MD01-2415), and “core-top” (i.e., surface-sediment) samples from Sagami Bay, and the continental margin of Costa Rica (Quepos Slide, core SO206-43-MUC) (Fig. 3.2). Here, we present a non-destructive, fast and statistically robust method for quantitatively describing the morphometrics in benthic foraminiferal tests. We applied an automated image recognition technique on scanning electron microscope (SEM) images using a deep learning

algorithm to analyse the morphological features of *B. spissa*. Deep learning is a type of machine learning which is used to identify objects in images and allows to process data in a way according to user's interest (LeCun et al., 2015).

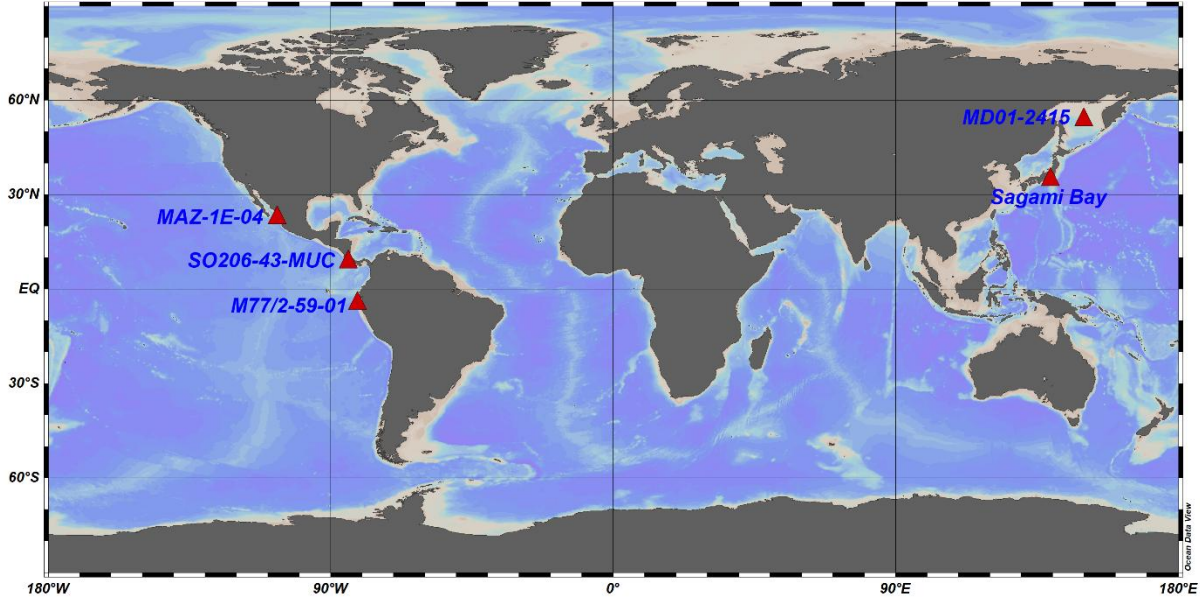


**Figure 3.2.** Map showing site locations studied: Gulf of Guayaquil (M77/2-59-01, depth: 997 m), Mexican Margin (MAZ-1E-04, depth: 1463 m), Sea of Okhotsk (MD01-2415, depth: 822 m), core-top samples from Costa Rica (Quepos Slide, SO206-43-MUC, depth: 568 m), and Sagami Bay (Japan, depth: 1410). The map was produced using Ocean Data View (Schlitzer, R., 2023).

We studied 1) the interdependence between the pore density, porosity and mean pore size of *B. spissa* to demonstrate whether total porosity is mainly influenced by the number or the size of pores and 2) whether porosity or pore density can be used as a robust proxy for bottom-water nitrate  $[\text{NO}_3^-]_{\text{BW}}$  reconstructions. Finally, we compare the pore density between *B. spissa*, *Bolivina subadvena*, *Bolivina subadvena accumeata*, and *Bolivina argentea*, and provide an extended nitrate vs. pore density calibration for *B. spissa* and *B. subadvena* from different locations around the Pacific.

## 3.2 Methods

### 3.2.1 Sampling of sediment cores

The piston core M77/2-059-1 (03°57.01' S, 81°19.23' W, recovery 13.59 m) was retrieved from the Gulf of Guayaquil at 997 m water depth during RV Meteor cruise M77/2 in 2008. The

chronostratigraphy is based on accelerator mass spectrometry radiocarbon dating (AMS<sup>14</sup>C) of planktonic foraminifers, supported by benthic stable oxygen isotope ( $\delta^{18}\text{O}$ ) stratigraphy from *Uvigerina peregrina* (Mollier-Vogel et al., 2013; Nürnberg et al., 2015). The CALYPSO giant piston core MD01-2415 (53°57.09' N, 149°57.52' E, recovery 46.23 m) was recovered from the northern slope of the Sea of Okhotsk at 822 m water depth during WEPAMA cruise MD122 of the R/V Marion Dufresne (Holbourn et al., 2002; Nürnberg & Tiedemann, 2004). The chronostratigraphic framework of core MD01-2415 is based on a combination of stable oxygen-isotope stratigraphy, AMS<sup>14</sup>C dating, and orbital tuning (Nürnberg & Tiedemann, 2004). The piston core MAZ-1E-04, Mexican Margin was collected on board the RV El Puma at a water depth of 1463 m. The core, SO206-43-MUC was retrieved in 2009 from a sea mound slope (Quepos Slide) off Costa Rica during RS Sonne cruise SO206 using a multicorer. Supernatant water of the multicorer SO206-43-MUC was carefully removed. Then, the core was gently pushed out of the multicorer tube. For the foraminiferal analyses, the core was cut into 10 mm thick slices (upto 20 cm depth) and samples were transferred to Whirl-Pack<sup>TM</sup> plastic bags and stored at a temperature of 4°C.

The sediment samples from central part of Sagami Bay were collected by a push core (inner diameter: 8.2 cm, tube length: 32.0 cm) using the manipulator of human occupied vehicle *Shinkai6500* in 2021 (Table 3.1 shows the details of all sampling locations). The surface 2 cm of the sediment was subsampled by extruding from the push core tube and then kept frozen prior to an isolation of foraminifera. Bottom-water temperature, salinity, and dissolved oxygen concentrations were 2.3 °C, 34.5, and 56.4  $\mu\text{M}$ , respectively, which were measured with the CTDO sensor (Seabird SBE19).

**Table 3.1.** Site location information and distribution of specimens (*B. spissa*) from different sampling locations used in the study.

Location	Latitude	Longitude	Water depth (m)	No of <i>B. spissa</i> specimens
Gulf of Guayaquil, (M77/2-59-01)	3.95° S	81.32° W	997	669
Mexican Margin, (MAZ-1E-04)	22.9° N	106.91° W	1463	455
Sea of Okhotsk, (MD01-2415)	53.95° N	149.96° E	822	144
Sagami Bay push core	35.09° N	135.38° E	1410	37
Costa Rica, (SO206-43-MUC)	8.87° N	84.23° W	568	39

### 3.2.2 Sample processing

All sediment samples from Gulf of Guayaquil (M77/2-59-01), Mexican Margin (MAZ-1E-04), Sea of Okhotsk (MD01-2415), Costa Rica (SO206-43-MUC), and Sagami Bay were washed and wet-sieved through a 63  $\mu\text{m}$  mesh sieve. The residues were dried in an oven at temperatures between 38-50°C. Afterwards the samples were fractionated into the grain-size fractions of 63–125, 125–250, 250–315, 315–355, 355–400, and >400  $\mu\text{m}$ . Specimens of *Bolivina spissa*, *Bolivina subadvena*, *Bolivina subadvena accumeata* and *Bolivina argentea* were picked from the 125–250  $\mu\text{m}$  fraction. Only megalospheric specimens of *B. spissa*, were used for the pore analysis.

### 3.2.3 Bottom-water nitrate analyses at core-top locations

Supernatant water was sampled for the analysis of bottom-water  $\text{NO}_3^-$  concentrations in a core replicate from the multicore deployment at Costa Rica, (SO206-43-MUC). For the bottom water sample, a total of 2 ml was passed through a cadmium (Cd) catalyst to reduce  $\text{NO}_3^-$  to  $\text{NO}_2^-$  (nitrite), which was then analysed on-board using photometry. The resulting concentration is a mixture of  $\text{NO}_3^-$ , and  $\text{NO}_2^-$ . Since  $\text{NO}_2^-$  is a transient intermediate species in the benthic nitrogen cycle and is generally present at lower concentrations than  $\text{NO}_3^-$ , the  $\text{NO}_2^-$  concentration determined is assumed to approximately represent the concentration of  $\text{NO}_3^-$ .

For Sagami Bay nitrate analyses, ~20 mL of overlying water was gently collected using a tube. The overlying water was filtered through a 0.45  $\mu\text{m}$  membrane filter and then stored at  $-25^\circ\text{C}$  before nutrient analyses back in land-based laboratory. Nutrient concentrations were measured with a continuous-flow analyzer (BL-Tech QUAATRO 2-HR system, Japan) (Nomaki et al., 2021). The data for the Peruvian OMZ cores has been taken from (Glock et al., 2011).

### 3.2.4 Bottom-water salinity, temperature and oxygen at core-top locations

Bottom-water conditions at the locations that have been used for the core-top calibrations are shown in **Table 3.2**. Salinity, oxygen and temperature for the Costa Rica core have been taken from the World Ocean Atlas location 24671(B), 84.5°W, 8.5°N and 550 m depth (Garcia et al., 2019). At the Sagami Bay location bottom-water temperature, salinity, and dissolved oxygen concentrations were measured with the CTDO sensor (Seabird SBE19). Data for bottom-water oxygen and temperature at the locations from the Peruvian OMZ were taken from (Glock et al., 2011). Salinity data for the Peruvian OMZ was taken from (Krahmann, 2012), using the Conductivity Temperature Depth-data at M77/1-501/CTD-RO-23.

**Table 3.2.** Bottom-water conditions at the sampling locations that have been used for the core-top calibration. Sampling locations in italic letters have been taken from [Glock et al. \(2011\)](#).

Location	Nitrate ( $\mu\text{M}$ )	Water depth (m)	Salinity	Oxygen ( $\mu\text{mol/kg}$ )	Temperature ( $^{\circ}\text{C}$ )
Costa Rica (SO206-43-MUC)	39.1	568	34.69	9.53	7.47
Sagami Bay push core (Japan)	42.2	1410	34.50	56.40	2.30
<i>M77/1-455/MUC-21 (OMZ, Peru)</i>	34.0	465	34.64	2.42	8.12
<i>M77/1-565/MUC-60 (OMZ, Peru)</i>	40.1	640	34.56	8.17	6.70
<i>M77/1-445/MUC-15 (OMZ, Peru)</i>	40.8	928	34.56	36.77	4.76
<i>M77/1-487/MUC-39 (OMZ, Peru)</i>	38.8	579	34.55	3.70	7.21
<i>M77/1-459/MUC-25 (OMZ, Peru)</i>	41.0	698	34.57	12.55	6.68
<i>M77/1-604/MUC-74 (OMZ, Peru)</i>	40.8	878	34.53	34.23	5.72
<i>M77/1-516/MUC-40 (OMZ, Peru)</i>	36.1	513	34.60	2.40	8.05

### 3.2.5 Image acquisition

A total number of 23 sample depths from the Mexican Margin (MAZ-1E-04), 37 sample depths from the Gulf of Guayaquil (M77/2-59-01), 12 sample depths from Sea of Okhotsk (MD01-2415), and 2 core-top samples from Sagami Bay (Japan) and Costa Rica, (SO206-43-MUC) were utilized. All specimens of *B. spissa* were mounted onto carbon pads and photographed using Scanning Electron Microscope (version: Hitachi Tabletop SEM TM4000 series). All images were captured at a magnification of 150x. Due to the more or less flat surface of *B. spissa*, pore openings were generally well-defined, and clearly distinguishable from the SEM images. The total area on the tests of the specimens were determined using the Zeiss ZEN lite software.

### 3.2.6 Size normalization

To reduce ontogenetic effects, the total area equivalent to the first (oldest) ~ten chambers (covering 50,000 - 70,000  $\mu\text{m}^2$ ) were measured for the quantification of pore parameters ([Glock et al., 2011](#)). The pore density increases with each newly built chamber (**Fig. 3.1**), related to a decrease in the surface/volume ratio with the size of the specimens. If the more recent 1-2 chambers would be analyzed, only specimens within the same ontogenetic stage could be used. i.e., the size of the specimen and the number of chambers should be the same in all the chosen specimens. It is practically impossible to use only specimens having exactly the same number of chambers. By sticking to the oldest chambers of the foraminifer the ontogenetic effects are minimized by size normalization. Moreover, the larger area provides a statistically robust, and larger dataset for each analysed specimen. ([Glock et al., 2022](#)).

### 3.2.7 Automated image analysis

A total number of 1344 fossil specimens of *B. spissa* sampled from five different sampling locations were analysed. Porosity measurements were made on 6 - 20 well-preserved specimens of *B. spissa* in each of the studied locations. The pore density, mean pore size, and porosity were determined with an automated image analyzing software Amira (version: Amira™3D pro) using a previously trained deep-learning algorithm. The deep learning algorithm that has been used for this study is included in the Amira software package. We used a convolutional neural network (CNN) model (UNet) backbone with a resnet18 model for the deep learning training. The deep learning algorithm was trained with manually segmented pores on 52 images of *B. spissa*. In total 17,649 pores have been segmented manually for the deep learning training.

Only those specimens that had a total area equivalent to at least 50,000  $\mu\text{m}^2$  were used for the automated analysis. The main steps for porosity measurements in Amira were:

- Import of multiple SEM images.
- The deep learning algorithm to recognize the pores was applied on imported images.
- Only the oldest chambers that fit within the total area of 50,000 to 70,000  $\mu\text{m}^2$  were taken into account (**Fig. 3.1b**). All chambers beyond this threshold were manually removed, using the segmentation tools in the Amira software.
- A table with all measured pore characteristics can be exported by the software at the end of each set of analysis.

### 3.2.8 Comparison of manual vs. automatic pore density determination

To assess the reliability of the deep learning algorithm pore density was determined manually for 31 specimens belonging to the species *B. spissa* (27 specimens) *B. subadvena* (3 specimens) and *B. subadvena accumeata* (1 specimen). For four additional specimens of *B. argentea* pore density was determined manually, since the pores in this species are very small and not recognized by the deep learning algorithm that was trained with images of *B. spissa*. The detailed procedure for manual pore density determinations are published in Glock et al. (2011).

### 3.2.9 Automated pore measurements with and without manual corrections

To explore whether manual corrections (i.e., corrections done on the specimens that were automatically pore analysed) made a significant difference on automated data, a total number of 858 specimens were randomly selected and analysed both with and without manual correction..

To apply manual corrections, we removed all artefacts (i.e., unwanted particles on the surface of *B. spissa*) on each specimen during the automated image analysis and obtained porosity data. For the automated image analysis without manual corrections, we applied the method of analyzing each specimen without manually removing the artefacts. Statistical analysis was carried out to decide if the porosity data obtained through either of these methods were significantly different or not. The preliminary statistical analysis was carried out in Excel and verified using RStudio (RStudio Team, 2023). To test the normality of the samples, we used Shapiro-Wilk normality test whenever necessary. To determine the correlation between pore parameters, a linear ordinary least-square regression was used. For normal distributions, we used the parametric Student's t-test (t), and for non-normal distributions we used the non-parametric Wilcoxon test (W). All the data generated or analyzed during this study have been included in Appendix A.

### 3.3 Results

#### 3.3.1 Comparison between manual and automated pore density analyses

Pore density measurements showed a 0-20% difference between manual and automated methods with an average individual difference at 4.2%. There was no significant difference in the mean pore density of all 31 specimens between the manual ( $0.0059 \pm 0.0002 \text{ P } \mu\text{m}^{-2}$ ; 1 SEM) and the automated ( $0.0059 \pm 0.0002 \text{ P } \mu\text{m}^{-2}$ ; 1 SEM) image analyses (T-test,  $p = 0.99$ ). In three out of 31 cases the difference was 0% and the algorithm was counting exactly the same number of pores that have been recognized manually (Appendix A; Supplementary Table ST1). Only two specimens of *B. subadvena* showed a relatively high offset (10% and 20%). The original training of the algorithm is based on *B. spissa*. For future studies, which include a closer analysis of other species, we recommend an individual training for each species.

#### 3.3.2 Automated pore measurements with and without manual corrections

There was no significant difference for porosity ( $t = 0.31$ ,  $p = 0.75$ ) and pore density ( $t = 0.58$ ,  $p = 0.56$ ) obtained through automated image analysis with and without manual corrections, where artefacts of the automated image analyses were manually removed (Appendix A; Supplementary Table ST2 and ST3).

#### 3.3.3 Interdependence between pore parameters of *B. spissa*

The overall porosity values of all locations varied between 2.66% to 16.03% with a mean ( $\pm$ SD) of 8.52% ( $\pm 2.14\%$ ). The mean pore size varied between  $5.98 \mu\text{m}^2$  and  $47.62 \mu\text{m}^2$  with a mean

( $\pm$ SD) of  $17.83 \mu\text{m}^2$  ( $\pm 3.83 \mu\text{m}^2$ ). The overall pore density varied between  $0.002 \text{ P}/\mu\text{m}^2$  to  $0.009 \text{ P}/\mu\text{m}^2$  with a mean ( $\pm$ SD) of  $0.004 \text{ P}/\mu\text{m}^2$  ( $\pm 0.001 \text{ P}/\mu\text{m}^2$ ).

Specimens of *B. spissa* from Gulf of Guayaquil, (M77/2-59-01) had the lowest porosity ( $7.14 \% \pm 1.62 \%$ ) and mean pore size ( $17.13 \mu\text{m}^2 \pm 4.37 \mu\text{m}^2$ ) of all analysed locations. The specimens from the Sea of Okhotsk, (MD01-2415) had the highest porosity ( $10.83 \% \pm 1.66 \%$ ) and mean pore size ( $20.67 \mu\text{m}^2 \pm 3.54 \mu\text{m}^2$ ). The mean pore density was not significantly different for the core top samples (Costa Rica and Sagami Bay) and the down core samples from the Mexican Margin (MAZ-1E-04) and the Sea of Okhotsk. The pore density at the Gulf of Guayaquil ( $0.0043 \text{ P}/\mu\text{m}^2 \pm 0.0008 \text{ P}/\mu\text{m}^2$ ) was lower than at the other locations (Appendix A; Supplementary Table ST4).

In general, there was a significant linear correlation between mean pore size and porosity (coefficient of determination,  $R^2 = 0.27$ ,  $p = 3.19\text{E-}93$ , **Fig. 3.3a**; Appendix A; Supplementary Table ST5) for all the analysed specimens. We observed strong regional differences in  $R^2$  among the studied sites. The  $R^2$  was highest for the specimens from the Gulf of Guayaquil ( $R^2 = 0.45$ ,  $p = 5.91\text{E-}89$ , **Fig. 3.3a**), and lowest for the specimens from core-top samples ( $R^2 = 0.05$ ,  $p = 0.047$ , **Fig. 3.3a**). We found a significant linear correlation between porosity and pore density ( $R^2 = 0.42$ ,  $p = 1.36\text{E-}15$ , **Fig. 3.3b**; Appendix A; Supplementary Table ST6) among all the sampling locations with the highest  $R^2$  of 0.45 at the Mexican Margin, while the specimens from the Gulf of Guayaquil showed the weakest correlation ( $R^2 = 0.1$ ,  $p = 3.21\text{E-}17$ , **Fig. 3.3b**) between porosity and pore density.

All analysed specimens showed a significant but weak negative linear correlation between pore density and mean pore size ( $R^2 = 0.085$ ,  $p = 1.34\text{E-}27$ , **Fig. 3.3c**; Appendix A; Supplementary Table ST7). We found a higher  $R^2$  for the core-top samples collected from Costa Rica and Sagami Bay ( $R^2 = 0.4$ ,  $p = 7.18\text{E-}10$ , **Fig. 3.3c**), and the weakest for the samples from the Gulf of Guayaquil ( $R^2 = 0.20$ ,  $p = 4.52\text{E-}35$ , **Fig. 3.3c**).

The combined data from all studied locations clearly fall apart into two distinguishable clusters for both porosity and pore density: “Cluster 1” (black dashed circle **Fig. 3.3**), grouped most of the specimens belonging to the Gulf of Guayaquil ( $n = 669$ ), and “Cluster 2” (red dashed circle, **Fig. 3.3**), consisted of specimens belonging to the Mexican Margin ( $n = 445$ ), the Sea of Okhotsk (144), and the core-top samples ( $n = 76$ ). The porosity was significantly different between Cluster 1 and Cluster 2 ( $W = 50716$ ;  $p < 2.2\text{e-}16$ ). This also accounts for the pore density ( $W = 79726$ ,  $p < 2.2\text{e-}16$ ).

-16) and the mean pore size ( $W = 170008$ ;  $p = 4.49e^{-15}$ ). All data have been included in the Appendix A as Supplementary Table ST8.

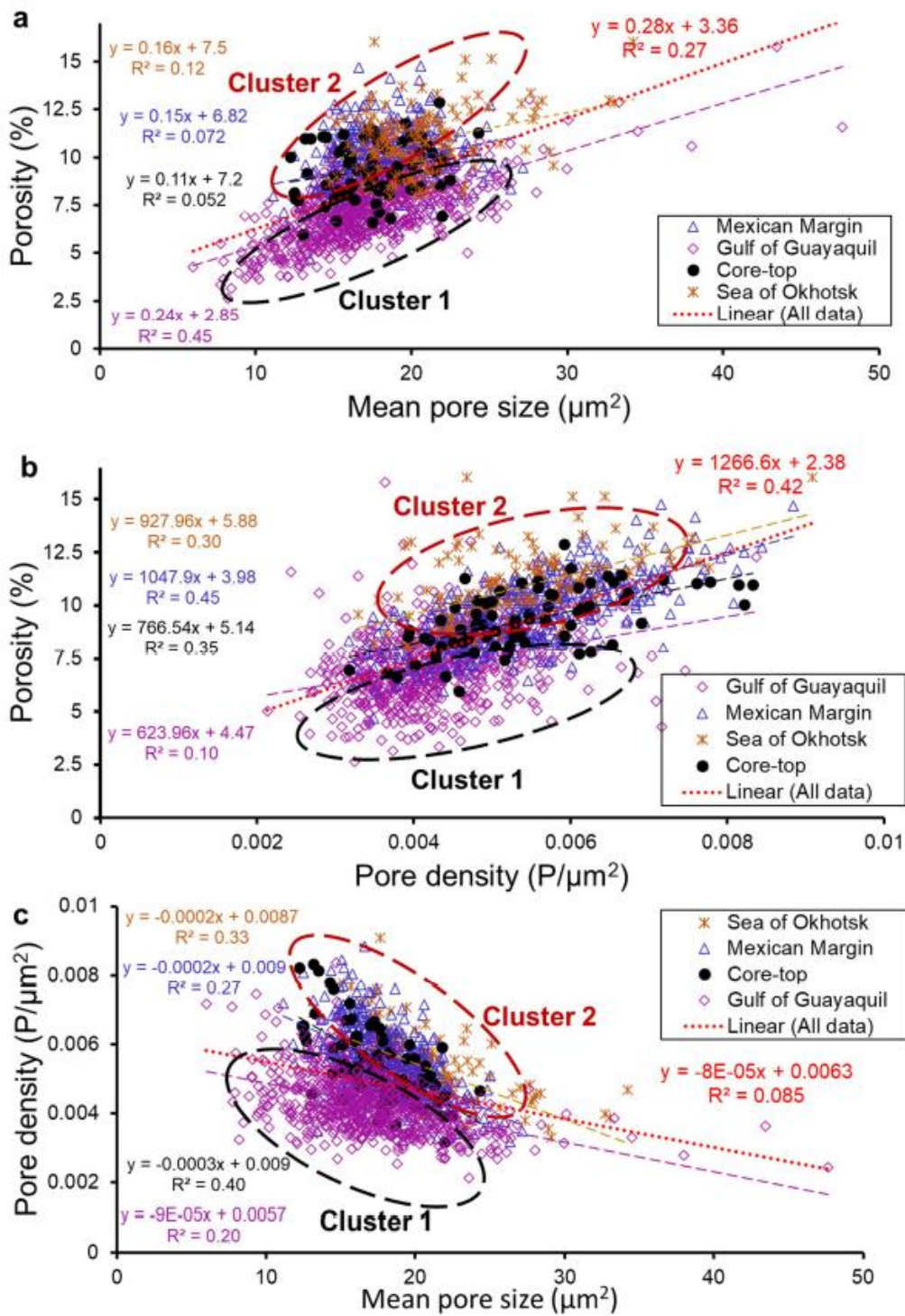


**Figure 3.3.** Relationship between a) porosity vs. mean pore size b) porosity vs. pore density, and c) pore density vs. mean pore size of *B. spissa* specimens from the Gulf of Guayaquil (M77/2-59-01), the Mexican Margin (MAZ-1E-04), the Sea of Okhotsk (MD01-2415), and the core-top samples (Sagami Bay and Costa Rica). Total number of specimens utilized,  $n = 1344$ .

### 3.3.4 Inter-species comparison of pore parameters and pore density vs $[\text{NO}_3^-]_{\text{BW}}$ calibration in the core-top samples

While core-top specimens of *B. spissa* and *B. subadvena* from Costa Rica (Quepos Slide), and Sagami Bay (Japan) had a very similar pore density, pore densities of *B. subadvena accumeata* and *B. argentea* were around 50-300% higher (**Fig. 3.4**; Appendix A; Supplementary Table ST9). The new data for *B. spissa* and *B. subadvena* from Quepos Slide and Sagami Bay fit well into the pore density correlation with  $[\text{NO}_3^-]_{\text{BW}}$  that has been found for *B. spissa* from the Peruvian OMZ (Glock et al., 2011) (**Fig. 3.4**). There was a highly significant linear correlation between the pore density of *B. spissa* and *B. subadvena* from Peru, Costa Rica, and Sagami Bay ( $R^2 = 0.93$ ,  $p < 0.0001$ , **Fig. 3.4b**). The data of *B. subadvena accumeata* and *B. argentea* were offset from this linear regression (**Fig. 3.4a**). The relationships between the pore density of *B. spissa* and *B. subadvena* from core-top samples (Costa Rica and Sagami Bay) and bottom water oxygen ( $R^2 = 0.43$ ,  $p = 0.028$ ; Appendix A as Supplementary Figure SF1), temperature ( $R^2 = 0.50$ ,  $p = 0.015$ ; Appendix A as Supplementary Figure SF2), salinity ( $R^2 = 0.41$ ,  $p = 0.035$ ; Appendix A as Supplementary Figure SF3), and water depth ( $R^2 = 0.48$ ,  $p = 0.018$ ; Appendix A as Supplementary Figure SF4) has been analysed to test, if nitrate is the main factor that controls the pore density. These correlations are significant ( $R^2$  varies between 0.41 and 0.50;  $P$  varies between 0.015 and 0.035) but clearly weaker than the correlation of the pore density to nitrate ( $R^2 = 0.93$ ,  $p = 1.4\text{E-}6$ ; **Fig. 3.4b**).

Since pores were manually counted for the core-top pore density dataset off Peru from Glock et al. (2011), no data was available for the porosity of these specimens. A comparison of the porosity in tests of core-top samples of *B. spissa* from Costa Rica ( $9.5\% \pm 0.2\%$ ; 1SE;  $N = 39$ ) and Sagami Bay ( $9.1\% \pm 0.2\%$ ; 1SE;  $N = 37$ ) showed no significant difference between these two locations ( $p = 0.25$ ). The Costa Rica  $[\text{NO}_3^-]_{\text{BW}}$  was lower and there was a significant difference in the pore density between these two locations ( $p = 8.7\text{E-}5$ , **Fig. 3.4**). This indicated that the pore density of *B. spissa* might be more sensitive to changes in the  $[\text{NO}_3^-]_{\text{BW}}$  than the porosity. In addition, while the pore density of *B. subadvena* fit very well into the pore density- $[\text{NO}_3^-]_{\text{BW}}$  correlation of *B. spissa* (see **Fig. 3.4**), the porosity of *B. subadvena* was significantly higher than the porosity of *B. spissa* ( $10.9\% \pm 0.5\%$  for *B. subadvena* vs.  $9.5\% \pm 0.2\%$  for *B. spissa* from Costa Rica;  $p = 0.0002$ ).

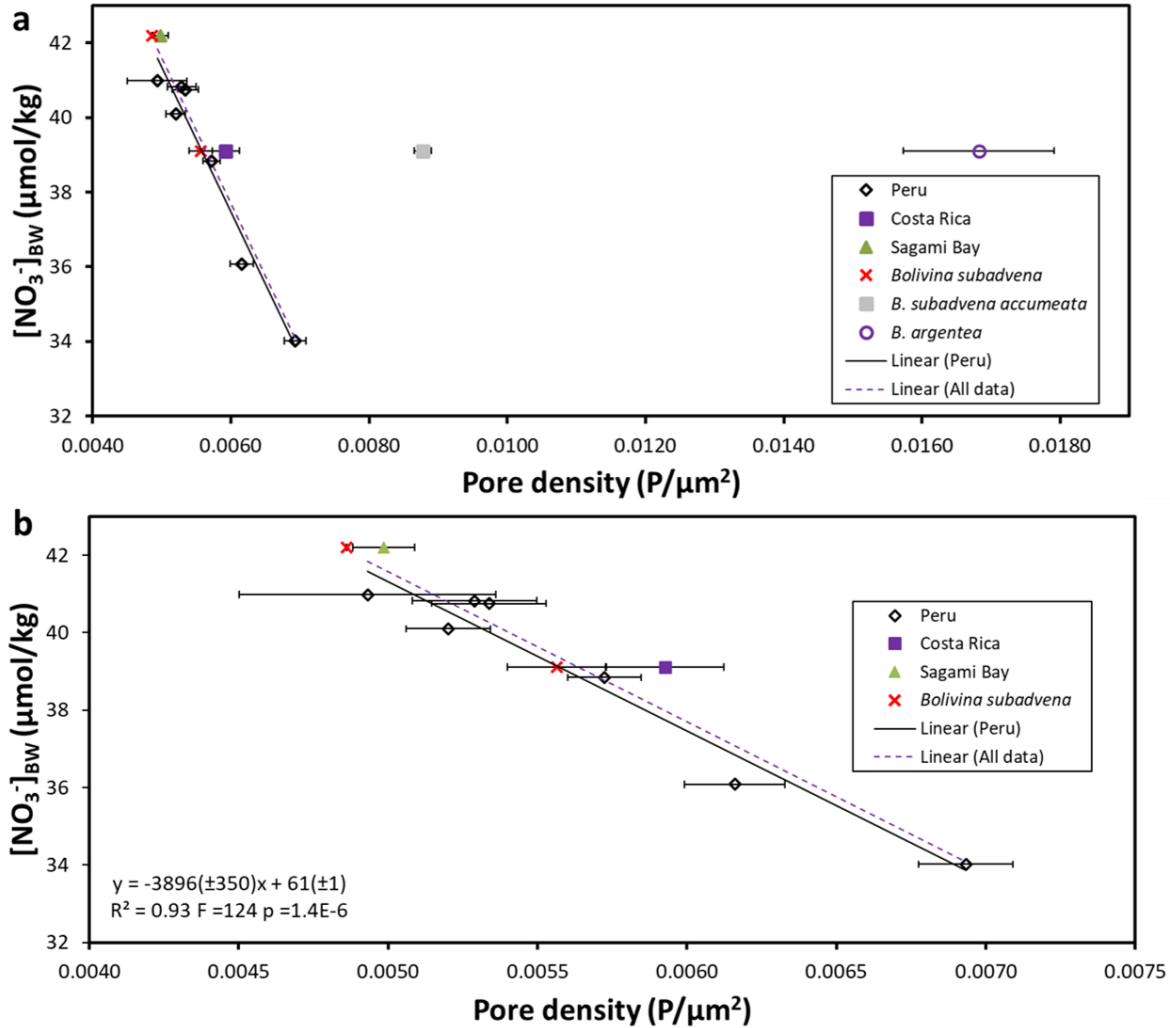


**Figure 3.4.** Correlation between the mean pore density of different closely related *Bolivina* species from core-top samples and  $[\text{NO}_3^-]_{\text{BW}}$ . If no species name is indicated, the analysed species was *B. spissa*. The specimens of *B. subadvena*, *B. subadvena accumeata* and *B. argentea* are all from location SO206-43-MUC off Costa Rica, except the one specimen of *B. subadvena* at  $\sim 42 \mu\text{mol/kg}$   $[\text{NO}_3^-]_{\text{BW}}$  that was collected at Sagami Bay (Japan). The linear fit (all data) has been applied to all available data for *B. spissa* and *B. subadvena*, except *B. subadvena accumeata* and *B. argentea*. **a**) Pore density vs  $[\text{NO}_3^-]_{\text{BW}}$  plot including all analysed *Bolivina* species. **b**) Pore density vs  $[\text{NO}_3^-]_{\text{BW}}$  plot only including *B. spissa* and *B. argentea*. The linear fit (Peru) alone was the published correlation from Glock et al. (2011 & 2018) and only included *B. spissa* collected off Peru. Error bars are the standard error of the mean (1SE).

### 3.4 Discussion

#### 3.4.1 Evaluation of the automatic image recognition technique

Our study tested the application of a newly developed automated image recognition method for the detection of pore parameters of the benthic foraminiferal species *B. spissa*. This method can be used to accurately measure pore parameters such as the mean pore size, porosity, and pore density of *B. spissa*. This allows a high and efficient sample throughput (less than 1 minute for one specimen) compared to manual analysis (5 – 6 minutes for one specimen) of pores. This automated deep learning approach produces results statistically identical to manual analyses. No significant improvement is found, if the results from the deep learning image analyses are manually corrected by removing artefacts from the images.

Both manual determination of pores using SEM images (Hayward et al., 2004; Glock et al., 2011; Constandache et al., 2013; Kuhnt et al., 2014) and automated measurements (Petersen et al., 2016; Tetard et al., 2017), have advantages and disadvantages. For example, manual methods can be laborious and time-consuming. The fully automated method by Tetard et al. (2017) is rapid, allows quick generation of data, and the image acquisition and processing require no monitoring, however, it needs a very specific setup and is destructive, since the specimens are broken to shards. The semi-automatic method by Petersen et al. (2016) can produce reliable data in a short amount of time, minimizes artefacts related to the curvature of the tests, and gives information on pore area, perimeter, and circularity indexes but focuses only on a small part of the shell, which limits the amount of data per specimen.

By contrast, porosity measurements using deep-learning as applied in this study are non-destructive and automatically determines various pore parameters on the fully visible test surface. Moreover, the fully automated method is reproducible in comparison to manual methods where the analyses are performed by different operators. The application of a non-destructive method allows the use of the foraminifera for other analyses, thereby providing the possibility to use a single sample population for a multiproxy paleo reconstruction.

Although this automated method generates large datasets, proper attention should be given to the processing of curved specimens of *B. spissa*, because the curvature can create artefacts on the edges of the specimen. Therefore, we suggest utilizing specimens with flat surfaces.

### 3.4.2 Variation of pore patterns in *B. spissa* from different environments

All specimens of *B. spissa* that have been analysed showed a positive but weak correlation between the porosity and the mean pore size ( $R^2 = 0.27$ ,  $p < 0.05$ ; **Fig. 3.3a**). Certain foraminifer's species increase their porosity by increasing the size of their pores to facilitate electron acceptor uptake from the environment (Moodley & Hess, 1992; Petersen et al., 2016). The strongest correlation between mean pore size and porosity at the Gulf of Guayaquil (M77/2-59-01) suggests that individuals at this location tend to increase the porosity by increasing their mean pore size rather than by increasing its pore density. Similar observations were documented on *Ammonia* spp that typically dwells in shallow marine environments such as tidal mudflats (Richirt et al., 2019a). These species tend to increase their porosity by building fewer but larger pores, which has been suggested to ensure optimal shell stability (Richirt et al., 2019b; Petersen et al., 2016). The notable weaker correlation between porosity and mean pore size, for the other analysed sites ( $R^2$  between 0.05 - 0.12, **Fig. 3.3a**) implies that most of the analysed *B. spissa* do not control their porosity by modifying the size of the pores. This weak correlation between porosity and the mean pore size in *B. spissa* is an indicator that the size of the pores is only a secondary control on overall porosity of *B. spissa* at most of the studied locations.

The strongest significant linear correlation between porosity and pore density has been found at the Mexican Margin (MAZ-1E-04) (**Fig. 3.3b**), which suggests that *B. spissa* adjusts its porosity by adapting the number of pores and not the pore-size. Specimens from the Gulf of Guayaquil are exceptional as they show only a weak correlation between porosity and pore density ( $R^2 = 0.1$ , **Fig. 3.3b**). Nevertheless, the negative correlation between pore density and mean pore size among the studied sites (**Fig. 3.3c**) are in good agreement with previous studies on *Ammonia* spp. (Richirt et al., 2019b; Petersen et al., 2016). Mechanical constraints like shell stability could be a controlling factor leading to the inverse relationship between pore density and mean pore size (Richirt et al., 2019b). Our new data shows that, except in the Gulf of Guayaquil, *B. spissa* mainly controls its porosity by the number of pores.

The different trends at different locations indicate that long-term environmental conditions or genetic factors likely play a pivotal role in contributing to the morphological differences in benthic foraminifera since the sediment cores cover periods of ~20 kyrs. Especially at the Gulf of Guayaquil, the pore parameters showed significant differences to the other studied locations. We

speculate that these differences could be related either to the mechanism of electron acceptor uptake or to genetic factors. Benthic foraminifera can actively migrate within the sediment to their preferred microhabitat (Geslin et al., 2004; Alve & Bernhard, 1995; Linke & Lutze, 1993) which exposes them to an oxygen/nitrate concentration gradient. The habitat preference of *B. spissa* in oxygen-deficient zones necessitates the use of alternate electron acceptors like nitrate for respiration (Glock et al., 2019a). In nitrate-depleted habitats, *B. spissa* optimizes its nitrate accumulation by building more pores to efficiently take up nitrate resulting in higher pore density (Glock et al., 2011). Previous observations found that the cell size of many denitrifying foraminifers is limited by nitrate availability instead of oxygen (Glock et al., 2019a). Several denitrifying foraminiferal species, including *B. spissa*, have been shown to encode a  $\text{NO}_3^-$  transporter in their genome and transcriptome (Woehle et al., 2018 & 2022). This means by using these  $\text{NO}_3^-$  transporters they can actively pump  $\text{NO}_3^-$  into their cells, since  $\text{NO}_3^-$  is a charged ion. This  $\text{NO}_3^-$  can be stored as intracellular nitrate (ICN) which can be utilized as a source of energy for metabolic activities (Risgaard-Petersen et al. 2006; Høglund et al., 2008; Pina-Ochoa et al., 2010a; Pina-Ochoa et al., 2010b; Koho et al., 2011) via complete denitrification during oxygen-depleted conditions.

### 3.4.3 Biogeochemical controls on the pore patterns in the Gulf of Guayaquil

The site from where core M77/2-59-01 was retrieved (3.95° S, 81.23° W) is outside the core oxygen minimum zone off Peru. The modern oxygen concentration recorded closest to this site is 55  $\mu\text{mol/kg}$ , which is higher than at the other studied locations (38 - 47  $\mu\text{mol/kg}$ ) (Garcia et al., 2019). When oxygen concentration increases above a certain threshold, there will be less overall denitrification (Parkin & Tiedje, 1984; Goering, 1968) resulting in higher nitrate availability. We speculate that if there is more nitrate in the Gulf of Guayaquil relative to the other studied locations in the modern ocean, this was likely also the case in the past. This is supported by a sedimentary nitrogen isotope record on the same core M77/2-59-01 by Mollier-Vogel et al. (2019) and Mollier-Vogel et al. (2012), which indicated that pelagic denitrification was low at this location over the entire last deglaciation. The regional differences in the patterns at Gulf of Guayaquil could be an adaptation to the continuously higher nitrate availability at this site.

### 3.4.4 Genetic controls on the pore patterns in the Gulf of Guayaquil

The *B. spissa* specimens from the Gulf of Guayaquil are except for their pore characteristics, morphologically similar to the *B. spissa* from the other locations but could be a different phylogenetic strain. Observations of *Ammonia* specimens by Hayward et al. (2004) suggested that genetically different species can also be morphologically distinguished. Later studies found genetically well-separated species of the *Ammonia* genus, which have earlier been considered as eco-phenotypes of *Ammonia*, can now be morphologically distinguished by their pore patterns and other subtle morphological features (Richirt et al., 2019a). Similarly, it is possible to have the existence of genetic variation and cryptic species within a *B. spissa* morpho-group due to the wide geographical distances, and variability in ecological conditions that separated oxygen-depleted regions in the Pacific. Nevertheless, the phylotypes of *B. spissa* without a combined morphometric molecular analysis would be very difficult to discriminate as a separate species.

### 3.4.5 An extended modern pore density vs. nitrate calibration

Since there are studies that use either the pore density or porosity to reconstruct past environmental conditions (Glock et al., 2011, 2018 & 2022; Rathburn et al., 2018; Lu et al., 2022) we intended to address whether pore density or porosity is a better proxy for quantitative nitrate reconstructions. Although pore density in *B. spissa* shows a significant correlation to nitrate (Fig. 3.4b), the correlation between porosity and nitrate availability has not been systematically tested, yet. In addition, an extension of the local nitrate vs. pore density calibration for the Peruvian OMZ (Glock et al., 2011) to other regions and foraminiferal species would increase the applicability of this proxy.

Figure 3.4 shows the relationship between pore density in other bolivinids and  $[\text{NO}_3^-]_{\text{BW}}$  from core-top samples at different locations of the Pacific. The linear correlation between the pore density of *B. spissa* and *B. subadvena* and  $[\text{NO}_3^-]_{\text{BW}}$  is highly significant and much stronger than the correlation to oxygen, temperature, salinity or water depth (Appendix A; Supplementary Figures SF1 to SF4), making their pore density a promising proxy for present and past  $[\text{NO}_3^-]_{\text{BW}}$ . This also suggests a close phylogenetic relationship with similar metabolic adaptations of both species. Indeed, *B. spissa* was originally classified as a variant of *B. subadvena* with the name *B. subadvena* var. *spissa* (Cushman, 1926) and 7 out of 7 *Bolivina* species that have been tested for denitrification were able to denitrify and 11 out of 12 analysed species intracellularly stored nitrate

(Glock, 2023 and references therein). Although *B. subadvena accumeata* is still considered a subspecies of *B. subadvena*, the pore characteristics are distinct from either *B. spissa* or *B. subadvena*. The pore density of *B. argentea* is elevated compared to the other species as it tends to build numerous but very small pores (see Fig. 3.5).

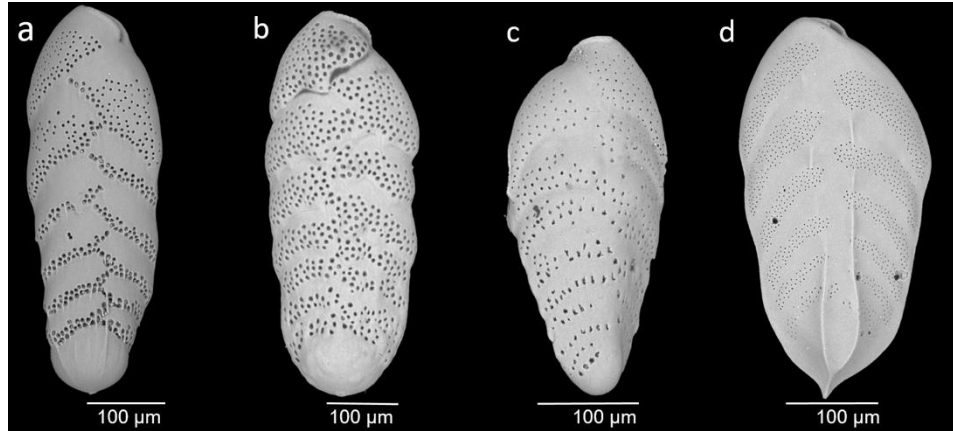


**Figure 3. 5.** Scanning Electron Microscopic images of bolivinids a) *B. spissa*, b) *B. subadvena* c) *B. subadvena accumeata*, and d) *B. argentea*

Therefore, the pore density of *B. spissa* and *B. subadvena* both can be used to reconstruct past  $[\text{NO}_3^-]_{\text{BW}}$  conditions according to the following equation (Eq. 3.1), However, *B. subadvena accumeata* and *B. argentea* should be avoided, when the calibration shown in Eq. 3.1 is used. Future studies will show, if the later two species also show species-specific relationships that might be used for paleoceanographic reconstructions.

$$[\text{NO}_3^-]_{\text{BW}} = -3896 (\pm 350) \text{PD} + 61 (\pm 1) \text{----- (Eq. 3.1)}$$

where PD is the pore density

While the pore characteristics of denitrifying foraminifera are promising paleoproxies for past  $[\text{NO}_3^-]_{\text{BW}}$  (Glock et al., 2011 & 2018), pore characteristics of the epifaunal species *Cibicidoides* and *Planulina* spp. that likely rely on  $\text{O}_2$  respiration seem to be good indicators for past bottom-water oxygen concentration  $[\text{O}_2]_{\text{BW}}$  (Rathburn et al., 2018; Glock et al., 2022). Intriguingly, while the new data on *B. subadvena*, and *B. spissa* indicate that pore density is more sensitive to ambient  $[\text{NO}_3^-]$  variations than the total porosity, it appears that the opposite is the case for epifaunal species. In *Cibicidoides* and *Planulina* spp. porosity is more sensitive to ambient  $[\text{O}_2]$  fluctuations than the pore density (Rathburn et al., 2018; Glock et al., 2022).

Data from only two sites for the correlation between total porosity of bolivinids and  $[\text{NO}_3^-]_{\text{BW}}$  are available. Future studies should address this issue and include both the pore density and total porosity. The fact that porosity of *B. spissa* from the Sagami Bay and Costa Rica core-tops are similar, but the pore density at Costa Rica is significantly higher indicates that the Sagami Bay specimens build larger pores than the specimens from Costa Rica.

The different pore characteristics of denitrifying bolivinids and the aerobic epifaunal species might be related to the mechanism of electron acceptor uptake. The uptake of  $\text{O}_2$  is limited by passive diffusion, since  $\text{O}_2$  is not charged and foraminifera have no respiratory organs that can actively take up  $\text{O}_2$ . Thus, aerobic foraminifera can only increase the  $\text{O}_2$  uptake through the pores by increasing the area of pores on their test (i.e., total porosity), which can be done by either creating more pores (increase in pore density) or larger pores (increase in mean pore size). Some foraminifera species ensure better shell stability by increasing their porosity through building less but larger pores (Richirt et al., 2019b). Thus, the increase of total porosity of epifaunal *Cibicidoides* and *Planulina* spp. might also be restricted by shell stability. They tend to build larger pores to increase their porosity, which might explain the weaker correlation between pore density and ambient  $[\text{O}_2]$  compared to total porosity (Rathburn et al., 2018; Glock et al., 2022). Denitrifying bolivinids can actively pump  $\text{NO}_3^-$  into their cells, since  $\text{NO}_3^-$  is a charged ion and they genetically encode nitrate transporters (Woehle et al 2018, 2022). Thus, we hypothesize that the denitrifying bolivinids do not rely on the increase of total porosity but rather on the number of pores to enhance electron acceptor uptake. For the moment, the empiric correlation between the pore density of *B. spissa* and *B. subadvena* appears to be solid, since a deglacial pore density record of *B. spissa* from the Peruvian margin reconstructed similar  $[\text{NO}_3^-]_{\text{BW}}$  as other proxies and various modeling studies (Glock et al., 2018).

### 3.5 Conclusions

The application of automated image analysis through deep-learning provided a robust method for determining the pore patterns in the shallow infaunal benthic foraminiferal species *B. spissa*. The differences in pore patterns of *B. spissa* found between different studied locations suggest caution in the interpretation of the results. Nevertheless, our new data shows that, except for the Gulf of Guayaquil, *B. spissa* mainly controls its porosity by the number of pores. This gives additional validation that the pore density of *B. spissa* is a robust and reliable paleo-proxy for nitrate

concentrations in bottom-waters. Quantitative reconstructions of past bottom-water nitrate concentrations could help us to predict the environmental and ecological impacts of future climate scenarios. Moreover, understanding the factors controlling porosity in bolivinids provides insight into benthic denitrification, which is indispensable for future biogeochemical studies. Future studies concerning foraminiferal porosity should consider both mean pore size and pore density, and a combined morphometric molecular approach for the complete description of foraminiferal pore patterns. The presence of cryptic species within a morphogroup might complicate paleoceanographic interpretation of pore density or porosity in benthic foraminifera. Thus, various phylogenetic analyses of *Bolivina* species are highly relevant for better proxy validations.

---

### **Data Availability**

All data generated or analysed in this chapter are included in the Appendix A as supplementary figures and tables.

### **Author Contributions**

A.G.M. wrote the core manuscript, did the sample preparation, electron microscopy of the fossil foraminifera and image and statistical analyses of all samples. N.G. planned the sampling strategy and study design, did onboard sampling during So206 and did the electron microscopy and analyses of the core-top samples. G.S. hosted the research group, and provided access to SEM, and lab facilities at the Universität Hamburg. D.N. provided sampling material for cores MD01-2415 and M77/2-59-01. C.D. provided sampling material for core MAZ-1E-04 and H.N. and I.S. provided the core-top samples and environmental parameters from Sagami Bay. All authors contributed to discussing the data and writing the manuscript.

### **Acknowledgements**

We are grateful to the micropaleontology group at the Universität Hamburg. We greatly acknowledge the help of Dr. Yvonne Milker with the SEM, Jutta Richarz, Kaya Oda for lab support, and student assistants Hanna Firrincielli and Hannah Krüger. In addition, we thank Anke Bleyer for performing the nitrate analyses during Sonne cruise So206. Funding was provided by the Deutsche Forschungsgemeinschaft (DFG) through both N.G.'s Heisenberg grant GL 999/3-1 and grant GL 999/4-1. Funding for the core MD01-2415 recovery was provided by the German Science Foundation (DFG) within project Ti240/11-1. We thank Yvon Balut, Agnes Baltzer, and

the Shipboard Scientific Party of RV Marion Dufresne cruise WEPAMA 2001 for their kind support. The recovery of core M77-59 recovery was a contribution of the German Science Foundation (DFG) Collaborative Research Project “Climate–Biogeochemistry interactions in the Tropical Ocean” (SFB 754). The study is a contribution to the Cluster of Excellence 'CLICCS - Climate, Climatic Change, and Society', and a contribution to the Center for Earth System Research and Sustainability (CEN) of Universität Hamburg.

## Chapter 4

### Quantitative reconstruction of deglacial bottom-water nitrate in marginal Pacific seas using the pore density of denitrifying benthic foraminifera

Anjaly Govindankutty Menon, Aaron Bieler, Hanna Firrincieli, Niko Lahajnar, Rachel Alcorn, Catherine V. Davis, Alfredo Martinez-Garcia, Ralf Schiebel, Dirk Nürnberg, Gerhard Schmiedl, Nicolaas Glock

#### Abstract

Quantification of past ocean nitrate ( $\text{NO}_3^-$ ) concentration is crucial for understanding the global nitrogen cycle. Here, we present deglacial bottom-water  $\text{NO}_3^-$  ( $[\text{NO}_3^-]_{\text{BW}}$ ) reconstruction in the oxygen deficient zones (ODZs) of the Sea of Okhotsk, the Gulf of California, the Mexican Margin, and the Gulf of Guayaquil. Using the pore density of denitrifying benthic foraminifera as a  $\text{NO}_3^-$  proxy, differences in  $[\text{NO}_3^-]_{\text{BW}}$  are observed at the study sites spanning the Last Glacial Maximum to the Holocene. Changes related to water-column denitrification, water-mass ventilation, primary productivity, and sea surface temperatures may account for  $\text{NO}_3^-$  differences at the study sites. The  $[\text{NO}_3^-]_{\text{BW}}$  in the Sea of Okhotsk, Gulf of California, and the Gulf of Guayaquil could be influenced by the changes in the intermediate water masses while the  $[\text{NO}_3^-]_{\text{BW}}$  in the Mexican Margin may be influenced by deglacial changes in the Pacific Deep Water. Furthermore, comparison of past and present  $[\text{NO}_3^-]_{\text{BW}}$  shows that the modern Gulf of Guayaquil and the Gulf of California have stronger ODZs with higher denitrification rates. In contrast, the modern Mexican Margin and the Sea of Okhotsk may have higher oxygen stability, indicated by low denitrification.

*Keywords: Bottom-water nitrate, Bolivina spissa, Bolivina subadvena, Oxygen deficient zones*

## 4.1 Introduction

Nitrogen is an abundant element in Earth's atmosphere (Sutton et al., 2019). The primary form of bioavailable nitrogen in the ocean is nitrate ( $\text{NO}_3^-$ ), together with nitrite ( $\text{NO}_2^-$ ), and ammonium ( $\text{NH}_4^+$ ), which are both present in lower concentrations (Casciotti 2016a). Nitrate is a limiting nutrient throughout the tropical and subtropical oceans (Moore et al., 2013). The marine nitrogen cycle is a complex web of microbially mediated processes controlling inventory and distribution of the reactive nitrogen in marine environments (Casciotti, 2016a & b). Biological nitrogen fixation by diazotrophs is the main source of reactive nitrogen in the ocean (Galloway et al., 2004). Denitrification (refers here to all processes that convert reactive forms of nitrogen,  $\text{NO}_3^-$  to molecular nitrogen,  $\text{N}_2$  (McKinney and Conway, 1957)) in the "oxygen-deficient zones" (ODZs) and continental margin sediments (Christensen et al., 1987) is a major sink of bioavailable nitrogen (Codispoti, 1989; Gruber and Galloway, 2008). Both the water column and the pore-water in the sediments are subject to these nitrogen loss processes (Christensen et al., 1987). Denitrification leads to a deficit in  $\text{NO}_3^-$  relative to phosphate (Deutsch et al., 2001). The marine nitrogen budget is regulated by the balance between nitrogen fixation and denitrification (Gruber and Galloway, 2008) and other nitrogen loss process such as anammox (Lam and Kuypers, 2011). The global  $\text{NO}_3^-$  inventory regulates marine productivity, and is sensitive to climate change (Gruber and Galloway, 2008).

Reactions within the nitrogen cycle are often accompanied by isotopic fractionation between the two stable isotopes,  $^{14}\text{N}$  and  $^{15}\text{N}$ , of nitrogen (Falkowski and Godfrey, 2008). The  $^{15}\text{N}/^{14}\text{N}$  in organic matter sinking from the surface ocean is a function of the  $\delta^{15}\text{N}$  of the source  $\text{NO}_3^-$  supplied from subsurface waters and the isotopic fractionation of  $\text{NO}_3^-$  during uptake by phytoplankton (Altabet et al., 1995). During photosynthesis, phytoplankton preferentially takes up lighter  $^{14}\text{NO}_3^-$  over heavier  $^{15}\text{NO}_3^-$  (Wada and Hattori, 1978; Montoya, et al 1990). Thus, the produced organic matter has low  $^{15}\text{N}$  values relative to the upwelled  $\text{NO}_3^-$  (Altabet and Francois, 1994).

Oxygen plays a key role in the marine nitrogen cycle (Keeling et al., 2010) because some microbial processes require oxygen while others are inhibited (Voss et al., 2013). In environments where oxygen concentrations are low,  $\text{NO}_3^-$  is used as an oxidant instead of oxygen to degrade organic matter (McKinney and Conway, 1957). This results in the isotopically light gaseous products  $\text{N}_2$  and  $\text{N}_2\text{O}$  (nitrous oxide) and the isotopically heavier residual  $\text{NO}_3^-$ . Gaseous products of denitrification such as  $\text{N}_2\text{O}$  and  $\text{N}_2$  are largely lost to the atmosphere. As denitrification proceeds,

the residual heavy  $\text{NO}_3^-$  becomes progressively enriched in  $^{15}\text{N}$  due to the large isotopic fractionation characteristic of denitrification. Some of this heavy nitrate is transported to the surface waters, incorporated into the phytoplankton biomass and eventually recorded in the sediments isotopically enriched in the heavy isotope of nitrogen (Cline and Kaplan, 1975). Therefore, denitrification in the water column can be inferred indirectly by using the stable isotope signature of nitrogen in the sedimentary organic matter ( $\delta^{15}\text{N}_{\text{bulk}}$ ) (Brandes and Devol, 2002; Chazen et al., 2009; Robinson et al., 2009; Meckler et al., 2011). Water column denitrification can be intensified by increased export production when organic carbon uses  $\text{NO}_3^-$  as the electron acceptor, especially in ODZs (Wang et al., 2019 and references therein).

The  $\delta^{15}\text{N}_{\text{bulk}}$  signatures can be affected by several processes and sources (Robinson et al., 2012). Post-depositional bacteria driven degradation can increase  $\delta^{15}\text{N}_{\text{bulk}}$  relative to the particulate organic nitrogen sinking from the surface ocean (Wang et al., 2018 and references therein). Terrestrial sources of organic and inorganic nitrogen can also act as contaminants in sedimentary  $^{15}\text{N}$ , particularly along the coasts (Kienast et al., 2005). In a similar way to  $\delta^{15}\text{N}_{\text{bulk}}$ , planktic foraminifera-bound nitrogen isotopes ( $\delta^{15}\text{N}_{\text{FB}}$ ) can effectively record processes within the oceanic nitrogen cycle (Ren et al., 2009; Ren et al., 2012). In addition,  $\delta^{15}\text{N}_{\text{FB}}$  is not affected by terrestrial sources and organic matter degradation (Altabet and Curry, 1989) resulting in discrepancies between  $\delta^{15}\text{N}_{\text{FB}}$  and  $\delta^{15}\text{N}_{\text{bulk}}$  data (Meckler et al., 2011; Ren et al., 2012; Studer et al., 2021). Therefore,  $\delta^{15}\text{N}_{\text{FB}}$  might preserve the original signal more effectively but further studies are needed to understand the processes and factors that lead to differences in  $\delta^{15}\text{N}_{\text{FB}}$  and  $\delta^{15}\text{N}_{\text{bulk}}$  from downcore records.

The nitrogen cycle in the ODZs is different from that in the well oxygenated ocean basins. This is because, on a global scale, ~30-50% of fixed nitrogen loss in the world oceans occurs in ODZs (Gruber, 2008), either through denitrification or anammox (Devol et al., 2006; Lam and Kuypers, 2011; Evans et al., 2023). Large-scale water column denitrification occurs, for example, in the Eastern Tropical North Pacific (ETNP), the Eastern Tropical South Pacific (ETSP), and the Arabian Sea (Christensen et al., 1987; Codipsoti, 1989). Over the past 50 years, ODZs have expanded under global warming particularly in the tropical oceans (Stramma et al., 2008; 2010; Schmidtko et al., 2017). Climate model simulations predicted the expansion of ODZs to continue at least until the year of 2100. However, the evolution of the ODZs on timescales of hundreds to thousands of years remains uncertain (Yamamoto et al., 2015; Takano et al., 2018, Fu et al., 2018;

Frölicher et al., 2020). Recent studies have shown that water column denitrification decreased and ODZs contracted during warmer-than-present periods of the Cenozoic (Auderset et al., 2022; Hess et al., 2023; Moretti et al., 2024).

During the last glacial period,  $\delta^{15}\text{N}_{\text{bulk}}$  measurements suggest that denitrification rates within ODZs increased from the Last Glacial Maximum (LGM) to the Holocene (Robinson et al., 2009; Martinez and Robinson, 2010). In contrast, recent measurement of  $\delta^{15}\text{N}_{\text{FB}}$  suggest that water column denitrification was at its peak during the deglaciation but was comparable during the LGM and the Holocene (Studer et al., 2021). Other studies (Riechelsohn et al., 2024) hypothesized that the decrease in  $\delta^{15}\text{N}$  values over the Holocene is related to a decrease in Southern Ocean nutrient utilization and not due to a decrease in denitrification. Studies (Deutsch et al., 2004; Eugster et al., 2013) have shown that reactive nitrogen inventories were elevated during glacial periods, largely due to reduced denitrification in the water column and sediments. Increased oxygen solubility, global sea level rise, enhanced atmospheric iron (Fe) deposition (Eugster and Gruber, 2012), nutrient input from continental shelves, upwelling productivity, water mass ventilation, thermal contrast between land and sea are some of the factors that can possibly influence reactive nitrogen inventory.

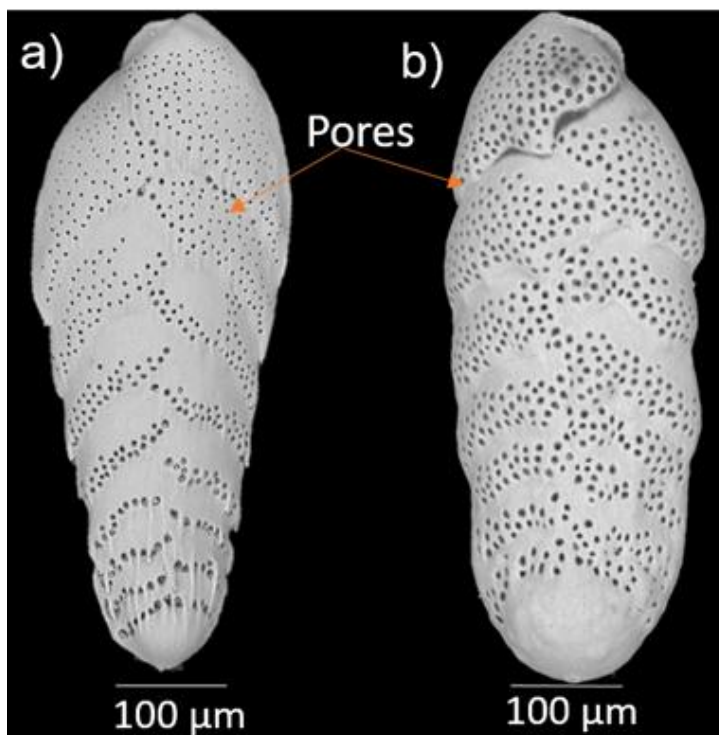


**Figure 4.1.** Scanning electron microscope images of a) *Bolivina spissa* (Mexican Margin) and b) *Bolivina subadvena* (Gulf of California) used for the current study.

In this study, we use the pore density of the denitrifying benthic foraminiferal species *Bolivina spissa* and *Bolivina subadvena* (**Fig. 4.1**) as a  $\text{NO}_3^-$  proxy (Govindankutty Menon et al., 2023) to reconstruct  $[\text{NO}_3^-]_{\text{BW}}$  in intermediate to deep water depths of the Sea of Okhotsk, the Gulf of California, the Gulf of Guayaquil, and of the Mexican Margin (**Fig. 4.2 and 4.3**). Foraminifera are responsible for a large fraction of benthic denitrification in the ODZs (Piña-Ochoa et al., 2010; Glock et al., 2013; Dale et al., 2016). In low-oxygen environments, such as the ODZs off Peru, Costa Rica and the hypoxic Sagami Bay, the benthic foraminifera species *B. spissa* and *B. subadvena* increase their pore density with decreasing ambient  $\text{NO}_3^-$  availability, so their pore density is significantly correlated with  $\text{NO}_3^-$  in their habitat (Glock et al., 2011; Govindankutty Menon et al., 2023). Here, we try to understand whether 1) there are differences in reconstructed  $[\text{NO}_3^-]_{\text{BW}}$  levels between cold and warm periods in all four studied sites, 2) the reconstructed  $[\text{NO}_3^-]_{\text{BW}}$  records are in agreement with the  $\delta^{15}\text{N}_{\text{bulk}}$  data and 3) if there is more/less  $[\text{NO}_3^-]_{\text{BW}}$  in the past than today.

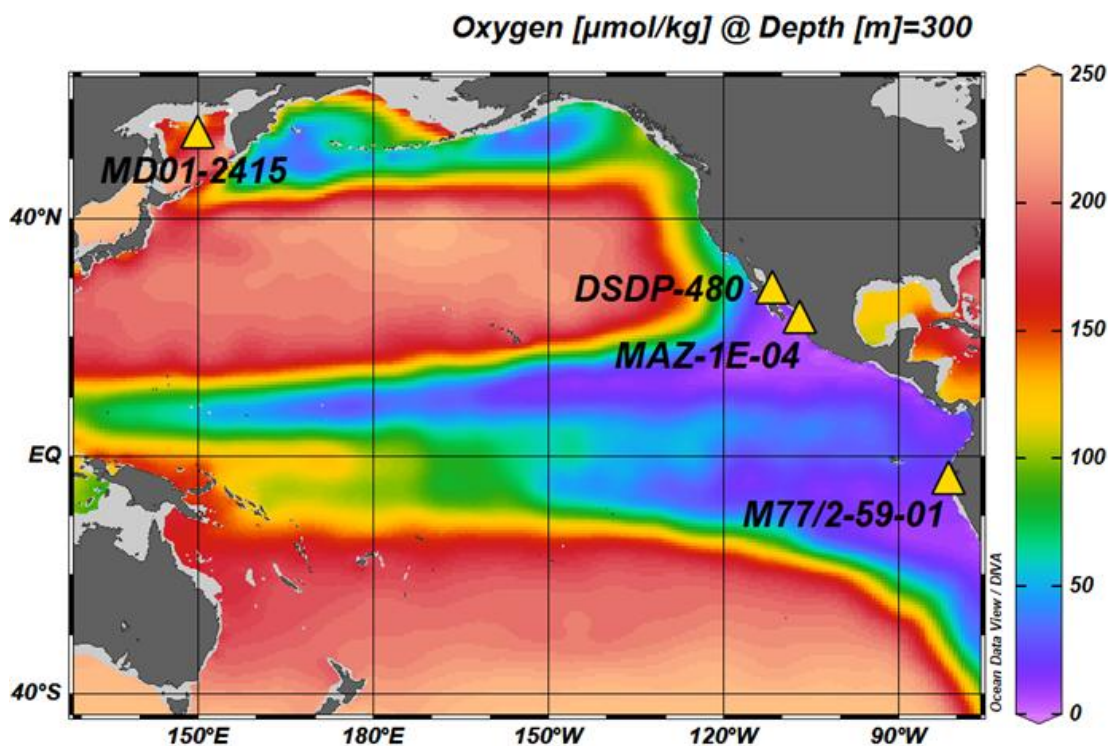


**Figure 4.2.** Location of sediment cores used in the current study and mean annual oxygen concentrations at 300 m depth (Garcia et al., 2019). The core sites of this study are in yellow triangles, and cores are taken from the Sea of Okhotsk (core MD01-2415; water depth: 822 m), the Gulf of California (core DSDP- 480; water depth: 747 m), the Mexican Margin (core MAZ-1E-04; water depth: 1468 m), and the Gulf of Guayaquil (Peru, core M77/2-59-01; water depth: 997 m). Ocean Data View software has been used to create the map (Schlitzer, R., 2023).

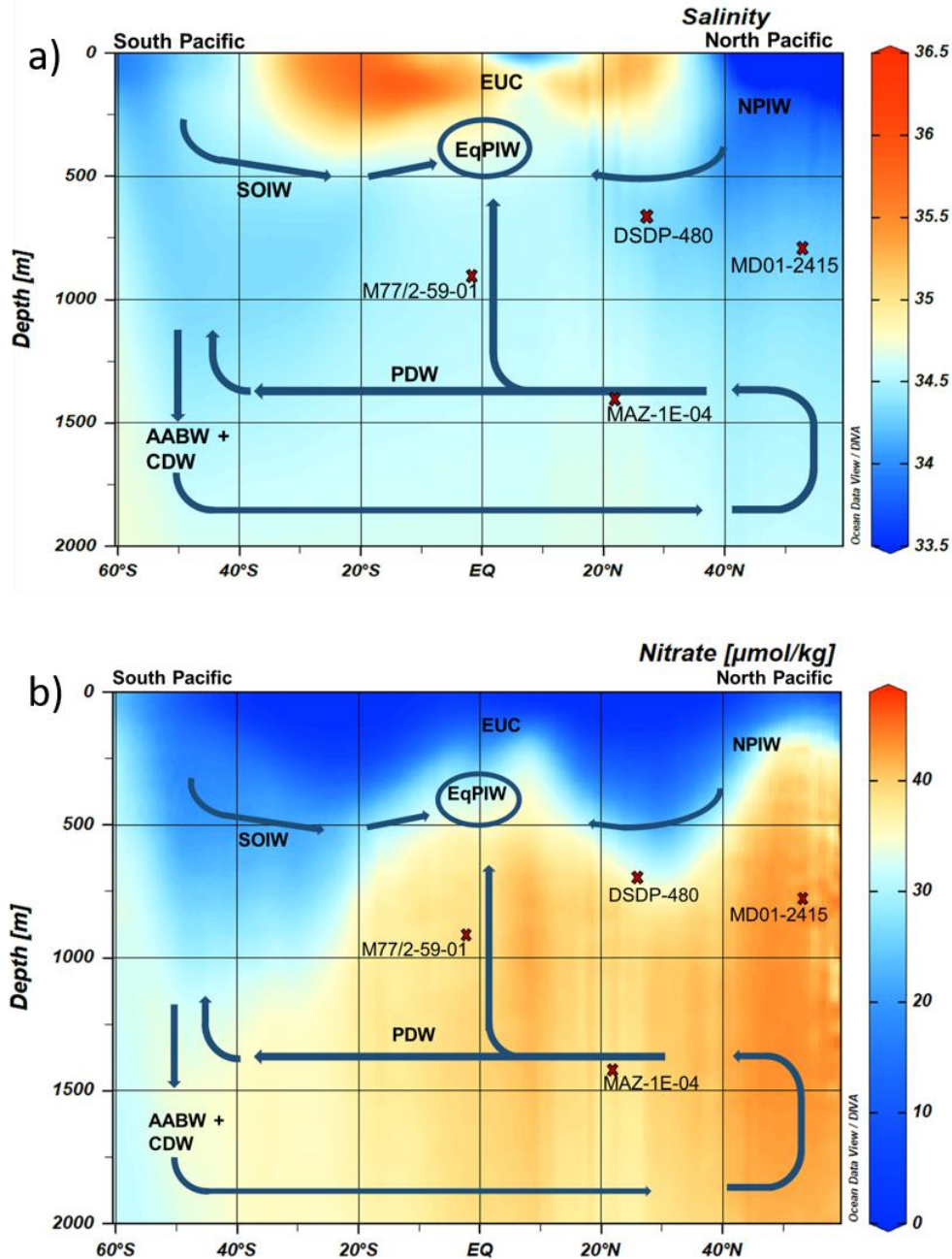


**Figure 4.3.** Modern oceanographic a) salinity and b) nitrate distribution of sediment cores used for  $[\text{NO}_3^-]_{\text{BW}}$  reconstruction. Overview of major deeper ocean currents in the Pacific Ocean. Formation areas of North Pacific Intermediate Water (NPIW) and Southern Ocean Intermediate Water (SOIW) are shown here. The blue arrows show the major subsurface to deep water masses such as Equatorial Pacific Intermediate Water (EqPIW), Equatorial Undercurrent (EUC), NPIW, SOIW, Pacific Deep Water (PDW), Antarctic Bottom Water (AABW), and Circumpolar Deep Water (CDW). The red crosses show the location of the studied cores MD01-2415, DSDP-480, MAZ-1E-04, and M77/2-59-01 projected to the N - S salinity transect. Map was generated using Ocean Data View (Schlitzer, R., 2023) using the data from World Ocean Atlas 2018 (Garcia et al., 2019).

## 4.2 Materials and methods

### 4.2.1 Study area and sampling of sediment cores

We used downcore samples from the ETSP such as the Gulf of Guayaquil (Peru, M77/2-59-01) and the ETNP such as the Mexican Margin (MAZ-1E-04), the Sea of Okhotsk (MD01-2415), and the Gulf of California (Guaymas Basin, DSDP-64-480) over the last ~20,000 years. Gulf of Guayaquil sediment core M77/2-59-01 was collected (03°57.01' S, 81°19.23' W, recovery 13.59 m) from the northern edge of the ODZ at a water depth of 997 m during RV Meteor cruise M77/2 in 2008. The piston core MAZ-1E-04, Mexican Margin (22.9°N, 106.91°W) was collected on board the RV El Puma at a water depth of 1468 m. The CALYPSO giant piston core MD01-2415 (53°57.09' N, 149°57.52' E, recovery 46.23 m) was recovered from the northern slope of the Sea of Okhotsk at 822 m water depth during WEPAMA cruise MD122 of the R/V Marion Dufresne (Holbourn et al., 2002; Nürnberg, D. & Tiedemann, 2004). The Deep-Sea Drilling Project core DSDP- 480 (27°54' N, 111°39' W) from the Gulf of California was retrieved at a water depth of 747 m close to the Guaymas Basin.

### 4.2.2 Sampling of foraminiferal specimens for the quantitative nitrate record

A total number of 1541 fossil specimens of *B. spissa* (number of specimens, n =1268) and *B. subadvena* (n = 273) were used for the  $[\text{NO}_3^-]_{\text{BW}}$  reconstructions at the four site locations. A total of 37 sample depths (n = 669) from the Gulf of Guayaquil (M77/2-059-1); 23 sample depths (n = 455) from the Mexican Margin (MAZ-1E-04); 16 sample depths (n = 273) from the Gulf of California (DSDP-480); 11 sample depths (n= 144) from the Sea of Okhotsk (MD01-2415) were utilized for the collection of benthic foraminifera. Porosity measurements were made on 6 – 20 well-preserved specimens of *B. spissa* and *B. subadvena* in each of the studied locations. The sediment samples were washed and wet-sieved through a 63  $\mu\text{m}$  mesh sieve. The residues were dried in an oven at temperatures at 38-50°C. The samples were sieved into the grain-size fractions of 63-125, >125-250, >250-315, >315-355, >355-400, and >400  $\mu\text{m}$ . Specimens of *B. spissa*, and *B. subadvena* were picked from the 125-250  $\mu\text{m}$  fraction.

### 4.2.3 Automated image analysis

All specimens of *B. spissa* and *B. subadvena* were imaged (**Fig. 4.1**) using a Scanning Electron Microscope (version: Hitachi Tabletop SEM TM4000 series) at the University of Hamburg with an accelerating voltage of 15 kV using back-scattered electron (BSE) detector. The specimens were not sputter coated due to future geochemical analyses. For porosity measurements, the total area on the first (oldest) ten chambers (equivalent to an area of 50,000 to 70,000  $\mu\text{m}^2$ ) was measured using the ZEN lite software (version: ZEN 3.4 blue edition). The pore parameters such as the pore density (PD), mean pore size, and the porosity were determined with the automated image analyzing software Amira (version: Amira<sup>TM</sup> 3D pro) using a previously trained deep-learning algorithm. The detailed methodology of the porosity measurements has been developed and is described in Govindankutty Menon et al. (2023). The deep learning algorithm that has been used for this study is included in the Amira software package. The deep learning algorithm was initially trained with manually segmented pores on 52 images of *B. spissa* and 60 images of *B. subadvena*. Only those specimens that had a total area equivalent to at least 50,000 to 70,000  $\mu\text{m}^2$  were used for the automated analysis. Smaller specimens were discarded.

Following the image analysis, pore density data of 1541 fossil specimens of benthic foraminifera from the four ODZs was used for the quantitative reconstruction of  $[\text{NO}_3^-]_{\text{BW}}$  (**Fig. 4.4**). This provided a statistically robust dataset. We distinguished five different time intervals, including the Last Glacial Maximum (LGM; 22–17 kyr BP), Heinrich Stadial 1 (H1; 17–15 kyr BP), Bølling-Allerød Event (BA; 14, 690- 12, 900 kyr BP), Younger Dryas (YD; 12,900–11,700 kyr BP), Early Holocene (EH; 11.7–8.2 kyr BP) and Middle to Late Holocene (MLH; 8–0 kyr BP) to describe the  $[\text{NO}_3^-]_{\text{BW}}$  in the East Pacific and the Sea of Okhotsk (**Fig. 4.4**). The  $[\text{NO}_3^-]_{\text{BW}}$  from all cores were calculated using the calibration equation, **Eq. 4.1**.

$$[\text{NO}_3^-]_{\text{BW}} = -3896 (\pm 350) \text{PD} + 61(\pm 1) \text{-----} \text{ (Eq. 4.1)}$$

where PD is the pore density of benthic foraminifera (Govindankutty Menon et al., 2023).

The standard error of the mean (SE) for one sample was calculated using the equation, **Eq. 4.2**.

$$\text{SE}_{[\text{NO}_3^-]_{\text{BW}}} = \frac{\text{SD}_{[\text{NO}_3^-]_{\text{BW}}}}{\sqrt{n}} \text{-----} \text{ (Eq. 4.2)}$$

where n is the number of specimens analyzed in each sample and SD is 1 standard deviation of mean reconstructed  $[\text{NO}_3^-]_{\text{BW}}$ .

$$SD_{[NO_3^-]_{BW}} = \sqrt{(350 \times PD)^2 + (-3896 \times SD_{PD})^2 + (1)^2} \text{ ----- (Eq. 4.3)}$$

A complete error propagation has been done for the calculation of the errors of the reconstructed  $[NO_3^-]_{BW}$  including both the uncertainty of the mean PD within the samples and the uncertainties of the calibration function (Eq. 4.3). The calculated SE and SD of each sample are shown in the Appendix B as Supplementary Table ST1.

#### 4.2.4 Optimization of age models

**a) Gulf of Guayaquil:** The already published age model (Mollier-Vogel et al., 2019) of core M77/2-59-01 is based on ten radiocarbon ( $^{14}C$ ) ages measured using planktic foraminifera species *Neogloboquadrina dutertrei* at the Leibniz Laboratory at Kiel University (Mollier-Vogel et al., 2019). For the current study, the age-depth model was updated (Appendix B; Supplementary Figure SF1) using Marine20 (Heaton et al., 2020) by Bchron package (Haslett & Parnell, 2008) in R studio (RStudio Team, 2023) with a DeltaR of  $200 \pm 50$  years (Mollier-Vogel et al., 2013).

**b) Sea of Okhotsk:** We used the age-tie points and  $^{14}C$ -ages published by Bubenshchikova et al. (2015); Table 3 (based on Nürnberg and Tiedemann, 2004) for the age model of core MD01-2415. The accelerator mass spectrometry (AMS) radiocarbon dates were incorporated in between the age-tie points to minimize the age uncertainty. For the current study, the age-depth model was updated (Appendix B; Supplementary Figure SF2) using Marine20 by Bchron package in R studio with a local DeltaR of 546 years from the Davydov Cape (Kuzmin et al., 2007).

**c) Mexican Margin:** The age model for this core MAZ-1E-04 has been entirely built in the framework of the PhD work. Planktic foraminifera *Globigerinoides ruber*, *Globigerinoides bulloides*, *Trilobatus sacculifer* were used for the  $^{14}C$  dating. Approximately 200 foraminiferal tests of these species were selected from the 125-250  $\mu m$  fraction. The radiocarbon measurements of planktic foraminifera were carried out at the Alfred-Wegener-Institute (AWI) in Bremerhaven using the MICADAS system, and at the National Ocean Sciences Accelerator Mass Spectrometry Facility (USA). We applied a manual continuous Marine Reservoir Age (MRA) correction using the MRAs from the closest available location to the core MAZ-1E-04 from the previously published literature (Butzin et al., 2020). Then the corresponding MRAs were subtracted from the raw  $^{14}C$  ages of planktic foraminifers to achieve the atmospheric  $^{14}C$  age. Radiocarbon age calibration has been done using Intcal20 (Reimer et al., 2020) in the Bchron package in R studio.

In the radiocarbon data for this core, age reversals were observed for the top-part above 52.5 cm depth onwards. These age reversal points are shown in the age model (Appendix B; Supplementary Figure SF3).

**d) Gulf of California:** We used raw  $^{14}\text{C}$  ages of planktic foraminifera from Keigwin, & Jones (1990) for updating the age-depth model for DSDP Site 480. Radiocarbon age calibration were done using Marine20 with a local DeltaR of 301 years from the Guaymas Basin (Goodfriend & Flessa, 1997). The Bchron package was used for determining the age-depth model and calibrating the age. The final age model of DSDP-480 is shown in Appendix B as Supplementary Figure SF4. All the data used for developing and updating the age models of all cores are shown in Appendix B as Supplementary Tables ST2, 3, 4, and 5).

#### 4.2.5 Sedimentary nitrogen isotope ( $\delta^{15}\text{N}_{\text{bulk}}$ ) measurements

An increase (or decrease) in the nutrient availability in relation to nutrient demand results in an increase (or decrease) in  $\delta^{15}\text{N}$  values (Wada and Hattori, 1978; Montoya, 1990). For the Gulf of Guayaquil core M77/2-59-01, sedimentary nitrogen isotope ( $\delta^{15}\text{N}_{\text{bulk}}$ ) data published by Mollier-Vogel et al. (2019) was used. Their measurements were done on ~5–50 mg of homogenized and freeze-dried bulk sediments using a Carlo-Erba CN analyzer 2500 interfaced directly to a Micromass-Isoprime mass spectrometer at Bordeaux University. Results were expressed in standard  $\delta$ -notation (equation, Eq. 4.4) relative to atmospheric dinitrogen gas ( $\text{N}_2$ ). The precision determined using laboratory standards calibrated to certified international reference standards was less than 0.3‰.

$$\delta^{15}\text{N} (\text{‰}) = \left[ \left( \frac{{}^{15}\text{N}:{}^{14}\text{N}_{\text{sample}}}{{}^{15}\text{N}:{}^{14}\text{N}_{\text{air}}} \right) - 1 \right] \times 1,000 \text{ ----- (Eq. 4.4)}$$

Prior to the  $\delta^{15}\text{N}$  measurements, the Total Nitrogen (TN%) content of 20 sediment samples from the Sea of Okhotsk and 54 samples from the Gulf of California were measured at the Institute for Geology, University of Hamburg using a flash combustion method with a Eurovector EA-3000 analyzer. The  $\delta^{15}\text{N}_{\text{bulk}}$  measurements for both the Sea of Okhotsk and Gulf of California were done at Max Planck Institute for Chemistry in Mainz using a DELTA V ADVANTAGE Isotope Ratio Mass Spectrometer (IRMS) equipped with a FLASH 2000 Organic Elemental Analyzer. The results were expressed in standard  $\delta$ -notation (Eq. 4.4). The precision determined on certified international reference standards USGS 40, USGS 41a, USGS 65, L-Phenylalanine, L-Glutamic

acid was less than 0.3‰. The standard deviation ( $\pm$  SD) of all the individual runs based on the reference standards weighed in to the same nitrogen amount was  $\leq 0.28$ ‰. The details of  $\delta^{15}\text{N}$  measurements are shown in Appendix B as Supplementary Table ST1.

#### 4.2.6 Nitrate offset to present conditions

The reconstructed  $[\text{NO}_3^-]_{\text{BW}}$  from each location is subtracted from the modern  $[\text{NO}_3^-]_{\text{BW}}$  present at the respective locations from similar water depths the cores were retrieved from. This provided the  $[\text{NO}_3^-]_{\text{BW}}$  offset ( $\Delta[\text{NO}_3^-]$  ( $\mu\text{M}$ )) which is the difference between the modern  $[\text{NO}_3^-]_{\text{BW}}$  and the past reconstructed  $[\text{NO}_3^-]_{\text{BW}}$ . The modern  $[\text{NO}_3^-]_{\text{BW}}$  for each location was taken from World Ocean Atlas 2018 (Garcia et al., 2019). The details are given in **Table 4.1**.

**Table 4.1.** Site location information of modern  $[\text{NO}_3^-]_{\text{BW}}$  taken for the nitrate offset from World Ocean Atlas 2018.

Locations	Latitude	Longitude	Water depth (m)	Station ID	$[\text{NO}_3^-]$ ( $\mu\text{mol/kg}$ )
Gulf of Guayaquil, (M77/2-59-01)	3.5° S	81.5°W	1050	21457 (B)	42.5
Mexican Margin, (MAZ-1E-04)	22.5°N	106.5°W	1100	28128	43.8
Sea of Okhotsk, (MDO1-2415)	53.5°N	149.5°E	850	33729 (B)	43.4
Gulf of California, (DSDP, 480)	27.5°N	111.5°W	750	29197 (B)	35.3

The statistical analyses presented in this paper were carried out using the RStudio. The T-test was used to test the significant difference between datasets of unequal sample sizes after carrying out an initial variance test whenever necessary. The confidence interval of 95% ( $p < 0.05$ ) was set for the significance test.

### 4.3 Results

We reconstructed deglacial  $[\text{NO}_3^-]_{\text{BW}}$  using downcore sediment samples from the Sea of Okhotsk (MD01-2415), the Gulf of California (DSDP- 480), Mexican Margin (MAZ-1E-04), and the Gulf of Guayaquil (M77/2-59-01). The reconstructed  $[\text{NO}_3^-]_{\text{BW}}$  were compared to high resolution  $\delta^{15}\text{N}_{\text{bulk}}$  records of all cores (**Fig. 4.4**), except for the Mexican Margin. Since no  $\delta^{15}\text{N}_{\text{bulk}}$  data was available for the Mexican Margin, the reconstructed  $[\text{NO}_3^-]_{\text{BW}}$  was compared with the  $\delta^{15}\text{N}_{\text{FB}}$  from published planktic foraminiferal  $\delta^{15}\text{N}$  data (Studer et al., 2021) from the close by Eastern Tropical Pacific. All data series presented cover the time-period starting from the LGM, except for the core from the Sea of Okhotsk, which covers the late deglacial to the Holocene.

#### 4.3.1 Sea of Okhotsk (MD01-2415)

The Sea of Okhotsk core covered the Younger Dryas, YD (12.8 ka BP) until the Middle to Late Holocene, MLH (4.9 ka BP). The pore density of *B. spissa* (n =144) were from  $0.0073 \text{ P}/\mu\text{m}^2$  to  $0.0043 \text{ P}/\mu\text{m}^2$  with a mean ( $\pm$  SD) of  $0.0054 \text{ P}/\mu\text{m}^2$  ( $\pm 0.00079 \text{ P}/\mu\text{m}^2$ ). Reconstructed  $[\text{NO}_3^-]_{\text{BW}}$  values were from  $32.5 \mu\text{mol}/\text{kg}$  to  $44.08 \mu\text{mol}/\text{kg}$  with a mean ( $\pm$  SD) of  $40 \mu\text{mol}/\text{kg}$  ( $\pm 3.1 \mu\text{mol}/\text{kg}$ ). Highest  $[\text{NO}_3^-]_{\text{BW}}$  (lowest pore density, Appendix B; Supplementary Table ST1) occurred during the MLH (**Fig. 4.4a**). A gradual increase in  $[\text{NO}_3^-]_{\text{BW}}$  values observed from the YD to the MLH. At the beginning of the YD at 12.8 ka BP, observed  $[\text{NO}_3^-]_{\text{BW}}$  were relatively high and then decreased to a minimum value of  $32.5 \mu\text{mol}/\text{kg}$  at 12.4 ka BP. Since then,  $[\text{NO}_3^-]_{\text{BW}}$  steadily increased until the MLH ( $44.08 \mu\text{mol}/\text{kg}$ ) (**Fig. 4.4a**). The  $[\text{NO}_3^-]_{\text{BW}}$  during the MLH (mean =  $41.1 \mu\text{mol}/\text{kg}$ ) were significantly (Two sample t-test,  $p = 0.023$ ) higher than during the YD (mean =  $36.7 \mu\text{mol}/\text{kg}$ ). The sedimentary  $\delta^{15}\text{N}_{\text{bulk}}$  record covered the interval from the Late Heinrich Stadial 1, H1 (15.44 ka BP) to the Middle Holocene (6.05 ka BP). The  $\delta^{15}\text{N}_{\text{bulk}}$  values were relatively high ranging from 7.1‰ to 9.4‰ with an average of 8.3‰. The  $\delta^{15}\text{N}_{\text{bulk}}$  values increased steadily from the Late H1 (15.44 ka BP) to the Early Holocene, EH (10.02 ka BP) with higher values centered between the Late YD (11.89 ka BP) and the beginning of the EH. Since then, the  $\delta^{15}\text{N}_{\text{bulk}}$  values decreased until the MLH.

### 4.3.2 Gulf of California (DSDP-480)

The analyzed sections of DSDP site 480 covered the LGM (22 ka BP) until the EH (10.84 ka BP). The pore density of *B. subadvena* ( $n = 273$ ) from the Gulf of California were from  $0.003 \text{ P}/\mu\text{m}^2$  to  $0.0050 \text{ P}/\mu\text{m}^2$  with an average of  $0.0040 \text{ P}/\mu\text{m}^2$  ( $\pm 0.00050 \text{ P}/\mu\text{m}^2$ ). The reconstructed  $[\text{NO}_3^-]_{\text{BW}}$  were from  $41.4 \mu\text{mol}/\text{kg}$  to  $49.1 \mu\text{mol}/\text{kg}$  with an average of  $45.0 \mu\text{mol}/\text{kg}$  ( $\pm 1.98 \mu\text{mol}/\text{kg}$ ). The highest  $[\text{NO}_3^-]_{\text{BW}}$  (lowest pore density, Appendix B; Supplementary Table ST1) of  $49.1 \mu\text{mol}/\text{kg}$  occurred during the LGM (18.24 ka BP). The data points from the EH (11.57 - 10.84 ka BP) were the only Holocene data from this core providing the lowest  $[\text{NO}_3^-]_{\text{BW}}$  estimate of  $42 \mu\text{mol}/\text{kg}$  during the Early Holocene (10.84 ka BP) (**Fig. 4.4b**). There were variations in the  $[\text{NO}_3^-]_{\text{BW}}$  throughout the glacial period. A distinct difference in  $[\text{NO}_3^-]_{\text{BW}}$  between the glacial cold period (mean =  $46 \mu\text{mol}/\text{kg}$ ) and the interglacial warm period ( $42.7 \mu\text{mol}/\text{kg}$ ) was observed with  $[\text{NO}_3^-]_{\text{BW}}$  found to be substantially higher during the glacial period (T-test,  $p = 0.0067$ ) (**Fig. 4.4b**). Accordingly, the  $[\text{NO}_3^-]_{\text{BW}}$  followed a decreasing pattern from the glacial period to the EH. The  $\delta^{15}\text{N}_{\text{bulk}}$  values were relatively high during the last 22 ka BP. The  $\delta^{15}\text{N}_{\text{bulk}}$  values varied between  $6.4\text{‰}$  and  $13\text{‰}$  with an average of  $11\text{‰}$  which is higher than the typical open-ocean  $\delta^{15}\text{N}_{\text{NO}_3^-}$  values (Sigman et al., 1997; Liu and Kaplan, 1989) (**Fig. 4.4b**). Our  $\delta^{15}\text{N}_{\text{bulk}}$  values from the Guaymas Basin were similar to the  $\delta^{15}\text{N}_{\text{bulk}}$  values (average  $9.6\text{‰}$ ) of of Pride (1997) and Altabet et al. (1999). During the last glacial period, the sedimentary  $\delta^{15}\text{N}_{\text{bulk}}$  values were low ranging from  $8.5\text{‰}$  to  $9.04\text{‰}$ . At the onset of the deglaciation, the  $\delta^{15}\text{N}_{\text{bulk}}$  values increased by more than  $2\text{‰}$  with large scale changes reaching a maximum of  $12.9\text{‰}$  during the YD. Afterwards, we observed a gradual decline in  $\delta^{15}\text{N}_{\text{bulk}}$  values throughout the MLH (mean  $10.7\text{‰}$ ) and this pattern continued to the present (**Fig. 4.4b**).

### 4.3.3 Mexican Margin (MAZ-1E-04)

This core covered the LGM (20.5 ka BP) until the EH (10.47 ka BP). The pore density of *B. spissa* ( $n = 455$ ) from the Mexican Margin ranged from  $0.0044 \text{ P}/\mu\text{m}^2$  to  $0.0059 \text{ P}/\mu\text{m}^2$  with an average of  $0.0054 \text{ P}/\mu\text{m}^2$  ( $\pm 0.00045 \text{ P}/\mu\text{m}^2$ ). The  $[\text{NO}_3^-]_{\text{BW}}$  values ranged from  $37.7 \mu\text{mol}/\text{kg}$  to  $43.5 \mu\text{mol}/\text{kg}$  with an average of  $39.7 \mu\text{mol}/\text{kg}$  ( $\pm 1.76 \mu\text{mol}/\text{kg}$ ). The highest  $[\text{NO}_3^-]_{\text{BW}}$  (lowest pore density, Appendix B; Supplementary Table ST1) was observed during the YD. From the beginning to the end of the LGM,  $[\text{NO}_3^-]_{\text{BW}}$  followed a decreasing trend (**Fig. 4.4c**). The  $[\text{NO}_3^-]_{\text{BW}}$  levels continued to steadily decrease until H1 and consistently stayed low throughout H1. Afterwards,

there was a strong change in  $[\text{NO}_3^-]_{\text{BW}}$  in our data from the end of H1 to the end of YD (**Fig. 4.4c**). We observed a peak in  $[\text{NO}_3^-]_{\text{BW}}$  from the beginning of Bølling-Allerød, BA (14.29 ka BP) and it continued throughout the YD (**Fig. 4.4c**). Afterwards,  $[\text{NO}_3^-]_{\text{BW}}$  declined during the EH.

#### 4.3.4 Gulf of Guayaquil (M77/2-59-01)

This core covered the LGM (18 ka BP) until the MLH (0.18 ka BP). The pore density of *B. spissa* from Gulf of Guayaquil ranged from 0.0037  $\text{P}/\mu\text{m}^2$  to 0.0052  $\text{P}/\mu\text{m}^2$  with a mean of 0.0042  $\text{P}/\mu\text{m}^2$  ( $\pm 0.00036 \text{ P}/\mu\text{m}^2$ ). Reconstructed  $[\text{NO}_3^-]_{\text{BW}}$  values ranged from 40.5  $\mu\text{mol}/\text{kg}$  to 46.5  $\mu\text{mol}/\text{kg}$  with an average of 44.4  $\mu\text{mol}/\text{kg}$  ( $\pm 1.41 \mu\text{mol}/\text{kg}$ ). The highest  $[\text{NO}_3^-]_{\text{BW}}$  (lowest pore density, Appendix B; Supplementary Table ST1) occurred during the LGM (**Fig. 4.4d**). The reconstructed  $[\text{NO}_3^-]_{\text{BW}}$  levels (**Fig. 4.4d**) during the LGM (mean = 45.9  $\mu\text{mol}/\text{kg}$ ) were slightly higher than during the MLH (mean = 44.9  $\mu\text{mol}/\text{kg}$ ) (T-test,  $p = 0.046$ ). The  $\delta^{15}\text{N}_{\text{bulk}}$  values were relatively low ranging between 4‰ and 6‰ (**Fig. 4.4d**). During the LGM, the  $\delta^{15}\text{N}_{\text{bulk}}$  values were low, varying between 4.4‰ and 4.6‰, close to the typical mean range of dissolved nitrate in the ocean (Sigman et al., 1997). Subsequently, the  $\delta^{15}\text{N}_{\text{bulk}}$  values increased from 16.7 ka BP (4.9‰), where we observed a decline in  $[\text{NO}_3^-]_{\text{BW}}$  to 8.9 ka BP (5.6‰). The highest  $\delta^{15}\text{N}_{\text{bulk}}$  values centered at ~14 ka BP (5.9‰). From 8.9 ka BP onwards, a long-term decrease in  $\delta^{15}\text{N}_{\text{bulk}}$  ( $< 4.4\text{‰}$ ) was observed until the Latest Holocene, consistent with higher  $[\text{NO}_3^-]_{\text{BW}}$  levels during the Holocene (**Fig. 4.4d**). Despite higher  $[\text{NO}_3^-]_{\text{BW}}$  levels, the reconstructions don't show any strong trends during the Holocene.

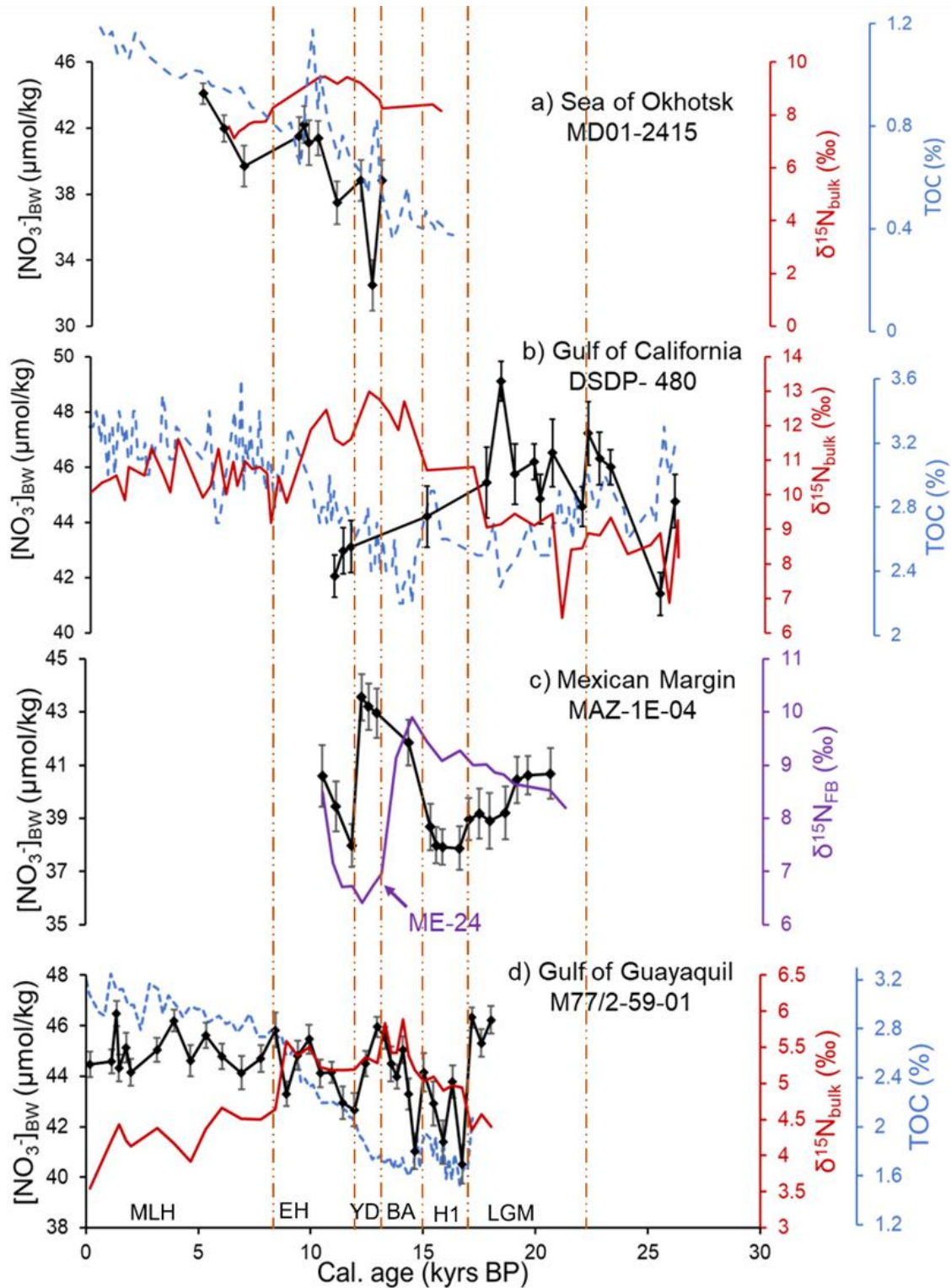


**Figure 4.4.** Quantitative  $[NO_3^-]_{BW}$  reconstruction using the pore density of 1541 fossil specimens of *B. spissa*, *B. subadvena* in comparison to the sedimentary nitrogen isotope ( $\delta^{15}N_{\text{bulk}}$ ) records of sediment cores from a) the Sea of Okhotsk (MD01-2415), b) the Gulf of California (DSDP-480), c) the Mexican Margin (MAZ-1E-04), and foraminifera-bound (Studer et al., 2021)  $\delta^{15}N_{\text{FB}}$  data

from core ME-24 (violet line) and d) the Gulf of Guayaquil (M77/2-59-01). The  $\delta^{15}\text{N}_{\text{bulk}}$  data was not available for the Mexican Margin. The error bars represent 1 SE including a complete error propagation (using equation Eq 4.2 and 4.3). Total Organic Carbon, TOC (%) data taken from published literature (Bubenshchikova et al., 2015; Leclaire & Kerry, 1982; Mollier-Vogel et al., 2019) is shown in blue dashed lines for the Sea of Okhotsk, the Gulf of California and the Gulf of Guayaquil cores respectively. The TOC data was not available for the Mexican Margin core. Time intervals such as Middle to Late Holocene (MLH), Early Holocene (EH), Younger Dryas (YD), Bølling-Allerød (BA), Heinrich Stadial 1 (H1), and Last Glacial Maximum (LGM) are shown in the figure.

#### 4.3.5 Comparison of nitrate offset ( $\Delta[\text{NO}_3^-]$ ) between the cores

To quantify the change in  $[\text{NO}_3^-]_{\text{BW}}$  between past and present conditions, we calculated the difference ( $\Delta[\text{NO}_3^-]$  ( $\mu\text{M}$ )) between the modern  $[\text{NO}_3^-]_{\text{BW}}$  (Garcia et al., 2019) and the  $[\text{NO}_3^-]_{\text{BW}}$  for each core. A  $\Delta[\text{NO}_3^-]$  value close to 0 implies that there is not offset to the modern value. A positive (or negative)  $\Delta[\text{NO}_3^-]$  implies higher (or lower) values than today. The Gulf of California had the highest  $\Delta[\text{NO}_3^-]$  values relative to other cores (see Fig. 4.5). In general, the  $\Delta[\text{NO}_3^-]$  values in Gulf of California and mostly in the Gulf of Guayaquil were positive (Fig. 4.5) which indicated that  $\text{NO}_3^-$  concentrations in the past were higher than today. The Mexican Margin and the Sea of Okhotsk had negative  $\Delta[\text{NO}_3^-]$ , implying that  $\text{NO}_3^-$  concentrations in the past were lower than today (Fig. 4.5)

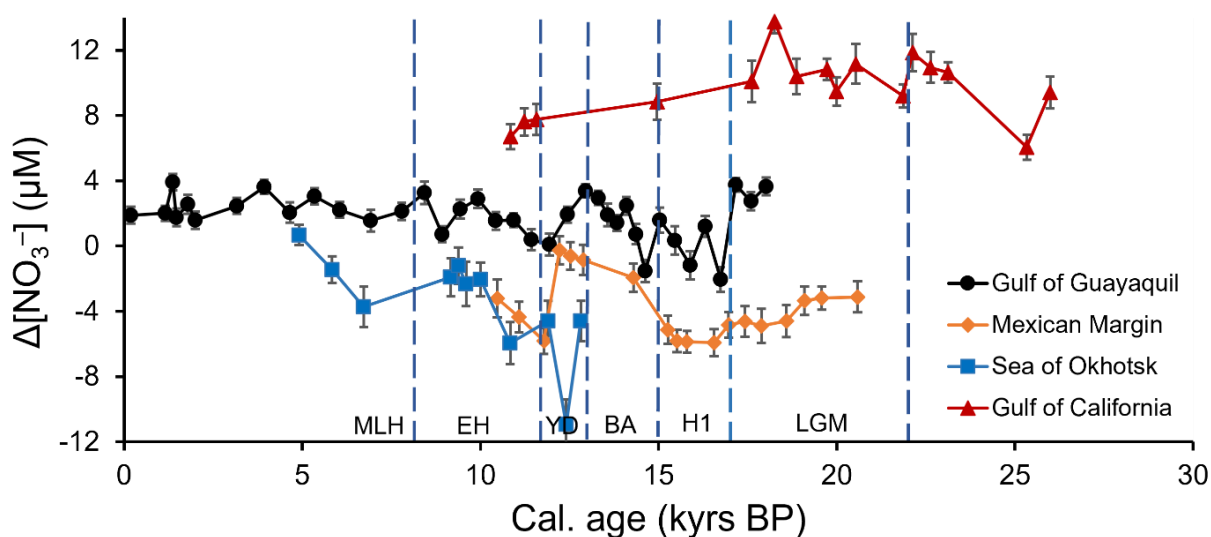


**Figure 4.5.** The relative changes of  $[\text{NO}_3^-]_{\text{BW}}$  calculated from the pore density of benthic foraminifera *B. spissa* and *B. subadvena* from all studied cores compared to modern  $\text{NO}_3^-$  at each location. This provides the nitrate offset ( $\Delta[\text{NO}_3^-]$  ( $\mu\text{M}$ )). The modern nitrate at the different locations has been taken from the World Ocean Atlas, 2018 (Garcia et al., 2019). Error bars represent 1 SE.

## 4.4 Discussion

Reconstruction of past  $\text{NO}_3^-$  is crucial for understanding the complex nutrient cycling in the ocean. Furthermore, comparison between past and modern  $\text{NO}_3^-$  will provide a foresight on the ecological and environmental impacts of climate change. Although,  $\delta^{15}\text{N}_{\text{bulk}}$  is widely applied as a proxy for water column denitrification (Thunell et al., 2004; Wang et al., 2019), diagenetic process, atmospheric deposition, terrestrial inputs and increasing anthropogenic atmospheric deposition can bias the  $\delta^{15}\text{N}_{\text{bulk}}$  signature (Robinson et al., 2012; Wang et al., 2019 and references therein). In addition, remotely advected water masses with different  $\delta^{15}\text{N}$  values can supply additional nitrogen to the photic zone in upwelling regions (for e.g., Southern Californian margin; Liu and Kaplan, 1989), and thus influence the  $\delta^{15}\text{N}$  signatures in sediments. This should be taken into account when interpreting the data. Here, we discuss the factors with a possible influence on the  $\text{NO}_3^-$  inventory in the study sites.

### 4.4.1 Sea of Okhotsk

Our data show that  $[\text{NO}_3^-]_{\text{BW}}$  levels gradually increased through time and reached modern concentrations during the Middle-Holocene (**Fig. 4.4a**). There was a distinct offset of  $[\text{NO}_3^-]_{\text{BW}}$  between the cold YD and warm Holocene time periods. Most of the nutrients in the northwestern Pacific including the Sea of Okhotsk are supplied by the upwelling of the North Pacific Deep Water (NPDW) (Gorbarenko et al., 2014). The weakened Kuroshio current (Ujiié and Ujiié, 1999) and increased sea ice extent (Ternois et al., 2001) weakened the upwelling of the NPDW during the LGM. Subsequent studies (Gray et al., 2020; Rae et al., 2020) have shown that the expansion of the North Pacific Gyre also resulted in reduced upwelling of NPDW during the LGM.

During the LGM, the subpolar North Pacific was better ventilated at intermediate depths (Keigwin, 1998) and export productivity was reduced (Ternois et al., 2001; Narita et al., 2002; Seki et al., 2004). This is consistent with a relatively slow meridional overturning circulation (Rafter et al., 2022), with enhanced formation of intermediate waters and advection of nutrient-depleted subtropical waters to high latitudes (Rae et al., 2020). Furthermore, the North Pacific subpolar gyre extended  $\sim 3^\circ$  further south during the LGM (Gray et al., 2020), which shifted the westerly winds southward during the LGM. This may have resulted in less upwelling of the NPDW during the LGM.

The prolonged ice cover with low biological productivity (Ternois et al., 2001; Narita et al., 2002; Seki et al., 2004; Rae et al., 2020) and well-oxygenated water masses (Keigwin, 1998) might have prevented the formation of an ODZ in the Sea of Okhotsk (Bubenshikova et al., 2015). This is possibly the reason why benthic foraminifera such as *B. spissa* which are adapted to living in dysoxic conditions were absent in our records during the LGM.

Deglacial low  $[\text{NO}_3^-]_{\text{BW}}$  levels which corresponds to higher  $\delta^{15}\text{N}_{\text{bulk}}$  values (Fig. 4.4a) could be due to the enhanced primary productivity. Increased nutrient supply from the Asian continental shelves and sea-ice retreat (Ternois et al., 2001) strengthened primary productivity. Indeed, the total organic carbon (TOC) was relatively higher during this time period (Bubenshikova et al., 2015) in our core (Fig. 4.4a). The increased oxygen demand and the weakened ventilation of intermediate waters in the subarctic Pacific (Lembke-Jene et al., 2018) gradually intensified the ODZ. These low oxygenated conditions conceivably strengthened the denitrification, resulting in low deglacial  $[\text{NO}_3^-]_{\text{BW}}$  levels. However, during the MLH the reorganization in atmospheric circulation favored enhanced formation of oxygenated North Pacific Intermediate Water (NPIW) (Wang et al., 2020). That is, the mid-depth ventilation in the North Pacific was closely associated with the atmospheric circulation in the Holocene (Wang et al., 2020). This weakened the ODZ (Ohkushi et al., 2013; Bubenshikova et al., 2015; Wang et al., 2020). These rising oxygen concentrations probably reduced denitrification (low  $\delta^{15}\text{N}_{\text{bulk}}$ ) in the Sea of Okhotsk, resulting in higher  $[\text{NO}_3^-]_{\text{BW}}$  comparable to today's conditions (Fig. 4.4 & 4.5). Although the  $\delta^{15}\text{N}_{\text{bulk}}$  values was high during the 13 ka till 10 ka BP, which indicates high water-column denitrification, the  $[\text{NO}_3^-]_{\text{BW}}$  already started to increase. This could be related to the sea level rise during that time (Waelbroeck et al., 2008), which increased the vertical distance of the sampling site from the center of denitrification.

#### 4.4.2 Gulf of California

The lower sedimentary  $\delta^{15}\text{N}_{\text{bulk}}$  values that correspond to the higher reconstructed  $[\text{NO}_3^-]_{\text{BW}}$  during the glacial period (Fig. 4.4b) suggest lower productivity (Ganeshram and Pedersen, 1998; Hendy et al., 2004; Chang et al., 2008, 2015, Cartapanis et al., 2011), and reduced denitrification and/or less import of enriched nitrate from the ETNP (Pride et al., 1999; Hendy et al., 2004). The Gulf of California ODZ is subjected to the intermediate and deep-water properties similar to that of the open Pacific Ocean. Thus, the ODZ intensity at Guaymas Basin is largely dependent on the oxygen

content and ventilation of inflowing NPIW from the Sea of Okhotsk (Pride et al., 1999) and the demand for oxygen at depth. During the glacial period, the dissolved oxygen concentrations were higher due to the better ventilated NPIW at the intermediate depths of the North East Pacific (Keigwin and Jones, 1990; Ganeshram et al., 1995; Keigwin 1998; Duplessy et al., 1988; Herguera et al., 2010; Cartapanis et al., 2011). Modelling studies show that the Laurentide and Cordilleran ice sheets increased in size (Benson et al., 2003), massively lowering the temperature of North America (Romanova et al., 2006) during the glacial period. The cold sinking air over the ice sheets established a semi-permanent high-pressure cell (Kutzbach & Wright Jr, 1985; Romanova et al., 2006) causing a substantially weaker North Pacific High-pressure cell (Ganeshram and Pedersen, 1998) or the southward displacement of Inter Tropical Convergence Zone (Cheshire and Thurow, 2013). This resulted in a weak California Current along the coast and reduced upwelling-favorable winds (COHMAP et al., 1988; Cartapanis et al., 2011) along the North American coastline. Thus, resulting in reduced productivity (Ganeshram and Pedersen, 1998; Cartapanis et al., 2011; Chang et al., 2015) within the ETNP and the Gulf of California during the glacial period. The nitrogen isotope ratios in the Guaymas Basin can be affected by subsurface denitrification in the Gulf and in the ETNP (Pride et al., 1999). The increase in dissolved oxygen might have strongly decreased water column denitrification (Ganeshram et al., 1995) during the glacial period thereby increasing the  $\text{NO}_3^-$  levels (Fig. 4.4b).

Our study observed a declining trend in reconstructed  $[\text{NO}_3^-]_{\text{BW}}$  levels (Fig. 4.4b) during the EH, slowly approaching modern concentrations. This coincides with the deglacial high  $\delta^{15}\text{N}_{\text{bulk}}$  values, suggesting reduced water column ventilation and/or strong denitrification. This agrees with previous studies in the ETNP (Kienast et al., 2002) and within the Gulf of California (Pride et al., 1999) that high denitrification most likely associated with warming temperatures, occurred during this period. Furthermore, the scarcity of benthic foraminifera after the EH period in our study coincides with laminations of the sediment core below 10,840 years BP, where reconstructed  $[\text{NO}_3^-]_{\text{BW}}$  begins to decrease (Fig. 4.4b). It is possible that redox conditions were too hostile for benthic foraminifers in the laminated periods, or that calcareous shells are not well preserved in these layers. Non-laminated sediments are associated with cooler climatic conditions until 13,000 years BP (Keigwin & Jones, 1990).

### 4.4.3 Mexican Margin

The highlight of the results from the core, MAZ-1E-04, is the steep rise in  $[\text{NO}_3^-]_{\text{BW}}$  observed between the BA and the YD (**Fig. 4.4c**). The transition period from the BA to the Holocene involved rapid oxygenation with increased oxygen levels at the onset of the YD (Jaccard & Galbraith, 2012; Ohkushi et al., 2013; Taylor et al., 2017). This has been linked to active ventilation by increased NPIW production at high latitudes in the North Pacific (Van Geen et al., 1996; Emmer and Thunell, 2000; Okazaki et al., 2010; Cartapanis et al., 2011; Chang et al., 2014). However, considering the deep-water depth of the Mexican site with less influence of NPIW (**Fig. 4.4c**), it is likely less reflected in the  $[\text{NO}_3^-]_{\text{BW}}$  at this site. Instead, the Mexican Margin site may be influenced more by the nitrate variability in the Pacific Deep Water, PDW (see **Fig. 4.3**). Reorganization of deep-water circulation and carbon ventilation during the LGM and the following deglaciation (Rafter et al., 2022) may have influenced the  $[\text{NO}_3^-]_{\text{BW}}$  at this site. At the onset of the deglaciation, deep Southern Ocean ventilation (reduced  $^{14}\text{C}$  ventilation ages) and atmospheric carbon dioxide ( $\text{CO}_2$ ) synchronously increased (Burke and Robinson, 2012; Rae et al., 2018). This deglacial increase in ventilation in the Pacific Ocean resulted most likely in an increase of atmospheric  $\text{CO}_2$  derived from carbon in the Southern and Pacific Oceans. The increase of the reconstructed  $[\text{NO}_3^-]_{\text{BW}}$  during the YD may reflect the release of nutrient- and dissolved inorganic carbon-rich waters during the deglaciation (Rafter et al., 2022).

In addition, there was low primary productivity (Hendy et al., 2004; Pospelova et al., 2015), and a higher influx of freshwater (Broecker et al., 1985; Clark et al., 2002) during the YD. Bulk sediment nitrogen records in the ETNP (Ganeshram et al., 1995; Pride et al., 1999; Emmer and Thunell, 2000; S. S. Kienast et al., 2002; Hendy et al., 2004) found a decrease in  $\delta^{15}\text{N}_{\text{bulk}}$  during the YD due to reduced denitrification. Furthermore, foraminifera-bound nitrogen isotope ( $\delta^{15}\text{N}_{\text{FB}}$ ) study (Studer et al., 2021) in the eastern tropical Pacific also found a decrease in  $\delta^{15}\text{N}_{\text{FB}}$  signatures during the YD (**Fig. 4.4c**). Although the ME-24 core site (Studer et al., 2021) is above the equator but further away from the Mexican Margin, the  $\delta^{15}\text{N}_{\text{FB}}$  signatures obtained from foraminiferal calcite shells agree that nitrate inventories can be sensitive to changes in denitrification in the ETNP (Rafter et al., 2012; Rafter & Sigman, 2016).

The relatively high  $[\text{NO}_3^-]_{\text{BW}}$  during the glacial period (**Fig. 4.4c**), before its decline in H1, is indicative of reduced water-column denitrification (Ganeshram et al., 1995; 2000). Decreased productivity due to coastal upwelling and the organic matter flux through the oxygen minimum

zone (Ganeshram et al., 1995, 2000; Ganeshram and Pedersen, 1998) are the main causes of reduced water-column denitrification during glacial periods. In the ETNP, including the Mexican Margin, coastal upwelling is driven by trade winds generated by subtropical high-pressure centers. These high-pressure centers are largely maintained by differential heating of the land and the ocean. As a result of glacial cooling on land, these high-pressure systems and the associated trade winds that drive the upwelling have been weakened (Ganeshram and Pedersen, 1998).

#### 4.4.4 Gulf of Guayaquil

The core M77/2-59-01 is in a region which is sensitive to changes in subsurface denitrification in the ETSP (Robinson et al., 2007, 2009; Dubois et al., 2011, 2014). The lower glacial  $\delta^{15}\text{N}_{\text{bulk}}$  values corresponding to elevated reconstructed  $[\text{NO}_3^-]_{\text{BW}}$  levels (Fig. 4.4d) suggests decreased water-column denitrification (Salvatteci et al., 2014; Erdem et al., 2020; Glock et al., 2022) and low marine productivity (Ganeshram et al., 2000; Robinson et al. 2007, 2009; Martinez and Robinson et al., 2010; Salvatteci et al., 2016). Nutrient export to the deep Southern Ocean waters increased due to the sluggish Atlantic Meridional Overturning Circulation (Skinner et al., 2010), and increased atmospheric iron (Fe) deposition (Somes et al., 2017) during the glacial period. This reduced the transport of preformed nitrate to the tropics via the Subantarctic Mode Water (SAMW), limiting productivity (Somes et al., 2017). In fact, the total organic carbon (Fig. 4.4d) depicts low productivity during this time period. Furthermore, the colder sea surface temperature (SST) and the accelerated formation of SAMW and Antarctic Intermediate Water masses (Russell & Dickson, 2003; Galbraith et al., 2004) and the stronger high-latitude winds in the Southern Hemisphere (Karstensen and Quadfasel, 2002) increased the ventilation rate (Meissner et al., 2005; Jaccard and Galbraith, 2012; Muratli et al., 2010) during the glacial period. The resulting increased oxygen concentrations (Robinson et al., 2005; Robinson et al., 2007) decreased the volume of ODZs, and nitrogen loss processes during the glacial period. In addition, enhanced Fe deposition (Somes et al., 2017), and the glacial low sea level (Clark and Mix, 2002; Wallmann et al., 2016), may have influenced the nitrate inventory in the tropical and subtropical southern hemisphere. Core M77/2-52-2 from Peru (Glock et al., 2018) also shows elevated  $[\text{NO}_3^-]_{\text{BW}}$  during the LGM, a similar decline in  $[\text{NO}_3^-]_{\text{BW}}$  during the H1 and thereafter a steady decrease in  $[\text{NO}_3^-]_{\text{BW}}$  throughout the Holocene.

The deglacial increase in  $\delta^{15}\text{N}_{\text{bulk}}$  values corresponds to the decline in  $[\text{NO}_3^-]_{\text{BW}}$ , especially during the H1 (**Fig. 4.4d**), thus indicating a gradual increase in surface productivity and bottom-water deoxygenation during the early deglacial period (Erdem et al., 2020). High export production strengthened the expansion of the ETSP ODZ during the deglaciation as compared to LGM and MLH (Salvatteci et al., 2016; Glock et al., 2018; Mollier-Vogel et al., 2019). This is consistent with the denitrification signal in the Eastern Equatorial Pacific through westward advection from the Southeast Pacific margins (Martinez and Robinson, 2010).

The shift towards low  $\delta^{15}\text{N}_{\text{bulk}}$  values from the Middle-Holocene, consistent with the higher  $[\text{NO}_3^-]_{\text{BW}}$  in our data (**Fig. 4.4d**), implies a profound change in the climatic state of the Peruvian upwelling system and the associated ODZ during this time (Mollier-Vogel et al., 2019). From the deglaciation toward the Late Holocene, there was a general increase in productivity (Mollier-Vogel et al., 2019) as shown by total organic carbon data (**Fig. 4.4d**). This increase in organic matter is related to an increase in upwelling-driven delivery of nutrients towards the surface (Mollier-Vogel et al., 2019). The nitrate supply at the equatorial sites is dominated by local upwelling (Wyrski, 1981; Rafter and Sigman, 2016). The gradual decrease in  $\delta^{15}\text{N}_{\text{bulk}}$  values and higher  $[\text{NO}_3^-]_{\text{BW}}$  likely related to a relaxation in nutrient utilization with a nutrient supply exceeding the biological demand (Riechelsohn et al., 2024). Moreover, the core M77/2-59-01 was retrieved outside of the core ODZ and is under the strong influence of the oxygen and nutrient-rich Equatorial Under Current subsurface waters (Salvatteci et al., 2019; Mollier-Vogel et al., 2019). These waters ventilated the Peruvian margin and deepened the Peruvian oxycline during the Middle-Holocene. Furthermore, enhanced zonal SST (Koutavas et al., 2006) and a northward shift of the ITCZ strengthened the Pacific Walker and Hadley circulation during the Middle-Holocene across the tropical Pacific (Koutavas et al., 2006; Mollier-Vogel et al., 2013; Salvatteci et al., 2019). These enhanced atmospheric circulations brought oxygen-rich waters to the intermediate depths off Peru via the equatorial subsurface countercurrents (Koutavas et al., 2006; Mollier-Vogel et al., 2013; Salvatteci et al., 2019). Hence, increased ventilation of the subsurface water (oxygen-rich) masses reduced the strength of nitrogen loss processes and nutrient uptake during the MLH.

#### 4.4.5 Comparison of past and present $[\text{NO}_3^-]_{\text{BW}}$ at the studied locations

The  $[\text{NO}_3^-]_{\text{BW}}$  during the present and past climatic conditions are compared to assess the resilience of our chosen study locations towards environmental and ecological impacts of climate change.

The generally positive  $\Delta[\text{NO}_3^-]$  that we found (**Fig. 4.5**) in the Gulf of California (Guaymas Basin) and the Gulf of Guayaquil (Peru) indicate that today the  $[\text{NO}_3^-]_{\text{BW}}$  are lower than in the past. This suggests that today the nitrogen loss processes at these two core sites are stronger, most likely related to ocean warming and a decline in oxygen concentration of bottom waters. In the case of the Gulf of California, the  $\text{NO}_3^-$  deficit due to elevated denitrification might not act as negative feedback because it might be countered by increased nitrogen fixation in surface waters. The uptake of  $\text{NO}_3^-$  is ultimately controlled by the availability of Fe in the Equatorial Pacific (Fitzwater et al., 1996). The sediments in the Gulf of California are enriched (Scholz et al., 2019) in reactive Fe. The decreasing  $\text{NO}_3^-$  concentrations in the bottom water reduce the flux of  $\text{NO}_3^-$  into the surface sediment. This will release the sedimentary Fe which enhances the nitrogen fixation in the Guaymas Basin. If the rate of nitrogen fixation exceeds denitrification in the Gulf of California, the high biological productivity would reduce oxygen concentrations and lead to a stronger ODZ with higher denitrification in the subsurface water masses, due to a positive feedback loop.

In the case of Gulf of Guayaquil, whether today's elevated denitrification could enhance  $\text{N}_2$  fixation also depends on the availability of Fe. The productivity of the Peruvian ODZ is presently limited by iron in which dissolved Fe is provided by the shelf and slope sediments. Modelling studies showed that productivity will be amplified in the Peruvian ODZ due to release of Fe from shelf and slope sediments (Wallmann et al., 2022). Under nitrogen-limitation, negative feedbacks (e.g., anammox) result in a decline in productivity (Naafs et al., 2019), which will stabilize the oxygen concentration. This can enhance the resilience of the Peruvian ODZ. However, if nitrogen fixation increases under low oxygen conditions, the positive feedback induced by sedimentary Fe recycling may induce deoxygenation and drive the expansion and intensification of Peruvian ODZ resulting in a positive feedback loop, like in the Gulf of California. This situation is indicated by the lower  $[\text{NO}_3^-]_{\text{BW}}$  today compared to the past ~20,000 years (**Fig. 4.5**).

The negative nitrate  $\Delta[\text{NO}_3^-]$  in the Sea of Okhotsk and the Mexican Margin (**Fig. 4.5**) indicates that modern  $[\text{NO}_3^-]_{\text{BW}}$  levels are higher than in the past. This suggests that modern nitrogen loss is decreased at these two core sites compared to the last deglaciation. The higher modern  $[\text{NO}_3^-]_{\text{BW}}$  in the Sea of Okhotsk is likely associated with less primary productivity and more oxygen in the water column similar to the situation that established in the MLH. The higher present  $[\text{NO}_3^-]_{\text{BW}}$  in the case of the Mexican Margin could be associated with sea level rise. The ODZ in the Mexican

Continental Margin might have shifted to shallower depths today with less/no benthic denitrification in the intermediate water depths at the core site, resulting in high  $[\text{NO}_3^-]_{\text{BW}}$  levels. During the glacial period, continental shelves were exposed due to lower sea level (Clark and Mix, 2002; Wallmann et al., 2016) and the main areas of primary productivity shifted to offshore sites. In addition, remineralization rates were reduced, due to the lower temperatures. The centers of deposition and production may have migrated offshore from the shallow shelf towards the continental slope relative to their Holocene positions. A similar situation occurred at the Benguela upwelling system during the LGM: TOC accumulation at the continental slope increased during the LGM in response to the seaward shift of centers of enhanced productivity (Mollenhauer et al., 2002). This offshore shift of the productivity centers and the most likely reduced remineralization rates, due to lower temperatures, indicate that the ODZ in the past Mexican Margin was deeper than today. However, with the deglacial eustatic sea-level rise, the ODZ may have shifted to shallower depths. This shifted the main zone of denitrification to shallower depths, resulting in the increased modern  $[\text{NO}_3^-]_{\text{BW}}$  in comparison to the LGM (Fig. 4.5).

#### 4.5 Conclusion

The quantitative reconstruction of  $[\text{NO}_3^-]_{\text{BW}}$  using the pore density of denitrifying benthic foraminifera over the last deglaciation at the four studied ODZs provided a comprehensive understanding of the past  $\text{NO}_3^-$  in intermediate depths. Ocean deoxygenation and warming alter the cycling of nutrients, and affect the functioning of marine ecosystems and the food web.

The Gulf of Guayaquil and Gulf of California data shows elevated  $[\text{NO}_3^-]_{\text{BW}}$  during the glacial period compared to deglacial and modern conditions. Considering the highly ventilated intermediate water masses in the Sea of Okhotsk, it is possible that the Sea of Okhotsk had also elevated  $[\text{NO}_3^-]_{\text{BW}}$  in the glacial period. For the Mexican Margin core,  $[\text{NO}_3^-]_{\text{BW}}$  was particularly strong during the YD. The reconstructed  $[\text{NO}_3^-]_{\text{BW}}$  from the Sea of Okhotsk, the Gulf of California, and the Gulf of Guayaquil may have been influenced by the formation of the NPIW. However, the  $[\text{NO}_3^-]_{\text{BW}}$  in the deeper site, the Mexican Margin likely influenced more by nutrient variations in the circulation of PDW. Spatial and temporal differences associated with water-mass ventilation, oxygen solubility, water-column denitrification, primary productivity, and temperature differences may account for the  $\text{NO}_3^-$  differences in the cold and warm periods. This makes the interpretation of  $[\text{NO}_3^-]_{\text{BW}}$  records highly complex. It is inconceivable to decipher all reasons for the observed

changes, considering that the pore density of denitrifying foraminifera is a relatively new proxy, which has been applied for the first time in a higher spatial resolution within this study.

The comparison of present and past  $[\text{NO}_3^-]_{\text{BW}}$  shows that the modern Gulf of Guayaquil and the Gulf of California have low  $[\text{NO}_3^-]_{\text{BW}}$  levels associated with increased denitrification and a strengthening ODZ. If nitrogen fixation exceeds the nitrogen loss under low oxygen conditions, ecological effects may be observed in these two regions, the Gulf of Guayaquil and the Gulf of California. Unlike this, higher modern  $[\text{NO}_3^-]_{\text{BW}}$  were observed in the Sea of Okhotsk and the Mexican Margin, suggesting that these two regions have a higher oxygen stability. This may make these two ecosystems more resilient to climate change than regions with a less well oxygenated intermediate water column.

---

### **Data availability**

All data generated or analysed during this study are included in Appendix B as supplementary figures and tables.

### **Author contributions**

A.G.M wrote the core manuscript, did the sample preparation, electron microscopy, image and statistical analyses of all the fossil foraminifera. N.G. planned the study design and sampling strategy. G.S. hosted the research group, and provided access to SEM, and lab facilities at the University of Hamburg. D.N. provided sampling material for cores MD01-2415 and M77/2-59-01. C.D. provided sampling material for core MAZ-1E-04. A.M.-G., N.L., R.S., and A.B. facilitated the measurement of nitrogen isotopes in the sediment samples of core MD01-2415 and DSDP-480. R.A. contributed to the age model development of core MAZ-1E-04, and H.F helped in the image processing of core DSDP-480. All authors contributed to the preparation of the manuscript.

### **Acknowledgements**

We are grateful to the micropaleontology group at the University of Hamburg. We acknowledge the help of Dr. Yvonne Milker with the SEM, Jutta Richarz, Kaya Oda for lab support, PhD student Sven Brömme (MPIC) and student assistant Hannah Krüger. Funding was provided by the Deutsche Forschungsgemeinschaft (DFG) through both N.G.'s Heisenberg grant GL 999/3-1 and

grant GL 999/4-1. Funding for the core MD01-2415 recovery was provided by the German Science Foundation (DFG) within project Ti240/11-1. We thank Yvon Balut, Agnes Baltzer, and the Shipboard Scientific Party of RV Marion Dufresne cruise WEPAMA 2001 for their kind support. We thank IODP for providing the sample for core DSDP-480. The recovery of core M77-59 recovery was a contribution of the German Science Foundation (DFG) Collaborative Research Project “Climate–Biogeochemistry interactions in the Tropical Ocean” (SFB 754). The study is a contribution to the Center for Earth System Research and Sustainability (CEN) of University of Hamburg.

## Chapter 5

### Reconstruction of redox conditions in the Oxygen Deficient Zones in the marginal seas of the Pacific Ocean using benthic foraminiferal Mn/Ca

Anjaly Govindankutty Menon, Christine Barras, Edmund Hathorne, Dirk Nürnberg, Catherine V. Davis, Gerhard Schmiedl, Nicolaas Glock

#### Abstract

Oxygen concentrations in the oceans are decreasing due to global warming and other anthropogenic activities. Oxygen deficient zones (ODZs) are expanding all around the world due to warming, and reduced oxygen solubility. In order to monitor oxygen dynamics and predict future dynamics of oxygen levels under rapidly changing climatic conditions, reliable proxies for oxygen concentrations are needed. Benthic foraminiferal Mn/Ca ratios are a promising redox proxy. This study documents three aspects related to the deglacial Mn/Ca ratios of the shallow infaunal foraminiferal species *Bolivina spissa* and *Bolivina subadvena* from four sediment cores around the Pacific. 1) The Mn/Ca ratios obtained by laser ablation of chemically cleaned specimens were compared to uncleaned specimens. Foraminiferal specimens from the Gulf of Guayaquil and the Mexican Margin show no major difference in Mn/Ca between cleaned and uncleaned specimens, while specimens from the Gulf of California show a clear difference, likely related to the presence of post-depositional organic matter in the foraminiferal tests. 2) The Mn/Ca ratios of bulk samples measured with solution-based quadrupole inductively coupled plasma mass spectrometry (Q-ICP-MS) and individual foraminiferal specimens measured with laser ablation Q-ICP-MS were compared. The data between both methods showed a good reproducibility and the same order of magnitude are observed. This suggests that individual foraminiferal specimens can be used when bulk foraminiferal specimens are insufficient. 3) Redox conditions in the Gulf of California, the Mexican Margin, the Gulf of Guayaquil and the Sea of Okhotsk exhibit variations during the last deglaciation, i.e., from the Last Glacial Maximum to the Holocene. The Gulf of California may have experienced continuous oxygen depletion to the extent of anoxia. The Mn/Ca ratios from the Mexican Margin may be influenced by the vertical shift of the ODZ due to lowered sea level during the Last Glacial Maximum. The Mn/Ca ratios for the Gulf of Guayaquil suggest a transition from glacial hypoxic conditions to Holocene suboxic conditions. The Mn/Ca ratios at the Sea of Okhotsk were strongly elevated compared to the other regions, which implies a strong continuous terrestrial Mn source in this region.

*Keywords: Benthic foraminifera, Mn/Ca, Laser ablation, Bottom-water oxygen*

## 5.1 Introduction

Oxygen concentrations in the open ocean and coastal waters have been declining since the mid-20<sup>th</sup> century (Keeling et al., 2010; Helm et al., 2011; Stramma et al., 2008; Schmidtko et al., 2017) and is of global concern due to its potential impacts on both the global and local marine ecosystems (Keeling et al., 2010; Stramma and Schmidtko, 2021). Dissolved oxygen is an important parameter to reconstruct for palaeoceanographic investigations as it plays an essential role in regulating the structure and biodiversity of benthic ecosystems (Levin, 2003; Levin et al., 2009). Insights on the processes and effects of deoxygenation can be obtained through records of past oxygen in seawater.

Manganese (Mn) is a redox sensitive element (Froelich et al., 1979). Under oxic conditions, Mn exists in the form of solid Mn (hydr)oxides, i.e., MnO<sub>2</sub> or MnOOH (Burdige and Gieskes, 1983; Burdige, 1993; Koho et al., 2017). Mn is transported to the seafloor in the form of coatings on sediment particles (Finney et al., 1988). When oxygen concentrations in the sediment decrease due to increased organic matter remineralization, MnO<sub>2</sub> or MnOOH are reduced to aqueous Mn<sup>2+</sup> (Froelich et al., 1979) in the upper part of the sediment. The released Mn into the pore waters diffuses upwards and reprecipitates in the oxic zone in the sediment, resulting in high subsurface MnO<sub>2</sub> or MnOOH concentrations (Burdige and Gieskes, 1983; De Lange et al., 1989). Thus, there is a continuous cycling of solid and aqueous Mn in sediments (Slomp et al., 1997). This will build up the pore water Mn<sup>2+</sup> concentration in the suboxic part of the sediment until a Mn carbonate phase starts to precipitate (De Lange, 1986; Middelburg et al., 1987; Calvert and Pedersen, 1993). Under permanently oxic bottom water conditions, most of the Mn initially deposited as MnO<sub>2</sub> or MnOOH, is ultimately buried as Mn carbonates. Contrary to this, under suboxic to anoxic bottom water conditions, MnO<sub>2</sub> or MnOOH are reduced either in the water column or at the sediment-water interface (Schenau et al., 2002). Since, no detrital Mn oxides are accumulating, pore water Mn<sup>2+</sup> concentrations remain low in anoxic and suboxic conditions and no Mn carbonates are formed (Schenau et al., 2002). Under hypoxic conditions, where Mn cannot escape to the overlying hypoxic bottom water, because it is oxidized to solid MnO<sub>2</sub> or MnOOH, which accumulate on the sediment surface, the Mn<sup>2+</sup> concentration increases in the porewater.

Benthic foraminifera precipitate their tests in the upper sediment layer, where the presence of Mn<sup>2+</sup> can depend on bottom-water oxygenation (Koho et al., 2015, 2017). Therefore, Mn incorporated

into the calcite of benthic foraminifera during calcification is a promising proxy for redox conditions (Koho et al., 2015; C. Barras et al., 2018; Petersen et al., 2018). Benthic foraminiferal Mn/Ca is expected to be high during hypoxic conditions (Groeneveld and Filipsson, 2013; McKay et al., 2015; Koho et al., 2015; Petersen et al., 2018; Brinkmann et al., 2023), and low during anoxic or suboxic conditions as dissolved  $Mn^{2+}$  in pore waters is low, and also low under oxygenated conditions because of solid  $MnO_2$  or  $MnOOH$ . Therefore, the Mn incorporation into benthic foraminiferal calcite varies significantly in oxic, hypoxic, suboxic and anoxic environments (McKay et al., 2015). In the case of ODZs,  $Mn^{2+}$  remain depleted (Law et al., 2009) in pore waters because,  $MnO_2$  or  $MnOOH$  can be reduced already in the water column and only small amounts of Mn will reach the seafloor via diffusion in the form of  $Mn^{2+}$ . In addition,  $Mn^{2+}$  present in the pore water will escape to the oxygen depleted bottom water (Koho et al., 2015).

The main advantage of Mn/Ca analyses in foraminifera is that once precipitated, the Mn concentration remains fixed in the foraminiferal calcite and is not prone to oxidation or reduction processes (Koho et al., 2015; Petersen et al., 2018) in contrast to bulk sediment Mn (Schenau et al., 2002), which can continue to be reduced and mobilized after deposition. Nevertheless, it is not straightforward to interpret the Mn/Ca in benthic foraminifera. Factors such as high surface productivity, poor intermediate water ventilation (Koho et al., 2017 and references therein), foraminiferal habitat preferences (living depth in the sediment; **Fig. 5.1**) and species-specific responses to oxygen availability can noticeably influence foraminiferal Mn signatures (Jorissen et al., 1995; Koho et al., 2015, 2017; C. Barras et al., 2018) even when bottom-water conditions are the same. For example, the foraminiferal species inhabiting deeper infaunal habitats usually have higher Mn/Ca ratios than those living near the sediment surface (Koho et al., 2015, 2017). Furthermore, the supply of Mn from different sources such as the atmosphere (Vedamati et al., 2015; Chen & Wu, 2019; Nakaguchi et al., 2022) via dust, or aerosols (Baker et al., 2016), and river discharge (Bolster et al., 2022; Nakaguchi et al., 2022) can also noticeably influence the Mn distribution in the ocean.

The Mn/Ca ratios in benthic foraminifera have been linked to ambient seawater Mn concentrations, and thus bottom-water oxygenation by studies of Glock et al. (2012b), Groeneveld and Filipsson, (2013), Koho et al. (2017), Ní Fhlaithearta et al. (2018) and Brinkmann et al. (2023). In this study, we used the shallow infaunal benthic foraminifera species *Bolivina spissa* and *Bolivina subadvena*

from four different ODZs in the Pacific Ocean and its marginal sea basins, such as the Sea of Okhotsk, the Gulf of California, the Mexican margin and the Gulf of Guayaquil. These foraminiferal species are capable of denitrification (Glock et al., 2011b; Govindankutty Menon et al., 2023) and thus can survive even under anoxic conditions. The Mn/Ca ratios in *B. spissa* have been found to correlate with bottom-water oxygen (Glock et al., 2012b; Koho et al., 2017), and are a promising proxy for palaeo redox conditions.

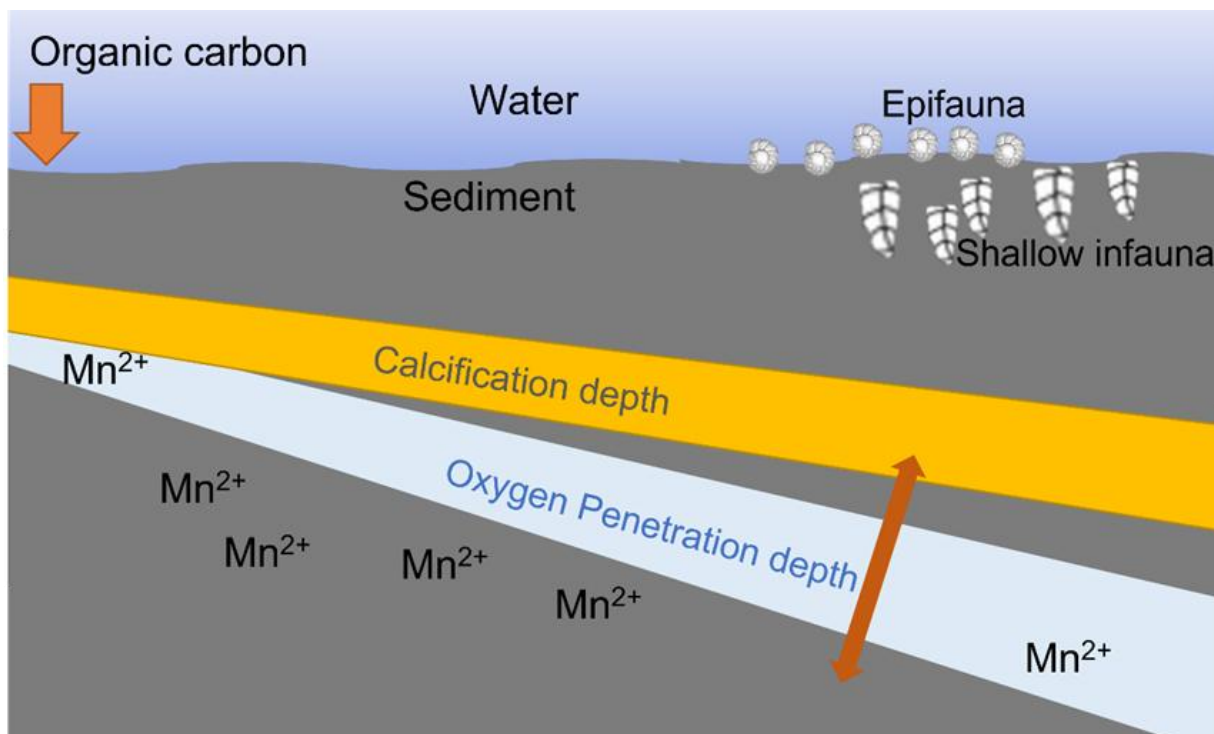


**Figure 5.1.** Schematic diagram of shallow infaunal benthic foraminifera and their relationship with the sediment redox boundaries and calcification depth. This image is inspired from Ní Fhlaithearta et al. (2018).

We investigated the redox conditions in the studied sites over the last 20, 000 years. For this purpose, we used Mn/Ca ratios from bulk and individual specimens of either *B. spissa* or *B. subadvena*. The Mn/Ca ratios of individual foraminiferal specimens are compared to the bulk foraminiferal analyses to see if the results are comparable, and if individual specimens are sufficient enough to reconstruct past oxygenation. Furthermore, the Mn/Ca ratios of cleaned and uncleaned foraminiferal specimens are compared to investigate the effect of cleaning on Mn/Ca ratios determined by laser ablation inductively coupled plasma mass spectrometer (LA-ICP-MS).

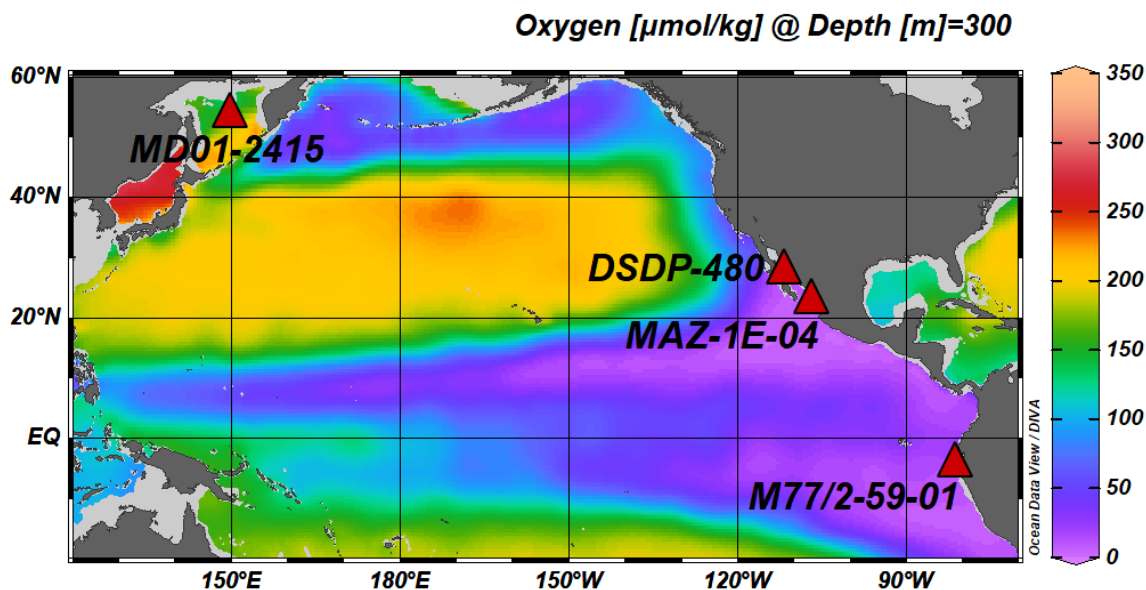


**Figure 5.2.** Study area of the Pacific Ocean with oxygen concentration at 300 m water depth and locations of study sites in the Sea of Okhotsk (MD01-2415), Gulf of California (DSDP-480), Mexican margin (MAZ-1E-04), and Gulf of Guayaquil (M77/2-59-01). Ocean Data View (Schlitzer, R., 2023) has been used for the construction of the map using the data from World Ocean Atlas, 2008.

## 5.2. Materials and methods

### 5.2.1 Study area and sampling of sediment cores

We used benthic foraminifera from sediment cores collected from the Gulf of Guayaquil (Peru, core M77/2-59-01), the Mexican Margin (core MAZ-1E-04), the Sea of Okhotsk (core MD01-2415), and the Gulf of California (Guaymas Basin, core DSDP-64-480). Gulf of Guayaquil sediment core M77/2-59-01 was collected (03°57.01' S, 81°19.23' W, recovery 13.59 m) from the northern edge of the ODZ at a water depth of 997 m during RV Meteor cruise M77/2 in 2008. The piston core MAZ-1E-04, Mexican Margin (22.9°N, 106.91°W) was collected on board of the RV El Puma at a water depth of 1468 m. The CALYPSO giant piston core MD01-2415 (53°57.09' N, 149°57.52' E, recovery 46.23 m) was recovered from the northern slope of the Sea of Okhotsk at 822 m water depth during WEPAMA cruise MD122 of the R/V Marion Dufresne (Holbourn et al., 2002; Nürnberg and Tiedemann, 2004). The Deep-Sea Drilling Project core DSDP- 480 (27°54' N, 111°39' W) from the Gulf of California was retrieved at a water depth of 747 m close to the Guaymas Basin.

### 5.2.2 Cleaning protocol for bulk foraminiferal tests for Quadrupole ICP-MS

For the bulk analysis of Mn/Ca ratios, 20 sample depths from Gulf of Guayaquil, 12 sample depths from the Mexican margin, and 6 sample depths from the Gulf of California were used. The sediment samples were washed and wet-sieved through a 63  $\mu\text{m}$  mesh sieve. The residues were dried in an oven at temperatures between 38-50°C. The samples were fractionated into the grain-size fractions of 63-125, 125-250, 250-315, 315-355, 355-400, and >400  $\mu\text{m}$ . Each bulk sample contains ~20 foraminiferal specimens, and all selected specimens were picked from the coarse fraction of 125-250  $\mu\text{m}$ . Only *B. spissa* specimens were used from the Gulf of Guayaquil, and from the Mexican margin. Instead, *B. subadvena* was picked from the Gulf of California, due to the lack of sufficient *B. spissa* specimens. Bulk analyses could not be done at the Sea of Okhotsk, since a sufficient number of *B. spissa* or *B. subadvena* specimens was not available in the sediment samples. Subsequently, all the 20 foraminiferal tests were gently crushed between two glass plates. The shell fragments were cleaned following the standard cleaning protocol for foraminiferal Mg/Ca analyses (modified after [Barker et al., 2003](#)). The test fragments were transferred into Teflon vials and rinsed three times with reverse osmosis water (ROW). After each rinsing, vials were sonicated for 20 seconds. Afterwards, the vials were rinsed 3 times using ethanol and put into ultrasonicator for 1 min after each rinsing step. Again, vials were rinsed with ROW two times to remove the residual ethanol. Fresh oxidative agent was prepared by mixing 100  $\mu\text{l}$  30 % hydrogen peroxide ( $\text{H}_2\text{O}_2$ ) to 10 ml of a 0.1 M sodium hydroxide (NaOH) solution. Subsequently, 250  $\mu\text{l}$  of this reagent were added to each vial. Then, the vials were put in a water bath at 92 °C for 15 min. Every 5 minutes, the vials were checked for air bubbles and gave a small shake to remove if any. After this step, the oxidative agent mix was removed from the vials. Then, the samples were rinsed with ROW two times without ultrasonification. Afterwards, the test fragments were transferred into clean vials with a pipette. Into these transferred vials 100  $\mu\text{l}$  of 0.001 M nitric acid ( $\text{HNO}_3$ ) (suprapure, Roth<sup>TM</sup>) were added. This step is done to leach the contaminants but not to dissolve the shells. The vials were put into the supersonic bath for 20 seconds. The added acid was removed and again vials were rinsed with ROW two times and, after that, rinsed two times with ethanol.

For the dissolution step, 400  $\mu\text{l}$  0.075 M  $\text{HNO}_3$  (suprapure, Roth<sup>TM</sup>) was added to the vials, centrifuged and transferred into clean vials. For initial determination of the Ca concentrations, 20  $\mu\text{l}$  from each sample were mixed with 480  $\mu\text{l}$  of 2%  $\text{HNO}_3$  with Scandium (Sc). The bulk analyses

were performed on Agilent Technologies 7500 Series Quadrupole ICP-MS. For the working conditions of the Q-ICP-MS analyses; see Glock et al. (2012b).

### 5.2.3 Cleaning protocol for single foraminiferal tests for laser ablation

Single foraminiferal tests of *B. spissa* and *B. subadvena* were cleaned before taking them for LA-ICP-MS ultrasonication and an oxidative chemical cleaning step. Ultrasonic cleaning was done to remove the clay particles which is present on the outside of the test. To achieve this, complete single foraminiferal specimens were rinsed with ethanol (96%) and ultrasonicated for 20 seconds. This step was repeated for three times. The pipette tip was rinsed in between with 10% HNO<sub>3</sub> and ROW to clean the tube. Thereafter, ROW was added to the sample vial and sucked it. This is repeated for two times.

The sample vials were rinsed with ROW for three times to remove rests of ethanol. Afterwards, an oxidative reagent was freshly mixed by adding 100 µl 30% H<sub>2</sub>O<sub>2</sub> to 10 ml of a 0.1 M NaOH (p.a., Roth™) solution. Subsequently, 100 µl of this reagent were added to each vial of foraminifera. Thereafter, the lids of the vials were closed, and the vials were kept in a 92°C hot water bath for 15 minutes. During this 15 minutes, every 5 minutes, the vials were tapped at the bottom to remove the bubbles. After the hot water bath, the vials were again ultrasonicated for 20 seconds. Then, the oxidative reagent (NaOH+ H<sub>2</sub>O<sub>2</sub>) was removed and the sample was rinsed twice with ROW. The foraminiferal specimens were then individually collected over a 125-mm mesh stainless steel sieve rinsed with ethanol and dried. Reductive cleaning was not done in order not to remove any Mn (oxyhydr) oxide coatings, if present since also such coatings might record information about the depositional redox conditions.

### 5.2.4 Operating conditions and instrument calibration for LA-ICP-MS

Single specimen Mn/Ca ratios were determined using LA-ICP-MS at the Laboratory of Planetology and Geodynamics, Université de Nantes (France). All laser ablations were performed using an ArF excimer laser (193 nm, Analyte G2, Teledyne Photon Machines) coupled to a Q-ICP-MS (ICP-MS; Varian Bruker 820-MS). The laser wavelength at 193 nm is essential for a reproducible ablation on the fragile *Bolivina* tests as carbonates do not absorb laser radiation well at higher wavelengths (Jackson et al., 1992). The ablations were conducted in a HelEx II two-volume cell with He as a carrier gas, a laser fluence of 0.91 J/cm<sup>2</sup> and a laser pulse repetition rate of 5 Hz. The spot sizes were adapted to the chamber size in order to maximize the amount of

ablated material. The spot sizes were varied between 65 and 85  $\mu\text{m}$  in diameter (Fig. 3). The isotope masses selected for the analyses were  $^{24}\text{Mg}$ ,  $^{25}\text{Mg}$ ,  $^{27}\text{Al}$ ,  $^{29}\text{Si}$ ,  $^{43}\text{Ca}$ ,  $^{44}\text{Ca}$ ,  $^{55}\text{Mn}$ ,  $^{57}\text{Fe}$ ,  $^{66}\text{Zn}$ ,  $^{88}\text{Sr}$ ,  $^{114}\text{Cd}$  and  $^{137}\text{Ba}$ . The dwell time to measure for each individual element was 20 ms. The ICP-MS was tuned with the NIST SRM 612 reference material before each analytical session to optimize the signal-to-noise ratio and to avoid oxide formation or elemental fractionation.

The NIST-612 glass reference material was analysed every 10 measurements. Four standards were kept in between every 10 measurements of 10 samples. NIST SRM 610 (silicate glass reference material), USGS MACS-3 (carbonate reference material) and NFHS (NIOZ, Netherlands Institute of Sea Research, foraminifera in-house standard; [Mezger et al., 2016](#)) were analysed between every 20 analytical spots on foraminifera samples. The laser settings for the ablation procedure are shown in **Table 5.1**.

**Table 5.1.** Laser controls for the standards

Mode	Fire
Rep Rate	5 Hz
Burst count	150 shots
Laser Energy	50%
Fluence	0.91 J /cm <sup>2</sup>
Spot size	85 $\mu\text{m}$ circle
Scan speed	20 $\mu\text{m}/\text{s}$
Spot spacing	20

A total of 297 measurements (including chemically cleaned and not cleaned) were made on *B. spissa* specimens from the Gulf of Guayaquil, 182 measurements on *B. spissa* from the Mexican Margin, 37 measurements on *B. spissa* from the Sea of Okhotsk, and 124 measurements on *B. subadvena* from the Gulf of California. Each specimen was ablated 2 - 4 times in 3 to 4 different chamber positions. The ablation profiles were very short due to the thin chamber walls of the fragile *Bolivina* specimens. The SEM images of *B. spissa* and *B. subadvena* with laser spots are shown in **Fig. 5.3**. These images were taken at the Institute for Geology, University of Hamburg using Hitachi Tabletop SEM TM4000 series with an accelerating voltage of 15 kV using back-scattered electron (BSE) detector.

All foraminiferal ablation profiles were normalized to the internal standard of  $^{43}\text{Ca}$  and element concentrations were calculated considering 40 wt% of calcium in calcium carbonate,  $\text{CaCO}_3$

(Petersen et al., 2018). This should be relatively consistent in all analyzed foraminiferal tests. Moreover, direct comparisons can be done with trace element to Ca ratios from wet-chemical investigations (Reichert et al., 2003). The NIST SRM 610 glass served as calibration standard for Mn/Ca of the benthic foraminiferal samples, using the values of Jochum et al. (2011). The results obtained from NIST SRM 612, USGS MACS-3 and NFHS were also normalized to NIST SRM 610 glass to evaluate the long-term reproducibility of our analyses.

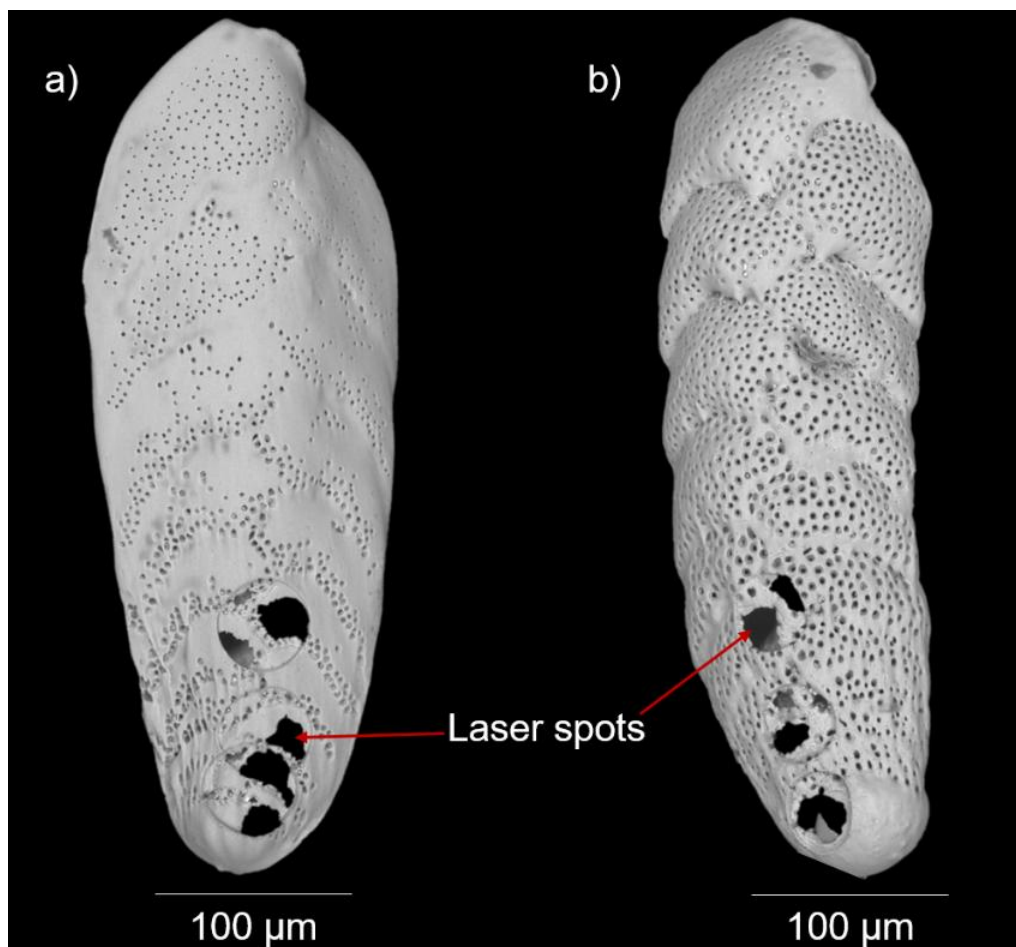


**Figure 5.3.** Scanning electron microscope (SEM) images of a) *Bolivina spissa* b) *Bolivina subadvena* specimens after laser ablation analysis of multiple chambers including the proloculus.

### 5.2.5 Data treatment of laser ablation profiles

All laser ablation profiles for each element (raw counts) and each sample or reference material were carefully examined and processed with the computer software GLITTER at the Laboratory of Planetology and Geodynamics, Université de Nantes (France). The integration interval was

based on constant raw counts of  $^{44}\text{Ca}$  for calcite ablation. Each laser ablation profile was screened for peaks in elements that indicate surface contamination such as  $^{27}\text{Al}$ ,  $^{57}\text{Fe}$ ,  $^{66}\text{Zn}$ . For the current study where Mn is the element of interest, peaks of Mn on outer and inner parts of ablation profile that collided with the peaks of contaminant elements were discarded from the data. High concentrations of Mn on the shell surfaces are generally also an indication of contamination (Petersen et al., 2018). In addition, integration intervals containing 10 data points with count rates below the limit of quantification were removed from the dataset. The element ratios were derived from the average of measured concentrations from each ablation after selecting the non-contaminated part of the ablation profile. The external reproducibility of our Mn/Ca analyses (Table 5.2) was determined on the foraminiferal carbonate standard NFHS. This carbonate standard is apt for this purpose since it has Mn concentration comparable to our samples.

**Table 5.2.** Absolute elemental values and external reproducibility for the duration of this study (relative standard deviation (r.s.d)) of NIST 610 silicate glass standard in comparison to absolute values from Jochum et al. (2011). NFHS is the calibration standard for Mn/Ca of the foraminiferal samples, using the recommended values for Jochum et al. (2011).

NIST SRM 610			
Isotope	This study (ppm)	External reproducibility (r.s.d)	Jochum et al. (2011) (ppm)
$^{24}\text{Mg}$	461.78	3.48	432
$^{25}\text{Mg}$	464.62	3.54	432
$^{27}\text{Al}$	n. a	n. a	10320
$^{43}\text{Ca}$	Internal standard		81475
$^{44}\text{Ca}$	81015.99	1.40	81475
$^{55}\text{Mn}$	465.11	3.77	444
$^{57}\text{Fe}$	n. a	n. a	458
$^{66}\text{Zn}$	471.12	8.46	460
$^{88}\text{Sr}$	524.55	3.28	515.5
$^{137}\text{Ba}$	457.05	4.96	452

## 5. 3 Results

### 5.3.1 Effect of oxidative cleaning on laser ablated benthic foraminiferal Mn/Ca ratios

The mean Mn/Ca ratios of cleaned specimens of *B. spissa* and *B. subadvena* that have been treated with an oxidative agent were compared to the ratios of uncleaned specimens (Fig. 5.4). For this comparison, there were 10 samples from the Gulf of Guayaquil, 7 samples from the Mexican margin, and 5 samples from the Gulf of California. In total 297 spots were measured on 120

specimens of *B. spissa* (27 cleaned and 272 uncleaned) from the Gulf of Guayaquil (**Table 5.3**) The heterogeneity of the uncleaned specimens varied between 9 to 322  $\mu\text{mol/mol}$  (1SD) or 2.9 to 83.2  $\mu\text{mol/mol}$  (1SE). For the cleaned specimen's heterogeneity varied between 2.9 to 151  $\mu\text{mol/mol}$  (1SD) or 1.6 to 75.5  $\mu\text{mol/mol}$  (1SE). For the Mexican margin, 182 spots were measured on 63 specimens of *B. spissa* (22 cleaned and 160 uncleaned). The heterogeneity for the uncleaned specimens varied between 33.4 to 328.9  $\mu\text{mol/mol}$  (1SD) or 8.1 to 87.1  $\mu\text{mol/mol}$  (1SE), while for cleaned specimens varied between 6 to 251.9  $\mu\text{mol/mol}$  (1SD) or 4.2 to 178.1  $\mu\text{mol/mol}$  (1SE). For the Gulf of California 124 spots were measured on 44 specimens of *B. subadvena* (15 cleaned and 109 uncleaned). The heterogeneity for the uncleaned specimens varied between 17.7 to 22.5  $\mu\text{mol/mol}$  (1SD) or 2.8 to 9.5  $\mu\text{mol/mol}$  (1SE), while for cleaned specimens varied between 1.6 to 11.2  $\mu\text{mol/mol}$  (1SD) or 0.9 to 6.4  $\mu\text{mol/mol}$  (1SE). All individual measurements on the different foraminiferal specimens and their corresponding standard deviation and standard error are shown in Appendix C as Supplementary table ST1. In the samples from the Gulf of California, the Mn/Ca values of chemically cleaned *B. subadvena* showed a clear distinction from the uncleaned specimens (**Fig. 5.4c**). Except for a few outliers that most likely represent inter-specimen variability of Mn/Ca our data from the Gulf of Guayaquil, and the Mexican margin, doesn't observe any major difference in Mn/Ca ratios between the cleaned and uncleaned specimens.

**Table 5.3.** Mean ( $\pm$ SD) of Mn/Ca ratios of cleaned and uncleaned benthic foraminiferal specimens of *B. spissa* and *B. subadvena* from different study locations. N is the number of laser ablations.

Location	Species	Cleaned/uncleaned	N	Mn/Ca ( $\mu\text{mol/mol}$ )
Gulf of Guayaquil	<i>B. spissa</i>	Cleaned	27	88.99 $\pm$ 24.40
Gulf of Guayaquil	<i>B. spissa</i>	Uncleaned	272	76.67 $\pm$ 71.33
Mexican margin	<i>B. spissa</i>	Cleaned	22	425 $\pm$ 89.06
Mexican margin	<i>B. spissa</i>	Uncleaned	160	270.80 $\pm$ 154.98
Gulf of California	<i>B. subadvena</i>	Cleaned	15	40.14 $\pm$ 7.33
Gulf of California	<i>B. subadvena</i>	Uncleaned	109	75.58 $\pm$ 22.54

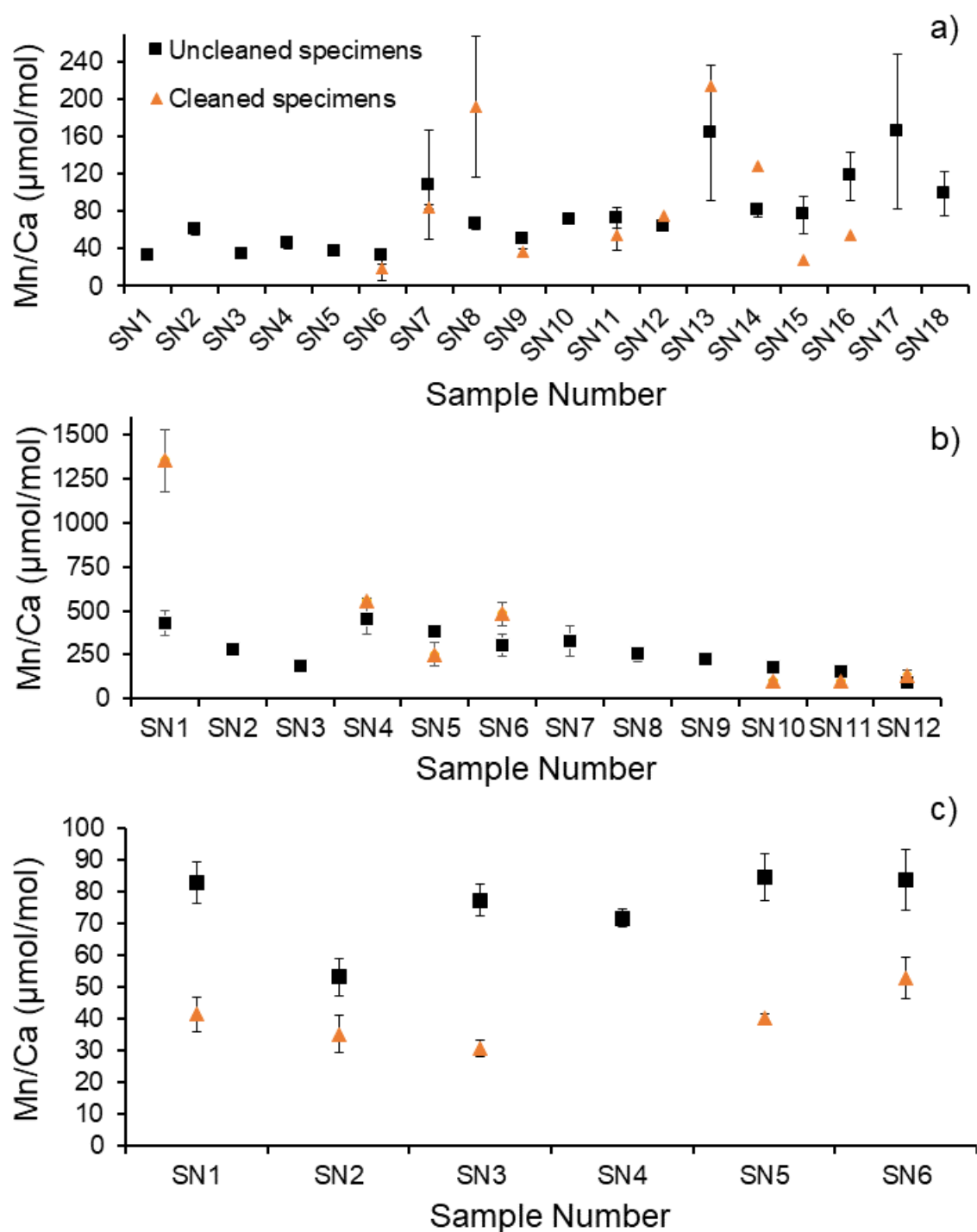


**Figure 5.4.** Comparison of Mn/Ca ratios of cleaned and uncleaned specimens of *B. spissa* and *B. subadvena* using LA-ICP-MS from the a) Gulf of Guayaquil, b) the Mexican margin c) the Gulf of California. The specimens indicated by black squares represents the average Mn/Ca value of uncleaned specimen while the orange triangles are the chemically cleaned specimens. SN depicts the Sample Number. Error bars show 1SE.

### 5.3.2 Comparison of laser ablation Mn/Ca ratios of cleaned specimens and bulk ICP-MS data

The Mn/Ca ratios of bulk (crushed) samples from Q-ICP-MS were compared with the mean of cleaned single specimen Mn/Ca ratios from LA-ICP-MS (**Fig. 5.5**). The Mn/Ca ratios of bulk samples from the Gulf of Guayaquil ranged from 20.8  $\mu\text{mol/mol}$  to 250.3  $\mu\text{mol/mol}$ , while the mean Mn/Ca ratios from LA-ICP-MS on individual cleaned specimens ranged from 18.7 to 215.3  $\mu\text{mol/mol}$ . The direct comparison of Mn/Ca ratios of specimens from Gulf of Guayaquil (**Fig. 5.5a**) showed that in general both methods overlapped within the range of heterogeneity due to the heterogeneity of the individual specimens in our data (**Fig. 5.5a**), except for a few samples that most likely represent real inter-specimen variability. The Mn/Ca ratios of bulk samples from the Mexican margin ranged from 77.9  $\mu\text{mol/mol}$  to 291.7  $\mu\text{mol/mol}$ , while the mean Mn/Ca ratios from LA-ICP-MS on individual cleaned specimens ranged from 101.1 to 554.7  $\mu\text{mol/mol}$ . The direct comparison of Mn/Ca ratios (**Fig. 5.5b**) showed that both methods overlapped within the range of heterogeneity most likely due to heterogeneity of the individual specimens. The Mn/Ca ratios of bulk samples from the Gulf of California ranged from 30.4 to 45.4  $\mu\text{mol/mol}$ , while the mean Mn/Ca ratios from LA-ICP-MS on individual cleaned specimens ranged from 30.7 to 52.3  $\mu\text{mol/mol}$ . The direct comparison of Mn/Ca ratios (**Fig. 5.5c**) showed that both methods overlapped with the range of heterogeneity. A statistical comparison was not possible in these three cases (**Fig. 5.5**) since only one measurement from each sample was available for the bulk analyses in our data. The Mn/Ca ratios of bulk (crushed) foraminifera samples measured from Q-ICP-MS are shown in Appendix C as Supplementary Table ST2.

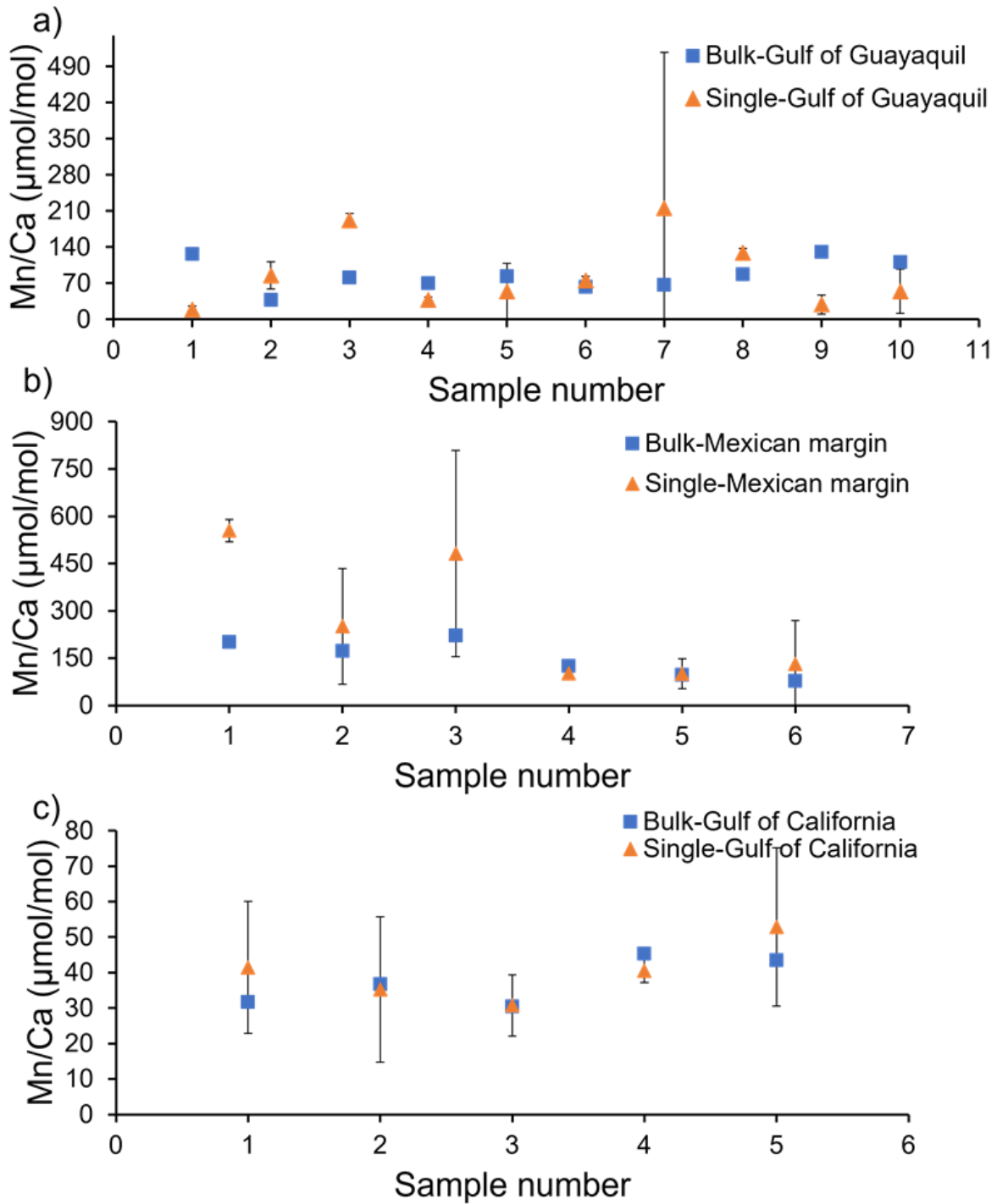


**Figure 5.5.** The Mn/Ca ratios of cleaned single specimens of *B. spissa* and *B. subadvena* and bulk Q-ICP-MS data from a) the Gulf of Guayaquil b) the Mexican margin, and c) the Gulf of California. The error bars show heterogeneity (2SD).

### 5.3.3 Trends in laser ablation-derived Mn/Ca ratios in the studied ODZs

**a) Sea of Okhotsk (MD01-2415):** Due to the lower number of specimens in our fractionated sample depths, only three sample depths (total number of ablations = 47, specimens = 16) were taken from the Sea of Okhotsk for Mn/Ca analysis. The chosen specimens from the Sea of Okhotsk core covered the time period spanning the Younger Dryas, YD (12.81 ka BP) until the Early Holocene, EH (9.83 ka BP). Overall, the Mn/Ca determined using LA-ICP-MS varied between 1288.3 to 6188.8  $\mu\text{mol/mol}$ , and displayed a decreasing trend in the downcore (**Fig. 5.6a**).

**b) Gulf of California (DSDP-480):** A total of 124 laser ablation measurements were done on 43 specimens of *B. subadvena* for the Mn/Ca analysis. The chosen specimens cover the time period spanning the Last Glacial Maximum, LGM (23.12 ka BP) until the EH (10.84 ka BP). The Mn/Ca values of *B. spissa* from the Gulf of California range from 50.1 to 75.6  $\mu\text{mol/mol}$ . The Mn/Ca followed a stable trend of low Mn/Ca values from the glacial period until the EH in our results, except one single data point (**Fig. 5.6b**).

**c) Mexican Margin (MAZ-1E-04):** A total of 181 laser ablations were done on 59 specimens of *B. spissa* for the Mn/Ca analysis. The chosen specimens cover the time period spanning the glacial period (20.58 ka BP) until the EH (11.08 ka BP). The Mn/Ca values of *B. spissa* collected from the Mexican Margin range from 97.3 to 538.5  $\mu\text{mol/mol}$ . The Mn/Ca data showed an increasing trend from the glacial period until the YD, and then dropped and thereafter increased (**Fig. 5.6c**).

**d) Gulf of Guayaquil (M77/2-59-01):** A total of 296 laser ablations were done on 121 specimens of *B. spissa* for the Mn/Ca analysis. The chosen specimens covered the late glacial period (18.01 ka BP) until the late Holocene, LH (1.99 ka BP). The Mn/Ca values ranged from 30.5 to 131  $\mu\text{mol/mol}$ . In general, overall Mn/Ca data showed a decreasing trend from the glacial period to the Holocene (**Fig. 5.6d**). The Mn/Ca values were high during the late glacial period and then it dropped during the Heinrich Stadial 1 (H1) and reached a peak during the Bolling-Allerod (BA) event, with lots of variations in the data. During the YD, Mn/Ca values was comparatively lower, and it increased in the EH, but decreased towards the MLH with variations in the data. The laser-ablation derived mean Mn/Ca from all locations are shown in Appendix C as supplementary table ST3.

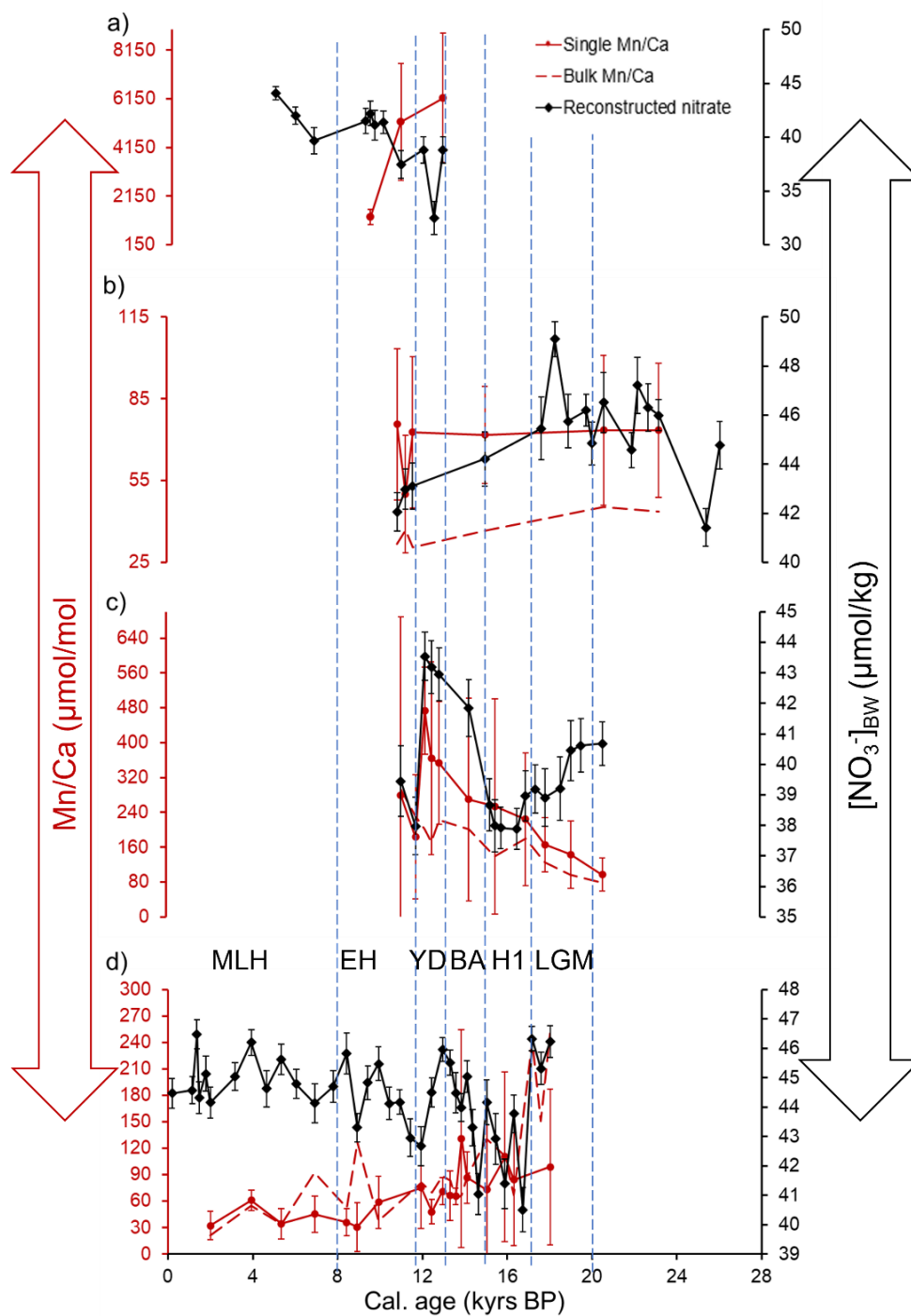


**Figure 5.6.** The Mn/Ca of benthic foraminiferal specimens *B. spissa* and *B. subadvena* from the a) Sea of Okhotsk b) Gulf of California c) Mexican margin and d) the Gulf of Guayaquil over the last 20,000 years ago. The red lines represent the average Mn/Ca ratios from single foraminiferal specimens using LA-ICP-MS. The dashed red lines represent the bulk Mn/Ca ratios, except for the Sea of Okhotsk. The bulk Mn/Ca was not measured for the Sea of Okhotsk core, due to lack of *B. spissa* specimens. The black lines represent the reconstructed [NO<sub>3</sub><sup>-</sup>]<sub>BW</sub> data using the pore density of *B. spissa* and *B. subadvena* from the same study sites as in Chapter 4. Error bars represent 1SD.

## 5.4 Discussion

Benthic foraminiferal Mn/Ca are a valuable proxy for redox conditions in the bottom- and pore waters (McKay et al., 2015). The incorporation of trace elements such as Mn into the benthic foraminiferal carbonate tests is governed by physical and chemical conditions of the surrounding environment (Reichert et al., 2003). However, the ecology of foraminiferal species and their growth rate (Koho et al., 2017), and the supply of Mn are crucial factors, as well. Porewater Mn is the dominant factor controlling Mn incorporation and thus organic matter fluxes and oxygen concentration and the depth habitat preferences (**Fig.5.1**) of foraminifera (Koho et al., 2015; Reichert et al., 2003) should be taken into account.

### 5.4.1 Laser ablation of single specimens

One highlight of the Mn/Ca results of laser ablated single specimens from all the four ODZs is that the southern core from the Gulf of Guayaquil shows the lowest Mn/Ca values, while the northern core from the Sea of Okhotsk shows the highest Mn/Ca values. In this section, the possible reasons for the low Mn/Ca values in Gulf of Guayaquil, and high Mn/Ca values in Sea of Okhotsk are discussed.

**a) Low Mn/Ca values in Gulf of Guayaquil:** In comparison with other studied locations, the Mn/Ca values of laser ablated single specimens from the Gulf of Guayaquil was lower. The Gulf of Guayaquil intersects the highly productive Peruvian coastal upwelling (Pennington et al., 2006) with an extensive anoxic continental shelf. Lateral transport of material from the continental margin can bring trace metals such as Mn into the ocean (Lam et al., 2006; Tagliabue et al., 2017). Determination of the dissolved Mn distribution in the Peruvian OMZ revealed that the dissolved Mn was depleted under the most reducing conditions, and subsurface Mn maxima were observed within the oxycline (Vedamati et al., 2015). Although the subsurface Mn maxima can be influenced by redox processes, their study concluded that the distribution of dissolved manganese on the Peruvian shelf is dominated by non-redox processes, and suggested mainly atmospheric Mn sources. A study on dissolved Mn in the tropical and equatorial Pacific (Chen and Wu, 2019) also suggested the possibility of atmospheric deposition and photo-chemical reduction as sources of Mn. A study on bulk aerosol samples (Baker et al., 2016) from the Peruvian coast observed low input of Mn from the aerosols into the ocean. Therefore, it is possible that the low Mn/Ca we found in the foraminiferal calcite (**Fig. 5.6d**) could be related to the low input of Mn from the atmosphere,

rivers and the continental shelf. Bolster et al. (2022) also suggested that the absence of large rivers at the Peruvian margin can be a major reason for the low Mn supply from the Peruvian shelf. Furthermore, the Mn concentration in the pore waters from the ODZ off Peru is known to be relatively low, too (Böning et al., 2004; Scholz et al., 2011; Glock et al., 2012b). This is because most of the Mn delivered to the ODZ is already reduced in the water column, leaving only small amounts of particle-bound Mn deposited on the seafloor (Böning et al., 2004; Scholz et al., 2011).

Another possible reason for the low Mn in the Gulf of Guayaquil could be related to seasonal variability and the uncertainty, when exactly the foraminifera calcified. However, without any concrete evidence to support this, it is speculative, and could be further investigated in the future.

**b) High Mn/Ca values in the Sea of Okhotsk:** The Sea of Okhotsk samples have strongly elevated Mn/Ca ratios (Fig. 5.6a) compared to the other sites studied (~100 times higher). Few studies and reports are made on the distribution of trace elements in the Sea of Okhotsk except for iron (Fe) (Nakaguchi et al., 2022). Shallow infaunal benthic foraminifera from the Bering Sea studied by Detlef et al. (2020) also found very high Mn/Ca using laser ablation, similar to our results. The high Mn/Ca values observed in the infaunal foraminifera from the Bering Sea were interpreted as to the presence of Mn-Fe-oxide coatings (Detlef et al., 2020). This may not be the case in our results, as we excluded the signal coming from outside of the test. Therefore, the possibility of surficial Mn contaminant coatings such as manganese carbonate or oxide influencing the data is low. Rather, we suspect that Mn-rich sources deliver Mn to the Sea of Okhotsk. High concentrations of dissolved Mn have been found in the Sea of Okhotsk at an intermediate water depth of 300 to 2000 m owing to the supply from continental sources via the Amur River and atmospheric deposition (Nakaguchi et al., 2022). Furthermore, it has been suggested that lateral transport of Mn by the intermediate waters of the Sea of Okhotsk can be an important source for the NPIW, revealing the Sea of Okhotsk itself as an important source of Mn to other water masses (Morton et al., 2019; Nakaguchi et al., 2022). This is because waters from the Sea of Okhotsk enter the North Pacific through the Kuril-Kamchatka Margin, mix with the waters from the Western Subarctic Gyre, and are transported south in the Oyashio Current (Morton et al., 2019). High inputs of Mn are also found along the Kuril-Kamchatka margin (Morton et al., 2019), which can be another possible source of Mn to the Sea of Okhotsk. The high concentrations of Mn found in the Sea of Okhotsk may be related to the extensive transport system, which is capable of advecting

margin-derived material along surface and intermediate water masses well beyond the immediate continental shelf (Morton et al., 2019). In addition, the high surface productivity between 700 and 1400 m water depth (Gorbarenko et al., 2014), results in enhanced remineralization of organic matter and poor ventilation at intermediate depths. Furthermore, the high Mn/Ca measured in *B. spissa* from the Sea of Okhotsk might suggest that *B. spissa* most likely grew under hypoxic bottom water conditions where pore water Mn concentrations are usually higher.

#### 5.4.2 Comparison of Mn/Ca ratios from Q-ICP-MS and LA-ICP-MS

The bulk Q-ICP-MS and LA-ICP-MS derived Mn/Ca ratios of cleaned foraminiferal specimens (Fig. 5.5) are comparable and of the same order of magnitude. Crushing of specimens prior to chemical cleaning increase the efficiency of cleaning in bulk samples (Glock et al., 2016). The comparable Mn/Ca ratios from both methods indicates that the cleaning procedure had the same effect on both LA-ICP-MS and Q-ICP-MS, and that the chemical cleaning sufficiently removes the contamination. Moreover, when sufficient foraminiferal specimens are not available (~20; Glock et al., 2016) for solution-based protocols like Q-ICP-MS, microanalytical technique upon single specimens such as laser ablation could be a valuable tool (McKay et al., 2015; Brinkmann et al., 2023).

Nardelli et al. (2014) showed that foraminifera can calcify even under anoxic conditions. For foraminiferal species, the calcification process starts with first chamber called the proloculus. All later chambers are constructed after this proloculus with each calcification event commonly covering all older chambers with a thin layer of calcite (Erez, 2003; Petersen et al., 2018). Thus, analysis of Mn/Ca from single specimens can provide the wide range of the redox conditions the foraminifera experienced in its lifetime.

The difference in Mn/Ca ratios in some samples in our data (Fig. 5.5) likely represent the variation between individual foraminiferal specimens and different parts of the shell. Some specimens might be calcified in different seasons or different microhabitats and one sample often covers hundreds of years. Thirumalai et al. (2013) have shown that paleo-reconstructions from individual foraminifera have multiple sources of uncertainty caused by either habitat or due to seasonal productivity. For example, ontogenetic (size-related) trends (Petersen et al., 2018) and biological effects (De Nooijer et al., 2014) can influence the element incorporation in foraminifera during

calcification. Environmental conditions, genetic differences between individuals can also cause inter and intra- specimen heterogeneity of foraminifera (De Nooijer et al., 2014; Burke et al., 2020). Therefore, it is possible that the variability observed in Mn/Ca ratios in some samples could be related to any of these above-mentioned factors. Future investigations should therefore consider experimental studies, which could be helpful in understanding the potential influence of different mechanisms in foraminiferal Mn/Ca signatures.

#### **5.4.3 Comparison of Mn/Ca ratios from cleaned and uncleaned specimens using LA-ICP-MS**

It is important to verify whether chemical cleaning procedures designed to remove contaminants made a difference in the elemental calcium ratio after laser ablation. Studies such as Cook and Hendy, (2024) support the use of a combination of physical and chemical cleaning methods for removing contaminants from foraminiferal tests prior to trace elemental analysis. Neither Mn/Ca ratios from the Gulf of Guayaquil, and the Mexican margin samples reveal a noticeable response to chemical cleaning (**Fig. 5.4a** and **b**). This suggests that regardless of the physical and chemical cleaning methods, the Mn/Ca data of *B. spissa* can be attained via laser ablation or solution protocols. Although our sample size is low, we don't expect a change in results with an increased sample size. Nevertheless, future studies could consider a higher sample size.

In contrary, the Mn/Ca ratios of samples from the Gulf of California reveals a clear distinction between cleaned and uncleaned specimens (**Fig. 5.4c**). One possible reason could be detrital contamination due to preservation of remnant organic material within interstitial spaces of the test (Glock et al., 2019b) or from post-depositional accumulation of particulate organic material on or in the test (Cook and Hendy, 2024). Samples collected from locations with high primary productivity, high sedimentation rates and low bottom-water oxygen like Gulf of California (<4.5  $\mu\text{mol/kg}$ ; Spiker & Simoneit, 1982) are more likely to have post-depositional, accumulated organic matter rich in trace elements in their tests (Cook and Hendy, 2024). This also indicates strong  $\text{O}_2$  depleted conditions in the Gulf of California, which could have led to the good preservation of organic matter. Since the effect of chemical cleaning with oxidative agents shown well in the Mn/Ca ratios in the cleaned samples from Gulf of California, this reiterates the strength of cleaning reactants to intrude deeply into the calcite (Glock et al., 2016), and removes a major amount of contamination.

#### 5.4.4 Variation in Mn/Ca over the past 20,000 years ago in the studied ODZs

The spatial and temporal variability of Mn/Ca ratios observed in the four ODZs (**Fig. 5.6**) suggests differences in redox conditions and local Mn sources. Nevertheless, the interpretation of the Mn/Ca data at these sites during the last deglaciation must be done with caution, as the lifespan of foraminifera (typically few months) is much less than the multiple millennia represented by the sediment samples.

**a) Mexican Margin:** The low Mn/Ca ratios at the Mexican margin observed during the glacial period (**Fig. 5.6c**) might suggest that the ODZ was deeper during the glacial period than today. Hence, less Mn reached the seafloor at this site. During the sea level low-stand of the LGM, the main areas of primary productivity likely shifted to offshore sites in the Mexican margin similar to what happened in the case of the Benguela upwelling system (Mollenhauer et al., 2002). That is, the glacial centers of deposition and production may have migrated offshore from the shallow shelf towards the continental slope relative to their Holocene positions (Mollenhauer et al., 2002). However, with the deglacial eustatic sea-level rise (Waelbroeck et al., 2008), the ODZ may have shifted to shallower depths, resulting in elevated Mn/Ca ratios similar to increased  $[\text{NO}_3^-]_{\text{BW}}$  as seen in our results (**Fig. 5.6c**). The generally higher Mn/Ca observed in the Mexican margin in comparison to the Gulf of Guayaquil (**Fig. 5.6**) might be related higher Mn input due to the presence of large rivers in this region such as the Rio Grande de Santiago (Bolster et al., 2022).

**b) Gulf of Guayaquil:** There are two possibilities under redox conditions that could lead to elevated Mn/Ca ratios. Firstly, under oxygenated conditions, there is no dissolved  $\text{Mn}^{2+}$  in the pore waters. But, when oxygen depletes,  $\text{Mn}^{2+}$  is formed and Mn/Ca ratios increase. This is unlikely to have happened at the Gulf of Guayaquil site, as most studies indicate higher oxygen concentrations during the glacial period (Erdem et al., 2020) at this site. The second possibility is the existence of lower than hypoxic oxygen concentrations, fostering low Mn/Ca, because most of the Mn is lost to the bottom waters. Then, when conditions became more oxygenated and shifted to hypoxia, this could lead to increased Mn/Ca ratios. The high Mn/Ca values observed in the tests of *B. spissa* during the glacial period (**Fig. 5.6d**) could indicate that hypoxic conditions ( $\text{O}_2 < 63 \mu\text{M}$ ) prevailed from 18 ka BP and continued until the mid BA (13.83 ka BP), due to the high concentrations of Mn in the pore waters, as Mn cannot escape to the overlying oxic bottom water. Thus, if benthic

foraminifera had calcified under hypoxic conditions, more Mn would have been incorporated into their calcite test, resulting in high Mn/Ca (McKay et al., 2015).

However, elevated Mn/Ca ratios in benthic foraminiferal tests are not just limited to remobilization of reduced  $\text{Mn}^{2+}$  in the porewaters but could also depend on the supply of Mn to the seafloor (Glock et al., 2016). In the case of modern Peruvian OMZ, Glock et al. (2012b), suggested that low supply of Mn could have resulted in low foraminiferal Mn/Ca.

The core M77/2-59-01 is located in a region which is under the influence of strong riverine input (Mollier-Vogel et al., 2013), and also high inputs of Mn from the atmosphere via dust (Maher et al., 2010). This might have enhanced the Mn input during the glacial period. Thereafter, the decline in Mn/Ca ratios during the late Bølling-Allerød event (13.56 ka BP) and stable ratios until the Middle to Late Holocene (Fig. 5.6d), suggests the possibility that suboxic conditions could have prevailed at the study site. Increasing bottom-water oxygenation was observed by Erdem et al. (2020) on the same core M77/2-59-01 which is in agreement with the other studies (Salvatteci et al., 2016; 2019) and Mollier-Vogel et al. (2019) in the ETSP. During the period where hypoxic conditions were recorded in the core M77/2-59-01 by Erdem et al. (2020), high Mn/Ca ratios were recorded in our data. The correlation of relatively stable and high  $[\text{NO}_3^-]_{\text{BW}}$  (Fig. 5.6d) during the Holocene with low Mn/Ca ratios suggests that bottom-waters were never severely oxygen depleted in the Gulf of Guayaquil. This could be due to a strong Walker circulation that brought oxygen-rich waters to intermediate depths, and low primary productivity (Salvatteci et al., 2019). Thus, we suspect that the Gulf of Guayaquil site could have experienced a transition from hypoxic conditions during the glacial period to suboxic conditions in the MLH.

**c) Gulf of California:** During the glacial period, primary productivity was lower at the Gulf of California (Chang et al., 2008, 2015), and dissolved oxygen concentrations were higher due to better ventilated North Pacific Intermediate Water (Herguera et al., 2010; Cartapanis et al., 2011). This has been reflected in our reconstructed  $[\text{NO}_3^-]_{\text{BW}}$  data (Fig. 5.6b). Although oxygen supply was high during the LGM in the Gulf of California, there exists strong  $\text{O}_2$ -depleted conditions in the bottom-water as evident from the good preservation of organic matter in the foraminiferal specimens. Thus, it is highly possible that the Gulf of California never reached hypoxic conditions. Rather, the  $[\text{O}_2]_{\text{BW}}$  were likely suboxic conditions during the LGM and it transitioned to anoxic  $[\text{O}_2]_{\text{BW}}$  conditions when primary productivity increased during the Early Holocene. This could be the reason why we observed relatively low Mn/Ca values at this site (Fig. 5.6b). Although this is

the case at the current study site, future studies should consider samples from the Northern Gulf of California to reconstruct the spatio-temporal patterns of the  $[O_2]_{BW}$  in the region.

**d) Sea of Okhotsk:** The high Mn/Ca ratios in Sea of Okhotsk especially during the Younger Dryas in our data (**Fig. 5.6a**) coincides with the period of high primary productivity ([Bubenshchikova et al., 2015](#)). However, with only three datapoints available due to insufficient *B. spissa* specimens, it is not appropriate to comment on the trend of redox conditions at this site for the time being. Therefore, a future study with suitable benthic foraminiferal specimens from the western part near the Amur River, and the eastern part near the Kamchatka margin should be considered.

## 5.5 Conclusion

Reconstructing the redox conditions in the ODZs can expand knowledge of the functioning of oceanic ecosystems, especially given the sensitivity of ODZs to rapidly changing climatic conditions. In addition, some of the ODZs are located in regions (e.g., Peru) that are economically important for the livelihood of the society.

In this study, different aspects related to the Mn/Ca ratios in *B. spissa* and *B. subadvena* are investigated: -

**a)** High Mn/Ca values are observed in the Sea of Okhotsk and low Mn/Ca values are observed in the Gulf of Guayaquil. This could be related to the supply of Mn from rivers, the atmosphere via dust and continental margins. The Amur River, and the Kamchatka margin are enriched sources of Mn, which may influence the foraminiferal Mn/Ca ratios in the Sea of Okhotsk. The low input of Mn from rivers and atmospheric deposition could be possible reasons for the low foraminiferal Mn/Ca values in the Gulf of Guayaquil.

**b)** Laser ablation foraminiferal Mn/Ca ratios of cleaned and uncleaned individual specimens show no difference between samples from the Gulf of Guayaquil and the Mexican Margin, indicating that chemical cleaning had no effect on the foraminiferal samples. However, samples from the Gulf of California show a clear difference in Mn/Ca ratios between cleaned and uncleaned specimens. This may be related to the preservation of organic matter during foraminiferal deposition, suggesting continuous, strongly oxygen-depleted conditions to the extent of anoxia in the Guaymas Basin.

c) The Mn/Ca data from both solution (bulk foraminifera) and laser ablation (individual foraminifera) based mass spectrometry are similar and comparable. Thus, the Mn/Ca ratios from individual foraminifera can be reliable for reconstructing redox conditions, when sufficient bulk foraminiferal samples are not available in the sediment cores.

d) It is not straightforward to interpret the spatial and temporal variations in redox conditions in the study sites during the last deglaciation. Several factors should be taken into account for the changes in redox conditions over time. Foraminiferal habitat preferences, ontogenetic trends, environmental conditions, and Mn supply can cause Mn/Ca variability even within the same foraminiferal species. Considering the good preservation of organic matter in the foraminiferal tests and the low foraminiferal Mn/Ca ratios, strong O<sub>2</sub> depletion to the extent of anoxia may have prevailed in the Gulf of California. In the case of the Mexican Margin, the deepening of the ODZ during glacial times compared to today may have resulted in less Mn reaching the sea floor or the leakage of soluble reduced Mn<sup>2+</sup> into the bottom water and thus low glacial Mn/Ca values. For the Gulf of Guayaquil, the high glacial Mn/Ca ratio and later a decline during the Holocene depicts a transition from glacial hypoxic conditions to Holocene suboxic conditions.

---

### **Data availability**

All data generated or analysed in this chapter are included in the Appendix C as supplementary tables.

### **Author contributions**

A.G.M wrote the core manuscript, did the sample preparation and chemical cleaning for the bulk and individual foraminiferal specimens, electron microscopy, and statistical analyses of all the samples. C. B facilitated the laser ablation of samples at University of Nantes, France, and the helped to process the ablation profiles using Glitter software at University of Nantes, and Angers, France. E. H facilitated the bulk measurement of samples at Geomar, Kiel. D.N. provided sampling material for cores MD01-2415 and M77/2-59-01, and provided access for chemical cleaning of samples at Geomar, Kiel. C.D. provided sampling material for core MAZ-1E-04. G.S. hosted the research group, and provided access to lab facilities at the University of Hamburg. N.G. planned the study design and sampling strategy.

### **Acknowledgements**

We are grateful to the micropaleontology group at the University of Hamburg. We acknowledge the help of lab engineer Miss Carole from University of Nantes for helping with the LA-ICP-MS. We thank Miss Nadine Gehre for the lab support in Geomar, Kiel, and Dr. Sha Ni for helping with the data processing. Funding was provided by the Deutsche Forschungsgemeinschaft (DFG) through both N.G.'s Heisenberg grant GL 999/3-1 and grant GL 999/4-1. Funding for the core MD01-2415 recovery was provided by the German Science Foundation (DFG) within project Ti240/11-1. We thank Yvon Balut, Agnes Baltzer, and the Shipboard Scientific Party of RV Marion Dufresne cruise WEPAMA 2001 for their kind support. We thank IODP for providing the sample for core DSDP-480. The recovery of core M77-59 recovery was a contribution of the German Science Foundation (DFG) Collaborative Research Project "Climate–Biogeochemistry interactions in the Tropical Ocean" (SFB 754). The study is a contribution to the Center for Earth System Research and Sustainability (CEN) of University of Hamburg.

## Chapter 6

### Conclusion

The application of automated image analysis using the deep learning algorithm provided a robust method for the determination of pore parameters such as the pore density, porosity and pore size in *B. spissa* and *B. subadvena*. Denitrifying bolivinids such as *B. spissa* and *B. subadvena* do not rely on the increase of total porosity, but rather on the number of pores (pore density) to enhance the electron acceptor ( $\text{NO}_3^-$ ) uptake. Therefore, the pore density of *B. spissa* and *B. subadvena* is a solid proxy for paleo  $[\text{NO}_3^-]_{\text{BW}}$  reconstruction. However, the different trends in pore patterns of *B. spissa* observed at different ODZs suggest that long-term environmental conditions or genetic factors could have a potential influence on the morphological differences, as the sediment cores cover periods of ~20,000 years.

The  $[\text{NO}_3^-]_{\text{BW}}$  in the ODZs of the Sea of Okhotsk, the Gulf of California, the Mexican Margin, and the Gulf of Guayaquil has been quantitatively reconstructed using the pore density as a  $\text{NO}_3^-$  proxy. This provided a comprehensive understanding about past  $[\text{NO}_3^-]_{\text{BW}}$  at these four ODZs in the Pacific and its marginal seas during the last deglaciation. The interpretation of the  $[\text{NO}_3^-]_{\text{BW}}$  records is highly complex, as differences associated with water-mass ventilation, oxygen solubility, water-column denitrification, primary productivity, and temperature differences can have an influence on  $[\text{NO}_3^-]_{\text{BW}}$ . The Gulf of Guayaquil and the Gulf of California shows elevated  $[\text{NO}_3^-]_{\text{BW}}$  during the glacial period compared to deglacial and modern conditions. The Sea of Okhotsk record didn't cover the LGM due to the lack of *B. spissa* during this time interval. Nevertheless, considering the highly ventilated intermediate water masses during the glacial cold period in the Sea of Okhotsk, it is indeed possible that the Sea of Okhotsk had elevated  $[\text{NO}_3^-]_{\text{BW}}$  due to reduced denitrification during the glacial period. The composition of the intermediate water masses has a potential influence on  $[\text{NO}_3^-]_{\text{BW}}$  in the Sea of Okhotsk, the Gulf of California and the Gulf of Guayaquil. However, for the deeper Mexican Margin core, high  $[\text{NO}_3^-]_{\text{BW}}$  found during the YD may be related to deglacial  $\text{NO}_3^-$  variability in the Pacific Deep Water. The low  $[\text{NO}_3^-]_{\text{BW}}$  in the Mexican Margin during the glacial period might be related to a deepening of the ODZ during the glacial period due to low sea level.

The reconstructed  $[\text{NO}_3^-]_{\text{BW}}$  has been compared with  $\delta^{15}\text{N}_{\text{bulk}}$  measurements from all cores except for the Mexican Margin. The benthic foraminiferal pore density represents the bottom water

conditions, while the  $\delta^{15}\text{N}_{\text{bulk}}$  record reconstructs processes in the (shallow) water column above. There may be coupling between these two records, but there are also differences. The discrepancies between the reconstructed  $[\text{NO}_3^-]_{\text{BW}}$  and the  $\delta^{15}\text{N}_{\text{bulk}}$  data in some time periods are probably related to the fact that  $\delta^{15}\text{N}$  can be influenced by various processes such as diagenesis, bacterial degradation, and terrestrial sources. For the Mexican Margin,  $[\text{NO}_3^-]_{\text{BW}}$  is compared with the planktic foraminiferal  $\delta^{15}\text{N}$  data, which is in agreement with reduced denitrification during the YD. Furthermore, the comparison of present and past  $[\text{NO}_3^-]_{\text{BW}}$  shows that the modern Gulf of Guayaquil and the Gulf of California have low  $[\text{NO}_3^-]_{\text{BW}}$  values, which may be associated with increased denitrification and a strengthening of the ODZ. In contrast, higher modern  $[\text{NO}_3^-]_{\text{BW}}$  was observed in the Sea of Okhotsk and the Mexican Margin, suggesting that these two regions have higher oxygen stability. It is unlikely that all the reasons for the observed changes in  $[\text{NO}_3^-]_{\text{BW}}$  can be unravelled, given that the pore density of denitrifying foraminifera is a relatively new proxy, applied at a higher spatial resolution for the first time in this PhD work.

The final part of the PhD investigates different aspects of Mn/Ca in *B. spissa* and *B. subadvena*. The highest Mn/Ca ratios are found in the Sea of Okhotsk and the lowest in the Gulf of Guayaquil. The Amur River and the Kamchatka margin are strong sources of Mn to the Sea of Okhotsk, which may be reflected in the foraminiferal Mn/Ca ratios. The low input of Mn from rivers and the atmosphere may have resulted in low Mn/Ca ratios in foraminiferal specimens from the Gulf of Guayaquil. Comparison of laser ablation Mn/Ca ratios of cleaned and uncleaned specimens shows no difference in Mn/Ca data, suggesting that the chemical cleaning had no effect on foraminiferal specimens from the Gulf of Guayaquil and the Mexican Margin. However, foraminiferal specimens of *B. subadvena* from the Gulf of California show a clear difference in laser ablation Mn/Ca ratios between cleaned and uncleaned specimens. This is likely related to the preservation of organic matter during foraminiferal deposition due to the strong  $\text{O}_2$  depletion at this site. The similarity in bulk and individual foraminiferal Mn/Ca ratios suggests the use of individual foraminiferal specimens to reconstruct redox conditions. This can be beneficial when sufficient bulk foraminiferal samples are not available in the sediment cores.

The spatial and temporal variations in redox conditions observed at the different ODZs during the last deglaciation can be related to foraminiferal microhabitat preferences, ontogenetic trends, environmental conditions, and Mn supply. The low Mn/Ca ratios observed at the Mexican Margin during the glacial period could be related to the deepening of the ODZ compared to today, resulting

in less Mn reaching the seafloor. For the Gulf of Guayaquil, the high Mn/Ca ratios during the glacial period and the subsequent decrease during the Holocene represent a transition from glacial hypoxic conditions to Holocene suboxic conditions. The stable but low Mn/Ca ratios observed for the Gulf of California from the glacial to early Holocene suggest strong O<sub>2</sub> depletion to the extent of anoxia. Today, this site has the lowest bottom water O<sub>2</sub> concentrations of all sites analysed. Further evidence of continuous O<sub>2</sub> depletion comes from the apparently good preservation of organic matter in the foraminiferal tests.

To conclude, the application of fully automated image recognition method enabled the creation of large datasets of pore parameters that resulted in the quantitative reconstruction of [NO<sub>3</sub><sup>-</sup>]<sub>BW</sub>. The pore density reconstructed [NO<sub>3</sub><sup>-</sup>]<sub>BW</sub> data provided a better understanding that different processes or factors can influence the nitrogen cycle in the ODZs. The [NO<sub>3</sub><sup>-</sup>]<sub>BW</sub> in general agrees with the sedimentary δ<sup>15</sup>N, though the disagreements in some time periods should be considered of serious scientific interest for future studies. The [NO<sub>3</sub><sup>-</sup>]<sub>BW</sub> in the studied ODZs could have been influenced by variations in redox conditions but the extent of this influence cannot be estimated from our results alone. Rather, this would require the calibration and application of more suitable proxies which does not fall under the scope of the current work.

## Chapter 7

### Limitations and implications for future research

The fully automated image recognition method provided a statistically robust dataset, and it is fast and efficient compared to manual pore counting methods. The foraminiferal specimens with flat surfaces such as *B. spissa* and *B. subadvena* work well with the automated image analysis methodology that has been developed within this thesis. However, special attention should be given to the processing of curved specimens of *B. spissa* and *B. subadvena*, as the curvature can make it difficult to count the exact number of pores and results in artefacts that make areas appear to be smaller than they are. This will need to be considered if similar studies in the future wish to use the current automated image recognition method. Nevertheless, training the deep learning algorithm in the software with specimens with curvature could help to improve the pore detection on specimens with strong curvature. This can be considered as a potential project for a bachelor's or master's student.

There is a lot of evidence that the pore density of infaunal species such as *B. spissa* and *B. subadvena* is useful as a nitrate proxy. However, the different pore patterns of individual foraminiferal specimens observed between different study sites in our study strongly suggest the use of a combined molecular morphometric approach. Future studies of foraminiferal pore patterns should consider both mean pore size and pore density to understand the factors controlling porosity in bolivinids, which may provide further insights into benthic denitrification. The presence of cryptic species within a morphogroup can complicate the paleoceanographic interpretation of pore density or porosity in benthic foraminifera. Therefore, future studies involving *Bolivina* species should consider phylogenetic analyses for better proxy validation.

Downcore  $\delta^{15}\text{N}$  can provide important insights into water column denitrification. However,  $\delta^{15}\text{N}_{\text{bulk}}$  records can be biased by various processes which can complicate the interpretation. Post-depositional bacteria driven degradation and terrestrial sources of organic and inorganic N, can notably influence the sedimentary organic nitrogen isotope signature, especially in locations near the coasts. Therefore, it is highly desirable to have a proxy that can record water column denitrification, without being affected by various processes or sources. Foraminifera-bound  $\delta^{15}\text{N}$  isotopes ( $\delta^{15}\text{N}_{\text{FB}}$ ) can provide information on the major nitrogen transformations occurring in the ocean. To achieve this, so far planktic foraminifera (Ren et al., 2012; Studer et al., 2021) are used.

Denitrifier method (Sigman et al., 2001) is used to measure  $\delta^{15}\text{N}_{\text{FB}}$ , and is based on the isotopic analysis of nitrous oxide ( $\text{N}_2\text{O}$ ) produced from  $\text{NO}_3^-$  by denitrifying bacteria that lack  $\text{N}_2\text{O}$ -reductase activity. This method can be used to conduct isotopic analysis of samples down to  $1\ \mu\text{M}$   $\text{NO}_3^-$ . However, very few laboratories in the world currently have the technical resources and trained personnel to carry out this method, making it inaccessible to many scientists and students. As part of an experimental trial (Appendix D), during the course of this PhD work  $\delta^{15}\text{N}_{\text{FB}}$  in benthic foraminifera, *B. spissa* is measured for the first time. However, the denitrifier method can be quite challenging for thin specimens like *B. spissa*. At least 300 - 500 specimens of *B. spissa* from one sample depth are required to achieve a minimum  $\delta^{15}\text{N}$  detection. This can be particularly difficult from sample depths with few specimens. Therefore, future studies could potentially consider larger specimens of *B. subadvena* and test its functionality with the denitrifier method.

Furthermore, the PhD work lacks sufficient benthic foraminiferal specimens of *B. spissa* from the Sea of Okhotsk. To have a better understanding of the  $[\text{NO}_3^-]_{\text{BW}}$  levels and redox conditions in the Sea of Okhotsk, a future study with more benthic foraminiferal samples is suggested. This can be a potential master's project. Collecting sediment cores from sites close to the Amur River basin and the Kamchatka margin could help to address the question of the extent to which the variations in the  $[\text{NO}_3^-]_{\text{BW}}$  levels in the Sea of Okhotsk and redox conditions are related. Given the sub-polar nature of the Sea of Okhotsk, further information on  $[\text{NO}_3^-]_{\text{BW}}$  and redox conditions will provide valuable information on the sensitivity of this region to past climate regimes.

Finally, the PhD work collected benthic foraminiferal specimens from four different ODZs in the Pacific. *Bolivina spissa* is present all around the Pacific. Extending the  $[\text{NO}_3^-]_{\text{BW}}$  reconstruction to other ODZs around the Pacific (e.g., Sagami Bay, Japan) would help to advance the knowledge of how these sensitive regions, and their benthic biodiversity behaved in the past climates, which may be effective in predicting future patterns of climate change. However, the absence of *B. spissa* in other ocean basins will make it difficult to extend the  $[\text{NO}_3^-]_{\text{BW}}$  reconstruction globally. Therefore, it would be of interest to identify and calibrate suitable foraminiferal species in the Atlantic or Indian Oceans to have a global  $[\text{NO}_3^-]_{\text{BW}}$  record.

### References

1. Ader, M., Thomazo, C., Sansjofre, P., Busigny, V., Papineau, D., Laffont, R., ... & Halverson, G. P. Interpretation of the nitrogen isotopic composition of Precambrian sedimentary rocks: Assumptions and perspectives. *Chemical Geology*, 429, 93-110 (2016).
2. Algeo, T. J., & Li, C. Redox classification and calibration of redox thresholds in sedimentary systems. *Geochimica et Cosmochimica Acta*, 287, 8-26 (2020).
3. Altabet, M. A., & Curry, W. B. Testing models of past ocean chemistry using foraminifera  $^{15}\text{N}/^{14}\text{N}$ . *Global Biogeochemical Cycles*, 3(2), 107-119 (1989).
4. Altabet, M. A., & Francois, R. Sedimentary nitrogen isotopic ratio as a recorder for surface ocean nitrate utilization. *Global biogeochemical cycles*, 8(1), 103-116 (1994).
5. Altabet, M. A., Pilskaln, C., Thunell, R., Pride, C., Sigman, D., Chavez, F., & Francois, R. The nitrogen isotope biogeochemistry of sinking particles from the margin of the Eastern North Pacific. *Deep Sea Research Part I: Oceanographic Research Papers*, 46(4), 655-679 (1999).
6. Altabet, M., Francois, R., Murray, D. et al. Climate-related variations in denitrification in the Arabian Sea from sediment  $^{15}\text{N}/^{14}\text{N}$  ratios. *Nature* 373, 506–509 (1995).
7. Alve, E. & Bernhard, J. M. Vertical migratory response of benthic foraminifera to controlled oxygen concentrations in an experimental mesocosm. *Mar. Ecol. Prog. Ser.* **116**, 137–152 (1995).
8. Arrigo, K. R. Marine microorganisms and global nutrient cycles. *Nature*, 437(7057), 349-355 (2005).
9. Auderset, A., Moretti, S., Taphorn, B., Ebner, P. R., Kast, E., Wang, X. T., ... & Martínez-García, A. Enhanced Ocean oxygenation during Cenozoic warm periods. *Nature*, 609(7925), 77-82 (2022).
10. Baker, A. R., Thomas, M., Bange, H. W. & Plasencia Sanchez, E. Soluble trace metals in aerosols over the tropical south-east Pacific offshore of Peru. *Biogeosciences* **13**, 817–825 (2016).
11. Barker, S., Greaves, M., & Elderfield, H. (2003). A study of cleaning procedures used for foraminiferal Mg/Ca paleothermometry. *Geochemistry, Geophysics, Geosystems*, 4(9) (2003).

12. Barras, C. *et al.* Experimental calibration of manganese incorporation in foraminiferal calcite. *Geochim. Cosmochim. Acta* **237**, 49–64 (2018).
13. Bé, A. W. H. Shell Porosity of Recent Planktonic Foraminifera as a Climatic Index. *Science*, 161(3844), 881 (1968).
14. Bé, A. W. H., Harrison, S. M., & Lott, L. *Orbulina universa* d'Orbigny in the Indian Ocean. *Micropaleontology*, 19(2), 150–192 (1973).
15. Benson, L., Lund, S., Negrini, R., Linsley, B., & Zic, M. Response of north American Great basin lakes to Dansgaard–Oeschger oscillations. *Quaternary Science Reviews*, 22(21-22), 2239-2251 (2003).
16. Bernhard, J. M., Edgcomb, V. P., Casciotti, K. L., McIlvin, M. R., & Beudoin, D. J. Denitrification likely catalyzed by endobionts in an allogromiid foraminifer. *The ISME journal*, 6(5), 951-960 (2012a).
17. Bernhard, J. *et al.* Potential importance of physiologically diverse benthic foraminifera in sedimentary nitrate storage and respiration. *J. Geophys. Res.* 117 (2012b).
18. Bijma, J., Faber, W. W., & Hemleben, C. Temperature and salinity limits for growth and survival of some planktonic foraminifers in laboratory cultures. *Journal of foraminiferal research*, 20(2), 95-116 (1990).
19. Bohlen, L., Dale, A. W., & Wallmann, K.. Simple transfer functions for calculating benthic fixed nitrogen losses and C: N: P regeneration ratios in global biogeochemical models. *Global biogeochemical cycles*, 26(3) (2012).
20. Bolster, K. M., Heller, M. I., Mulholland, M. R. & Moffett, J. W. Iron and manganese accumulation within the Eastern Tropical North Pacific oxygen deficient zone. *Geochim. Cosmochim. Acta* **334**, 259–272 (2022).
21. Böning, P., Brumsack, H. J., Böttcher, M. E., Schnetger, B., Kriete, C., Kallmeyer, J., & Borchers, S. L.. Geochemistry of Peruvian near-surface sediments. *Geochimica et cosmochimica acta*, 68(21), 4429-4451 (2004).
22. Brandes, J. A., & Devol, A. H. A global marine-fixed nitrogen isotopic budget: Implications for Holocene nitrogen cycling. *Global biogeochemical cycles*, 16(4), 67-1 (2002).
23. Brandes, J.A., Devol, A.H., Yoshinari, T., Jayakumar, D.A., Naqvi, W.A. Isotopic composition of nitrate in the central Arabian Sea and eastern tropical North Pacific: a tracer for mixing and nitrogen cycles. *Limnol. Oceanogr.* 43, 1680–1689 (1998).

24. Bray, N. A. Thermohaline circulation in the Gulf of California. *Journal of Geophysical Research: Oceans*, 93(C5), 4993-5020 (1988).
25. Bray, N. A. Water mass formation in the Gulf of California. *Journal of Geophysical Research: Oceans*, 93(C8), 9223-9240 (1988).
26. Breitburg, D., Levin, L. A., Oschlies, A., Grégoire, M., Chavez, F. P., Conley, D. J., & Zhang, J. Declining oxygen in the global ocean and coastal waters. *Science*, 359(6371), eaam7240 (2018).
27. Brinkmann, I., Barras, C., Jilbert, T., Paul, K. M., Somogyi, A., Ni, S., ... & Filipsson, H. L. Benthic Foraminiferal Mn/Ca as Low-Oxygen Proxy in Fjord Sediments. *Global Biogeochemical Cycles*, 37(5), e2023GB007690 (2023).
28. Broecker, W. S., Peteet, D. M., & Rind, D. Does the ocean-atmosphere system have more than one stable mode of operation? *Nature*, 315(6014), 21-26 (1985).
29. Bubenshchikova, N., Nürnberg, D., & Tiedemann, R. Variations of Okhotsk Sea oxygen minimum zone: Comparison of foraminiferal and sedimentological records for latest MIS 12–11c and latest MIS 2–1. *Marine Micropaleontology*, 121, 52-69 (2015).
30. Burdige, D. J. The biogeochemistry of manganese and iron reduction in marine sediments. *Earth-Science Reviews*, 35(3), 249-284 (1993).
31. Burdige, D. J., & Gieskes, J. M. A pore water/solid phase diagenetic model for manganese in marine sediments. *American Journal of Science*, 283(1), 29-47 (1983).
32. Burke, A., & Robinson, L. F. The Southern Ocean's role in carbon exchange during the last deglaciation. *science*, 335(6068), 557-561 (2012).
33. Burke, J. E., Renema, W., Schiebel, R., & Hull, P. M.. Three-dimensional analysis of inter-and intraspecific variation in ontogenetic growth trajectories of planktonic foraminifera. *Marine Micropaleontology*, 155, 101794 (2020).
34. Butzin, M., Heaton, T. J., Köhler, P., & Lohmann, G. A short note on marine reservoir age simulations used in IntCal20. *Radiocarbon*, 62(4), 865-871 (2020).
35. Calvert, S. E. & Pedersen, T. F. Geochemistry of Recent oxic and anoxic marine sediments: Implications for the geological record. *Mar. Geol.* **113**, 67–88 (1993).
36. Calvert, S. E. Origin of diatom-rich, varved sediments from the Gulf of California. *The Journal of Geology*, 74(5, Part 1), 546-565 (1966).

37. Campbell, A. C., Gieskes, J. M., Lupton, J. E., & Lonsdale, P. F. Manganese geochemistry in the Guaymas Basin, Gulf of California. *Geochimica et Cosmochimica Acta*, 52(2), 345-357 (1988).
38. Canfield, D. E., Glazer, A. N. & Falkowski, P. G. The evolution and future of earth's nitrogen cycle. *Science (80-.)*. **330**, 192–196 (2010).
39. Cardich, J. et al. Calcareous benthic foraminifera from the upper central Peruvian margin: control of the assemblage by pore water redox and sedimentary organic matter. *Mar. Ecol. Prog. Ser.* 535, 63–87 (2015).
40. Cartapanis, O., Tachikawa, K., & Bard, E. Northeastern Pacific oxygen minimum zone variability over the past 70 kyr: Impact of biological production and oceanic ventilation. *Paleoceanography*, 26(4) (2011).
41. Casciotti, K. L. Inverse kinetic isotope fractionation during bacterial nitrite oxidation. *Geochimica et Cosmochimica Acta*, 73(7), 2061-2076 (2009).
42. Casciotti, K. L. Nitrogen and oxygen isotopic studies of the marine nitrogen cycle. *Annual review of marine science*, 8(1), 379-407 (2016a).
43. Casciotti, K. L. Nitrite isotopes as tracers of marine N cycle processes. *Philos. Trans. R. Soc. A* 374:20150295 (2016b).
44. Casciotti, K. L., Buchwald, C., & McIlvin, M. Implications of nitrate and nitrite isotopic measurements for the mechanisms of nitrogen cycling in the Peru oxygen deficient zone. *Deep Sea Research Part I: Oceanographic Research Papers*, 80, 78-93 (2013).
45. Casciotti, K. L., Marshall, T. A., Fawcett, S. E., & Knapp, A. N. Advances in understanding the marine nitrogen cycle in the GEOTRACES era. *Oceanography*, 37(2) (2024).
46. Chang, A. S., Pedersen, T. F., & Hendy, I. L. Effects of productivity, glaciation, and ventilation on late Quaternary sedimentary redox and trace element accumulation on the Vancouver Island margin, western Canada. *Paleoceanography*, 29(7), 730–746 (2014).
47. Chang, A. S., Pedersen, T. F., & Hendy, I. L. Late Quaternary paleoproductivity history on the Vancouver Island margin, western Canada: a multiproxy geochemical study. This article is one of a series of papers published in this Special Issue on the theme Polar Climate Stability Network. *Canadian Journal of Earth Sciences*, 45(11), 1283-1297 (2008).

48. Chang, A. S., Pichevin, L., Pedersen, T. F., Gray, V., & Ganeshram, R. New insights into productivity and redox-controlled trace element (Ag, Cd, Re, and Mo) accumulation in a 55 kyr long sediment record from Guaymas Basin, Gulf of California. *Paleoceanography*, 30(2), 77-94 (2015).
49. Chazen, C.R., Altabet, M.A., Herbert, T.D.,. Abrupt mid-holocene onset of centennial-scale climate variability on the Peru-Chile margin. *Geophys. Res. Lett.* 36 (2009).
50. Chen, C. T. A., Andreev, A., Kim, K. R., & Yamamoto, M. Roles of continental shelves and marginal seas in the biogeochemical cycles of the North Pacific Ocean. *Journal of Oceanography*, 60, 17-44 (2004).
51. Chen, G. & Wu, J. Meridional distribution of dissolved manganese in the tropical and equatorial pacific. *Geochim. Cosmochim. Acta* **263**, 50–67 (2019).
52. Cheshire, H., & Thurow, J. High-resolution migration history of the Subtropical High/Trade Wind system of the northeastern Pacific during the last~ 55 years: Implications for glacial atmospheric reorganization. *Paleoceanography*, 28(2), 319-333 (2013).
53. Christensen, J. P., Murray, J. W., Devol, A. H., and Codispoti, L. A. Denitrification in continental shelf sediments has major impact on the oceanic nitrogen budget. *Global Biogeochem. Cycles* 1, 97–116 (1987).
54. Clark, P. U., & Mix, A. C. Ice sheets and sea level of the Last Glacial Maximum. *Quaternary Science Reviews*, 21(1-3), 1-7 (2002).
55. Clark, P., Pisias, N., Stocker, T. *et al.* The role of the thermohaline circulation in abrupt climate change. *Nature* 415, 863–869 (2002).
56. Cline, J. D., & Kaplan, I. R. Isotopic fractionation of dissolved nitrate during denitrification in the eastern tropical North Pacific Ocean. *Marine Chemistry*, 3(4), 271-299 (1975).
57. Codispoti, L. A. *et al.* The oceanic fixed nitrogen and nitrous oxide budgets: Moving targets as we enter the anthropocene? *Sci. Mar.* **65**, 85–105 (2001).
58. Codispoti, L. A. Is the ocean losing nitrate? *Nature*, 376(6543) (1995).
59. Codispoti, L. A., Barber, R. T., & Friederich, G. E. Do nitrogen transformations in the poleward undercurrent off Peru and Chile have a globally significant influence? *Poleward Flows Along Eastern Ocean Boundaries*, 34, 281-314 (1989).

60. Codispoti, L.A. Phosphorus vs nitrogen limitation of new and export production. In: Berger, W.H., Smetacek, V.S., Wefer, G. (Eds.), *Productivity of the Ocean: Present and Past*. Jhon Wiley, New York, pp. 377–394 (1989).
61. Cohmap Members. Climatic changes of the last 18,000 years: observations and model simulations. *Science*, 241(4869), 1043-1052 (1988).
62. Constandache, M., Yerly, F. & Spezzaferri, S. Internal pore measurements on macroperforate planktonic Foraminifera as an alternative morphometric approach. *Swiss J. Geosci.* **106**, 179–186 (2013).
63. Cook, M. K., & Hendy, I. L. Using element/Ca response to cleaning in foraminifera from endmember depositional environments to infer contaminants and inform pretreatment. *Geochemistry, Geophysics, Geosystems*, 25(2), e2023GC010885 (2024).
64. Cushman, J. A. Foraminifera of the typical Monterey of California. *Contributions from the Cushman Laboratory for Foraminiferal Research*, 2(30), 53-69 (1926).
65. Dale, A. W., Sommer, S., Lomnitz, U., Bourbonnais, A. & Wallmann, K. Biological nitrate transport in sediments on the Peruvian margin mitigates benthic sulfide emissions and drives pelagic N loss during stagnation events. *Deep. Res. Part I Oceanogr. Res. Pap.* **112**, 123–136 (2016).
66. Davis, C. V., Ontiveros-Cuadras, J. F., Benitez-Nelson, C., Schmittner, A., Tappa, E. J., Osborne, E., & Thunell, R. C. Ongoing increase in Eastern Tropical North Pacific denitrification as interpreted through the Santa Barbara Basin sedimentary  $\delta^{15}\text{N}$  record. *Paleoceanography and Paleoclimatology*, 34(9), 1554-1567 (2019).
67. De Lange, G. J. Early diagenetic reactions in interbedded pelagic and turbiditic sediments in the Nares Abyssal Plain (western North Atlantic): Consequences for the composition of sediment and interstitial water. *Geochimica et Cosmochimica Acta*, 50(12), 2543-2561(1986).
68. De Lange, G. J., Middelburg, J. J., Poorter, R. P., & Shofiyah, S. Ferromanganese encrustations on the seabed west of Misool, eastern Indonesia. *Netherlands journal of sea research*, 24(4), 541-553 (1989).
69. De Nooijer, L. J., Hathorne, E. C., Reichart, G. J., Langer, G. & Bijma, J. Variability in calcitic Mg/Ca and Sr/Ca ratios in clones of the benthic foraminifer *Ammonia tepida*. *Mar. Micropaleontol.* **107**, 32–43 (2014).

70. Debenay, J. -P. (Ed.): A Guide to 1,000 Foraminifera from Southwestern Pacific New Caledonia, IRD Éditions, Publications scientifiques du Muséum, Muséum national d'Histoire naturelle, Paris, France, 384 pp., ISBN 978-2-7099-1729-2 (2012).
71. Detlef, H., Sosdian, S. M., Kender, S., Lear, C. H. & Hall, I. R. Multi-elemental composition of authigenic carbonates in benthic foraminifera from the eastern Bering Sea continental margin (International Ocean Discovery Program Site U1343). *Geochim. Cosmochim. Acta* **268**, 1–21 (2020).
72. Deutsch, C., N. Gruber, R. M. Key, J. L. Sarmiento, and A. Ganaschaud, Denitrification and N<sub>2</sub> fixation in the Pacific Ocean, *Global Biogeochem. Cycles*, 15(2), 483–506 (2001).
73. Deutsch, C., Sarmiento, J. L., Sigman, D. M., Gruber, N., & Dunne, J. P.. Spatial coupling of nitrogen inputs and losses in the ocean. *Nature*, 445(7124), 163-167 (2007).
74. Deutsch, C., Sigman, D.M., Thunell, R. C., Meckler, A. N., and Haug, G. H. Isotopic constraints on glacial/interglacial changes in the oceanic nitrogen budget. *Global Biogeochemical Cycles*, 18(4) (2004).
75. Devol, A. H., & Hartnett, H. E. Role of the oxygen-deficient zone in transfer of organic carbon to the deep ocean. *Limnology and Oceanography*, 46(7), 1684-1690 (2001).
76. Devol, A. H., Uhlenhopp, A. G., Naqvi, S. W. A., Brandes, J. A., Jayakumar, D. A., Naik, H. & Yoshinari, T. Denitrification rates and excess nitrogen gas concentrations in the Arabian Sea oxygen deficient zone. *Deep Sea Research Part I: Oceanographic Research Papers*, 53(9), 1533-1547 (2006).
77. DeVries, T., Deutsch, C., Rafter, P. A., & Primeau, F.. Marine denitrification rates determined from a global 3-D inverse model. *Biogeosciences*, 10(4), 2481-2496 (2013).
78. Dubois, N., Kienast, M., Kienast, S. S., & Timmermann, A. Millennial-scale Atlantic/East Pacific Sea surface temperature linkages during the last 100,000 years. *Earth and Planetary Science Letters*, 396, 134–142 (2014).
79. Dubois, N., Kienast, M., Kienast, S., Normandeau, C., Calvert, S. E., Herbert, T. D., & Mix, A. Millennial-scale variations in hydrography and biogeochemistry in the Eastern Equatorial Pacific over the last 100 kyr. *Quaternary Science Reviews*, 30(1–2), 210–223 (2011).

80. Duplessy, J. C., Shackleton, N. J., Fairbanks, R. G., Labeyrie, L., Oppo, D., & Kallel, N. Deepwater source variations during the last climatic cycle and their impact on the global deepwater circulation. *Paleoceanography*, 3(3), 343-360 (1988).
81. Emmer, E., & Thunell, R. C. Nitrogen isotope variations in Santa Barbara Basin sediments: Implications for denitrification in the eastern tropical North Pacific during the last 50,000 years. *Paleoceanography*, 15(4), 377-387 (2000).
82. Erdem, Z., Schönfeld, J., Rathburn, A. E., Pérez, M. E., Cardich, J., & Glock, N. Bottom-water deoxygenation at the Peruvian margin during the last deglaciation recorded by benthic foraminifera. *Biogeosciences*, 17(12), 3165-3182 (2020).
83. Erez, J. The source of ions for biomineralization in foraminifera and their implications for paleoceanographic proxies. *Reviews in mineralogy and geochemistry*, 54(1), 115-149 (2003).
84. Erisman, J. W., Sutton, M. A., Galloway, J., Klimont, Z., & Winiwarter, W. How a century of ammonia synthesis changed the world. *Nature geoscience*, 1(10), 636-639 (2008).
85. Eugster, O., & Gruber, N. A probabilistic estimate of global marine N-fixation and denitrification. *Global Biogeochemical Cycles*, 26(4) (2012).
86. Eugster, O., Gruber, N., Deutsch, C., Jaccard, S. L., and Payne, M. R. The dynamics of the marine nitrogen cycle across the last deglaciation. *Paleoceanography* 28, 116–129 (2013).
87. Evans, N., Tichota, J., Ruef, W., Moffett, J., & Devol, A. Rapid Expansion of Fixed Nitrogen Deficit in the Eastern Pacific Ocean Revealed by 50-Year Time Series. *Global Biogeochemical Cycles*, 37(10), e2022GB007575 (2023).
88. Falkowski, P. G., & Godfrey, L. V. Electrons, life and the evolution of Earth's oxygen cycle. *Philosophical Transactions of the Royal Society B: Biological Sciences*, 363(1504), 2705-2716 (2008).
89. Finney, B. P., Lyle, M. W., & Heath, G. R. Sedimentation at MANOP Site H (eastern equatorial Pacific) over the past 400,000 years: climatically induced redox variations and their effects on transition metal cycling. *Paleoceanography*, 3(2), 169-189 (1988).
90. Fitzwater, S.E., Coale, K.H., Gordon, R.M., Johnson, K.S., Ondrusek, M.E. Iron deficiency and phytoplankton growth in the equatorial Pacific. *Deep-Sea Research II* 43, 995e1015 (1996).

91. Fontanier, C. *et al.* Living (stained) deep-sea foraminifera off hachinohe (NE Japan, western Pacific): Environmental interplay in oxygen-depleted ecosystems. *J. Foraminifer. Res.* **44**, 281–299 (2014).
92. Fowler, D., Coyle, M., Skiba, U., Sutton, M. A., Cape, J. N., Reis, S., & Voss, M. The global nitrogen cycle in the twenty-first century. *Philosophical Transactions of the Royal Society B: Biological Sciences*, *368*(1621), 20130164 (2013).
93. Frerichs, W. E., Heiman, M. E., Borgman, L. E., & Be, A. W. Latitudinal variations in planktonic foraminiferal test porosity; Part 1, Optical studies. *The Journal of Foraminiferal Research*, *2*(1), 6-13 (1972).
94. Frerichs, W. E. & Ely, R. L. Test porosity as a paleoenvironmental tool in the Late Cretaceous of the Western Interior. *Rocky Mountain Geology*, *16* (2), 89–94 (1978).
95. Froelich, P. N. *et al.* Early oxidation of organic matter in pelagic sediments of the eastern equatorial Atlantic: suboxic diagenesis. *Geochim. Cosmochim. Acta* **43**, 1075–1090 (1979).
96. Frölicher, T. L., Ashwanden, M. T., Gruber, N., Jaccard, S. L., Dunne, J. P., & Paynter, D. Contrasting upper and deep ocean oxygen response to protracted global warming. *Global biogeochemical cycles*, *34*(8), e2020GB006601 (2020).
97. Fry, B. *Stable isotope ecology* (Vol. 521). New York: Springer (2006).
98. Fu, W., Primeau, F., Keith Moore, J., Lindsay, K., & Randerson, J. T. Reversal of increasing tropical ocean hypoxia trends with sustained climate warming. *Global Biogeochemical Cycles*, *32*(4), 551-564 (2018).
99. Galbraith, E. D., Kienast, M., Pedersen, T. F., & Calvert, S. E. Glacial-interglacial modulation of the marine nitrogen cycle by high-latitude O<sub>2</sub> supply to the global thermocline. *Paleoceanography*, *19*(4) (2004).
100. Galloway, J. N., Aber, J. D., Erisman, J. W., Seitzinger, S. P., Howarth, R. W., Cowling, E. B., & Cosby, B. J. The nitrogen cascade. *Bioscience*, *53*(4), 341-356 (2003).
101. Galloway, J. N., Dentener, F. J., Capone, D. G., Boyer, E. W., Howarth, R. W., Seitzinger, S. P., ... & Vöosmarty, C. J. Nitrogen cycles: past, present, and future. *Biogeochemistry*, *70*, 153-226 (2004).
102. Galloway, J. N., Townsend, A. R., Erisman, J. W., Bekunda, M., Cai, Z., Freney, J. R., & Sutton, M. A. Transformation of the nitrogen cycle: recent trends, questions, and potential solutions. *Science*, *320*(5878), 889-892 (2008).

103. Ganeshram, R. S., & Pedersen, T. F. Glacial-interglacial variability in upwelling and bioproductivity off NW Mexico: Implications for quaternary paleoclimate. *Paleoceanography*, 13(6), 634-645 (1998).
104. Ganeshram, R. S., Pedersen, T. F., Calvert, S. E., & Murray, J. W. Large changes in oceanic nutrient inventories from glacial to interglacial periods. *Nature*, 376(6543), 755-758 (1995).
105. Ganeshram, R. S., Pedersen, T. F., Calvert, S. E., McNeill, G. W., & Fontugne, M. R. Glacial-interglacial variability in denitrification in the world's oceans: Causes and consequences. *Paleoceanography*, 15(4), 361-376 (2000).
106. Ganeshram, R. S., Pedersen, T. F., Calvert, S., & François, R. Reduced nitrogen fixation in the glacial ocean inferred from changes in marine nitrogen and phosphorus inventories. *Nature*, 415(6868), 156-159 (2002).
107. Garcia H.E., Boyer, T. P., Baranova, O. K., Locarnini, R.A., Mishonov, A.V., Grodsky, A., Paver, C.R., Weathers, K.W., Smolyar, I.V., Reagan, J.R., Seidov, M.M., Zweng, D., World Ocean Atlas 2018: Product Documentation. A. Mishonov, Technical Editor (2019).
108. Garcia, H. E., R. A. Locarnini, T. P. Boyer, and J. I. Antonov, World Ocean Atlas 2005, Dissolved Oxygen, Apparent Oxygen Utilization, and Oxygen Saturation, NOAA Atlas NESDIS 63, 342 pp., vol. 3, edited by S. Levitus, U.S. Gov. Print. Off., Washington, D. C. (2006).
109. Gary, A. C., Healy-Williams, N. & Ehrlich, R. Water-mass relationships and morphologic variability in the benthic foraminifer *Bolivina albatrossi* Cushman, northern Gulf of Mexico. *J. Foraminifer. Res.* **19**, 210–221 (1989).
110. Geslin, E., Heinz, P., Jorissen, F. & Hemleben, C. Migratory responses of deep-sea benthic foraminifera to variable oxygen conditions: Laboratory investigations. *Mar. Micropaleontol.* **53**, 227–243 (2004).
111. Glasby, G. P. Manganese: predominant role of nodules and crusts. In *Marine geochemistry* (pp. 371-427). Berlin, Heidelberg: Springer Berlin Heidelberg (2006).
112. Gleckler, P. J., Durack, P. J., Stouffer, R. J., Johnson, G. C., & Forest, C. E. Industrial-era global ocean heat uptake doubles in recent decades. *Nature Climate Change*, 6(4), 394-398 (2016).

113. Glock, N. Benthic foraminifera and gromiids from oxygen-depleted environments – survival strategies, biogeochemistry and trophic interactions. *Biogeosciences* **20**, 3423–3447 (2023).
114. Glock, N. *et al.* EMP and SIMS studies on Mn/Ca and Fe/Ca systematics in benthic foraminifera from the Peruvian OMZ: A contribution to the identification of potential redox proxies and the impact of cleaning protocols. *Biogeosciences* **9**, 341–359 (2012b).
115. Glock, N. *et al.* Environmental influences on the pore density of *Bolivina spissa* (Cushman). *J. Foraminifer. Res.* **41**, 22–32 (2011).
116. Glock, N. *et al.* Metabolic preference of nitrate over oxygen as an electron acceptor in foraminifera from the Peruvian oxygen minimum zone. *Proc. Natl. Acad. Sci. U. S. A.* **116**, 2860–2865 (2019a).
117. Glock, N. *et al.* The role of benthic foraminifera in the benthic nitrogen cycle of the Peruvian oxygen minimum zone. *Biogeosciences* **10**, 4767–4783 (2013).
118. Glock, N., Erdem, Z. & Schönfeld, J. The Peruvian oxygen minimum zone was similar in extent but weaker during the Last Glacial Maximum than Late Holocene. *Commun. Earth Environ.* **3**, 1–14 (2022).
119. Glock, N., Erdem, Z., Wallmann, K., Somes, C. J., Liebetrau, V., Schönfeld, J., ... & Eisenhauer, A. Coupling of oceanic carbon and nitrogen facilitates spatially resolved quantitative reconstruction of nitrate inventories. *Nature communications*, 9(1), 1217 (2018).
120. Glock, N., Liebetrau, V., Eisenhauer, A. & Rocholl, A. High resolution I/Ca ratios of benthic foraminifera from the Peruvian oxygen-minimum-zone: A SIMS derived assessment of a potential redox proxy. *Chem. Geol.* **447**, 40–53 (2016).
121. Glock, N., Liebetrau, V., Vogts, A., & Eisenhauer, A. Organic heterogeneities in foraminiferal calcite traced through the distribution of N, S, and I measured with nanoSIMS: a new challenge for element-ratio-based paleoproxies? *Frontiers in Earth Science*, 7, 175 (2019b).
122. Glock, N., Schoenfeld, J. & Mallon, J. The functionality of pores in benthic foraminifera in view of bottom water oxygenation; a review. *In Anoxia*, A. V. Altenbach, J. M. Bernhard, and J. Seckbach, eds. (Springer), 539–552 (2012a).
123. Goering, J. J. Denitrification in the oxygen minimum layer of the eastern tropical Pacific Ocean. *Deep. Res. Oceanogr. Abstr.* **15**, 157–164 (1968).

124. Goldstein, S. T. Foraminifera: A biological overview. *Mod. Foraminifera* 37–55 doi:10.1007/0-306-48104-9\_3 (1999).
125. Gooday, A. J. Benthic foraminifera (Protista) as tools in deep-water palaeoceanography: Environmental influences on faunal characteristics. *Advances in Marine Biology*, 46, 1–90 (2003).
126. Goodfriend, G. A., & Flessa, K. W. Radiocarbon reservoir ages in the Gulf of California: roles of upwelling and flow from the Colorado River. *Radiocarbon*, 39(2), 139-148 (1997).
127. Gorbarenko, S. A., Artemova, A. V., Goldberg, E. L., & Vasilenko, Y. P. The response of the Okhotsk Sea environment to the orbital-millennium global climate changes during the Last Glacial Maximum, deglaciation and Holocene. *Global and Planetary Change*, 116, 76-90 (2014).
128. Govindankutty Menon, A., Davis, C.V., Nürnberg, D. et al. A deep-learning automated image recognition method for measuring pore patterns in closely related bolivinids and calibration for quantitative nitrate paleo-reconstructions. *Sci Rep* 13, 19628 (2023).
129. Gray, W. R., Wills, R. C., Rae, J. W., Burke, A., Ivanovic, R. F., Roberts, W. H., ... & Valdes, P. J. Wind-driven evolution of the North Pacific subpolar gyre over the last deglaciation. *Geophysical Research Letters*, 47(6), e2019GL086328 (2020).
130. Groeneveld, J. & Filipsson, H. L. Mg/Ca and Mn/Ca ratios in benthic foraminifera: the potential to reconstruct past variations in temperature and hypoxia in shelf regions. *Biogeosciences* **10**, 5125–5138 (2013).
131. Groeneveld, J., Filipsson, H. L., Austin, W. E., Darling, K., McCarthy, D., Quintana Krupinski, N. B., ... & Schweizer, M. Assessing proxy signatures of temperature, salinity, and hypoxia in the Baltic Sea through foraminifera-based geochemistry and faunal assemblages. *Journal of Micropalaeontology*, 37(2), 403-429 (2018).
132. Gruber, N. The Dynamics of the Marine Nitrogen Cycle and its Influence on Atmospheric CO<sub>2</sub> Variations. *Ocean Carbon Cycle Clim.* 97–148 doi:10.1007/978-1-4020-2087-2\_4 (2004).
133. Gruber, N. The marine nitrogen cycle: overview and challenges. *Nitrogen in the marine environment*, 2, 1-50 (2008).
134. Gruber, N., & Galloway, J. N. An Earth-system perspective of the global nitrogen cycle. *Nature*, 451(7176), 293-296 (2008).

135. Gruber, N., & Sarmiento, J. L. Global patterns of marine nitrogen fixation and denitrification. *Global biogeochemical cycles*, 11(2), 235-266 (1997).
136. Guo, X., Wei, Q., Xu, B., Burnett, W. C., Bernhard, J. M., Nan, H., ... & Yu, Z. A benthic monitor for coastal water dissolved oxygen variation: Mn/Ca ratios in tests of an epifaunal foraminifer. *Journal of Geophysical Research: Oceans*, 126(12), e2021JC017860 (2021).
137. Guo, X., Xu, B., Burnett, W. C., Yu, Z., Yang, S., Huang, X., & Sun, F. A potential proxy for seasonal hypoxia: LA-ICP-MS Mn/Ca ratios in benthic foraminifera from the Yangtze River Estuary. *Geochimica et Cosmochimica Acta*, 245, 290-303 (2019).
138. Harman, R. A. Distribution of Foraminifera in the Santa Barbara Basin, California. *Micropaleontology* **10**, 81 (1964).
139. Hartnett, H. E., & Devol, A. H. Role of a strong oxygen-deficient zone in the preservation and degradation of organic matter: A carbon budget for the continental margins of northwest Mexico and Washington State. *Geochimica et Cosmochimica Acta*, 67(2), 247-264 (2003).
140. Haslett J, & Parnell AC. “A simple monotone process with application to radiocarbon-dated depth chronologies.” *Journal of the Royal Statistical Society: Series C (Applied Statistics)*, 57(4), 399–418 (2008).
141. Hayward, B. W., Holzmann, M., Grenfell, H. R., Pawlowski, J. & Triggs, C. M. Morphological distinction of molecular types in *Ammonia* - Towards a taxonomic revision of the world’s most commonly misidentified foraminifera. *Mar. Micropaleontol.* **50**, 237–271 (2004).
142. Heaton, T. J., Köhler, P., Butzin, M., Bard, E., Reimer, R. W., Austin, W. E., ... & Skinner, L. C. Marine20—the marine radiocarbon age calibration curve (0–55,000 cal BP). *Radiocarbon*, 62(4), 779-820 (2020).
143. Helly, J. J., & Levin, L. A. Global distribution of naturally occurring marine hypoxia on continental margins. *Deep Sea Research Part I: Oceanographic Research Papers*, 51(9), 1159-1168 (2004).
144. Helm, K. P., Bindoff, N. L., & Church, J. A. Observed decreases in oxygen content of the global ocean. *Geophysical Research Letters*, 38(23) (2011).

145. Hendy, I. L., Pedersen, T. F., Kennett, J. P., & Tada, R. Intermittent existence of a southern Californian upwelling cell during submillennial climate change of the last 60 kyr. *Paleoceanography*, 19(3) (2004).
146. Henry, R. B. C., Edmunds, M. G., & Köppen, J.. On the cosmic origins of carbon and nitrogen. *The Astrophysical Journal*, 541(2), 660 (2000).
147. Herguera, J. C., Herbert, T., Kashgarian, M., & Charles, C. Intermediate and deep-water mass distribution in the Pacific during the Last Glacial Maximum inferred from oxygen and carbon stable isotopes. *Quaternary Science Reviews*, 29(9-10), 1228-1245 (2010).
148. Hess, A. V., Auderset, A., Rosenthal, Y., Miller, K. G., Zhou, X., Sigman, D. M., & Martínez-García, A. A well-oxygenated eastern tropical Pacific during the warm Miocene. *Nature*, 619(7970), 521-525 (2023).
149. Høgslund, S., Revsbech, N. P., Cedhagen, T., Nielsen, L. P. & Gallardo, V. A. Denitrification, nitrate turnover, and aerobic respiration by benthic foraminiferans in the oxygen minimum zone off Chile. *J. Exp. Mar. Bio. Ecol.* 359(2), 85–91 (2008).
150. Holbourn, A., Kiefer, T., Pflaumann, U., & Rothe, S. WEPAMA Cruise MD 122/IMAGES VII, Rapp. *Campagnes Mer OCE/2002/01, Inst. Polaire Fr. Paul Emile Victor (IPEV), Plouzane, France* (2002).
151. Hoogakker, B., Davis, C., Wang, Y., Kusch, S., Nilsson-Kerr, K., Hardisty, D. & Zhou, Y.. Reviews and syntheses: Review of proxies for low-oxygen paleoceanographic reconstructions. *EGUsphere*, 2024, 1-154 (2024).
152. Hutchins, D. A., & Capone, D. G. The marine nitrogen cycle: new developments and global change. *Nature Reviews Microbiology*, 20(7), 401- 414, (2022).
153. IPCC. *Global warming of 1.5°C. An IPCC Special Report on the impacts of global warming of 1.5°C above pre-industrial levels and related global greenhouse gas emission pathways, in the context of strengthening the global response to the threat of climate change, sustainable development, and efforts to eradicate poverty* [V. Masson-Delmotte, P. Zhai, H. O. Pörtner, D. Roberts, J. Skea, P.R. Shukla, A. Pirani, W. Moufouma-Okia, C. Péan, R. Pidcock, S. Connors, J. B. R. Matthews, Y. Chen, X. Zhou, M. I. Gomis, E. Lonnoy, T. Maycock, M. Tignor, T. Waterfield (eds.)] (2018).
154. IPCC: *Climate Change 2007: The Physical Science Basis. Contribution of Working Group I to the Fourth Assessment Report of the Intergovernmental Panel on Climate Change* [Solomon, S., D. Qin, M. Manning, Z. Chen, M. Marquis, K.B. Averyt, M.

- Tignor and H.L. Miller (eds.)]. Cambridge University Press, Cambridge, United Kingdom and New York, NY, USA, 996 pp (2007).
155. Ito, M., Watanabe, Y. W., Shigemitsu, M., Tanaka, S. S., & Nishioka, J. Application of chemical tracers to an estimate of benthic denitrification in the Okhotsk Sea. *Journal of oceanography*, 70, 415-424 (2014).
156. Ito, T., Nenes, A., Johnson, M. S., Meskhidze, N., & Deutsch, C.. Acceleration of oxygen decline in the tropical Pacific over the past decades by aerosol pollutants. *Nature Geoscience*, 9(6), 443-447 (2016).
157. Itoh, M., K. I. Ohshima, and M. Wakatsuchi, Distribution and formation of Okhotsk Sea Intermediate Water: An analysis of isopycnal climatology data, *J. Geophys. Res.*, 108(C8), 3257, (2003).
158. Jaccard, S. L., & Galbraith, E. D. Large climate-driven changes of oceanic oxygen concentrations during the last deglaciation. *Nature Geoscience*, 5(2), 151-156 (2012).
159. Jackson, S. E., Longerich, H. P., Dunning, G. R., & Fryer, B. J. The application of laser-ablation microprobe-inductively coupled plasma-mass spectrometry (LAM-ICP-MS) to in situ trace-element determinations in minerals. *Canadian Mineralogist*, 30, 1049-1049 (1992).
160. Jochum, K. P. *et al.* Determination of reference values for NIST SRM 610-617 glasses following ISO guidelines. *Geostand. Geoanalytical Res.* **35**, 397–429 (2011).
161. Johnson, B. W., Mettam, C., & Poulton, S. W. Combining nitrogen isotopes and redox proxies strengthens paleoenvironmental interpretations: examples from Neoproterozoic Snowball Earth sediments. *Frontiers in Earth Science*, 10, 745830 (2022).
162. Johnson, K. S., Berelson, W. M., Coale, K. H., Coley, T. L., Elrod, V. A., Fairey, W. R., ... & Nowicki, J. L. Manganese flux from continental margin sediments in a transect through the oxygen minimum. *Science*, 257(5074), 1242-1245 (1992).
163. Jorissen, F. J., de Stigter, H. C. & Widmark, J. G. V. A conceptual model explaining benthic foraminiferal microhabitats. *Mar. Micropaleontol.* **26**, 3–15 (1995).
164. Kahru, M., Marinone, S. G., Lluch-Cota, S. E., Parés-Sierra, A., & Mitchell, B. G. Ocean-color variability in the Gulf of California: scales from days to ENSO. *Deep Sea Research Part II: Topical Studies in Oceanography*, 51(1-3), 139-146 (2004).

165. Kamp, A., Høglund, S., Risgaard-Petersen, N., & Stief, P.. Nitrate storage and dissimilatory nitrate reduction by eukaryotic microbes. *Frontiers in microbiology*, 6, 1492 (2015).
166. Kamykowski, D.Z., Zentara, S.J.,. Hypoxia in the world oceans recorded in the historical data set. *Deep Sea Res* 37, 1861–1874 (1990).
167. Karl, D., Michaels, A., Bergman, B., Capone, D., Carpenter, E., Letelier, R., & Stal, L. Dinitrogen fixation in the world’s oceans. *The nitrogen cycle at regional to global scales*, 47-98 (2002).
168. Karstensen, J., & Quadfasel, D. Formation of Southern Hemisphere thermocline waters: Water mass conversion and subduction. *Journal of Physical Oceanography*, 32(11), 3020-3038 (2002).
169. Karstensen, J., Stramma, L. & Visbeck, M. Oxygen minimum zones in the eastern tropical Atlantic and Pacific oceans. *Prog. Oceanogr.* **77**, 331–350 (2008).
170. Keeling, R. F., Kortzinger, A. & Gruber, N. Ocean Deoxygenation in a Warming World. *Ann. Rev. of Mar. Sci.* **2**, 199–229 (2010).
171. Keigwin, L. D. Glacial-age hydrography of the far northwest Pacific Ocean. *Paleoceanography*, 13(4), 323-339 (1998).
172. Keigwin, L. D., & Jones, G. A. Deglacial climatic oscillations in the Gulf of California. *Paleoceanography*, 5(6), 1009-1023 (1990).
173. Kessler, W.S. The circulation of the eastern tropical pacific: a review. *Prog. Oceanogr.* 69, 181–217 (2006).
174. Kienast, M., Higginson, M. J., Mollenhauer, G., Eglinton, T. I., Chen, M. T., & Calvert, S. E.. On the sedimentological origin of down-core variations of bulk sedimentary nitrogen isotope ratios. *Paleoceanography*, 20(2) (2005).
175. Kienast, S. S., Calvert, S. E., & Pedersen, T. F. Nitrogen isotope and productivity variations along the northeast Pacific margin over the last 120 kyr: Surface and subsurface paleoceanography. *Paleoceanography*, 17(4), 7-1 (2002).
176. Kimura, N., & Wakatsuchi, M. Processes controlling the advance and retreat of sea ice in the Sea of Okhotsk. *Journal of Geophysical Research: Oceans*, 104(C5), 11137-11150 (1999).
177. Kitani, K., An oceanographic study of the Sea of Okhotsk, particularly in regard to cold waters, *Bull. Far Seas Fish. Res. Lab.*, 9, 45– 77(1973).

178. Klotz, M. G. & Stein, L. Y. Nitrifier genomics and evolution of the nitrogen cycle. *FEMS Microbiol. Lett.* **278**, 146–156 (2008).
179. Kobayashi, T. Study of the formation of North Pacific Intermediate Water by a general circulation model and the particle-tracking method: 2. Formation mechanism of salinity minimum from the view of the “critical gradient” of the Oyashio mixing ratio. *Journal of Geophysical Research: Oceans*, *105*(C1), 1055-1069 (2000).
180. Koho, K. A., de Nooijer, L. J. & Reichart, G. J. Combining benthic foraminiferal ecology and shell Mn/Ca to deconvolve past bottom water oxygenation and paleoproductivity. *Geochim. Cosmochim. Acta* **165**, 294–306 (2015).
181. Koho, K. A., De Nooijer, L. J., Fontanier, C., Toyofuku, T., Oguri, K., Kitazato, H., & Reichart, G. J. Benthic foraminiferal Mn/Ca ratios reflect microhabitat preferences. *Biogeosciences*, *14*(12), 3067-3082 (2017).
182. Koho, K. A., Nierop, K. G. J., Moodley, L., Middelburg, J. J., Pozzato, L., Soetaert, K., ... & Reichart, G. J. Microbial bioavailability regulates organic matter preservation in marine sediments. *Biogeosciences*, *10*(2), 1131-1141 (2013).
183. Koho, K. A., Piña-Ochoa, E., Geslin, E. & Risgaard-Petersen, N. Vertical migration, nitrate uptake and denitrification: survival mechanisms of foraminifers (*Globobulimina turgida*) under low oxygen conditions. *FEMS Microbiol. Ecol.* **75**, 273–283 (2011).
184. Korom, S. F. Natural denitrification in the saturated zone: A review. *Water Resour. Res.* **28**, 1657–1668 (1992).
185. Koutavas, A., Demenocal, P. B., Olive, G. C., & Lynch-Stieglitz, J. Mid-Holocene El Niño–Southern Oscillation (ENSO) attenuation revealed by individual foraminifera in eastern tropical Pacific sediments. *Geology*, *34*(12), 993-996 (2006).
186. Krahnmann, G. Physical oceanography during METEOR cruise M77/1. IFM-GEOMAR Leibniz-Institute of Marine Sciences, Kiel University, PANGAEA, <https://doi.org/10.1594/PANGAEA.777978> (2012).
187. Kuhnt, T. *et al.* Automated and manual analyses of the pore density-to-oxygen relationship in *Globobulimina Turgida* (Bailey). *J. Foraminifer. Res.* **44**, 5–16 (2014).
188. Kuhnt, T. *et al.* Relationship between pore density in benthic foraminifera and bottom-water oxygen content. *Deep. Res. Part I Oceanogr. Res. Pap.* **76**, 85–95 (2013).

189. Kutzbach, J. E., & Wright Jr, H. E. Simulation of the climate of 18,000 years BP: Results for the North American/North Atlantic/European sector and comparison with the geologic record of North America. *Quaternary Science Reviews*, 4(3), 147-187 (1985).
190. Kuzmin, Y. V., Burr, G. S., Gorbunov, S. V., Rakov, V. A., & Razjigaeva, N. G. A tale of two seas: reservoir age correction values (R,  $\Delta R$ ) for the Sakhalin Island (Sea of Japan and Okhotsk Sea). *Nuclear Instruments and Methods in Physics Research Section B: Beam Interactions with Materials and Atoms*, 259(1), 460-462 (2007).
191. Lam, P. & Kuypers, M. M. M. Microbial nitrogen cycling processes in oxygen minimum zones. *Annual review of marine science*, 3(1), 317-345 (2011).
192. Lam, P. J., Bishop, J. K., Henning, C. C., Marcus, M. A., Waychunas, G. A., & Fung, I. Y. Wintertime phytoplankton bloom in the subarctic Pacific supported by continental margin iron. *Global Biogeochemical Cycles*, 20(1) (2006).
193. Lam, P., Lavik, G., Jensen, M. M., van de Vossenberg, J., Schmid, M., Woebken, D., ... & Kuypers, M. M. Revising the nitrogen cycle in the Peruvian oxygen minimum zone. *Proceedings of the National Academy of Sciences*, 106(12), 4752-4757 (2009).
194. Lavín, M. F., & Marinone, S. G. An overview of the physical oceanography of the Gulf of California. *Nonlinear Processes in Geophysical Fluid Dynamics: A tribute to the scientific work of Pedro Ripa*, 173-204 (2003).
195. Law, G. T., Shimmiel, T. M., Shimmiel, G. B., Cowie, G. L., Breuer, E. R., & Harvey, S. M. Manganese, iron, and sulphur cycling on the Pakistan margin. *Deep Sea Research Part II: Topical Studies in Oceanography*, 56(6-7), 305-323 (2009).
196. Leclaire, J., & Kerry, K. Calcium carbonate and organic carbon stratigraphy of late Quaternary laminated and homogeneous diatom oozes from the Guaymas Slope, HPC Site 480, Gulf of California (1982).
197. Lecun, Y., Bengio, Y. & Hinton, G. Deep learning. *Nature* **521**, 436–444 (2015).
198. Leduc, G., Garbe-Schönberg, D., Regenber, M., Contoux, C., Etourneau, J., & Schneider, R.. The late Pliocene Benguela upwelling status revisited by means of multiple temperature proxies. *Geochemistry, Geophysics, Geosystems*, 15(2), 475-491(2014).
199. Lembke-Jene, L., Tiedemann, R., Nürnberg, D., Gong, X., & Lohmann, G. Rapid shift and millennial-scale variations in Holocene North Pacific Intermediate Water ventilation. *Proceedings of the National Academy of Sciences*, 115(21), 5365-5370 (2018).

200. Leutenegger, S. & Hansen, H. J. Ultrastructural and radiotracer studies of pore function in foraminifera. *Mar. Biol.* **54**, 11–16 (1979).
201. Levin LA.. Oxygen minimum zone benthos: Adaptation and community response to hypoxia. In *Oceanography and Marine Biology*, vol. 41, pp. 1–45 (2003). London: Taylor & Francis.
202. Levin, L. A., Rathburn, A. E., Gutiérrez, D., Muñoz, P., & Shankle, A. Bioturbation by symbiont-bearing annelids in near-anoxic sediments: implications for biofacies models and paleo-oxygen assessments. *Palaeogeography, Palaeoclimatology, Palaeoecology*, *199*(1-2), 129-140 (2003).
203. Levin, L. A. Manifestation, drivers, and emergence of open ocean deoxygenation. *Annual review of marine science*, *10*(1), 229-260 (2018).
204. Levin, L. A., Whitcraft, C. R., Mendoza, G. F., Gonzalez, J. P. & Cowie, G. Oxygen and organic matter thresholds for benthic faunal activity on the Pakistan margin oxygen minimum zone (700-1100 m). *Deep. Res. Part II Top. Stud. Oceanogr.* **56**, 449–471 (2009).
205. Levshina, S. I. Dissolved and suspended organic matter in the Amur and Songhua River water. *Water resources*, *35*, 716-724 (2008).
206. Li, M., Luo, Q., Chen, J., Shi, S., Yang, J., Xu, X., ... & Dong, Q. Redox conditions and nitrogen cycling in the late Ordovician Yangtze Sea (South China). *Palaeogeography, Palaeoclimatology, Palaeoecology*, *567*, 110305 (2021).
207. Li, N., Somes, C. J., Landolfi, A., Chien, C. T., Pahlow, M., & Oschlies, A. Global impact of benthic denitrification on marine N<sub>2</sub> fixation and primary production simulated by a variable-stoichiometry Earth system model. *EGUsphere*, *2024*, 1-30 (2024).
208. Limburg, K. E., Breitburg, D., Swaney, D. P., & Jacinto, G. Ocean deoxygenation: A primer. *One Earth*, *2*(1), 24-29, (2020).
209. Linke, P. & Lutze, G. F. Microhabitat preferences of benthic foraminifera—a static concept or a dynamic adaptation to optimize food acquisition? *Mar. Micropaleontol.* **20**, 215–234 (1993).
210. Liu, K. K., & Kaplan, I. R. The eastern tropical Pacific as a source of <sup>15</sup>N-enriched nitrate in seawater off southern California. *Limnology and Oceanography*, *34*(5), 820-830 (1989).

211. Loeblich, A. R., Jr. and Tappan, H. (Eds.): Foraminiferal Genera and Their Classification, Van Nostrand Reinhold, New York, 4010 868 pp., ISBN 9781489957627, (1988).
212. Long, M. C., Deutsch, C., & Ito, T. Finding forced trends in oceanic oxygen. *Global Biogeochemical Cycles*, 30(2), 381-397 (2016).
213. Longhurst, A., Sathyendranath, S., Platt, T., & Caverhill, C. An estimate of global primary production in the ocean from satellite radiometer data. *Journal of plankton Research*, 17(6), 1245-1271 (1995).
214. Lourey, M. J., Trull, T. W., & Sigman, D. M. Sensitivity of  $\delta^{15}\text{N}$  of nitrate, surface suspended and deep sinking particulate nitrogen to seasonal nitrate depletion in the Southern Ocean. *Global Biogeochemical Cycles*, 17(3) (2003).
215. Lu, W., Wang, Y., Oppo, D. W., Nielsen, S. G. & Costa, K. M. Comparing paleo-oxygenation proxies (benthic foraminiferal surface porosity, I/Ca, authigenic uranium) on modern sediments and the glacial Arabian Sea. *Geochim. Cosmochim. Acta* **331**, 69–85 (2022).
216. Maher, B. A., Prospero, J. M., Mackie, D., Gaiero, D., Hesse, P. P., & Balkanski, Y. Global connections between aeolian dust, climate and ocean biogeochemistry at the present day and at the last glacial maximum. *Earth-Science Reviews*, 99(1-2), 61-97 (2010).
217. Mariotti, A. Atmospheric nitrogen is a reliable standard for natural  $^{15}\text{N}$  abundance measurements. *Nature*, 303(5919), 685-687 (1983).
218. Martin, S., Drucker, R., Yamashita, K.,. The production of ice and dense shelf water in the Okhotsk Sea polynyas. *Journal of Geophysical Research* 103, 27771–27782 (1998).
219. Martinez, P., & Robinson, R. S. Increase in water column denitrification during the last deglaciation: the influence of oxygen demand in the eastern equatorial Pacific. *Biogeosciences*, 7(1), 1-9 (2010).
220. Matear, R. J., Hirst, A. C., & McNeil, B. I. Changes in dissolved oxygen in the Southern Ocean with climate change. *Geochemistry, geophysics, geosystems*, 1(11) (2000).
221. McKay, C. L. *et al.* A comparison of benthic foraminiferal Mn / Ca and sedimentary Mn / Al as proxies of relative bottom-water oxygenation in the low-latitude NE Atlantic upwelling system. *Biogeosciences* **12**, 5415–5428 (2015).

222. McKinney, R. E., & Conway, R. A. Chemical oxygen in biological waste treatment. *Sewage and Industrial Wastes*, 29(10), 1097-1106 (1957).
223. Meckler, A. N., Ren, H., Sigman, D. M., Gruber, N., Plessen, B., Schubert, C. J., & Haug, G. H. Deglacial nitrogen isotope changes in the Gulf of Mexico: Evidence from bulk sedimentary and foraminifera-bound nitrogen in Orca Basin sediments. *Paleoceanography*, 26(4) (2011).
224. Meissner, K. J., Galbraith, E. D., & Völker, C. Denitrification under glacial and interglacial conditions: A physical approach. *Paleoceanography*, 20(3) (2005).
225. Mezger, E. M., De Nooijer, L. J., Boer, W., Brummer, G. J. A., & Reichart, G. J.. Salinity controls on Na incorporation in Red Sea planktonic foraminifera. *Paleoceanography*, 31(12), 1562-1582 (2016).
226. Middelburg, J. J., & Levin, L. A. Coastal hypoxia and sediment biogeochemistry. *Biogeosciences*, 6(7), 1273-1293, (2009).
227. Middelburg, J. J., De Lange, G. J., & van Der Weijden, C. H.. Manganese solubility control in marine pore waters. *Geochimica et Cosmochimica Acta*, 51(3), 759-763 (1987).
228. Moffitt, S. E., Hill, T. M., Roopnarine, P. D. & Kennett, J. P. Response of seafloor ecosystems to abrupt global climate change. *Proc. Natl. Acad. Sci. U. S. A.* **112**, 4684–4689 (2015).
229. Mojtahid, M. *et al.* Evaluation and application of foraminiferal element/calcium ratios: Assessing riverine fluxes and environmental conditions during sapropel S1 in the Southeastern Mediterranean. *Mar. Micropaleontol.* **153**, 101783 (2019).
230. Mollenhauer, G., Schneider, R. R., Müller, P. J., Spieß, V., & Wefer, G. Glacial/interglacial variability in the Benguela upwelling system: Spatial distribution and budgets of organic carbon accumulation. *Global Biogeochemical Cycles*, 16(4), 81-1 (2002).
231. Mollier-Vogel, E. *et al.* Mid-Holocene deepening of the Southeast Pacific oxycline. *Glob. Planet. Change* **172**, 365–373 (2019).
232. Mollier-Vogel, E. *et al.* Nitrogen isotope gradients off Peru and Ecuador related to upwelling, productivity, nutrient uptake and oxygen deficiency. *Deep. Res. Part I Oceanogr. Res. Pap.* **70**, 14–25 (2012).

233. Mollier-Vogel, E., Leduc, G., Bösch, T., Martinez, P. & Schneider, R. R. Rainfall response to orbital and millennial forcing in northern Peru over the last 18ka. *Quat. Sci. Rev.* **76**, 29–38 (2013).
234. Montes, I., Dewitte, B., Gutknecht, E., Paulmier, A., Dadou, I., Oschlies, A., & Garçon, V.. High-resolution modeling of the Eastern Tropical Pacific oxygen minimum zone: Sensitivity to the tropical oceanic circulation. *Journal of Geophysical Research: Oceans*, *119*(8), 5515-5532 (2014).
235. Montoya, J. P., Horrigan, S. G., & McCarthy, J. J. Natural abundance of <sup>15</sup>N in particulate nitrogen and zooplankton in the Chesapeake Bay. *Marine Ecology Progress Series*, 35-61 (1990).
236. Moodley, L. & Hess, C. Tolerance of infaunal benthic foraminifera for low and high oxygen concentrations. *Biol. Bull.* **183**, 94–98 (1992).
237. Moore, C. M., Mills, M. M., Arrigo, K. R., Berman-Frank, I., Bopp, L., Boyd, P. W., & Ulloa, O. Processes and patterns of oceanic nutrient limitation. *Nature geoscience*, *6*(9), 701-710 (2013).
238. Moretti, S., Auderset, A., Deutsch, C., Schmitz, R., Gerber, L., Thomas, E., ... & Martínez-García, A. Oxygen rise in the tropical upper ocean during the Paleocene-Eocene Thermal Maximum. *Science*, *383*(6684), 727-731 (2024).
239. Morton, P. L. *et al.* Shelf inputs and lateral transport of Mn, Co, and Ce in the western north pacific ocean. *Front. Mar. Sci.* **6** (2019).
240. Muratli, J. M., Chase, Z., Mix, A. C., & McManus, J. Increased glacial-age ventilation of the Chilean margin by Antarctic Intermediate Water. *Nature Geoscience*, *3*(1), 23-26 (2010).
241. Naafs, B. D. A., Monteiro, F. M., Pearson, A., Higgins, M. B., Pancost, R. D., & Ridgwell, A. Fundamentally different global marine nitrogen cycling in response to severe ocean deoxygenation. *Proceedings of the National Academy of Sciences*, *116*(50), 24979-24984 (2019).
242. Nakaguchi, Y. *et al.* Distribution and stoichiometry of Al, Mn, Fe, Co, Ni, Cu, Zn, Cd, and Pb in the Seas of Japan and Okhotsk. *Mar. Chem.* **241**, 104108 (2022).
243. Nakatsuka T, Yoshikawa C, Toda M, Kawamura K, Wakatsuchi M. An extremely turbid intermediate water in the Sea of Okhotsk: implication for the transport of particulate organic matter in a seasonally ice-bound sea. *Geophys Res Lett* *29*, 4-1-4-4 (2002).

244. Nakatsuka T, Toda M, Kawamura K, Wakatsuchi M. Dissolved and particulate organic carbon in the Sea of Okhotsk: Transport from continental shelf to ocean interior. *J Geophys Res* 109, C09S14 (2004).
245. Nardelli, M. P., Barras, C., Metzger, E., Mouret, A., Filipsson, H. L., Jorissen, F., & Geslin, E. (2014). Experimental evidence for foraminiferal calcification under anoxia. *Biogeosciences*, 11(14), 4029-4038 (2014).
246. Narita, H., Sato, M., Tsunogai, S., Murayama, M., Ikehara, M., Nakatsuka, T., & Ujiie, Y. Biogenic opal indicating less productive northwestern North Pacific during the glacial ages. *Geophysical Research Letters*, 29(15), 22-1 (2002).
247. Navarrete-Forero, G., Morales Baren, L., Dominguez-Granda, L., Pontón Cevallos, J., & Marín Jarrín, J. R. Heavy metals contamination in the Gulf of Guayaquil: even limited data reflects environmental impacts from anthropogenic activity. *Revista internacional de contaminación ambiental*, 35(3), 731-755 (2019).
248. Ni, S., Quintana Krupinski, N. B., Groeneveld, J., Fanget, A. S., Böttcher, M. E., Liu, B., ... & Filipsson, H. L. Holocene hydrographic variations from the Baltic-North Sea transitional area (IODP site M0059). *Paleoceanography and Paleoclimatology*, 35(2), e2019PA003722 (2020).
249. Ní Fhlaithearta, S. *et al.* Manganese incorporation in living (stained) benthic foraminiferal shells: A bathymetric and in-sediment study in the Gulf of Lions (NW Mediterranean). *Biogeosciences* **15**, 6315–6328 (2018).
250. Nishioka, J., Mitsudera, H., Yasuda, I., Liu, H., Nakatsuka, T., & Volkov, Y. N. Biogeochemical and physical processes in the Sea of Okhotsk and the linkage to the Pacific Ocean. *Progress in Oceanography*, 126, 1-7 (2014).
251. Nomaki, H. *et al.* In situ experimental evidences for responses of abyssal benthic biota to shifts in phytodetritus compositions linked to global climate change. *Glob. Chang. Biol.* **27**, 6139–6155 (2021).
252. Nomaki, H., Heinz, P., Hemleben, C., & Kitazato, H. Behavior and response of deep-sea benthic foraminifera to freshly supplied organic matter: a laboratory feeding experiment in microcosm environments. *The Journal of Foraminiferal Research*, 35(2), 103-113 (2005).

253. Nomaki, H., Heinz, P., Nakatsuka, T., Shimanaga, M., Ohkouchi, N., Ogawa, N. O., & Kitazato, H. Different ingestion patterns of  $^{13}\text{C}$ -labeled bacteria and algae by deep-sea benthic foraminifera. *Marine Ecology Progress Series*, 310, 95-108 (2006).
254. Nürnberg, D. & Tiedemann, R. Environmental change in the Sea of Okhotsk during the last 1.1 million years. *Paleoceanography* **19**, 1–23 (2004).
255. Nürnberg, D. *et al.* Sea surface and subsurface circulation dynamics off equatorial Peru during the last  $\sim 17$  kyr. *Paleoceanography* **30** (7), 984–999 (2015).
256. Ohkushi, K., Kennett, J. P., Zeleski, C. M., Moffitt, S. E., Hill, T. M., Robert, C., ... & Behl, R. J. Quantified intermediate water oxygenation history of the NE Pacific: A new benthic foraminiferal record from Santa Barbara basin. *Paleoceanography*, 28(3), 453-467 (2013).
257. Okazaki, Y., Timmermann, A., Menviel, L., Harada, N., Abe-Ouchi, A., Chikamoto, M. O., & Asahi, H. Deepwater formation in the North Pacific during the last glacial termination. *Science*, 329(5988), 200-204 (2010).
258. Ontiveros-Cuadras, J. F., Thunell, R., Ruiz-Fernández, A. C., Benitez-Nelson, C., Machain-Castillo, M. L., Tappa, E., & Sanchez-Cabeza, J. A. Centennial OMZ changes in the NW Mexican Margin from geochemical and foraminiferal sedimentary records. *Continental Shelf Research*, 176, 64-75 (2019).
259. Oeschies, A., Brandt, P., Stramma, L., & Schmidtko, S.. Drivers and mechanisms of ocean deoxygenation. *Nature Geoscience*, 11(7), 467-473 (2018).
260. Parkin, T. B. & Tiedje, J. M. Application of a soil core method to investigate the effect of oxygen concentration on denitrification. *Soil Biol. Biochem.* **16**, 331–334 (1984).
261. Parsons, M. L., & Dortch, Q. Sedimentological evidence of an increase in *Pseudonitzschia* (Bacillariophyceae) abundance in response to coastal eutrophication. *Limnology and Oceanography*, 47(2), 551-558, (2002).
262. Paulmier, A., Ruiz-Pino, D., & Garçon, V. The oxygen minimum zone (OMZ) off Chile as intense source of  $\text{CO}_2$  and  $\text{N}_2\text{O}$ . *Continental Shelf Research*, 28(20), 2746-2756 (2008).
263. Paulmier, A., Ruiz-Pino, D., Garçon, V., & Farias, L. Maintaining of the eastern south Pacific oxygen minimum zone (OMZ) off Chile. *Geophysical Research Letters*, 33(20) (2006).

264. Pennington, J. T., Mahoney, K. L., Kuwahara, V. S., Kolber, D. D., Calienes, R., & Chavez, F. P. Primary production in the eastern tropical Pacific: A review. *Progress in oceanography*, 69(2-4), 285-317 (2006).
265. Pérez-Cruz, L. & Machain Castillo, M. L. Benthic foraminifera of the oxygen minimum zone, continental shelf of the Gulf of Tehuantepec, Mexico. *Jour. Foram. Res.* 20(4), 312–325 (1990).
266. Petersen, J. *et al.* Improved methodology for measuring pore patterns in the benthic foraminiferal genus *Ammonia*. *Mar. Micropaleontol.* **128**, 1–13 (2016).
267. Petersen, J. *et al.* Mn/Ca intra- and inter-test variability in the benthic foraminifer *Ammonia tepida*. *Biogeosciences* **15**, 331–348 (2018).
268. Phleger, F. B. & Soutar, A. Production of Benthic Foraminifera in Three East Pacific Oxygen Minima. *Micropaleontology* **19**, 110 (1973).
269. Piña-Ochoa, E. *et al.* Widespread occurrence of nitrate storage and denitrification among Foraminifera and Gromiida. *Proc. Natl. Acad. Sci. U. S. A.* **107**, 1148–1153 (2010a).
270. Piña-Ochoa, E., Koho, K. A., Geslin, E. & Risgaard-Petersen, N. Survival and life strategy of the foraminiferan *Globobulimina turgida* through nitrate storage and denitrification. *Mar. Ecol. Prog. Ser.* **417**, 39–49 (2010b).
271. Pospelova, V., Price, A. M., & Pedersen, T. F. Palynological evidence for late Quaternary climate and marine primary productivity changes along the California margin. *Paleoceanography*, 30(7), 877-894 (2015).
272. Pride, C. J. An evaluation and application of paleoceanographic proxies in the Gulf of California. University of South Carolina (1997).
273. Pride, C., Thunell, R., Sigman, D., Keigwin, L., Altabet, M., & Tappa, E. Nitrogen isotopic variations in the Gulf of California since the last deglaciation: Response to global climate change. *Paleoceanography*, 14(3), 397-409 (1999).
274. Quillévéré, F. *et al.* Global scale same-specimen morpho-genetic analysis of *Truncorotalia truncatulinoides*: A perspective on the morphological species concept in planktonic foraminifera. *Palaeogeogr. Palaeoclimatol. Palaeoecol.* **391**, 2–12 (2013).
275. Rabalais, N. N., Cai, W. J., Carstensen, J., Conley, D. J., Fry, B., Hu, X., ... & Zhang, J. (2014). Eutrophication-driven deoxygenation in the coastal ocean. *Oceanography*, 27(1), 172-183 (2014).

276. Rabalais, N. N., Diaz, R. J., Levin, L. A., Turner, R. E., Gilbert, D., & Zhang, J. Dynamics and distribution of natural and human-caused hypoxia. *Biogeosciences*, 7(2), 585-619 (2010).
277. Rae, J. W., Gray, W. R., Wills, R. C. J., Eisenman, I., Fitzhugh, B., Fotheringham, M., ... & Burke, A. Overturning circulation, nutrient limitation, and warming in the Glacial North Pacific. *Science advances*, 6(50), eabd1654 (2020).
278. Rae, J.W.B., Burke, A., Robinson, L.F. et al. CO<sub>2</sub> storage and release in the deep Southern Ocean on millennial to centennial timescales. *Nature* 562, 569–573 (2018).
279. Rafter, P. A., & Sigman, D. M. Spatial distribution and temporal variation of nitrate nitrogen and oxygen isotopes in the upper equatorial Pacific Ocean. *Limnology and Oceanography*, 61(1), 14-31 (2016).
280. Rafter, P. A., Gray, W. R., Hines, S. K., Burke, A., Costa, K. M., Gottschalk, J., ... & DeVries, T. Global reorganization of deep-sea circulation and carbon storage after the last ice age. *Science Advances*, 8(46), eabq5434 (2022).
281. Rafter, P. A., Sigman, D. M., Charles, C. D., Kaiser, J., & Haug, G. H. Subsurface tropical Pacific nitrogen isotopic composition of nitrate: Biogeochemical signals and their transport. *Global Biogeochemical Cycles*, 26(1) (2012).
282. Rathburn, A. E., Willingham, J., Ziebis, W., Burkett, A. M. & Corliss, B. H. A New biological proxy for deep-sea paleo-oxygen: Pores of epifaunal benthic foraminifera. *Sci. Rep.* **8**, 1–8 (2018).
283. Reichart, G. J., Jorissen, F., Anschutz, P. & Mason, P. R. D. Single foraminiferal test chemistry records the marine environment. *Geology* **31**, 355–358 (2003).
284. Reimer, P. J., Austin, W. E., Bard, E., Bayliss, A., Blackwell, P. G., Ramsey, C. B., ... & Talamo, S. The IntCal20 Northern Hemisphere radiocarbon age calibration curve (0–55 cal kBP). *Radiocarbon*, 62(4), 725-757 (2020).
285. Ren, H., Sigman, D. M., Chen, M. T., & Kao, S. J.. Elevated foraminifera-bound nitrogen isotopic composition during the last ice age in the South China Sea and its global and regional implications. *Global Biogeochemical Cycles*, 26(1) (2012).
286. Ren, H., Sigman, D. M., Meckler, A. N., Plessen, B., Robinson, R. S., Rosenthal, Y., & Haug, G. H. Foraminiferal isotope evidence of reduced nitrogen fixation in the ice age Atlantic Ocean. *Science*, 323(5911), 244-248 (2009).

287. Richirt, J. *et al.* Morphological distinction of three Ammonia phylotypes occurring along European coasts. *J. Foraminifer. Res.* **49**, 76–93 (2019a).
288. Richirt, J. *et al.* Scaling laws explain foraminiferal pore patterns. *Sci. Rep.* **9**, 1–11 (2019b).
289. Richter, D. D., & Markewitz, D.. *Understanding soil change: soil sustainability over millennia, centuries, and decades*, Cambridge University Press, (2001).
290. Riechelson, H., Rosenthal, Y., Bova, S., & Robinson, R. S. Southern Ocean biological pump role in driving Holocene atmospheric CO<sub>2</sub>: Reappraisal. *Geophysical Research Letters*, **51**(4), e2023GL105569 (2024).
291. Rincón-Martínez, D., Lamy, F., Contreras, S., Leduc, G., Bard, E., Saukel, C., ... & Tiedemann, R. More humid interglacials in Ecuador during the past 500 kyr linked to latitudinal shifts of the equatorial front and the Intertropical Convergence Zone in the eastern tropical Pacific. *Paleoceanography*, **25**(2) (2010).
292. Risgaard-Petersen, N. *et al.* Evidence for complete denitrification in a benthic foraminifer. *Nature* **443**, 93–96 (2006).
293. Robinson, R. S., Kienast, M., Luiza Albuquerque, A., Altabet, M., Contreras, S., De Pol Holz, R., & Yang, J. Y. A review of nitrogen isotopic alteration in marine sediments. *Paleoceanography*, **27**(4), (2012).
294. Robinson, R. S., Martinez, P., Pena, L. D., & Cacho, I. Nitrogen isotopic evidence for deglacial changes in nutrient supply in the eastern equatorial Pacific. *Paleoceanography*, **24**(4) (2009).
295. Robinson, R. S., Mix, A., & Martinez, P. Southern Ocean control on the extent of denitrification in the southeast Pacific over the last 70 ka. *Quaternary Science Reviews*, **26**(1-2), 201-212 (2007).
296. Robinson, R. S., Sigman, D. M., DiFiore, P. J., Rohde, M. M., Mashiotta, T. A., & Lea, D. W. Diatom-bound <sup>15</sup>N/<sup>14</sup>N: New support for enhanced nutrient consumption in the ice age subantarctic. *Paleoceanography*, **20**(3) (2005).
297. Roden, G. I. Oceanographic aspects of Gulf of California (1964).
298. Roden, G.I. Large-scale upwelling off northwestern Mexico. *J. Phys. Oceanogr.* **2**, 184–189 (1972).

299. Romanova, V., Lohmann, G., Grosfeld, K., & Butzin, M. The relative role of oceanic heat transport and orography on glacial climate. *Quaternary science reviews*, 25(7-8), 832-845 (2006).
300. RStudio Team. RStudio: Integrated Development for R. RStudio, Inc., Boston, MA (2023).
301. Russell, J. L., & Dickson, A. G. Variability in oxygen and nutrients in South Pacific Antarctic intermediate water. *Global biogeochemical cycles*, 17(2) (2003).
302. Rykaczewski, R. R., & Dunne, J. P. Enhanced nutrient supply to the California Current Ecosystem with global warming and increased stratification in an earth system model. *Geophysical Research Letters*, 37(21) (2010).
303. Saitoh S, Kishino M, Kiyofuji H, Taguchi S, Takahashi M Seasonal Variability of Phytoplankton Pigment Concentration in the Okhotsk Sea. *J Remote Sens Soc Jpn* 16:172–178 (1996).
304. Salvattecchi, R. *et al.* smaller fish species in a warm and oxygen-poor Humboldt Current system. *Science (80-.)*. **375**, 101–104 (2022).
305. Salvattecchi, R., Gutiérrez, D., Field, D., Sifeddine, A., Ortlieb, L., Bouloubassi, I., & Cetin, F. The response of the Peruvian Upwelling Ecosystem to centennial-scale global change during the last two millennia. *Climate of the Past*, 10(2), 715-731 (2014).
306. Salvattecchi, R., Gutiérrez, D., Sifeddine, A., Ortlieb, L., Druffel, E., Boussafir, M., & Schneider, R. Centennial to millennial-scale changes in oxygenation and productivity in the Eastern Tropical South Pacific during the last 25,000 years. *Quaternary Science Reviews*, 131, 102-117 (2016).
307. Salvattecchi, R., Schneider, R. R., Blanz, T., & Mollier-Vogel, E.. Deglacial to Holocene Ocean temperatures in the Humboldt Current System as indicated by alkenone paleothermometry. *Geophysical Research Letters*, 46(1), 281-292 (2019).
308. Schenau, S. J., Reichert, G. J. & De Lange, G. J. Oxygen minimum zone controlled Mn redistribution in Arabian Sea sediments during the late Quaternary. *Paleoceanography* **17**, 10-1-10–12 (2002).
309. Schlitzer, Reiner, Ocean Data View, [odv.awi.de](https://odv.awi.de), 2023.
310. Schmiedl, G. Use of foraminifera in climate science. In *Oxford Research Encyclopedia of Climate Science*. Oxford University Press (2019).

311. Schmidtko, S., Stramma, L. & Visbeck, M. Decline in global oceanic oxygen content during the past five decades. *Nature* **542**, 335–339 (2017).
312. Scholz, F., Hensen, C., Noffke, A., Rohde, A., Liebetrau, V., & Wallmann, K.. Early diagenesis of redox-sensitive trace metals in the Peru upwelling area—response to ENSO-related oxygen fluctuations in the water column. *Geochimica et Cosmochimica Acta*, *75*(22), 7257–7276 (2011).
313. Scholz, F., Schmidt, M., Hensen, C., Eroglu, S., Geilert, S., Gutjahr, M., & Liebetrau, V. Shelf-to-basin iron shuttle in the Guaymas Basin, Gulf of California. *Geochimica et Cosmochimica Acta*, *261*, 76–92 (2019).
314. Schönfeld, J., Beccari, V., Schmidt, S. & Spezzaferri, S. Biometry and taxonomy of Adriatic Ammonia species from Bellaria-Igea Marina (Italy). *J. Micropalaeontology* **40**, 195–223 (2021).
315. Schubert, C. J., & Calvert, S. E. Nitrogen and carbon isotopic composition of marine and terrestrial organic matter in Arctic Ocean sediments: implications for nutrient utilization and organic matter composition. *Deep Sea Research Part I: Oceanographic Research Papers*, *48*(3), 789–810 (2001).
316. Seki, O., Harada, N., Sato, M., Kawamura, K., Ijiri, A., & Nakatsuka, T. Assessment for paleoclimatic utility of terrestrial biomarker records in the Okhotsk Sea sediments. *Deep Sea Research Part II: Topical Studies in Oceanography*, *61*, 85–92 (2012).
317. Seki, O., Ikehara, M., Kawamura, K., Nakatsuka, T., Ohnishi, K., Wakatsuchi, M., & Sakamoto, T. Reconstruction of paleoproductivity in the Sea of Okhotsk over the last 30 kyr. *Paleoceanography*, *19*(1) (2004).
318. Sen Gupta, B. (Ed.). *Modern foraminifera* (p. 371). Dordrecht: Kluwer Academic Publishers (1999).
319. Sen Gupta, B. K.: *Systematics of modern Foraminifera BT - Modern Foraminifera*, edited by: Sen Gupta, B. K., Springer 4580 Netherlands, Dordrecht, 7–36 (2003).
320. Sigman, D. M., Altabet, M. A., McCorkle, D. C., Francois, R., & Fischer, G. The  $\delta^{15}\text{N}$  of nitrate in the Southern Ocean: Nitrogen cycling and circulation in the ocean interior. *Journal of Geophysical Research: Oceans*, *105*(C8), 19599–19614 (2000).
321. Sigman, D. M., Altabet, M. A., Michener, R., McCorkle, D. C., Fry, B., & Holmes, R. M. Natural abundance-level measurement of the nitrogen isotopic composition of

- oceanic nitrate: an adaptation of the ammonia diffusion method. *Marine chemistry*, 57(3-4), 227-242 (1997).
322. Sigman, D. M., Casciotti, K. L., Andreani, M., Barford, C., Galanter, M. B. J. K., & Böhlke, J. K. A bacterial method for the nitrogen isotopic analysis of nitrate in seawater and freshwater. *Analytical chemistry*, 73(17), 4145-4153 (2001).
323. Sigman, D. M., DiFiore, P. J., Hain, M. P., Deutsch, C., Wang, Y., Karl, D. M., ... & Pantoja, S. The dual isotopes of deep nitrate as a constraint on the cycle and budget of oceanic fixed nitrogen. *Deep Sea Research Part I: Oceanographic Research Papers*, 56(9), 1419-1439 (2009).
324. Skinner, L. C., Fallon, S., Waelbroeck, C., Michel, E., & Barker, S. Ventilation of the deep Southern Ocean and deglacial CO<sub>2</sub> rise. *Science*, 328(5982), 1147-1151 (2010).
325. Slomp, C. P., Malschaert, J. F. P., Lohse, L., & Van Raaphorst, W. Iron and manganese cycling in different sedimentary environments on the North Sea continental margin. *Continental Shelf Research*, 17(9), 1083-1117 (1997).
326. Smil, V. *Enriching the earth: Fritz Haber, Carl Bosch, and the transformation of world food production*. MIT press (2004).
327. Sollai, M., Hopmans, E. C., Schouten, S., Keil, R. G., & Sinninghe Damsté, J. S. Intact polar lipids of Thaumarchaeota and anammox bacteria as indicators of N cycling in the eastern tropical North Pacific oxygen-deficient zone. *Biogeosciences*, 12(15), 4725-4737 (2015).
328. Somes, C. J., Oschlies, A., & Schmittner, A. Isotopic constraints on the pre-industrial oceanic nitrogen budget. *Biogeosciences*, 10(9), 5889-5910 (2013).
329. Somes, C. J., Schmittner, A., Muglia, J., & Oschlies, A. A three-dimensional model of the marine nitrogen cycle during the last glacial maximum constrained by sedimentary isotopes. *Frontiers in Marine Science*, 4, 108 (2017).
330. Sorokin Y.I & Sorokin P.Y Production in the Sea of Okhotsk. *J Plankton Res* 21:201–230 (1999).
331. Sperling, E. A., Frieder, C. A., & Levin, L. A. Biodiversity response to natural gradients of multiple stressors on continental margins. *Proceedings of the Royal Society B: Biological Sciences*, 283(1829), 20160637 (2016).
332. Spiker, E.C. & Simoneit, B.R.T. Radiocarbon dating of Recent sediments from Leg 64, Gulf of California. In: CURRAY, J.R., MOORE, D.G. et al. (eds) Initial Reports of the

- Deep-Sea Drilling Project. US Government Printing Office, Washington, DC, 757-758 (1982).
333. Spitzzy, A., Leenheer, J. Dissolved organic carbon in rivers. In: Degens, E.T., Kempe, S., Richey, J.E. (Eds.), *Biogeochemistry of Major World Rivers*. SCOPE, New York, pp. 213–232 (1991).
334. Stramma, L., & Schmidtko, S. Tropical deoxygenation sites revisited to investigate oxygen and nutrient trends. *Ocean Science*, 17(3), 833-847 (2021).
335. Stramma, L., Johnson, G. C., Sprintall, J., & Mohrholz, V. Expanding oxygen-minimum zones in the tropical oceans. *science*, 320(5876), 655-658 (2008).
336. Stramma, L., Schmidtko, S., Levin, L. A. & Johnson, G. C. Ocean oxygen minima expansions and their biological impacts. *Deep-Sea Res. Part I: Ocean. Res. Pap.* 57(4), 587–595 (2010).
337. Studer, A. S., Mekik, F., Ren, H., Hain, M. P., Oleynik, S., Martínez-García, A., ... & Sigman, D. M.. Ice age-Holocene similarity of foraminifera-bound nitrogen isotope ratios in the eastern equatorial Pacific. *Paleoceanography and Paleoclimatology*, 36(5), e2020PA004063 (2021).
338. Stüeken, E. E., Kipp, M. A., Koehler, M. C., & Buick, R.. The evolution of Earth's biogeochemical nitrogen cycle. *Earth-Science Reviews*, 160, 220-239 (2016).
339. Sutton, M., *et al.* The nitrogen fix: from nitrogen cycle pollution to nitrogen circular economy. In *Frontiers 2018/2019* (pp. 52-64). United Nations Environment Programme, (2019).
340. Tagliabue, A., Bowie, A. R., Boyd, P. W., Buck, K. N., Johnson, K. S., & Saito, M. A. The integral role of iron in ocean biogeochemistry. *Nature*, 543(7643), 51-59 (2017).
341. Takano, Y., Ito, T., & Deutsch, C. Projected centennial oxygen trends and their attribution to distinct ocean climate forcings. *Global Biogeochemical Cycles*, 32(9), 1329-1349 (2018).
342. Talley, L. D., Feely, R. A., Sloyan, B. M., Wanninkhof, R., Baringer, M. O., Bullister, J. L., ... & Zhang, J. Z. Changes in ocean heat, carbon content, and ventilation: A review of the first decade of GO-SHIP global repeat hydrography. *Annual review of marine science*, 8(1), 185-215 (2016).

343. Talley, L. D. An Okhotsk Sea water anomaly: implications for ventilation in the North Pacific. *Deep Sea Research Part A. Oceanographic Research Papers*, 38, S171-S190 (1991).
344. Taylor, M. A., Hendy, I. L., & Chappaz, A. Assessing oxygen depletion in the Northeastern Pacific Ocean during the last deglaciation using I/Ca ratios from multiple benthic foraminiferal species. *Paleoceanography*, 32(8), 746-762 (2017).
345. Telang, *et al.* Carbon and mineral transport in major North American, Russian Arctic, and Siberian rivers: the St. Lawrence, the Mackenzie, the Yukon, the Arctic Alaskan rivers, the Arctic basin rivers in the Soviet Union, and the Yenisei. In: Degens, E.T., Kempe, S., Richey, J.E. (Eds.), *Biogeochemistry of Major World Rivers*. SCOPE, New York, pp. 75–104 (1991).
346. Ternois, Y., Kawamura, K., Keigwin, L., Ohkouchi, N., & Nakatsuka, T. A biomarker approach for assessing marine and terrigenous inputs to the sediments of Sea of Okhotsk for the last 27,000 years. *Geochimica et Cosmochimica Acta*, 65(5), 791-802 (2001).
347. Tetard, M., Beaufort, L. & Licari, L. A new optical method for automated pore analysis on benthic foraminifera. *Mar. Micropaleontol.* **136**, 30–36 (2017).
348. Thirumalai, K., Partin, J. W., Jackson, C. S., & Quinn, T. M. Statistical constraints on El Niño Southern Oscillation reconstructions using individual foraminifera: A sensitivity analysis. *Paleoceanography*, 28(3), 401-412 (2013).
349. Thunell, R. C. Seasonal and annual variability in particle fluxes in the Gulf of California: A response to climate forcing, *Deep Sea Res., Part I*, 45, 2059–2083 (1998).
350. Thunell, R. C., Sigman, D. M., Muller-Karger, F., Astor, Y., & Varela, R. Nitrogen isotope dynamics of the Cariaco Basin, Venezuela. *Global Biogeochemical Cycles*, 18(3) (2004).
351. Turner, R. E., & Rabalais, N. N. Coastal eutrophication near the Mississippi river delta. *Nature*, 368(6472), 619-621, (1994).
352. Turner, R. E., & Rabalais, N. N. Nitrogen and phosphorus phytoplankton growth limitation in the northern Gulf of Mexico. *Aquatic Microbial Ecology*, 68(2), 159-169, (2013).
353. Twilley, R. R., Cárdenas, W., Rivera-Monroy, V. H., Espinoza, J., Suescum, R., Armijos, M. M., & Solórzano, L. The Gulf of Guayaquil and the Guayas River estuary, Ecuador.

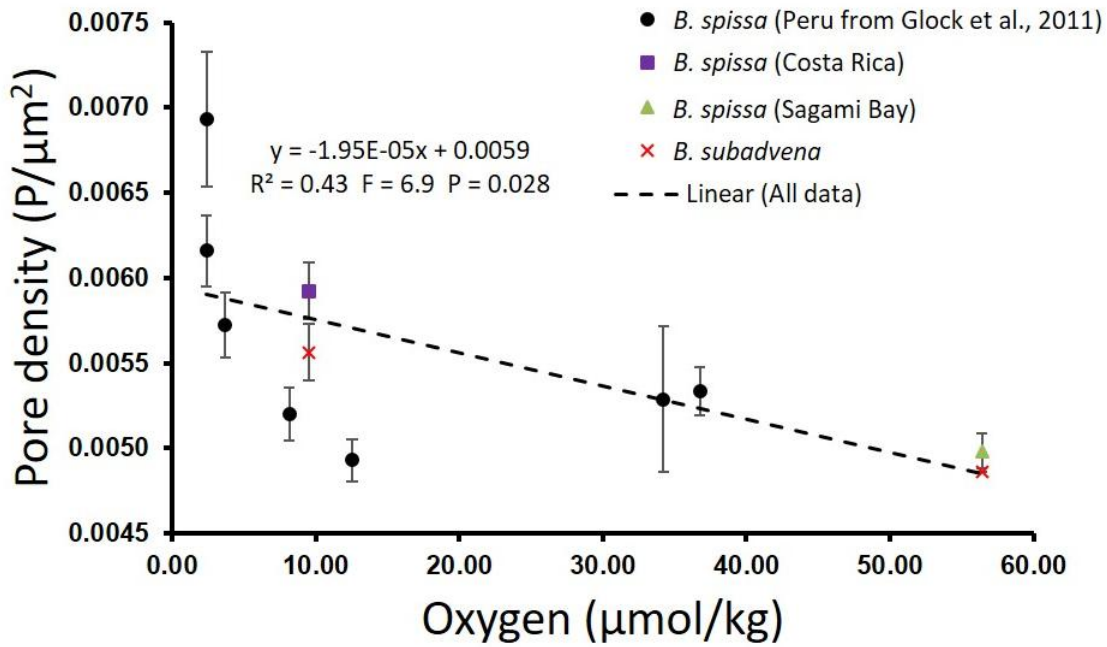
- In Coastal marine ecosystems of Latin America (pp. 245-263). Berlin, Heidelberg: Springer Berlin Heidelberg (2001).
354. Tyrrell, T. The relative influences of nitrogen and phosphorus on oceanic primary production. *Nature*, *400*(6744), 525-531 (1999).
355. Ujiie, H., & Ujiie, Y. Late Quaternary course changes of the Kuroshio Current in the Ryukyu Arc region, northwestern Pacific Ocean. *Marine Micropaleontology*, *37*(1), 23-40 (1999).
356. Van Geen, A., Fairbanks, R. G., Dartnell, P., McGann, M., Gardner, J. V., & Kashgarian, M. Ventilation changes in the northeast Pacific during the last deglaciation. *Paleoceanography*, *11*(5), 519-528 (1996).
357. Vaquer-Sunyer, R., & Duarte, C. M. Thresholds of hypoxia for marine biodiversity. *Proceedings of the National Academy of Sciences*, *105*(40), 15452-15457 (2008).
358. Vedamati, J., Chan, C. & Moffett, J. W. Distribution of dissolved manganese in the Peruvian Upwelling and Oxygen Minimum Zone. *Geochim. Cosmochim. Acta* **156**, 222–240 (2015).
359. Voss, M. *et al.* The marine nitrogen cycle: Recent discoveries, uncertainties and the potential relevance of climate change. *Philos. Trans. R. Soc. B Biol. Sci.* **368**, (2013).
360. Wada, E., and Hattori, A. Nitrogen isotope effects in the assimilation of inorganic nitrogenous compounds by marine diatoms. *Geomicrobiol. J.* *1*, 85–101 (1978).
361. Wada, E., Kadonaga, T., & Matsuo, S.. <sup>15</sup>N abundance in nitrogen of naturally occurring substances and global assessment of denitrification from isotopic viewpoint. *Geochemical Journal*, *9*(3), 139-148 (1975).
362. Waelbroeck, C., Frank, N., Jouzel, J., Parrenin, F., Masson-Delmotte, V., & Genty, D. Transferring radiometric dating of the last interglacial sea level high stand to marine and ice core records. *Earth and Planetary Science Letters*, *265*(1-2), 183-194 (2008).
363. Wakeham, S. G. Organic biogeochemistry in the oxygen-deficient ocean: a review. *Organic Geochemistry*, *149*, 104096 (2020).
364. Wallmann, K. Feedbacks between oceanic redox states and marine productivity: A model perspective focused on benthic phosphorus cycling. *Global Biogeochem. Cycles* **17**, (2003).
365. Wallmann, K., José, Y. S., Hopwood, M. J., Somes, C. J., Dale, A. W., Scholz, F., ... & Oeschler, A. Biogeochemical feedbacks may amplify ongoing and future ocean

- deoxygenation: a case study from the Peruvian oxygen minimum zone. *Biogeochemistry*, 159(1), 45-67 (2022).
366. Wallmann, K., Schneider, B. & Sarntheim, M. Effects of eustatic sea-level change, ocean dynamics, and nutrient utilization on atmospheric pCO<sub>2</sub> and seawater composition over the last 130 000 years: a model study. *Clim. Past*, 12, 339–375 (2016).
367. Wang, T., Ravelo, A. C., Ren, H., Dang, H., Jin, H., Liu, J., & Jian, Z. (2018). Nitrogen isotope variations in the northern South China Sea since marine isotopic stage 3: Reconstructed from foraminifera-bound and bulk sedimentary nitrogen. *Paleoceanography and Paleoclimatology*, 33(6), 594-605 (2018).
368. Wang, Y., Hendy, I. L., & Thunell, R. Local and remote forcing of denitrification in the northeast Pacific for the last 2,000 years. *Paleoceanography and Paleoclimatology*, 34(8), 1517-1533 (2019).
369. Wang, Y., Hendy, I. L., & Zhu, J. Expansion of the Southern California oxygen minimum zone during the early-to mid-Holocene due to reduced ventilation of the Northeast Pacific. *Quaternary Science Reviews*, 238, 106326 (2020).
370. Watson, A. J. Oceans on the edge of anoxia. *Science*, 354(6319), 1529-1530 (2016).
371. Wishner, K. F., Seibel, B. A., Roman, C., Deutsch, C., Outram, D., Shaw, C. T., ... & Riley, S. Ocean deoxygenation and zooplankton: Very small oxygen differences matter. *Science advances*, 4(12), eaau5180 (2018).
372. Woehle, C. *et al.* A Novel Eukaryotic Denitrification Pathway in Foraminifera. *Curr. Biol.* **28**, 2536-2543.e5 (2018).
373. Woehle, C. *et al.* Denitrification in foraminifera has an ancient origin and is complemented by associated bacteria. *Proc. Natl. Acad. Sci. U. S. A.* **119**, (2022).
374. Wong, C. S., Matear, R. J., Freeland, H. J., Whitney, F. A., & Bychkov, A. S. WOCE line P1W in the Sea of Okhotsk: 2. CFCs and the formation rate of intermediate water. *Journal of Geophysical Research: Oceans*, 103(C8), 15625-15642 (1998).
375. Wrightson, L., & Tagliabue, A. Quantifying the impact of climate change on marine diazotrophy: Insights from earth system models. *Frontiers in Marine Science*, 7, 635 (2020).
376. Wyrski, K. An estimate of equatorial upwelling in the Pacific. *J. Phys. Oceanogr.* 11: 1205–1214 (1981).
377. Wyrski, K. Equatorial pacific ocean1. *Int. J. Oceanol. & Limnol.*, 1(2), 117-147 (1967).

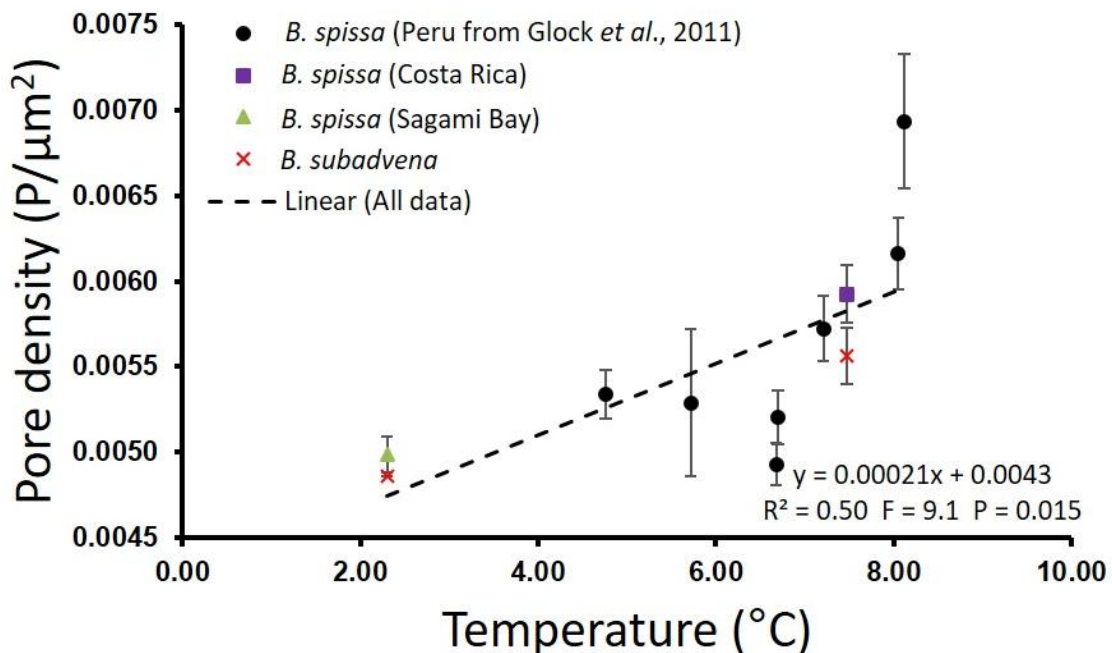
378. Wyrski, K. The oxygen minima in relation to ocean circulation. In *Deep Sea research and oceanographic abstracts* (Vol. 9, No. 1-2, pp. 11-23), Elsevier (1962).
379. Yamamoto, A., Abe-Ouchi, A., Shigemitsu, M., Oka, A., Takahashi, K., Ohgaito, R., & Yamanaka, Y. Global deep ocean oxygenation by enhanced ventilation in the Southern Ocean under long-term global warming. *Global Biogeochemical Cycles*, 29(10), 1801-1815 (2015).
380. Yamamoto, M., Watanabe, S., Tsunogai, S., Wakatsuchi, M. Effects of sea ice formation and diapycnal mixing on the Okhotsk Sea intermediate water clarified with oxygen isotopes. *Deep-Sea Res Part I* 49:1165–1174 (2002).
381. Yamamoto-Kawai, M., Watanabe, S., Tsunogai, S., Wakatsuchi, M. Chlorofluorocarbons in the Sea of Okhotsk: ventilation of the intermediate water. *J Geophys Res* 109, C09S11 (2004).
382. Yoshikawa, C., Nakatsuka, T., Wakatsuchi, M. Distribution of N\* in the Sea of Okhotsk and its use as a biogeochemical tracer of the Okhotsk Sea Intermediate Water formation process. *J Mar Syst* 63:49–62 (2006).

## Appendix A

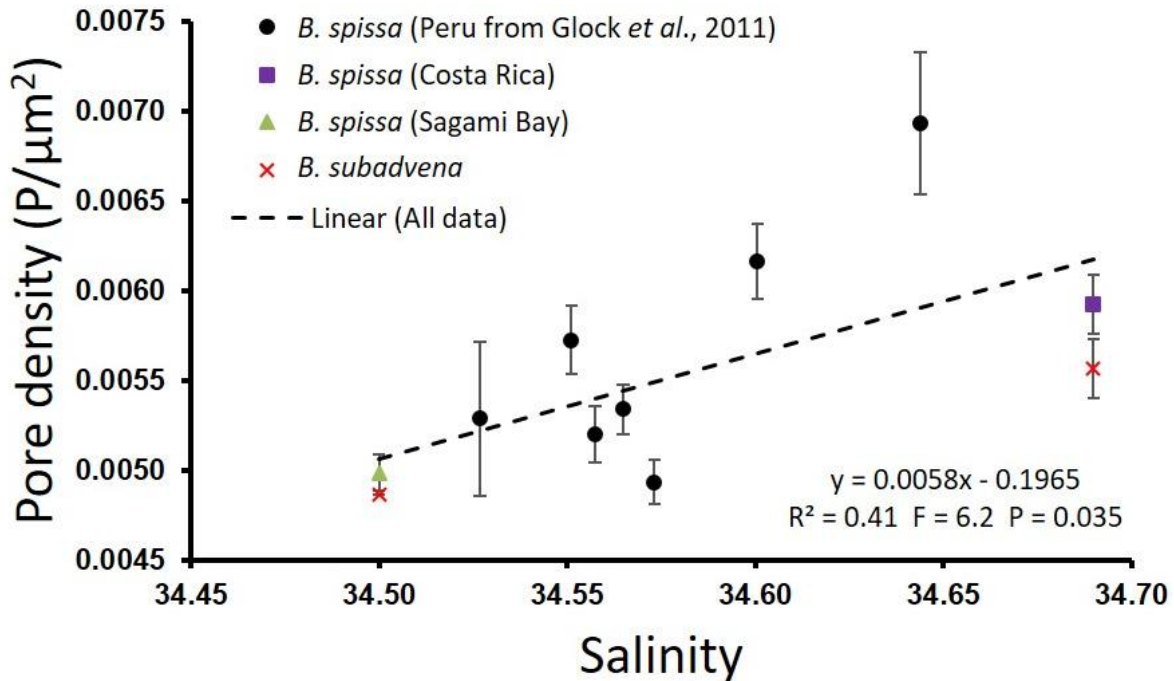
**Supplementary Figure SF1.** Relationship between the mean pore density of different closely related *Bolivina spissa* and *Bolivina subadvena* from core-top samples (Costa Rica and Sagami Bay) and oxygen concentration ( $R^2 = 0.43$ ,  $p = 0.028$ ). The error bars are the standard error of the mean (1SEM).



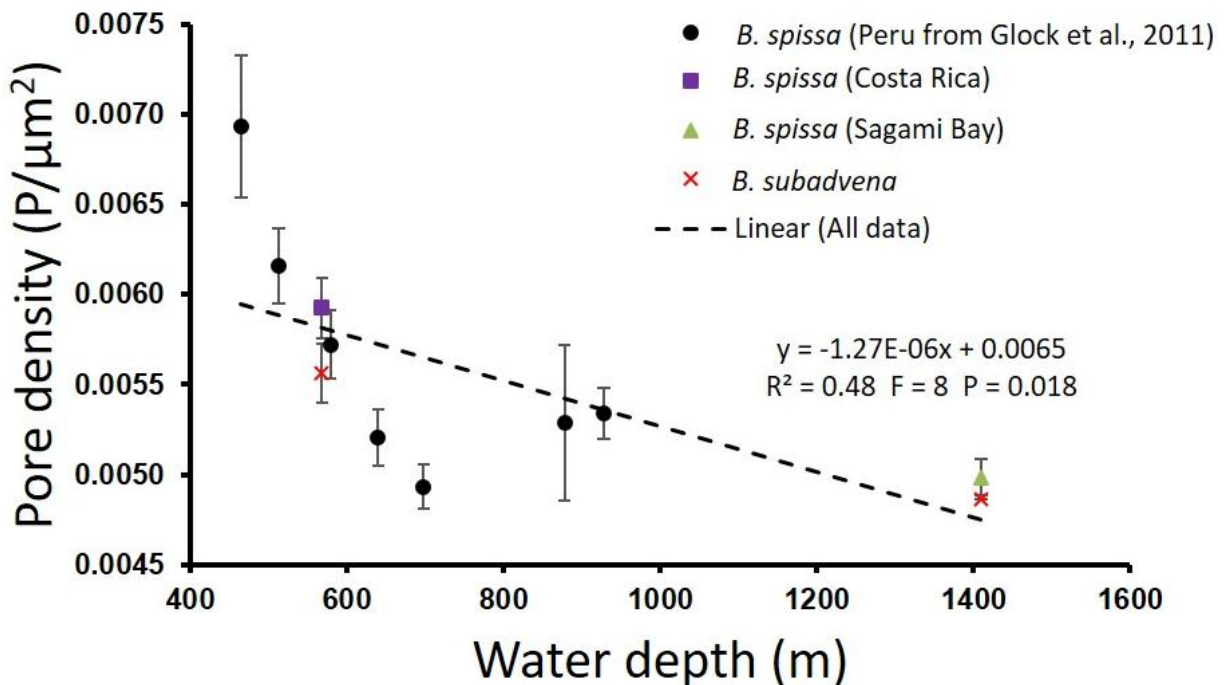
**Supplementary Figure SF2.** Relationship between the mean pore density of different closely related *Bolivina spissa* and *Bolivina subadvena* from core-top samples (Costa Rica and Sagami Bay) and temperature ( $R^2 = 0.50$ ,  $p = 0.015$ ). The error bars are the standard error of the mean (1SEM).



**Supplementary Figure SF3.** Relationship between the mean pore density of different closely related *Bolivina spissa* and *Bolivina subadvena* from core-top samples (Costa Rica and Sagami Bay) and salinity ( $R^2=0.41$ ,  $p = 0.035$ ). The error bars are the standard error of the mean (1SEM).



**Supplementary Figure SF4.** Relationship between the mean pore density of different closely related *Bolivina spissa* and *Bolivina subadvena* from core-top samples (Costa Rica and Sagami Bay) and water depth. The error bars are the standard error of the mean (1SEM).



**Supplementary Table ST1.** Details of manual and automatic (deep-learning) pore density calculations of a total of 31 specimens belonging to species *B. spissa* (27 specimens) *B. subadvena* (3 specimens) and *B. subadvena* *accumeata* (1 specimen) from core-top samples (Costa Rica and Sagami Bay). “Sp” is the Specimen number.

Species	Manual			Automatic		
	Sp	Pores	Pore Density	Sp	Pores	Pore Density
<i>B. spissa</i>	8	311	0.006196453	8	306	0.00609683
<i>B. spissa</i>	54	348	0.006342379	54	341	0.0062148
<i>B. spissa</i>	3	259	0.005502443	3	237	0.00503505
<i>B. spissa</i>	4	242	0.004273504	4	222	0.00392032
<i>B. spissa</i>	5	309	0.006052178	5	311	0.00609135
<i>B. spissa</i>	6	389	0.006589981	6	354	0.00599705
<i>B. spissa</i>	7	219	0.004746115	7	212	0.00459441
<i>B. spissa</i>	8	184	0.004955028	8	178	0.00479345
<i>B. spissa</i>	9	348	0.006864041	9	317	0.00625259
<i>B. spissa</i>	10	345	0.005906017	10	326	0.00558076
<i>B. spissa</i>	11	354	0.00675637	11	343	0.00654643
<i>B. spissa</i>	15	252	0.005329017	15	232	0.00457901
<i>B. spissa</i>	16	378	0.006656922	16	371	0.00653365
<i>B. spissa</i>	17	209	0.003783559	17	209	0.00378356
<i>B. spissa</i>	18	296	0.006639302	18	308	0.00690846
<i>B. spissa</i>	19	349	0.006533501	19	349	0.0065335
<i>B. spissa</i>	20	325	0.006371175	20	319	0.00625355
<i>B. spissa</i>	21	354	0.005902558	21	360	0.0060026
<i>B. spissa</i>	22	353	0.006176728	22	349	0.00610674
<i>B. spissa</i>	23	260	0.004781521	23	260	0.00478152
<i>B. spissa</i>	24	156	0.003108746	24	159	0.00316853
<i>B. spissa</i>	26	449	0.007404933	26	443	0.00822152
<i>B. spissa</i>	27	435	0.00787915	27	420	0.00760746
<i>B. spissa</i>	28	460	0.007326141	28	457	0.00832847
<i>B. spissa</i>	32	265	0.004903866	32	286	0.00529247
<i>B. spissa</i>	36	317	0.005374339	36	311	0.00527262
<i>B. spissa</i>	43	332	0.006275399	43	330	0.0062376
<i>B. subadvena</i>	38	235	0.004075262	38	283	0.00490766
<i>B. subadvena</i>	39	259	0.004833893	39	286	0.00533781
<i>B. subadvena</i>	40	303	0.005723785	40	320	0.00604492
<i>B. subadvena</i> <i>accumeata</i>	31	496	0.008653628	31	520	0.00907235

**Supplementary Table ST2.** Results of statistical analysis on pore measurements with manual corrections (Total number of pores =8,194; number of specimens = 858)

Depth (cm)	Location	Pore density (P/ $\mu\text{m}^2$ )	Mean pore area ( $\mu\text{m}^2$ )	Porosity (%)
8	Gulf of Guayaquil	0.0042	19.82	8.31
53	Gulf of Guayaquil	0.0042	19.16	7.99
588	Gulf of Guayaquil	0.0043	15.42	6.60
18.5	Mexican Margin	0.0057	18.41	10.43
43.5	Mexican Margin	0.0056	19.63	10.92

**Supplementary Table ST3.** Results of statistical analysis on pore measurements without manual corrections (Total number of pores = 7,788; number of specimens = 858)

Depth (cm)	Location	Pore density (P/ $\mu\text{m}^2$ )	Mean pore area ( $\mu\text{m}^2$ )	Porosity (%)
8	Gulf of Guayaquil	0.0041	20.09	8.2
53	Gulf of Guayaquil	0.0041	19.58	7.97
588	Gulf of Guayaquil	0.0042	15.31	6.37
18.5	Mexican Margin	0.0055	18.94	10.3
43.5	Mexican Margin	0.0053	20.39	10.78

**Supplementary Table ST4.** Statistical results of mean + standard deviation (SD) of all pore parameters of *B. spissa* all locations used.

Pore parameter	Mean $\pm$ SD Gulf of Guayaquil	Mean $\pm$ SD Mexican Margin	Mean $\pm$ SD Sea of Okhotsk	Mean $\pm$ SD Core-top samples
Pore density	0.0043 $\pm$ 0.0008	0.0054 $\pm$ 0.0009	0.0053 $\pm$ 0.0009	0.0054 $\pm$ 0.001
Porosity	7.14 $\pm$ 1.62	9.69 $\pm$ 1.56	10.83 $\pm$ 1.66	9.33 $\pm$ 1.41
Mean Pore area	17.13 $\pm$ 4.37	18.03 $\pm$ 2.63	20.67 $\pm$ 3.54	17.41 $\pm$ 2.73

**Supplementary Table ST5.** Results of linear regression tests performed between porosity and mean pore size measurements of *B. spissa* from different studied locations.

Location	R square	p value	Significance
Gulf of Guayaquil	0.45	5.91E-89	P < 0.05
Mexican Margin	0.072	6.86E-09	P < 0.05
Sea of Okhotsk	0.12	2.56E-05	P < 0.05
Core-top samples	0.052	0.047	P < 0.05
All data	0.27	3.19E-93	P < 0.05

**Supplementary Table ST6.** Results of linear regression tests performed between porosity and pore density measurements of *B. spissa* from different of studied locations.

Location	R square	P value	Significance
Gulf of Guayaquil	0.1	3.2141E-17	P < 0.05
Mexican Margin	0.45	3.45E-60	P < 0.05
Sea of Okhotsk	0.3	7.46E-13	P < 0.05
Core-top samples	0.35	2.34E-08	P < 0.05
All data	0.42	1.36E-15	P < 0.05

**Supplementary Table ST7.** Results of linear regression tests performed between pore density and mean pore size measurements of *B. spissa* from different studied locations.

Location	R square	p value	Significance
Gulf of Guayaquil	0.2	4.52E-35	P < 0.05
Mexican Margin	0.27	4.2E-33	P < 0.05
Sea of Okhotsk	0.33	3.55E-14	P < 0.05
Core-top samples	0.40	7.18E-10	P < 0.05
All data	0.085	1.34E-27	P < 0.05

**Supplementary Table ST8.** Data table showing analysed porosity, pore density, mean pore size of *Bolivina spissa* from Gulf of Guayaquil (M77/2-59-01), Mexican Margin (MAZ-1E-04), Sea of Okhotsk (MDO1-2415), and the core-top samples – Sagami Bay (Japan), continental margin off Costa Rica (SO206-43-MUC).

Appendix A

Core	Specimen#	Depth	Pore density (P/ $\mu\text{m}^2$ )	Porosity (%)	Mean pore size ( $\mu\text{m}^2$ )
M77/2-59-01	1	8cm	0.004260843	10.66402777	25.02797817
M77/2-59-01	2	8cm	0.002684386	6.837264275	25.4705
M77/2-59-01	3	8cm	0.004842464	8.851721514	18.2793737
M77/2-59-01	4	8cm	0.003275603	7.858078435	23.98971264
M77/2-59-01	7	8cm	0.00497003	9.936473323	19.99278195
M77/2-59-01	8	8cm	0.005244183	9.24795006	17.63468235
M77/2-59-01	9	8cm	0.005139345	8.873932191	17.26666071
M77/2-59-01	10	8cm	0.004269753	7.77768444	18.21577294
M77/2-59-01	11	8cm	0.004709253	9.086162313	19.294275
M77/2-59-01	12	8cm	0.00377459	5.779255352	15.31094933
M77/2-59-01	13	8cm	0.004532813	8.272257324	18.24972069
M77/2-59-01	14	8cm	0.003273282	7.355363336	22.47091
M77/2-59-01	15	8cm	0.004175088	8.456442056	20.2545253
M77/2-59-01	17	8cm	0.004335014	8.554689296	19.73393654
M77/2-59-01	18	8cm	0.00404215	7.87899386	19.49208698
M77/2-59-01	39	8cm	0.004348929	7.634169414	17.55413776
M77/2-59-01	40	8cm	0.004281714	7.100572428	16.58348214
M77/2-59-01	41	8cm	0.004168818	8.523214386	20.44515708
M77/2-59-01	42	8cm	0.003941346	8.684854034	22.03524977
M77/2-59-01	43	8cm	0.004608448	8.846676925	19.19665
M77/2-59-01	3	53cm	0.003926804	7.499542518	19.0983375
M77/2-59-01	4	53cm	0.003477113	7.76444254	22.33014249
M77/2-59-01	5	53cm	0.004640917	8.365028375	18.02451691
M77/2-59-01	6	53cm	0.004186275	7.01441734	16.75575
M77/2-59-01	7	53cm	0.004306593	7.352906972	17.07360628
M77/2-59-01	8	53cm	0.004414298	7.988701644	18.09733259
M77/2-59-01	9	53cm	0.003394611	6.513602171	19.18806597
M77/2-59-01	10	53cm	0.004296492	8.438300938	19.63997773
M77/2-59-01	11	53cm	0.003808371	6.831108476	17.93708654
M77/2-59-01	13	53cm	0.004208873	8.443432876	20.06102869
M77/2-59-01	15	53cm	0.00449057	8.515260474	18.9625392
M77/2-59-01	16	53cm	0.005595825	9.883481366	17.66224198
M77/2-59-01	17	53cm	0.004017578	7.083227224	17.63058971
M77/2-59-01	18	53cm	0.004105456	8.10177391	19.734165
M77/2-59-01	19	53cm	0.004915923	9.27497932	18.86721986
M77/2-59-01	20	53cm	0.004774829	7.71346049	16.154424
M77/2-59-01	23	53cm	0.003347164	8.523644603	25.465275
M77/2-59-01	24	53cm	0.004850697	8.489130165	17.50084787
M77/2-59-01	25	53cm	0.003493764	7.626491924	21.8288722

Appendix A

M77/2-59-01	26	53cm	0.004058354	8.575203765	21.12975652
M77/2-59-01	1	68cm	0.0052588	9.406583095	17.88732
M77/2-59-01	2	68cm	0.003926768	6.266301653	15.95791343
M77/2-59-01	4	68cm	0.00328788	6.526650438	19.85063313
M77/2-59-01	5	68cm	0.004551247	8.716753468	19.15245
M77/2-59-01	6	68cm	0.005150309	8.906275991	17.29270213
M77/2-59-01	7	68cm	0.003572711	7.623079844	21.33696293
M77/2-59-01	8	68cm	0.004548348	7.782187138	17.10991931
M77/2-59-01	9	68cm	0.003077078	7.805106698	25.36532308
M77/2-59-01	10	68cm	0.004406434	9.336402264	21.18811255
M77/2-59-01	11	68cm	0.004733951	10.02095933	21.16827778
M77/2-59-01	12	68cm	0.004804594	8.952200039	18.63258453
M77/2-59-01	13	68cm	0.004602101	9.062896242	19.69295393
M77/2-59-01	14	68cm	0.004885907	9.099738543	18.62446235
M77/2-59-01	15	68cm	0.004619162	8.40787461	18.20216339
M77/2-59-01	17	68cm	0.005214331	9.081792914	17.4169861
M77/2-59-01	18	68cm	0.004116695	9.385013806	22.79745
M77/2-59-01	19	68cm	0.003903137	8.268479744	21.18419135
M77/2-59-01	20	68cm	0.003207211	7.168574496	22.35142582
M77/2-59-01	21	68cm	0.003460457	9.062875666	26.18982414
M77/2-59-01	1	93cm	0.004269613	8.196290568	19.19680125
M77/2-59-01	2	93cm	0.003571567	7.758192003	21.72209707
M77/2-59-01	3	93cm	0.003927204	7.775005197	19.79781549
M77/2-59-01	4	93cm	0.004749504	8.634607026	18.18001731
M77/2-59-01	5	93cm	0.004483306	9.119711183	20.34148696
M77/2-59-01	8	93cm	0.00367714	8.66266556	23.55815821
M77/2-59-01	13	93cm	0.003835933	6.820871889	17.78152075
M77/2-59-01	14	93cm	0.00412198	5.59347986	13.56988696
M77/2-59-01	17	93cm	0.004519851	8.660378707	19.16075976
M77/2-59-01	22	93cm	0.003347164	7.503112998	22.41632919
M77/2-59-01	23	93cm	0.005235324	7.908650045	15.10632391
M77/2-59-01	24	93cm	0.004927393	10.02172844	20.33880357
M77/2-59-01	26	93cm	0.004878518	9.535201203	19.54528125
M77/2-59-01	28	93cm	0.004608115	9.089862583	19.72576988
M77/2-59-01	29	93cm	0.003811738	8.369152246	21.95626082
M77/2-59-01	30	93cm	0.003869089	9.253167418	23.91562262
M77/2-59-01	31	93cm	0.003772226	8.588754638	22.76839714
M77/2-59-01	32	93cm	0.006183019	10.67249332	17.26097411
M77/2-59-01	33	93cm	0.004810501	8.983459681	18.6746874
M77/2-59-01	34	93cm	0.003870978	8.754365689	22.615384

Appendix A

M77/2-59-01	1	188cm	0.004243171	9.431482376	22.22743696
M77/2-59-01	2	188cm	0.004488649	7.021297967	15.64233991
M77/2-59-01	5	188cm	0.003416456	8.283856473	24.24693121
M77/2-59-01	6	188cm	0.003764149	6.780534597	18.01345872
M77/2-59-01	8	188cm	0.003981107	7.054756681	17.7205894
M77/2-59-01	12	188cm	0.003452527	7.320480997	21.20325587
M77/2-59-01	13	188cm	0.004880571	8.48160714	17.37830769
M77/2-59-01	15	188cm	0.003019322	6.95216748	23.02558824
M77/2-59-01	16	188cm	0.003618414	7.22985767	19.98073596
M77/2-59-01	17	188cm	0.004249056	7.961391978	18.73685
M77/2-59-01	19	188cm	0.003223368	6.775174763	21.01893051
M77/2-59-01	20	188cm	0.003229956	6.593532463	20.4136918
M77/2-59-01	21	188cm	0.003295299	7.388814796	22.42228776
M77/2-59-01	25	188cm	0.004421454	6.845020766	15.48137835
M77/2-59-01	28	188cm	0.003346254	6.822610623	20.3888025
M77/2-59-01	35	188cm	0.003918613	8.081707347	20.6239
M77/2-59-01	38	188cm	0.003637687	7.871324903	21.63826583
M77/2-59-01	39	188cm	0.0041941	7.5547703	18.0128504
M77/2-59-01	1	228cm	0.0035351	8.173320772	23.12048041
M77/2-59-01	2	228cm	0.004591555	8.223930388	17.91099101
M77/2-59-01	3	228cm	0.004119209	9.004055275	21.85870084
M77/2-59-01	4	228cm	0.002545611	4.777096594	18.76600827
M77/2-59-01	5	228cm	0.004698455	9.397581719	20.00142964
M77/2-59-01	6	228cm	0.003987478	7.042541141	17.661644
M77/2-59-01	7	228cm	0.00404667	10.11255049	24.98980462
M77/2-59-01	8	228cm	0.003631281	8.344565075	22.97967554
M77/2-59-01	9	228cm	0.00311292	6.328813128	20.33079231
M77/2-59-01	10	228cm	0.004657881	8.881847896	19.06843205
M77/2-59-01	11	228cm	0.004212406	9.765190206	23.18197683
M77/2-59-01	12	228cm	0.004005875	7.746093221	19.33683094
M77/2-59-01	13	228cm	0.005221531	9.776715671	18.72384894
M77/2-59-01	19	228cm	0.004148016	8.114929784	19.56340253
M77/2-59-01	21	228cm	0.004668869	9.39371228	20.1198891
M77/2-59-01	22	228cm	0.005900526	11.02069154	18.67747434
M77/2-59-01	24	228cm	0.002903521	6.354574189	21.8857526
M77/2-59-01	25	228cm	0.003656005	8.217737237	22.47736901
M77/2-59-01	27	228cm	0.005215294	8.388262391	16.08396949
M77/2-59-01	28	228cm	0.005203403	9.45756326	18.17572718

Appendix A

M77/2-59-01	3	308cm	0.004540673	7.71625801	16.99364333
M77/2-59-01	4	308cm	0.004133941	6.647615785	16.08057876
M77/2-59-01	6	308cm	0.004353709	7.157432791	16.43985
M77/2-59-01	7	308cm	0.005571783	8.565724306	15.37339904
M77/2-59-01	8	308cm	0.003505477	8.018126629	22.87314293
M77/2-59-01	9	308cm	0.003957895	6.219356018	15.71379652
M77/2-59-01	10	308cm	0.004111409	6.465102235	15.72478448
M77/2-59-01	12	308cm	0.003960789	7.437942928	18.77894034
M77/2-59-01	13	308cm	0.004564113	6.05393436	13.26420776
M77/2-59-01	14	308cm	0.004717995	8.034263406	17.02897871
M77/2-59-01	18	308cm	0.003651738	7.656886782	20.9677875
M77/2-59-01	20	308cm	0.005211913	8.419604895	16.15453714
M77/2-59-01	21	308cm	0.004057863	6.369197594	15.69594074
M77/2-59-01	22	308cm	0.00343689	6.396514748	18.61134337
M77/2-59-01	23	308cm	0.004170561	7.812778156	18.73315714
M77/2-59-01	26	308cm	0.003415326	6.24585699	18.28773257
M77/2-59-01	31	308cm	0.004351916	5.623530478	12.92196552
M77/2-59-01	32	308cm	0.004804563	6.005937243	12.50048717
M77/2-59-01	33	308cm	0.003413824	6.238987353	18.27565385
M77/2-59-01	34	308cm	0.00328725	7.379241223	22.44807047
M77/2-59-01	1	348cm	0.006713725	9.177204345	13.66931739
M77/2-59-01	2	348cm	0.004380942	8.64947011	19.74340116
M77/2-59-01	3	348cm	0.004499141	8.010475571	17.80445489
M77/2-59-01	4	348cm	0.003636981	7.724152821	21.23781702
M77/2-59-01	6	348cm	0.003077846	4.963573181	16.12677363
M77/2-59-01	9	348cm	0.004194574	7.437589925	17.73145663
M77/2-59-01	10	348cm	0.003598518	5.299653036	14.72732165
M77/2-59-01	12	348cm	0.003403515	6.621900823	19.45606294
M77/2-59-01	15	348cm	0.004031619	7.761990908	19.25278702
M77/2-59-01	16	348cm	0.005570089	8.546420575	15.34341735
M77/2-59-01	17	348cm	0.005217992	5.661032137	10.84906314
M77/2-59-01	21	348cm	0.005713206	6.481964144	11.34558165
M77/2-59-01	22	348cm	0.00349424	6.186384105	17.70451728
M77/2-59-01	27	348cm	0.003939003	6.621291766	16.80956422
M77/2-59-01	28	348cm	0.003939804	7.545118665	19.151
M77/2-59-01	29	348cm	0.004273138	6.55593232	15.342195
M77/2-59-01	30	348cm	0.003446187	6.893855351	20.00429563
M77/2-59-01	31	348cm	0.004750344	8.332109683	17.54001184
M77/2-59-01	32	348cm	0.00436164	7.011726439	16.0758931

Appendix A

M77/2-59-01	2	468cm	0.004830005	8.249670556	17.08004472
M77/2-59-01	3	468cm	0.004692763	5.754218231	12.26189889
M77/2-59-01	5	468cm	0.004771742	6.807138026	14.26551923
M77/2-59-01	7	468cm	0.004302378	6.996951089	16.26298548
M77/2-59-01	8	468cm	0.004584136	7.270329171	15.85975858
M77/2-59-01	10	468cm	0.005302192	7.562419804	14.26281792
M77/2-59-01	11	468cm	0.003348813	6.437432603	19.223028
M77/2-59-01	12	468cm	0.003758213	6.410738285	17.05794505
M77/2-59-01	13	468cm	0.003650176	5.12852961	14.05008904
M77/2-59-01	14	468cm	0.004945262	7.558229697	15.28378163
M77/2-59-01	15	468cm	0.004690467	6.908061325	14.72787422
M77/2-59-01	17	468cm	0.005181353	9.317576238	17.9829029
M77/2-59-01	18	468cm	0.004603019	6.182521419	13.43144815
M77/2-59-01	21	468cm	0.004225017	5.450649466	12.90089483
M77/2-59-01	24	468cm	0.005269414	6.873773573	13.04466429
M77/2-59-01	1	508cm	0.005166974	6.430914705	12.44619215
M77/2-59-01	2	508cm	0.003964808	7.224910877	18.2226
M77/2-59-01	3	508cm	0.003042819	6.988098809	22.96587035
M77/2-59-01	4	508cm	0.004411279	7.382377065	16.73523077
M77/2-59-01	5	508cm	0.005272413	6.398945786	12.13665588
M77/2-59-01	6	508cm	0.003886717	5.620855011	14.46170542
M77/2-59-01	7	508cm	0.003914648	4.620127284	11.80215385
M77/2-59-01	8	508cm	0.006309978	7.82702198	12.40419761
M77/2-59-01	10	508cm	0.004288498	6.265294172	14.60952983
M77/2-59-01	11	508cm	0.003659148	5.863630718	16.02457887
M77/2-59-01	12	508cm	0.003931591	5.640287437	14.34606894
M77/2-59-01	13	508cm	0.003750657	7.456846174	19.88144151
M77/2-59-01	15	508cm	0.004136603	6.38278049	15.43000345
M77/2-59-01	16	508cm	0.003567975	5.591455511	15.67122857
M77/2-59-01	18	508cm	0.003526838	6.179982454	17.52272802
M77/2-59-01	20	508cm	0.003922913	3.672313677	9.361191304
M77/2-59-01	25	508cm	0.003211347	6.032284752	18.78428343
M77/2-59-01	27	508cm	0.005151655	8.497894014	16.49546523
M77/2-59-01	28	508cm	0.00409757	6.538662646	15.95741659
M77/2-59-01	30	508cm	0.00380254	7.516497192	19.767044
M77/2-59-01	1	588cm	0.003015782	5.679297409	18.83192143
M77/2-59-01	2	588cm	0.004837063	7.114652705	14.70862038
M77/2-59-01	3	588cm	0.003624412	5.617463701	15.49896563
M77/2-59-01	4	588cm	0.004959745	7.70253498	15.53010306

Appendix A

M77/2-59-01	6	588cm	0.003957264	8.021599731	20.27057015
M77/2-59-01	7	588cm	0.005025633	7.199406827	14.32537306
M77/2-59-01	8	588cm	0.004870265	6.388013991	13.11635769
M77/2-59-01	9	588cm	0.003921637	6.88456569	17.55533668
M77/2-59-01	10	588cm	0.004612986	7.102531099	15.39681967
M77/2-59-01	11	588cm	0.004853735	5.441811123	11.21159531
M77/2-59-01	12	588cm	0.003779169	6.699143499	17.7265
M77/2-59-01	13	588cm	0.005631235	7.475836804	13.27566216
M77/2-59-01	14	588cm	0.002965015	4.67548998	15.76885962
M77/2-59-01	15	588cm	0.005406454	7.404535669	13.69573333
M77/2-59-01	18	588cm	0.003837057	3.848522687	10.02988274
M77/2-59-01	20	588cm	0.004279889	6.721292845	15.70436189
M77/2-59-01	22	588cm	0.004040952	6.588238876	16.3036792
M77/2-59-01	23	588cm	0.004546216	7.460139777	16.40955809
M77/2-59-01	25	588cm	0.004399927	7.007490062	15.92637973
M77/2-59-01	28	588cm	0.004089243	7.021601065	17.17090833
M77/2-59-01	1	628cm	0.004422886	7.517675248	16.99721781
M77/2-59-01	2	628cm	0.004399232	6.501257432	14.7781656
M77/2-59-01	3	628cm	0.004243497	6.383522143	15.04306988
M77/2-59-01	4	628cm	0.003935981	5.985657721	15.20753745
M77/2-59-01	5	628cm	0.004197785	6.173578958	14.70675395
M77/2-59-01	6	628cm	0.003655857	5.841150504	15.97751152
M77/2-59-01	7	628cm	0.004166296	6.070832836	14.57129348
M77/2-59-01	8	628cm	0.004853591	6.525226521	13.44412048
M77/2-59-01	9	628cm	0.004361743	6.470094332	14.83373571
M77/2-59-01	10	628cm	0.00376818	6.471637015	17.1744375
M77/2-59-01	11	628cm	0.003653875	4.467644796	12.2271403
M77/2-59-01	13	628cm	0.003894543	5.592477248	14.35977931
M77/2-59-01	14	628cm	0.004396609	4.843463006	11.01636076
M77/2-59-01	15	628cm	0.005179633	5.353190804	10.33507723
M77/2-59-01	16	628cm	0.004932283	5.404850522	10.9581106
M77/2-59-01	17	628cm	0.003845675	5.891791582	15.320567
M77/2-59-01	19	628cm	0.005021939	7.011041445	13.96082553
M77/2-59-01	20	628cm	0.004671559	5.621992195	12.03450934
M77/2-59-01	21	628cm	0.004589306	4.455114266	9.707598876
M77/2-59-01	23	628cm	0.004237718	8.518941945	20.10266314
M77/2-59-01	1	708cm	0.004353985	6.277769503	14.41844643
M77/2-59-01	3	708cm	0.003826501	6.175289793	16.13821579
M77/2-59-01	4	708cm	0.005822666	7.806286029	13.40672143
M77/2-59-01	6	708cm	0.005999089	6.740129304	11.23525559

Appendix A

M77/2-59-01	7	708cm	0.007238777	10.66588296	14.73437074
M77/2-59-01	8	708cm	0.003309967	6.526831359	19.71872155
M77/2-59-01	9	708cm	0.003487942	6.557556867	18.80065
M77/2-59-01	11	708cm	0.005412996	8.358949055	15.44237129
M77/2-59-01	12	708cm	0.00429195	6.375083929	14.85358448
M77/2-59-01	13	708cm	0.004745648	6.960912788	14.66799231
M77/2-59-01	17	708cm	0.00460089	6.988550987	15.18956277
M77/2-59-01	18	708cm	0.004938909	5.363531885	10.85975
M77/2-59-01	19	708cm	0.003968368	6.369853447	16.0515683
M77/2-59-01	20	708cm	0.004173395	5.407435006	12.956922
M77/2-59-01	22	708cm	0.005008994	7.683872849	15.34015313
M77/2-59-01	23	708cm	0.004579764	8.574952408	18.72356836
M77/2-59-01	25	708cm	0.004884682	9.118033637	18.66658655
M77/2-59-01	26	708cm	0.004253362	5.882527192	13.8303
M77/2-59-01	27	708cm	0.00423581	6.920876729	16.33896802
M77/2-59-01	30	708cm	0.004934045	8.71411232	17.66119315
M77/2-59-01	1	748cm	0.004199348	5.55709244	13.23322759
M77/2-59-01	2	748cm	0.003520776	5.880316342	16.70176166
M77/2-59-01	3	748cm	0.003495353	5.889286595	16.84890429
M77/2-59-01	4	748cm	0.003958275	6.362835798	16.07477143
M77/2-59-01	7	748cm	0.004622906	5.822668233	12.59525581
M77/2-59-01	10	748cm	0.00320452	4.72416499	14.74219421
M77/2-59-01	11	748cm	0.005635663	7.809738633	13.8577102
M77/2-59-01	12	748cm	0.0034915	5.97140197	17.10268516
M77/2-59-01	13	748cm	0.004203405	4.256505666	10.12632731
M77/2-59-01	14	748cm	0.004725227	7.870850251	16.65708233
M77/2-59-01	15	748cm	0.003814416	6.220099225	16.30681974
M77/2-59-01	16	748cm	0.004579054	6.688340421	14.60637918
M77/2-59-01	17	748cm	0.005079652	4.597960994	9.051724585
M77/2-59-01	18	748cm	0.003934079	5.603392072	14.2432125
M77/2-59-01	19	748cm	0.004025555	5.804780246	14.41982596
M77/2-59-01	20	748cm	0.004702359	5.586748054	11.88073477
M77/2-59-01	22	748cm	0.0046752	7.488230331	16.01692125
M77/2-59-01	23	748cm	0.00475373	5.764696922	12.12668094
M77/2-59-01	24	748cm	0.003755103	6.501405143	17.31352174
M77/2-59-01	26	748cm	0.004322092	3.349170707	7.748956627
M77/2-59-01	2	828cm	0.004274325	7.637618534	17.86859609
M77/2-59-01	3	828cm	0.004047145	4.671579629	11.54290046
M77/2-59-01	6	828cm	0.003269621	6.413643738	19.61586
M77/2-59-01	8	828cm	0.004138031	6.592952706	15.93258412

Appendix A

M77/2-59-01	9	828cm	0.004650899	7.247575066	15.58317115
M77/2-59-01	13	828cm	0.00334405	5.709548138	17.07375405
M77/2-59-01	15	828cm	0.004023472	6.117949726	15.20564866
M77/2-59-01	16	828cm	0.004242068	4.914753629	11.58575
M77/2-59-01	18	828cm	0.003880726	5.704080632	14.69848894
M77/2-59-01	20	828cm	0.004867404	6.685682416	13.73562201
M77/2-59-01	21	828cm	0.003758391	8.329220436	22.16166368
M77/2-59-01	22	828cm	0.003702534	4.941580453	13.3464806
M77/2-59-01	23	828cm	0.004789415	9.06615727	18.92957286
M77/2-59-01	24	828cm	0.00455091	7.197738838	15.81604444
M77/2-59-01	25	828cm	0.003914477	5.642448317	14.41430791
M77/2-59-01	26	828cm	0.00401163	3.803833384	9.48201375
M77/2-59-01	27	828cm	0.004088837	7.00797976	17.13929731
M77/2-59-01	28	828cm	0.00329668	3.820038524	11.58753316
M77/2-59-01	32	828cm	0.003221152	6.408484101	19.89500718
M77/2-59-01	33	828cm	0.00340426	6.672228675	19.59964541
M77/2-59-01	7	868cm	0.004140612	4.726367538	11.41465805
M77/2-59-01	8	868cm	0.004347491	6.85004456	15.75631614
M77/2-59-01	10	868cm	0.004792296	6.775267464	14.13783034
M77/2-59-01	11	868cm	0.005202833	6.073573301	11.67358872
M77/2-59-01	12	868cm	0.003697043	7.359714859	19.90702836
M77/2-59-01	14	868cm	0.003653656	5.66447563	15.50358082
M77/2-59-01	15	868cm	0.004418844	7.176422877	16.2405
M77/2-59-01	16	868cm	0.00551229	5.463980055	9.912359032
M77/2-59-01	17	868cm	0.003767675	6.067813688	16.10492958
M77/2-59-01	18	868cm	0.003248329	6.66256013	20.51073051
M77/2-59-01	20	868cm	0.004765855	6.493508374	13.62506538
M77/2-59-01	23	868cm	0.002922934	8.182747644	27.99497885
M77/2-59-01	24	868cm	0.007095786	5.486783711	7.732454198
M77/2-59-01	27	868cm	0.003248171	2.659645444	8.188133684
M77/2-59-01	29	868cm	0.004509093	6.44905653	14.30233494
M77/2-59-01	30	868cm	0.003617292	5.069191432	14.01377283
M77/2-59-01	31	868cm	0.003254189	5.350960965	16.44330165
M77/2-59-01	32	868cm	0.004651939	6.587203205	14.16012258
M77/2-59-01	33	868cm	0.004065484	3.925412123	9.655460748
M77/2-59-01	34	868cm	0.003862937	6.858075968	17.75352857
M77/2-59-01	2	948cm	0.003073564	5.911512476	19.23341538
M77/2-59-01	5	948cm	0.005041421	6.872940184	13.63294332
M77/2-59-01	6	948cm	0.004370366	6.664216784	15.24864534
M77/2-59-01	8	948cm	0.004728118	7.167468694	15.15924149

Appendix A

M77/2-59-01	9	948cm	0.003721478	6.785629843	18.23369689
M77/2-59-01	10	948cm	0.004159178	7.048558711	16.947
M77/2-59-01	13	948cm	0.004578315	4.764620334	10.40693077
M77/2-59-01	14	948cm	0.003569888	5.482312198	15.3571
M77/2-59-01	15	948cm	0.004773737	6.123180346	12.82680667
M77/2-59-01	17	948cm	0.003959648	5.412352782	13.66877368
M77/2-59-01	22	948cm	0.002930708	5.289081373	18.04710993
M77/2-59-01	24	948cm	0.005520543	9.05461102	16.40166635
M77/2-59-01	31	948cm	0.003801191	5.258794642	13.83459868
M77/2-59-01	34	948cm	0.003850591	4.476893183	11.62650789
M77/2-59-01	35	948cm	0.003367963	5.18517948	15.39559421
M77/2-59-01	38	948cm	0.004103945	5.041641658	12.28486696
M77/2-59-01	1	988cm	0.003978707	8.196332071	20.600492
M77/2-59-01	4	988cm	0.003475474	6.5373664	18.81
M77/2-59-01	7	988cm	0.004602789	8.010474216	17.40352308
M77/2-59-01	8	988cm	0.002910196	7.418324741	25.49080479
M77/2-59-01	9	988cm	0.005138678	9.303228658	18.10432362
M77/2-59-01	11	988cm	0.004484687	7.833181032	17.46650743
M77/2-59-01	12	988cm	0.003632536	15.78543239	43.45568526
M77/2-59-01	13	988cm	0.004295013	7.469825594	17.39185771
M77/2-59-01	15	988cm	0.005061231	8.95657272	17.6964309
M77/2-59-01	17	988cm	0.004655516	7.469399919	16.04419213
M77/2-59-01	18	988cm	0.005531386	10.3684456	18.74475281
M77/2-59-01	19	988cm	0.004183046	8.686889091	20.7669
M77/2-59-01	20	988cm	0.005823159	9.549755504	16.399614
M77/2-59-01	23	988cm	0.004937044	7.896383376	15.99415157
M77/2-59-01	24	988cm	0.00461221	7.724950188	16.74891229
M77/2-59-01	25	988cm	0.00379462	6.936900604	18.28088451
M77/2-59-01	26	988cm	0.0037465	7.84748686	20.94618358
M77/2-59-01	27	988cm	0.004378107	6.570452103	15.00751744
M77/2-59-01	30	988cm	0.006151036	8.831656719	14.35799829
M77/2-59-01	35	988cm	0.005467201	9.278958854	16.97204642
M77/2-59-01	2	1068cm	0.00361997	5.475622559	15.12615528
M77/2-59-01	3	1068cm	0.005699942	8.815681982	15.46626699
M77/2-59-01	4	1068cm	0.004233117	6.707652527	15.84565714
M77/2-59-01	5	1068cm	0.003294858	11.3725695	34.51611429
M77/2-59-01	7	1068cm	0.004620213	8.223024053	17.79793373
M77/2-59-01	8	1068cm	0.004272448	8.176423153	19.13756087
M77/2-59-01	10	1068cm	0.0040797	7.912211176	19.3941
M77/2-59-01	12	1068cm	0.00491048	7.019897227	14.29574667

Appendix A

M77/2-59-01	15	1068cm	0.004579122	9.058732643	19.78268427
M77/2-59-01	17	1068cm	0.004086145	5.692779941	13.93190962
M77/2-59-01	22	1068cm	0.005727411	7.187675396	12.54960616
M77/2-59-01	23	1068cm	0.003434197	6.76986636	19.7131
M77/2-59-01	26	1068cm	0.002675271	3.957195183	14.79175274
M77/2-59-01	27	1068cm	0.007038487	7.614199713	10.81795
M77/2-59-01	28	1068cm	0.005764382	7.466303729	12.95247994
M77/2-59-01	30	1068cm	0.003530599	7.771039405	22.01054362
M77/2-59-01	34	1068cm	0.003602987	7.49778113	20.80990102
M77/2-59-01	36	1068cm	0.002821163	6.901309291	24.46264118
M77/2-59-01	37	1068cm	0.003866896	12.89725906	33.35299846
M77/2-59-01	41	1068cm	0.004616789	9.804358042	21.23631269
M77/2-59-01	2	1148cm	0.004111627	6.53397398	15.89145451
M77/2-59-01	4	1148cm	0.004973455	8.039135701	16.1640875
M77/2-59-01	5	1148cm	0.003400238	6.96857041	20.49435771
M77/2-59-01	6	1148cm	0.004592205	3.635470292	7.916611154
M77/2-59-01	7	1148cm	0.003305847	6.541784084	19.78852615
M77/2-59-01	8	1148cm	0.007465409	6.948333219	9.307371127
M77/2-59-01	10	1148cm	0.004576977	9.032001199	19.7335512
M77/2-59-01	11	1148cm	0.00543057	8.027523309	14.78210033
M77/2-59-01	12	1148cm	0.004727773	8.898198037	18.82111786
M77/2-59-01	13	1148cm	0.003450466	8.805846169	25.52074264
M77/2-59-01	14	1148cm	0.005017951	7.979998052	15.90290036
M77/2-59-01	16	1148cm	0.006691477	9.960660134	14.88559286
M77/2-59-01	19	1148cm	0.005599902	8.544234213	15.25782939
M77/2-59-01	20	1148cm	0.00686095	6.826694016	9.950070605
M77/2-59-01	21	1148cm	0.0050966	8.853453955	17.37129395
M77/2-59-01	22	1148cm	0.004030262	7.316036402	18.15275696
M77/2-59-01	23	1148cm	0.004843737	9.526160422	19.66696448
M77/2-59-01	25	1148cm	0.005206498	6.892615805	13.23848764
M77/2-59-01	26	1148cm	0.004131642	7.055276788	17.07620676
M77/2-59-01	27	1148cm	0.007167598	4.287457626	5.981721429
M77/2-59-01	1	1188cm	0.004544241	7.078779255	15.57747251
M77/2-59-01	3	1188cm	0.005949988	8.562698917	14.39111931
M77/2-59-01	4	1188cm	0.003439945	4.388423363	12.75725
M77/2-59-01	5	1188cm	0.005539497	5.410032354	9.766288125
M77/2-59-01	6	1188cm	0.004821886	8.79608747	18.24200654
M77/2-59-01	7	1188cm	0.004179188	6.025208477	14.41717531
M77/2-59-01	14	1188cm	0.004292411	5.959808051	13.88452218
M77/2-59-01	16	1188cm	0.00618166	8.352445755	13.51165562

Appendix A

M77/2-59-01	17	1188cm	0.004284019	9.24224247	21.5737646
M77/2-59-01	18	1188cm	0.004722968	13.01856959	27.56438313
M77/2-59-01	19	1188cm	0.00475496	5.690962407	11.96847605
M77/2-59-01	25	1188cm	0.004913925	7.524514259	15.31263462
M77/2-59-01	27	1188cm	0.003696759	6.147686956	16.6299375
M77/2-59-01	28	1188cm	0.004603479	7.127221347	15.48225
M77/2-59-01	31	1188cm	0.003108319	7.367990147	23.70409728
M77/2-59-01	32	1188cm	0.00406703	10.71553945	26.34733562
M77/2-59-01	33	1188cm	0.003342019	7.87605761	23.56676667
M77/2-59-01	34	1188cm	0.00431886	7.195216919	16.65999176
M77/2-59-01	35	1188cm	0.004890106	11.09836408	22.6955504
M77/2-59-01	36	1188cm	0.002788225	10.59259038	37.9904497
M77/2-59-01	2	668cm	0.004326034	6.185771448	14.29894231
M77/2-59-01	3	668cm	0.003715782	6.478875158	17.4361
M77/2-59-01	5	668cm	0.003318313	7.739851522	23.32466053
M77/2-59-01	6	668cm	0.003852568	7.07067046	18.35313695
M77/2-59-01	7	668cm	0.00351756	6.287876207	17.87567571
M77/2-59-01	8	668cm	0.006410056	9.236200635	14.40892398
M77/2-59-01	9	668cm	0.004494532	7.476621693	16.63492875
M77/2-59-01	10	668cm	0.005329572	8.9997717	16.88648077
M77/2-59-01	11	668cm	0.005364521	7.06708546	13.17374855
M77/2-59-01	12	668cm	0.003378413	5.45274284	16.13995522
M77/2-59-01	13	668cm	0.004106366	5.646335392	13.7502
M77/2-59-01	14	668cm	0.005375532	7.810768443	14.53022373
M77/2-59-01	15	668cm	0.00457225	5.94290507	12.99777061
M77/2-59-01	16	668cm	0.004608384	7.726016798	16.76513222
M77/2-59-01	17	668cm	0.004735728	5.302866343	11.19757419
M77/2-59-01	18	668cm	0.005345652	5.628493272	10.52910614
M77/2-59-01	19	668cm	0.003722502	5.904849021	15.86258143
M77/2-59-01	20	668cm	0.00556928	5.064832414	9.094231788
M77/2-59-01	21	668cm	0.005390692	7.564938011	14.0333339
M77/2-59-01	22	668cm	0.005481607	7.253643497	13.23269444
M77/2-59-01	1	1228cm	0.006226518	6.035224416	9.692776398
M77/2-59-01	3	1228cm	0.00374713	4.446089201	11.86531902
M77/2-59-01	9	1228cm	0.006659433	9.965008417	14.96374898
M77/2-59-01	10	1228cm	0.004968795	7.772064064	15.64174891
M77/2-59-01	13	1228cm	0.005087808	8.812574573	17.32096667
M77/2-59-01	20	1228cm	0.004865616	7.038834266	14.46648261
M77/2-59-01	2	1268cm	0.002914364	5.491155216	18.84169207
M77/2-59-01	6	1268cm	0.003333406	6.942213149	20.82618621

Appendix A

M77/2-59-01	7	1268cm	0.003989372	5.884761388	14.75109802
M77/2-59-01	8	1268cm	0.003587258	5.999061698	16.72325217
M77/2-59-01	9	1268cm	0.00341639	4.587056806	13.42661897
M77/2-59-01	10	1268cm	0.004326499	8.086550823	18.69075
M77/2-59-01	14	1268cm	0.003385351	5.406204903	15.96940714
M77/2-59-01	17	1268cm	0.003390744	6.583077831	19.41484523
M77/2-59-01	18	1268cm	0.003733235	6.243405123	16.72384712
M77/2-59-01	19	1268cm	0.004548437	9.004725294	19.79740524
M77/2-59-01	24	1268cm	0.003498332	5.113810727	14.61785217
M77/2-59-01	27	1268cm	0.003580551	7.373857741	20.5942
M77/2-59-01	28	1268cm	0.004147907	5.936691671	14.31249907
M77/2-59-01	30	1268cm	0.004120905	6.400086494	15.53078033
M77/2-59-01	33	1268cm	0.004540038	9.915836676	21.84086806
M77/2-59-01	2	1348cm	0.003970794	7.29976838	18.3836493
M77/2-59-01	3	1348cm	0.003184781	7.009449145	22.00920314
M77/2-59-01	6	1348cm	0.003867925	6.798693767	17.57710693
M77/2-59-01	8	1348cm	0.00517267	7.020097864	13.57151613
M77/2-59-01	10	1348cm	0.003801771	7.065456796	18.58464474
M77/2-59-01	13	1348cm	0.003139225	9.406163025	29.96332849
M77/2-59-01	14	1348cm	0.002890949	6.283054194	21.733536
M77/2-59-01	17	1348cm	0.004778977	7.962386465	16.66127954
M77/2-59-01	18	1348cm	0.003126269	3.772691513	12.06771067
M77/2-59-01	19	1348cm	0.002128975	5.021352046	23.58577623
M77/2-59-01	23	1348cm	0.004266263	8.528496606	19.9905552
M77/2-59-01	25	1348cm	0.004237311	7.460065101	17.60565852
M77/2-59-01	27	1348cm	0.003554261	6.36308897	17.90270625
M77/2-59-01	28	1348cm	0.003886742	6.374243712	16.39996609
M77/2-59-01	32	1348cm	0.004880647	8.097964897	16.59198893
M77/2-59-01	33	1348cm	0.00415238	7.02203895	16.91087797
M77/2-59-01	35	1348cm	0.003388074	5.289143836	15.6110625
M77/2-59-01	36	1348cm	0.004093221	6.743308737	16.47433493
M77/2-59-01	37	1348cm	0.003530282	5.829462888	16.51273834
M77/2-59-01	1	1108cm	0.00332023	5.441293496	16.38830368
M77/2-59-01	2	1108cm	0.004445314	8.276540333	18.61857118
M77/2-59-01	6	1108cm	0.004221822	8.176963817	19.36832794
M77/2-59-01	7	1108cm	0.006153408	9.394308132	15.26683889
M77/2-59-01	9	1108cm	0.008366569	12.29661445	14.69732
M77/2-59-01	10	1108cm	0.00560973	7.067483554	12.59861584
M77/2-59-01	12	1108cm	0.004870865	7.077858867	14.53100902
M77/2-59-01	15	1108cm	0.003746684	6.395810726	17.07058868

Appendix A

M77/2-59-01	16	1108cm	0.004383681	8.765324483	19.99535431
M77/2-59-01	19	1108cm	0.005188798	8.617376286	16.60765333
M77/2-59-01	21	1108cm	0.004275882	5.102093923	11.9322618
M77/2-59-01	23	1108cm	0.004006728	6.13727921	15.3174344
M77/2-59-01	24	1108cm	0.00444785	10.84148331	24.37466087
M77/2-59-01	25	1108cm	0.003977394	11.96303138	30.07756066
M77/2-59-01	29	1108cm	0.004373756	8.185466653	18.71496
M77/2-59-01	31	1108cm	0.003774971	6.911143295	18.30780417
M77/2-59-01	35	1108cm	0.005889834	7.538071652	12.79844554
M77/2-59-01	36	1108cm	0.004675088	5.236604189	11.20108256
M77/2-59-01	37	1108cm	0.0024331	11.5860715	47.61855672
M77/2-59-01	3	148cm	0.003526151	6.300575499	17.86814118
M77/2-59-01	4	148cm	0.004723044	7.591329325	16.07295938
M77/2-59-01	5	148cm	0.004127883	9.327777052	22.59699863
M77/2-59-01	8	148cm	0.003427609	8.838833194	25.78717059
M77/2-59-01	12	148cm	0.004212647	9.090025835	21.57794458
M77/2-59-01	13	148cm	0.004216285	7.208709091	17.0973
M77/2-59-01	15	148cm	0.00361967	7.244282111	20.0136534
M77/2-59-01	16	148cm	0.003877584	8.274837581	21.3401913
M77/2-59-01	17	148cm	0.004875514	9.712530101	19.92103667
M77/2-59-01	18	148cm	0.003053463	6.593654729	21.59402143
M77/2-59-01	20	148cm	0.003380221	6.26949662	18.54759176
M77/2-59-01	22	148cm	0.004351016	10.14027175	23.30552681
M77/2-59-01	23	148cm	0.004370436	9.854021264	22.54699765
M77/2-59-01	24	148cm	0.003963326	8.152041854	20.56868867
M77/2-59-01	25	148cm	0.00502699	7.099714002	14.12318989
M77/2-59-01	27	148cm	0.003894942	8.678633061	22.28180352
M77/2-59-01	28	148cm	0.003458932	5.781907134	16.7158736
M77/2-59-01	30	148cm	0.005039909	7.558182817	14.99666667
M77/2-59-01	33	148cm	0.004713921	9.344185897	19.82253389
M77/2-59-01	1	83cm	0.003457276	8.492192115	24.56324322
M77/2-59-01	2	83cm	0.003709851	6.034912504	16.26726316
M77/2-59-01	3	83cm	0.003280184	8.526688983	25.99454227
M77/2-59-01	5	83cm	0.004382328	8.796485924	20.07263372
M77/2-59-01	8	83cm	0.005582441	10.09789119	18.08866552
M77/2-59-01	13	83cm	0.004463356	8.96293672	20.08116
M77/2-59-01	14	83cm	0.003623314	7.311349046	20.1786255
M77/2-59-01	1	63cm	0.004281351	7.0248582	16.40804268
M77/2-59-01	2	63cm	0.003665578	10.42846481	28.44971457
M77/2-59-01	3	63cm	0.003579914	6.610300954	18.46497231

Appendix A

M77/2-59-01	4	63cm	0.00367273	9.842224092	26.798112
M77/2-59-01	5	63cm	0.002898377	6.817295849	23.52108
M77/2-59-01	6	63cm	0.003814393	9.033419082	23.68245767
M77/2-59-01	7	63cm	0.003011255	6.877994654	22.84095988
M77/2-59-01	9	63cm	0.005074852	9.63240052	18.98065358
M77/2-59-01	10	63cm	0.003537322	9.043217056	25.56515323
M77/2-59-01	1	788cm	0.003561443	5.840962327	16.40055146
M77/2-59-01	2	788cm	0.004325734	6.647964517	15.36840698
M77/2-59-01	3	788cm	0.003888979	8.839737467	22.73022478
M77/2-59-01	4	788cm	0.003575864	5.368260017	15.01248247
M77/2-59-01	5	788cm	0.00372582	5.29338411	14.2072991
M77/2-59-01	6	788cm	0.004577476	6.915426785	15.10751208
M77/2-59-01	8	788cm	0.003469224	6.773628406	19.52490743
M77/2-59-01	9	788cm	0.003925296	6.920484255	17.63047871
M77/2-59-01	10	788cm	0.002959343	3.858294962	13.03767342
M77/2-59-01	11	788cm	0.003710868	4.794643033	12.92054211
M77/2-59-01	12	788cm	0.004048492	6.452332685	15.93761971
M77/2-59-01	13	788cm	0.004226387	5.490554273	12.99112941
M77/2-59-01	14	788cm	0.003288491	4.202517618	12.77947113
M77/2-59-01	15	788cm	0.003998983	5.960010928	14.90381659
M77/2-59-01	16	788cm	0.003539979	6.225375767	17.58590952
M77/2-59-01	17	788cm	0.004012918	4.68055286	11.6637131
M77/2-59-01	18	788cm	0.004168622	6.138498661	14.72548678
M77/2-59-01	19	788cm	0.004096444	6.821590924	16.65247119
M77/2-59-01	20	788cm	0.004804397	6.02063004	12.53150082
M77/2-59-01	21	788cm	0.003333535	5.286201594	15.8576456
M77/2-59-01	1	548cm	0.004788052	9.061515311	18.92526429
M77/2-59-01	2	548cm	0.003997306	5.040812581	12.61052489
M77/2-59-01	3	548cm	0.00378899	6.233053717	16.450434
M77/2-59-01	4	548cm	0.003865414	5.295359638	13.69933216
M77/2-59-01	6	548cm	0.004025647	6.250337382	15.52629114
M77/2-59-01	7	548cm	0.005181235	6.656280254	12.8469
M77/2-59-01	8	548cm	0.003379349	8.412616354	24.89418871
M77/2-59-01	9	548cm	0.002981791	5.714824207	19.16574398
M77/2-59-01	12	548cm	0.005190715	6.333297017	12.20120404
M77/2-59-01	13	548cm	0.004006679	5.693761157	14.21067583
M77/2-59-01	14	548cm	0.005318904	10.673108	20.06636604
M77/2-59-01	15	548cm	0.003234781	7.65014402	23.64965393
M77/2-59-01	16	548cm	0.003873396	5.31504934	13.72193645
M77/2-59-01	17	548cm	0.003831483	4.918808262	12.8378717

Appendix A

M77/2-59-01	18	548cm	0.004459642	7.561216587	16.95476293
M77/2-59-01	19	548cm	0.003469615	5.423141986	15.63038465
M77/2-59-01	21	548cm	0.005073514	6.227214986	12.27396755
M77/2-59-01	22	548cm	0.003422421	4.958449021	14.48813198
M77/2-59-01	23	548cm	0.002876297	7.510070539	26.11020789
M77/2-59-01	24	548cm	0.002975839	7.455688068	25.05407143
M77/2-59-01	1	268cm	0.004136594	10.00153018	24.17817773
M77/2-59-01	5	268cm	0.00392002	7.913011057	20.18614806
M77/2-59-01	6	268cm	0.003996949	8.323598164	20.82487706
M77/2-59-01	7	268cm	0.003659265	9.208563303	25.16505981
M77/2-59-01	8	268cm	0.003138353	6.849587536	21.82542353
M77/2-59-01	9	268cm	0.003734077	9.738871132	26.08106384
M77/2-59-01	12	268cm	0.004190458	8.694827506	20.74911256
M77/2-59-01	13	268cm	0.003536136	6.126668579	17.32588726
M77/2-59-01	14	268cm	0.002691045	5.917438697	21.98936903
M77/2-59-01	18	268cm	0.00523933	7.842461249	14.9684426
M77/2-59-01	19	268cm	0.00422388	8.318013651	19.69282723
M77/2-59-01	20	268cm	0.003436783	7.729223501	22.48970625
M77/2-59-01	21	268cm	0.003344296	6.122414528	18.30703696
M77/2-59-01	24	268cm	0.00363881	8.073305139	22.18666522
M77/2-59-01	25	268cm	0.003745242	4.97420578	13.2814
M77/2-59-01	26	268cm	0.004559926	8.303367301	18.20943626
M77/2-59-01	27	268cm	0.004961855	8.402757806	16.93471154
M77/2-59-01	28	268cm	0.004895721	7.205661935	14.71828534
M77/2-59-01	1	428cm	0.003302804	5.433106602	16.4499838
M77/2-59-01	2	428cm	0.006104203	8.675804698	14.21283726
M77/2-59-01	4	428cm	0.003630791	6.492007035	17.88041912
M77/2-59-01	5	428cm	0.003981125	4.648873634	11.67728571
M77/2-59-01	6	428cm	0.003154332	5.414036978	17.16381377
M77/2-59-01	9	428cm	0.003391897	6.712888813	19.79095622
M77/2-59-01	10	428cm	0.003285839	8.679912583	26.41612229
M77/2-59-01	11	428cm	0.003435388	6.705937977	19.52017784
M77/2-59-01	12	428cm	0.005857184	8.423128204	14.38085
M77/2-59-01	14	428cm	0.002732542	5.937788972	21.729906
M77/2-59-01	15	428cm	0.003444588	6.805669623	19.75757143
M77/2-59-01	16	428cm	0.005481315	9.179860243	16.74755061
M77/2-59-01	17	428cm	0.003732794	6.257023053	16.76230286
M77/2-59-01	19	428cm	0.003622216	5.760133999	15.90223594
M77/2-59-01	20	428cm	0.00290354	6.704079565	23.08933256
M77/2-59-01	22	428cm	0.003985124	7.113038693	17.84897561

Appendix A

M77/2-59-01	24	428cm	0.00415723	7.718198261	18.56572534
M77/2-59-01	1	1028cm	0.00424036	5.891957282	13.89494582
M77/2-59-01	5	1028cm	0.005392726	7.854185085	14.56440583
M77/2-59-01	9	1028cm	0.006648912	7.096989618	10.67391047
M77/2-59-01	13	1028cm	0.006331765	9.441835773	14.91185385
M77/2-59-01	14	1028cm	0.005561668	7.437574208	13.37292
M77/2-59-01	17	1028cm	0.003826429	4.884717824	12.7657361
M77/2-59-01	19	1028cm	0.006047242	7.867272392	13.00968581
M77/2-59-01	22	1028cm	0.005033119	4.562088036	9.064136496
M77/2-59-01	27	1028cm	0.004353782	6.310517056	14.49433477
M77/2-59-01	28	1028cm	0.005091964	7.819250464	15.35605851
M77/2-59-01	29	1028cm	0.005310796	7.202115999	13.56127526
M77/2-59-01	30	1028cm	0.00592497	10.17923307	17.18022672
M77/2-59-01	32	1028cm	0.00564709	6.104428435	10.80986604
M77/2-59-01	33	1028cm	0.003765482	6.088487818	16.16921194
M77/2-59-01	34	1028cm	0.003431603	4.496812851	13.10411759
M77/2-59-01	35	1028cm	0.005389912	9.456514545	17.5448392
M77/2-59-01	4	1308cm	0.004274309	5.74126777	13.43203714
M77/2-59-01	6	1308cm	0.004124059	8.291416758	20.10499303
M77/2-59-01	7	1308cm	0.003354142	6.018475562	17.94341309
M77/2-59-01	8	1308cm	0.004557859	9.112052652	19.99195809
M77/2-59-01	9	1308cm	0.003996582	6.135680748	15.35231943
M77/2-59-01	10	1308cm	0.002715707	5.965165554	21.96542432
M77/2-59-01	11	1308cm	0.003919641	5.865749488	14.96501745
M77/2-59-01	15	1308cm	0.003765868	6.721628036	17.84881274
M77/2-59-01	18	1308cm	0.002844024	7.133875411	25.08373735
M77/2-59-01	19	1308cm	0.004219876	6.765909386	16.03343077
M77/2-59-01	20	1308cm	0.004914307	6.087444129	12.38718724
M77/2-59-01	21	1308cm	0.003238572	6.054911598	18.69623892
M77/2-59-01	23	1308cm	0.004534692	7.471260483	16.47578327
M77/2-59-01	24	1308cm	0.004558217	6.85302826	15.03444836
M77/2-59-01	37	1308cm	0.003344124	6.166358796	18.43938603
M77/2-59-01	40	1308cm	0.004292709	7.419325825	17.28355357
M77/2-59-01	41	1308cm	0.003951012	8.024542126	20.31009417
M77/2-59-01	44	1308cm	0.005867949	11.02519313	18.78883448
M77/2-59-01	46	1308cm	0.004037054	6.651347699	16.47574811
M77/2-59-01	2	388cm	0.0043641	4.298837867	9.850456769
M77/2-59-01	3	388cm	0.003584768	5.446803344	15.1943
M77/2-59-01	4	388cm	0.00563382	7.587161985	13.46717218
M77/2-59-01	5	388cm	0.004302438	5.651347651	13.13522222

Appendix A

M77/2-59-01	7	388cm	0.003803023	5.277501742	13.87712174
M77/2-59-01	8	388cm	0.004855079	5.089541045	10.48292143
M77/2-59-01	9	388cm	0.003857954	4.840060149	12.54566549
M77/2-59-01	10	388cm	0.003078048	4.288317835	13.93194
M77/2-59-01	12	388cm	0.005607318	6.30991545	11.253
M77/2-59-01	15	388cm	0.003170676	3.810248092	12.01714576
M77/2-59-01	16	388cm	0.003891721	5.128446096	13.17783476
M77/2-59-01	17	388cm	0.004222547	4.248487057	10.06143319
M77/2-59-01	21	388cm	0.004240271	4.158694127	9.80761336
M77/2-59-01	22	388cm	0.00437645	4.573498521	10.45024703
M77/2-59-01	23	388cm	0.004532069	4.698236806	10.36665
M77/2-59-01	27	388cm	0.003593779	3.661435386	10.18825902
M77/2-59-01	29	388cm	0.004495441	3.986488902	8.867848
M77/2-59-01	30	388cm	0.003731465	3.153407365	8.450856716
M77/2-59-01	2	908cm	0.004131701	4.629044182	11.20372468
M77/2-59-01	3	908cm	0.003983963	7.594204549	19.06193484
M77/2-59-01	5	908cm	0.00400453	5.916069045	14.77344299
M77/2-59-01	6	908cm	0.003938808	5.818793218	14.77298062
M77/2-59-01	7	908cm	0.003681849	6.945841358	18.86509119
M77/2-59-01	8	908cm	0.004074689	7.522664676	18.46193684
M77/2-59-01	9	908cm	0.004597951	7.735428089	16.82364354
M77/2-59-01	10	908cm	0.005751366	4.559826464	7.92825
M77/2-59-01	11	908cm	0.004542979	7.081041259	15.58677833
M77/2-59-01	14	908cm	0.004330227	8.513501936	19.66063846
M77/2-59-01	15	908cm	0.004163888	7.415926197	17.8101
M77/2-59-01	16	908cm	0.004789301	4.53093492	9.460535688
M77/2-59-01	17	908cm	0.004628755	6.538495714	14.12581923
M77/2-59-01	18	908cm	0.004635895	4.593729282	9.909045882
M77/2-59-01	20	908cm	0.004611897	6.735809342	14.60529135
M77/2-59-01	22	908cm	0.00379363	8.13596934	21.44639415
M77/2-59-01	23	908cm	0.003383279	4.346392851	12.8466871
M77/2-59-01	24	908cm	0.00469504	6.328044835	13.47814828
M77/2-59-01	26	908cm	0.005592723	6.606006311	11.8117883
M77/2-59-01	29	908cm	0.004025764	5.290812725	13.14238259
MAZ-1E-04	1	10.5cm	0.007187263	7.994310549	11.12288571
MAZ-1E-04	2	10.5cm	0.005925451	10.40459199	17.55915534
MAZ-1E-04	3	10.5cm	0.006310162	9.503066512	15.0599397
MAZ-1E-04	5	10.5cm	0.003574669	7.567369843	21.16943096
MAZ-1E-04	6	10.5cm	0.007916319	12.2698246	15.49940593
MAZ-1E-04	7	10.5cm	0.006712584	11.06751801	16.48771624

Appendix A

MAZ-1E-04	8	10.5cm	0.00633946	12.6349048	19.93056838
MAZ-1E-04	9	10.5cm	0.004225908	8.459979852	20.01931752
MAZ-1E-04	10	10.5cm	0.005905533	11.69482309	19.8031625
MAZ-1E-04	17	10.5cm	0.005652051	9.363576856	16.5666887
MAZ-1E-04	1	18.5cm	0.00517589	10.06845974	19.45261556
MAZ-1E-04	3	18.5cm	0.005050465	10.20191269	20.19994785
MAZ-1E-04	6	18.5cm	0.004173538	8.668723939	20.77068293
MAZ-1E-04	8	18.5cm	0.004488736	8.669965102	19.31493498
MAZ-1E-04	9	18.5cm	0.0063245	11.81996027	18.68916176
MAZ-1E-04	11	18.5cm	0.006389129	10.90370778	17.06603168
MAZ-1E-04	12	18.5cm	0.005866374	8.52518283	14.53228615
MAZ-1E-04	13	18.5cm	0.008036446	12.70702227	15.81174411
MAZ-1E-04	14	18.5cm	0.004439743	10.34806971	23.30781476
MAZ-1E-04	16	18.5cm	0.0060065	11.85698392	19.7402531
MAZ-1E-04	17	18.5cm	0.004664041	9.439525465	20.23894244
MAZ-1E-04	18	18.5cm	0.005002371	10.19646043	20.3832531
MAZ-1E-04	22	18.5cm	0.00619395	11.21095143	18.09984309
MAZ-1E-04	23	18.5cm	0.005322729	9.114119861	17.12302178
MAZ-1E-04	27	18.5cm	0.007003663	13.38210613	19.10729723
MAZ-1E-04	29	18.5cm	0.007254839	12.06936118	16.63629
MAZ-1E-04	31	18.5cm	0.005615757	9.612312476	17.11668051
MAZ-1E-04	33	18.5cm	0.005454691	8.289278616	15.19660504
MAZ-1E-04	34	18.5cm	0.006791367	10.79700472	15.89813077
MAZ-1E-04	35	18.5cm	0.005234337	10.42453342	19.91566923
MAZ-1E-04	37	18.5cm	0.005908641	10.68279023	18.07994439
MAZ-1E-04	1	26.5cm	0.006212413	10.56288489	17.00287095
MAZ-1E-04	4	26.5cm	0.004783331	9.309639546	19.46267206
MAZ-1E-04	5	26.5cm	0.006462762	10.98835465	17.00256811
MAZ-1E-04	7	26.5cm	0.006142481	12.99781046	21.1605237
MAZ-1E-04	8	26.5cm	0.005418803	9.874969441	18.22352602
MAZ-1E-04	17	26.5cm	0.004931238	8.807165174	17.85994571
MAZ-1E-04	18	26.5cm	0.00704409	11.38054244	16.15615795
MAZ-1E-04	19	26.5cm	0.00600616	8.353911089	13.90890647
MAZ-1E-04	21	26.5cm	0.005627265	11.26009662	20.00989172
MAZ-1E-04	24	26.5cm	0.006856524	12.61519255	18.39881582
MAZ-1E-04	29	26.5cm	0.004377735	5.978783319	13.65725342
MAZ-1E-04	39	26.5cm	0.006642079	11.37860506	17.13108868
MAZ-1E-04	40	26.5cm	0.005722598	8.15655762	14.25324334
MAZ-1E-04	41	26.5cm	0.005807676	11.65786293	20.07319612
MAZ-1E-04	1	43.5cm	0.00633621	8.711417273	13.748625

Appendix A

MAZ-1E-04	3	43.5cm	0.005035027	10.95095654	21.74954772
MAZ-1E-04	5	43.5cm	0.006119656	12.56907878	20.53886427
MAZ-1E-04	6	43.5cm	0.005608142	11.53087133	20.56094882
MAZ-1E-04	7	43.5cm	0.006121216	11.09934695	18.13258383
MAZ-1E-04	12	43.5cm	0.006706538	11.68325835	17.4207
MAZ-1E-04	13	43.5cm	0.005993969	12.34224099	20.5911
MAZ-1E-04	15	43.5cm	0.007593931	14.14572725	18.627675
MAZ-1E-04	20	43.5cm	0.004861802	8.945452908	18.39945836
MAZ-1E-04	21	43.5cm	0.005293141	8.917963297	16.84815
MAZ-1E-04	22	43.5cm	0.005335586	11.01752501	20.6491396
MAZ-1E-04	24	43.5cm	0.005293691	10.29452489	19.44677915
MAZ-1E-04	25	43.5cm	0.00452638	9.936374518	21.95214317
MAZ-1E-04	28	43.5cm	0.005622655	9.948983019	17.69445797
MAZ-1E-04	30	43.5cm	0.005306058	10.82372461	20.3988061
MAZ-1E-04	33	43.5cm	0.004801905	9.639903198	20.07516261
MAZ-1E-04	34	43.5cm	0.007492095	12.75264463	17.0214668
MAZ-1E-04	35	43.5cm	0.0049143	11.36343679	23.12320552
MAZ-1E-04	36	43.5cm	0.005089688	12.74178974	25.03451862
MAZ-1E-04	37	43.5cm	0.004349101	8.94137559	20.55913706
MAZ-1E-04	1	48.5cm	0.005250736	9.510736013	18.11314833
MAZ-1E-04	3	48.5cm	0.004556375	10.71192936	23.50976314
MAZ-1E-04	4	48.5cm	0.005625108	7.355369824	13.07596136
MAZ-1E-04	5	48.5cm	0.005957321	11.59160263	19.45774286
MAZ-1E-04	6	48.5cm	0.00689104	11.63758361	16.8879922
MAZ-1E-04	7	48.5cm	0.005677185	10.86325942	19.13494
MAZ-1E-04	8	48.5cm	0.008220502	12.52766214	15.23953469
MAZ-1E-04	11	48.5cm	0.005407246	9.999510146	18.49279826
MAZ-1E-04	13	48.5cm	0.005726034	9.295892877	16.23443556
MAZ-1E-04	14	48.5cm	0.004981	7.675721479	15.4100021
MAZ-1E-04	19	48.5cm	0.004259337	8.243901521	19.354896
MAZ-1E-04	20	48.5cm	0.004836911	8.078582424	16.70194565
MAZ-1E-04	22	48.5cm	0.005497995	10.1196215	18.40602015
MAZ-1E-04	24	48.5cm	0.004519555	8.942444599	19.78611959
MAZ-1E-04	25	48.5cm	0.005577497	12.10052815	21.69526513
MAZ-1E-04	26	48.5cm	0.004689946	10.14801028	21.63779725
MAZ-1E-04	27	48.5cm	0.005922109	11.01764788	18.60426324
MAZ-1E-04	28	48.5cm	0.005274005	7.760778674	14.71515313
MAZ-1E-04	30	48.5cm	0.005795891	8.430586607	14.5458
MAZ-1E-04	33	48.5cm	0.006238612	10.05070149	16.11047778
MAZ-1E-04	6	53.5cm	0.003965539	8.439221856	21.28139655

Appendix A

MAZ-1E-04	7	53.5cm	0.004344337	9.204105042	21.18644281
MAZ-1E-04	9	53.5cm	0.00684125	14.01405136	20.48463699
MAZ-1E-04	10	53.5cm	0.007513102	12.70231604	16.90688673
MAZ-1E-04	11	53.5cm	0.003483589	9.461084018	27.15901398
MAZ-1E-04	12	53.5cm	0.004695037	8.843283026	18.83538713
MAZ-1E-04	13	53.5cm	0.005631725	12.31508941	21.86734688
MAZ-1E-04	15	53.5cm	0.0059691	10.57879038	17.72258797
MAZ-1E-04	16	53.5cm	0.00574835	11.71914017	20.38696447
MAZ-1E-04	17	53.5cm	0.006234302	9.562883524	15.33914186
MAZ-1E-04	18	53.5cm	0.005521955	11.92636274	21.59808035
MAZ-1E-04	19	53.5cm	0.003908718	7.688942629	19.67126502
MAZ-1E-04	20	53.5cm	0.004530862	9.816191575	21.66517347
MAZ-1E-04	22	53.5cm	0.005150486	11.05872308	21.47122453
MAZ-1E-04	23	53.5cm	0.005752062	11.88050317	20.65433791
MAZ-1E-04	24	53.5cm	0.005294478	11.46187699	21.64873661
MAZ-1E-04	26	53.5cm	0.005383739	11.04268212	20.51117538
MAZ-1E-04	27	53.5cm	0.005609391	11.11442765	19.81396607
MAZ-1E-04	28	53.5cm	0.004273411	8.307713547	19.44047175
MAZ-1E-04	30	53.5cm	0.004910667	11.09048442	22.58447714
MAZ-1E-04	4	58.5cm	0.005675625	11.06700484	19.49918218
MAZ-1E-04	6	58.5cm	0.007720336	12.64778243	16.38242419
MAZ-1E-04	8	58.5cm	0.005899934	8.784478906	14.88911269
MAZ-1E-04	10	58.5cm	0.006096787	10.44409445	17.13048857
MAZ-1E-04	11	58.5cm	0.005231404	10.49368698	20.05902776
MAZ-1E-04	12	58.5cm	0.005216578	10.50541777	20.13852423
MAZ-1E-04	13	58.5cm	0.004585972	9.48801575	20.68921475
MAZ-1E-04	14	58.5cm	0.00554375	8.338932598	15.04204322
MAZ-1E-04	15	58.5cm	0.00470497	9.802191514	20.83369655
MAZ-1E-04	17	58.5cm	0.005344177	10.54370538	19.72933359
MAZ-1E-04	24	58.5cm	0.005635919	10.67784112	18.94605263
MAZ-1E-04	26	58.5cm	0.003168421	8.35199234	26.36011304
MAZ-1E-04	29	58.5cm	0.005857939	11.9312258	20.36761675
MAZ-1E-04	30	58.5cm	0.007158343	14.75262719	20.60899699
MAZ-1E-04	34	58.5cm	0.005606671	8.238799925	14.69463781
MAZ-1E-04	36	58.5cm	0.00523354	7.594228156	14.51069231
MAZ-1E-04	37	58.5cm	0.004958131	9.602711838	19.36760571
MAZ-1E-04	39	58.5cm	0.005280283	11.10047736	21.02250441
MAZ-1E-04	41	58.5cm	0.005688299	10.46849267	18.4035555
MAZ-1E-04	42	58.5cm	0.005966668	11.21040633	18.78838586
MAZ-1E-04	43	58.5cm	0.005564534	11.30140988	20.30971421

Appendix A

MAZ-1E-04	2	63.5cm	0.004934956	9.755543308	19.7682479
MAZ-1E-04	3	63.5cm	0.006406615	11.59050156	18.09146051
MAZ-1E-04	5	63.5cm	0.00673188	9.330747364	13.86053688
MAZ-1E-04	6	63.5cm	0.00674127	12.99113362	19.27104794
MAZ-1E-04	7	63.5cm	0.005312244	11.18744056	21.0597262
MAZ-1E-04	8	63.5cm	0.006065525	10.98264945	18.10667714
MAZ-1E-04	10	63.5cm	0.005676148	9.701855206	17.09232339
MAZ-1E-04	13	63.5cm	0.005731171	11.24629364	19.62303095
MAZ-1E-04	14	63.5cm	0.005262717	10.48725397	19.92745186
MAZ-1E-04	15	63.5cm	0.005335513	8.826443993	16.54282225
MAZ-1E-04	16	63.5cm	0.00739525	10.29280963	13.91813704
MAZ-1E-04	17	63.5cm	0.007093756	10.85506161	15.30227718
MAZ-1E-04	18	63.5cm	0.005746709	10.48165769	18.23940887
MAZ-1E-04	20	63.5cm	0.005462755	11.24053154	20.57667008
MAZ-1E-04	25	63.5cm	0.006385305	11.07975389	17.35195846
MAZ-1E-04	28	63.5cm	0.005441502	9.905733973	18.20404213
MAZ-1E-04	29	63.5cm	0.004452052	8.957412866	20.11973959
MAZ-1E-04	30	63.5cm	0.004774231	8.552581047	17.91405
MAZ-1E-04	33	63.5cm	0.007664195	11.44718851	14.93593117
MAZ-1E-04	35	63.5cm	0.005581123	9.46705436	16.96263211
MAZ-1E-04	2	68.5cm	0.005478224	9.773772074	17.84113158
MAZ-1E-04	3	68.5cm	0.003737761	7.725313929	20.66829498
MAZ-1E-04	5	68.5cm	0.004290696	10.34923123	24.1201663
MAZ-1E-04	6	68.5cm	0.004377188	8.401258786	19.19328038
MAZ-1E-04	7	68.5cm	0.00479351	9.506726623	19.83249387
MAZ-1E-04	9	68.5cm	0.00420641	8.540998467	20.30472065
MAZ-1E-04	10	68.5cm	0.004742777	8.367427621	17.64246606
MAZ-1E-04	11	68.5cm	0.004735247	10.48810319	22.14900912
MAZ-1E-04	12	68.5cm	0.005428229	10.80970951	19.9138775
MAZ-1E-04	13	68.5cm	0.004710338	7.461765924	15.84125278
MAZ-1E-04	14	68.5cm	0.004035774	8.733270153	21.63964
MAZ-1E-04	15	68.5cm	0.005399046	10.43680041	19.33082366
MAZ-1E-04	18	68.5cm	0.003283751	7.039716379	21.43803364
MAZ-1E-04	20	68.5cm	0.003741856	9.476071545	25.32451935
MAZ-1E-04	21	68.5cm	0.003749844	9.745234313	25.98836987
MAZ-1E-04	24	68.5cm	0.005627772	9.415030195	16.72958571
MAZ-1E-04	29	68.5cm	0.004197746	7.071532754	16.8460249
MAZ-1E-04	30	68.5cm	0.004433493	9.064377234	20.44522911
MAZ-1E-04	36	68.5cm	0.005238171	8.140396333	15.54053262
MAZ-1E-04	37	68.5cm	0.003404092	7.717342688	22.67078289

Appendix A

MAZ-1E-04	38	68.5cm	0.004459972	7.943412588	17.81045357
MAZ-1E-04	3	73.5cm	0.004433503	9.419672812	21.24656852
MAZ-1E-04	4	73.5cm	0.003650523	8.421047525	23.06805492
MAZ-1E-04	5	73.5cm	0.004260929	8.18827929	19.21712055
MAZ-1E-04	6	73.5cm	0.005498779	10.53858	19.16530827
MAZ-1E-04	10	73.5cm	0.005176305	8.75722155	16.9179
MAZ-1E-04	13	73.5cm	0.004284284	9.984353361	23.3046
MAZ-1E-04	14	73.5cm	0.003468319	8.041491467	23.18555951
MAZ-1E-04	15	73.5cm	0.004435534	8.503342461	19.17095331
MAZ-1E-04	17	73.5cm	0.004052269	6.642020535	16.39086691
MAZ-1E-04	19	73.5cm	0.005149972	10.56122701	20.50734661
MAZ-1E-04	23	73.5cm	0.005397643	9.881437327	18.30694974
MAZ-1E-04	24	73.5cm	0.005083881	8.882966032	17.47280579
MAZ-1E-04	25	73.5cm	0.004612558	8.256333531	17.89968589
MAZ-1E-04	26	73.5cm	0.006117465	9.948154312	16.26188873
MAZ-1E-04	27	73.5cm	0.00451857	9.396433731	20.79514933
MAZ-1E-04	28	73.5cm	0.004202408	6.731167181	16.01740535
MAZ-1E-04	32	73.5cm	0.004104744	8.834973671	21.52381079
MAZ-1E-04	33	73.5cm	0.004585962	10.10329857	22.03092692
MAZ-1E-04	37	73.5cm	0.004620622	7.548952587	16.33752417
MAZ-1E-04	38	73.5cm	0.003765802	6.785238035	18.01804057
MAZ-1E-04	3	78.5cm	0.004479262	10.5905976	23.6436208
MAZ-1E-04	4	78.5cm	0.004921421	10.27408354	20.87625517
MAZ-1E-04	5	78.5cm	0.005547377	8.240724304	14.85517321
MAZ-1E-04	6	78.5cm	0.004746077	8.175702909	17.22623177
MAZ-1E-04	7	78.5cm	0.004384585	8.610520628	19.63816752
MAZ-1E-04	9	78.5cm	0.004883007	7.538555708	15.43834704
MAZ-1E-04	11	78.5cm	0.005707082	10.25012075	17.96035287
MAZ-1E-04	12	78.5cm	0.006100745	8.275966246	13.56550105
MAZ-1E-04	13	78.5cm	0.003912388	7.507639683	19.18940704
MAZ-1E-04	14	78.5cm	0.005668958	11.13904349	19.64919
MAZ-1E-04	15	78.5cm	0.004548375	9.629282802	21.17082
MAZ-1E-04	16	78.5cm	0.00348856	7.069020006	20.26343361
MAZ-1E-04	17	78.5cm	0.00377957	6.196017637	16.3934444
MAZ-1E-04	18	78.5cm	0.004361694	7.521549902	17.2445625
MAZ-1E-04	19	78.5cm	0.004607803	8.665230852	18.80555644
MAZ-1E-04	20	78.5cm	0.003487823	4.703045859	13.48418739
MAZ-1E-04	23	78.5cm	0.00354835	8.723769572	24.58542385
MAZ-1E-04	27	78.5cm	0.004597477	7.986955986	17.37247742
MAZ-1E-04	29	78.5cm	0.006374236	11.69236058	18.34315596

Appendix A

MAZ-1E-04	30	78.5cm	0.00350357	5.99421383	17.10887598
MAZ-1E-04	2	83.5cm	0.00480096	9.156641703	19.07252069
MAZ-1E-04	4	83.5cm	0.003629673	6.81167213	18.76662857
MAZ-1E-04	6	83.5cm	0.005184551	7.805861464	15.05600426
MAZ-1E-04	8	83.5cm	0.005211664	8.61040705	16.52141671
MAZ-1E-04	9	83.5cm	0.004560713	7.117606445	15.60634684
MAZ-1E-04	10	83.5cm	0.004212479	8.414338245	19.97478876
MAZ-1E-04	12	83.5cm	0.006438093	10.43779026	16.21255023
MAZ-1E-04	15	83.5cm	0.004959684	10.58430128	21.34067692
MAZ-1E-04	16	83.5cm	0.004686552	8.367023024	17.85325993
MAZ-1E-04	17	83.5cm	0.007008134	10.26253875	14.64375344
MAZ-1E-04	19	83.5cm	0.004319412	9.764751428	22.60666701
MAZ-1E-04	20	83.5cm	0.00477538	7.765695183	16.26194051
MAZ-1E-04	24	83.5cm	0.004919671	8.811943252	17.91165283
MAZ-1E-04	27	83.5cm	0.003959747	6.9466757	17.54323043
MAZ-1E-04	29	83.5cm	0.004574175	6.967987808	15.23331986
MAZ-1E-04	31	83.5cm	0.004655258	7.762397108	16.67447222
MAZ-1E-04	33	83.5cm	0.005303037	9.033916882	17.03536496
MAZ-1E-04	36	83.5cm	0.00386714	9.513050738	24.59970333
MAZ-1E-04	38	83.5cm	0.005278473	9.76182542	18.49365387
MAZ-1E-04	54	83.5cm	0.005947173	11.12700985	18.70974773
MAZ-1E-04	2	88.5cm	0.005548092	10.01099285	18.04402742
MAZ-1E-04	3	88.5cm	0.007596611	13.22076852	17.4035093
MAZ-1E-04	5	88.5cm	0.004883321	10.08219994	20.64619543
MAZ-1E-04	6	88.5cm	0.006206288	11.71689974	18.87907781
MAZ-1E-04	7	88.5cm	0.005011504	10.63147208	21.21413354
MAZ-1E-04	8	88.5cm	0.005259681	10.75070205	20.43983757
MAZ-1E-04	9	88.5cm	0.006233106	12.66174	20.31369197
MAZ-1E-04	10	88.5cm	0.005751104	9.180601544	15.9632
MAZ-1E-04	11	88.5cm	0.003882505	9.274367891	23.88758675
MAZ-1E-04	12	88.5cm	0.006471252	10.46474057	16.17112136
MAZ-1E-04	14	88.5cm	0.006347422	11.45295192	18.04347136
MAZ-1E-04	15	88.5cm	0.005463189	10.06201895	18.41785
MAZ-1E-04	16	88.5cm	0.007514195	12.09877678	16.101228
MAZ-1E-04	18	88.5cm	0.006034109	10.89893446	18.06221132
MAZ-1E-04	20	88.5cm	0.004868842	9.635640902	19.79041429
MAZ-1E-04	21	88.5cm	0.007204437	11.56975534	16.05920854
MAZ-1E-04	22	88.5cm	0.005069945	8.602941001	16.96850805
MAZ-1E-04	23	88.5cm	0.006466891	12.03429469	18.60908824
MAZ-1E-04	25	88.5cm	0.005143209	9.27533497	18.03413836

Appendix A

MAZ-1E-04	28	88.5cm	0.005166178	8.62788046	16.7007043
MAZ-1E-04	36	88.5cm	0.004210861	9.60746068	22.81590641
MAZ-1E-04	1	93.5cm	0.00691369	11.87193925	17.17164041
MAZ-1E-04	2	93.5cm	0.005488339	8.738924903	15.9227129
MAZ-1E-04	3	93.5cm	0.006833577	10.25945863	15.01330561
MAZ-1E-04	5	93.5cm	0.005431541	10.55703832	19.4365442
MAZ-1E-04	8	93.5cm	0.007066207	11.68065852	16.53030978
MAZ-1E-04	9	93.5cm	0.005636488	8.32921039	14.77730571
MAZ-1E-04	10	93.5cm	0.003832463	6.524400416	17.02404
MAZ-1E-04	13	93.5cm	0.005983971	10.15887957	16.97682076
MAZ-1E-04	14	93.5cm	0.00536883	10.25785629	19.10631724
MAZ-1E-04	16	93.5cm	0.006607695	11.47529381	17.3665611
MAZ-1E-04	17	93.5cm	0.005523141	10.54972089	19.10094415
MAZ-1E-04	18	93.5cm	0.008443525	12.75311466	15.10401646
MAZ-1E-04	19	93.5cm	0.006148293	9.966809599	16.21069463
MAZ-1E-04	25	93.5cm	0.005555136	8.686298652	15.63651774
MAZ-1E-04	26	93.5cm	0.005823944	10.16794934	17.45887087
MAZ-1E-04	27	93.5cm	0.006944352	11.45483682	16.49518557
MAZ-1E-04	28	93.5cm	0.006198835	13.17949136	21.26124
MAZ-1E-04	30	93.5cm	0.004493737	8.009844201	17.82445974
MAZ-1E-04	32	93.5cm	0.004386884	6.899131946	15.72672637
MAZ-1E-04	33	93.5cm	0.003820021	7.490868905	19.60949514
MAZ-1E-04	36	93.5cm	0.006247617	9.38432205	15.02064139
MAZ-1E-04	44	93.5cm	0.00721043	12.73487539	17.66174259
MAZ-1E-04	1	98.5cm	0.005796158	9.428432238	16.26669254
MAZ-1E-04	3	98.5cm	0.006424714	12.12928958	18.87911143
MAZ-1E-04	7	98.5cm	0.005378891	8.919991793	16.58332977
MAZ-1E-04	8	98.5cm	0.007265123	11.29813676	15.55119745
MAZ-1E-04	9	98.5cm	0.00436936	9.566674427	21.89490828
MAZ-1E-04	11	98.5cm	0.00659576	11.04443204	16.74474604
MAZ-1E-04	13	98.5cm	0.006157449	10.24291856	16.63500364
MAZ-1E-04	15	98.5cm	0.006237961	10.61208055	17.01209707
MAZ-1E-04	16	98.5cm	0.0052419	8.654774406	16.51075818
MAZ-1E-04	17	98.5cm	0.004767315	9.894433997	20.75472926
MAZ-1E-04	19	98.5cm	0.00468589	8.812607819	18.80668969
MAZ-1E-04	20	98.5cm	0.005585324	11.43024435	20.4647813
MAZ-1E-04	23	98.5cm	0.005873045	10.57144326	17.99993505
MAZ-1E-04	26	98.5cm	0.004394287	9.651044297	21.96270598
MAZ-1E-04	27	98.5cm	0.005316424	8.508580548	16.00432969
MAZ-1E-04	28	98.5cm	0.006218145	10.42231456	16.76113043

Appendix A

MAZ-1E-04	30	98.5cm	0.005438168	10.23141108	18.81407647
MAZ-1E-04	31	98.5cm	0.007217764	10.74977333	14.89349543
MAZ-1E-04	32	98.5cm	0.006692851	11.17284583	16.69370132
MAZ-1E-04	33	98.5cm	0.008837968	14.68458824	16.61534392
MAZ-1E-04	41	98.5cm	0.005885011	10.82359293	18.39179639
MAZ-1E-04	2	103.5cm	0.00663845	10.73554651	16.17176561
MAZ-1E-04	3	103.5cm	0.004799983	10.20818512	21.26712665
MAZ-1E-04	4	103.5cm	0.005177398	9.635609958	18.61091306
MAZ-1E-04	6	103.5cm	0.004975618	9.023592765	18.13562078
MAZ-1E-04	8	103.5cm	0.006494086	10.28711441	15.84074192
MAZ-1E-04	10	103.5cm	0.005134197	8.745435024	17.03369469
MAZ-1E-04	11	103.5cm	0.006693797	10.75140281	16.06173959
MAZ-1E-04	14	103.5cm	0.004504912	9.246786674	20.52601104
MAZ-1E-04	16	103.5cm	0.005875605	8.318874785	14.15832805
MAZ-1E-04	17	103.5cm	0.005411524	9.376691914	17.3272676
MAZ-1E-04	19	103.5cm	0.006689022	10.70303128	16.00089031
MAZ-1E-04	22	103.5cm	0.004887969	9.170455287	18.7612793
MAZ-1E-04	23	103.5cm	0.005405394	9.70868066	17.96109603
MAZ-1E-04	26	103.5cm	0.005873887	10.4681001	17.82141778
MAZ-1E-04	30	103.5cm	0.00813089	11.68619093	14.37258508
MAZ-1E-04	33	103.5cm	0.006254286	9.341649915	14.93639783
MAZ-1E-04	36	103.5cm	0.006319235	11.35167012	17.96367692
MAZ-1E-04	40	103.5cm	0.006949129	9.193730737	13.23004841
MAZ-1E-04	42	103.5cm	0.00614289	10.16370655	16.54548145
MAZ-1E-04	43	103.5cm	0.006317135	12.07921966	19.1213562
MAZ-1E-04	1	108.5cm	0.006535744	10.0178906	15.32784989
MAZ-1E-04	4	108.5cm	0.00499341	8.952056799	17.92774401
MAZ-1E-04	6	108.5cm	0.004863886	9.787622015	20.12304956
MAZ-1E-04	9	108.5cm	0.005998199	11.01657147	18.36646544
MAZ-1E-04	10	108.5cm	0.004397831	8.865780109	20.15943861
MAZ-1E-04	12	108.5cm	0.006842181	9.890337549	14.45494836
MAZ-1E-04	13	108.5cm	0.005825095	10.09990153	17.3386036
MAZ-1E-04	14	108.5cm	0.00486618	9.54064938	19.60603333
MAZ-1E-04	15	108.5cm	0.005634894	8.582172214	15.23040444
MAZ-1E-04	16	108.5cm	0.006469859	9.755247019	15.07798986
MAZ-1E-04	17	108.5cm	0.005477105	8.370638841	15.28296345
MAZ-1E-04	20	108.5cm	0.004723136	9.095975059	19.25833738
MAZ-1E-04	21	108.5cm	0.006791128	11.05892103	16.28436659
MAZ-1E-04	24	108.5cm	0.005581132	10.98767364	19.68717638
MAZ-1E-04	26	108.5cm	0.006097827	11.8062758	19.36144859

Appendix A

MAZ-1E-04	29	108.5cm	0.005385749	10.11096676	18.77355828
MAZ-1E-04	30	108.5cm	0.005925447	9.593121244	16.18970055
MAZ-1E-04	31	108.5cm	0.005854611	10.34743222	17.67398719
MAZ-1E-04	33	108.5cm	0.00526437	6.963343042	13.22730514
MAZ-1E-04	35	108.5cm	0.005418944	8.085148119	14.92015524
MAZ-1E-04	45	108.5cm	0.005783469	8.886656065	15.36561622
MAZ-1E-04	1	114.5cm	0.005677823	9.381257074	16.52262982
MAZ-1E-04	2	114.5cm	0.005805598	8.392452481	14.45579248
MAZ-1E-04	3	114.5cm	0.005305147	8.556412312	16.12851009
MAZ-1E-04	5	114.5cm	0.005765559	7.413515542	12.85827698
MAZ-1E-04	6	114.5cm	0.006038044	9.531170509	15.78519462
MAZ-1E-04	10	114.5cm	0.004247322	8.479570841	19.96451275
MAZ-1E-04	11	114.5cm	0.004843869	8.847397928	18.26514643
MAZ-1E-04	12	114.5cm	0.003219738	6.160915669	19.13483478
MAZ-1E-04	13	114.5cm	0.004810546	8.914978706	18.53215505
MAZ-1E-04	17	114.5cm	0.006709287	9.197467167	13.70856026
MAZ-1E-04	20	114.5cm	0.007714223	11.71281585	15.18340237
MAZ-1E-04	21	114.5cm	0.006417736	8.140920176	12.685035
MAZ-1E-04	22	114.5cm	0.004917218	9.01591012	18.33538929
MAZ-1E-04	25	114.5cm	0.00468273	11.62281069	24.82058449
MAZ-1E-04	26	114.5cm	0.005732736	7.365918459	12.84887195
MAZ-1E-04	32	114.5cm	0.005880098	8.139449605	13.8423702
MAZ-1E-04	33	114.5cm	0.004915086	9.291428514	18.90389722
MAZ-1E-04	37	114.5cm	0.007275376	9.603322209	13.19976069
MAZ-1E-04	39	114.5cm	0.005046378	8.539019402	16.92108641
MAZ-1E-04	42	114.5cm	0.006503949	11.41841457	17.55612512
MAZ-1E-04	44	114.5cm	0.006058024	9.390422419	15.50079976
MAZ-1E-04	2	119.5cm	0.005542733	10.23380983	18.46347203
MAZ-1E-04	3	119.5cm	0.006276759	10.25101437	16.3317
MAZ-1E-04	4	119.5cm	0.004813314	8.517671722	17.69606416
MAZ-1E-04	5	119.5cm	0.005875077	9.403785939	16.00623415
MAZ-1E-04	6	119.5cm	0.005860538	9.630860859	16.43340703
MAZ-1E-04	8	119.5cm	0.005777638	9.764731104	16.90090541
MAZ-1E-04	10	119.5cm	0.005432528	8.639102789	15.9025474
MAZ-1E-04	11	119.5cm	0.003922192	6.957401132	17.73855179
MAZ-1E-04	13	119.5cm	0.005232694	8.218549734	15.70615305
MAZ-1E-04	14	119.5cm	0.005886477	8.739253167	14.84632286
MAZ-1E-04	16	119.5cm	0.005784095	9.735178463	16.83094407
MAZ-1E-04	17	119.5cm	0.00545445	6.476686154	11.87413333
MAZ-1E-04	19	119.5cm	0.005508712	7.74191856	14.05395484

Appendix A

MAZ-1E-04	21	119.5cm	0.008082133	10.09779674	12.4939743
MAZ-1E-04	24	119.5cm	0.007015054	10.59376585	15.10147378
MAZ-1E-04	26	119.5cm	0.005899146	8.20753862	13.91309564
MAZ-1E-04	29	119.5cm	0.004781367	8.634145352	18.05790101
MAZ-1E-04	30	119.5cm	0.005026197	9.027920499	17.96173402
MAZ-1E-04	32	119.5cm	0.00491303	8.202055322	16.69449375
MAZ-1E-04	33	119.5cm	0.006319694	9.873259158	15.6230027
MAZ-1E-04	1	124.5cm	0.006425862	10.74259171	16.71774366
MAZ-1E-04	4	124.5cm	0.005509046	9.560872421	17.35486185
MAZ-1E-04	6	124.5cm	0.006890574	10.21772278	14.82855
MAZ-1E-04	9	124.5cm	0.007006076	11.16993397	15.94321034
MAZ-1E-04	10	124.5cm	0.00578348	9.977891763	17.2524
MAZ-1E-04	12	124.5cm	0.005368724	8.352757996	15.55818
MAZ-1E-04	13	124.5cm	0.004774555	7.171204985	15.01963082
MAZ-1E-04	14	124.5cm	0.006824485	10.83882142	15.8822561
MAZ-1E-04	15	124.5cm	0.00617134	9.931409338	16.09279138
MAZ-1E-04	16	124.5cm	0.00692736	10.45079806	15.08626445
MAZ-1E-04	17	124.5cm	0.005134988	10.75242704	20.9395379
MAZ-1E-04	18	124.5cm	0.006302749	10.12386577	16.06261816
MAZ-1E-04	19	124.5cm	0.003626949	9.062391577	24.98626731
MAZ-1E-04	20	124.5cm	0.004292913	8.974132377	20.90452941
MAZ-1E-04	21	124.5cm	0.004156426	9.116197655	21.93277912
MAZ-1E-04	23	124.5cm	0.005763432	11.35348836	19.6991811
MAZ-1E-04	24	124.5cm	0.005129187	8.633040411	16.83120522
MAZ-1E-04	27	124.5cm	0.00550543	9.652773883	17.53318886
MAZ-1E-04	30	124.5cm	0.007151714	10.85822612	15.18269154
MAZ-1E-04	31	124.5cm	0.004897339	9.183714439	18.75245625
MAZ-1E-04	33	124.5cm	0.004717127	8.696656577	18.43634013
MAZ-1E-04	35	124.5cm	0.004671897	7.892631266	16.89384611
MAZ-1E-04	1	129.5cm	0.00440661	6.999063164	15.88310204
MAZ-1E-04	2	129.5cm	0.005132351	8.083859054	15.75079061
MAZ-1E-04	3	129.5cm	0.004673016	10.29360083	22.0277475
MAZ-1E-04	4	129.5cm	0.005047091	8.138962019	16.12604622
MAZ-1E-04	5	129.5cm	0.00484984	9.184299453	18.93732337
MAZ-1E-04	8	129.5cm	0.004795755	8.175515997	17.04740268
MAZ-1E-04	10	129.5cm	0.004708098	6.721954659	14.27743059
MAZ-1E-04	11	129.5cm	0.006495298	10.23639354	15.75969755
MAZ-1E-04	12	129.5cm	0.005629159	8.843648136	15.71042647
MAZ-1E-04	13	129.5cm	0.005968664	9.326495493	15.62576674
MAZ-1E-04	15	129.5cm	0.005314491	8.511020006	16.01474197

Appendix A

MAZ-1E-04	16	129.5cm	0.005583856	9.781296196	17.51710104
MAZ-1E-04	17	129.5cm	0.004771867	7.834564075	16.41823567
MAZ-1E-04	19	129.5cm	0.005002385	7.966098585	15.92460257
MAZ-1E-04	20	129.5cm	0.004711264	10.23203081	21.71822632
MAZ-1E-04	21	129.5cm	0.004960542	8.078696713	16.28591373
MAZ-1E-04	23	129.5cm	0.0068284	10.03954643	14.70263438
MAZ-1E-04	24	129.5cm	0.00492624	9.357106316	18.9944196
MAZ-1E-04	25	129.5cm	0.006039799	10.88478279	18.02176344
MAZ-1E-04	28	129.5cm	0.005640305	8.489492966	15.05147838
MAZ-1E-04	2	134.5cm	0.004225023	9.466080197	22.40480396
MAZ-1E-04	3	134.5cm	0.004740432	7.836358222	16.530893
MAZ-1E-04	6	134.5cm	0.005746741	9.079084253	15.7986675
MAZ-1E-04	8	134.5cm	0.004397913	8.067693129	18.34436754
MAZ-1E-04	23	134.5cm	0.003395866	8.12491129	23.92588846
MAZ-1E-04	24	134.5cm	0.004218378	8.457244237	20.04857127
MAZ-1E-04	32	134.5cm	0.00462927	8.020182552	17.32493832
MAZ-1E-04	33	134.5cm	0.005466479	8.717694883	15.94755116
MAZ-1E-04	34	134.5cm	0.004717368	7.187631505	15.23653043
MAZ-1E-04	35	134.5cm	0.006019198	7.117222485	11.82420449
MAZ-1E-04	37	134.5cm	0.007725243	11.19123358	14.48657744
MAZ-1E-04	41	134.5cm	0.005318284	9.950882276	18.7107
MAZ-1E-04	42	134.5cm	0.004700878	10.40346584	22.1309
MAZ-1E-04	43	134.5cm	0.005193385	10.46949723	20.15929426
MAZ-1E-04	44	134.5cm	0.005264554	11.18571274	21.2472189
MAZ-1E-04	45	134.5cm	0.004742348	8.887508868	18.74073345
MAZ-1E-04	46	134.5cm	0.006020798	10.14490948	16.84977671
MAZ-1E-04	48	134.5cm	0.006612159	10.25011243	15.501915
MAZ-1E-04	49	134.5cm	0.006303816	10.66161079	16.91294786
MAZ-1E-04	50	134.5cm	0.005166391	8.765682387	16.96674375
MAZ-1E-04	3	141.5cm	0.004717657	8.726600178	18.49774013
MAZ-1E-04	4	141.5cm	0.004904871	7.61428625	15.52392883
MAZ-1E-04	6	141.5cm	0.004307635	7.267122263	16.87032947
MAZ-1E-04	7	141.5cm	0.007168522	11.69529035	16.31478503
MAZ-1E-04	8	141.5cm	0.004568199	6.974065641	15.26655397
MAZ-1E-04	10	141.5cm	0.004130071	7.476787753	18.10328943
MAZ-1E-04	11	141.5cm	0.004475041	8.37987964	18.72581514
MAZ-1E-04	12	141.5cm	0.004943173	9.70176364	19.62659032
MAZ-1E-04	13	141.5cm	0.004440567	8.650361467	19.48030973
MAZ-1E-04	14	141.5cm	0.005587942	8.451564801	15.12464601
MAZ-1E-04	16	141.5cm	0.007021465	11.20193948	15.95385

Appendix A

MAZ-1E-04	17	141.5cr	0.004887066	9.980617975	20.42251698
MAZ-1E-04	18	141.5cr	0.004872796	7.842847362	16.09516821
MAZ-1E-04	19	141.5cr	0.006035885	11.92205652	19.75196066
MAZ-1E-04	20	141.5cr	0.00454202	7.575143552	16.67791915
MAZ-1E-04	22	141.5cr	0.005400566	10.71146602	19.83396811
MAZ-1E-04	23	141.5cr	0.005663416	11.82778266	20.88453873
MAZ-1E-04	24	141.5cr	0.006868428	10.94429682	15.93420822
MAZ-1E-04	25	141.5cr	0.004965195	9.325699987	18.78214324
MAZ-1E-04	28	141.5cr	0.004808718	9.652178798	20.07225
MD01-2415	1	130	0.003966076	8.471111011	21.35892
MD01-2416	2	130	0.004484174	8.903882874	19.85623962
MD01-2417	3	130	0.004417249	8.803379483	19.92955412
MD01-2418	4	130	0.00449921	8.773705646	19.50054615
MD01-2419	2	150	0.00532147	9.470216282	17.79624
MD01-2420	3	150	0.005192965	9.318390127	17.94425856
MD01-2421	4	150	0.004702392	10.53372392	22.40077595
MD01-2422	5	150	0.00431101	9.351650861	21.69248219
MD01-2423	1	170	0.006318804	10.31621446	16.32621268
MD01-2424	2	170	0.004547321	8.412583584	18.50008696
MD01-2425	3	170	0.005543787	12.54934594	22.63677616
MD01-2426	1	215A	0.004429313	12.35910153	27.90297665
MD01-2427	2	215A	0.005677035	9.363186983	16.49309276
MD01-2428	3	215A	0.004172343	10.72176188	25.69722375
MD01-2429	4	215A	0.003293828	9.584948777	29.09972616
MD01-2430	5	215A	0.004351788	9.51610778	21.86712
MD01-2431	6	215A	0.005098222	8.58454152	16.83830428
MD01-2432	7	215A	0.00505859	11.11880716	21.98005333
MD01-2433	8	215A	0.006097343	14.17493284	23.24772229
MD01-2434	9	215A	0.005178258	10.06317155	19.43350651
MD01-2435	10	215A	0.006458707	11.68774895	18.09611239
MD01-2436	11	215A	0.005173496	10.81484501	20.90432466
MD01-2437	12	215A	0.005789293	10.65152039	18.398655
MD01-2438	13	215A	0.004786312	9.900989788	20.68605
MD01-2439	14	215A	0.005583256	11.97540974	21.4487914
MD01-2440	15	215A	0.003945654	9.494527519	24.06325263
MD01-2441	1	220	0.003800852	10.38647856	27.32670849
MD01-2442	2	220	0.005857414	10.82095274	18.47394164
MD01-2443	3	220	0.00514096	10.74059013	20.89218814
MD01-2444	4	220	0.003661133	8.578702735	23.43182452
MD01-2445	5	220	0.005765893	11.86267153	20.57386701

Appendix A

MD01-2446	6	220	0.004325534	8.978017115	20.755856
MD01-2447	7	220	0.004320622	12.00621095	27.78815618
MD01-2448	8	220	0.004572948	10.26687631	22.45133133
MD01-2449	10	220	0.004539477	9.894858663	21.79735458
MD01-2450	11	220	0.003918029	8.113204111	20.70736056
MD01-2451	12	220	0.00560789	11.49932039	20.50561071
MD01-2452	13	220	0.004946809	11.08745614	22.41334982
MD01-2453	14	220	0.005695368	12.04709568	21.15244652
MD01-2454	15	220	0.004447588	8.911898829	20.0376
MD01-2455	17	220	0.00529671	11.60383199	21.90762316
MD01-2456	18	220	0.005631998	11.26661585	20.00465255
MD01-2457	19	220	0.0061252	11.28513189	18.42410204
MD01-2458	20	220	0.003500241	8.159566469	23.31143913
MD01-2459	21	220	0.004486612	9.402923709	20.95773887
MD01-2460	1	225A	0.004265414	7.949254214	18.63653478
MD01-2461	2	225A	0.004273264	8.639717075	20.2180754
MD01-2462	3	225A	0.003555801	10.27233524	28.88895071
MD01-2463	4	225A	0.005052761	12.6136275	24.96383322
MD01-2464	5	225A	0.004854952	8.567813366	17.647575
MD01-2465	6	225A	0.004822453	10.58134018	21.94181928
MD01-2466	7	225A	0.005849348	10.32426087	17.65027725
MD01-2467	8	225A	0.004895365	9.919755183	20.2635675
MD01-2468	9	225A	0.006854735	11.91692331	17.38495
MD01-2469	10	225A	0.003900604	8.13274851	20.84997455
MD01-2470	11	225A	0.006018041	10.72047305	17.81389268
MD01-2471	12	225A	0.004780065	8.264164911	17.28881379
MD01-2472	13	225A	0.005425958	10.15936448	18.72363103
MD01-2473	14	225A	0.003884077	12.83350056	33.04131542
MD01-2474	15	225A	0.006024341	15.13634702	25.12531389
MD01-2475	16	225A	0.005296726	12.13824951	22.91651369
MD01-2476	17	225A	0.004363473	9.314363473	21.346215
MD01-2477	18	225A	0.007657171	12.00952269	15.68402
MD01-2478	19	225A	0.005495653	10.32678864	18.79082968
MD01-2479	20	225A	0.004025312	8.248510124	20.49160563
MD01-2480	21	225A	0.005911115	9.194207232	15.55409907
MD01-2481	1	230	0.005072054	10.19958379	20.109375
MD01-2482	2	230	0.004555779	8.547816141	18.76258016
MD01-2483	10	230	0.00453784	10.23322713	22.5508748
MD01-2484	12	230	0.004573604	12.10680774	26.47104483
MD01-2485	13	230	0.006691512	10.65716341	15.92638963

Appendix A

MD01-2486	14	230	0.005209286	12.41986076	23.84177019
MD01-2487	15	230	0.003970449	12.98177059	32.69597615
MD01-2488	16	230	0.004680521	16.02777225	34.24356279
MD01-2489	17	230	0.004803799	9.71883137	20.23155328
MD01-2490	18	230	0.005792593	12.24383729	21.13705728
MD01-2491	19	230	0.004490658	8.529023688	18.99281504
MD01-2492	20	230	0.006151145	13.31485775	21.64614375
MD01-2493	21	230	0.004579504	9.068270865	19.80186353
MD01-2494	22	230	0.005385151	10.89223882	20.22642981
MD01-2495	23	230	0.005045076	9.953596362	19.72932923
MD01-2496	1	245A	0.005920134	8.998502206	15.19982895
MD01-2497	2	245A	0.007271827	12.42228891	17.08276099
MD01-2498	3	245A	0.005095282	11.33042227	22.23708367
MD01-2499	4	245A	0.0058517	11.05783335	18.89678718
MD01-2500	6	245A	0.005980136	11.44406068	19.13678973
MD01-2501	7	245A	0.005451201	11.83805491	21.71641645
MD01-2502	8	245A	0.007770669	11.80121857	15.18687564
MD01-2503	9	245A	0.006579207	13.6097135	20.68594794
MD01-2504	10	245A	0.004827952	13.35721474	27.66641908
MD01-2505	11	245A	0.006443475	15.11700183	23.46094724
MD01-2506	12	245A	0.005232297	10.18375529	19.46325907
MD01-2507	1	255A	0.005456314	13.24908877	24.28212466
MD01-2508	2	255A	0.005571207	11.33589936	20.34729459
MD01-2509	3	255A	0.005514503	12.95134769	23.48597611
MD01-2510	4	255A	0.00691268	12.16579428	17.59924442
MD01-2511	5	255A	0.004992311	11.12049003	22.27523571
MD01-2512	6	255A	0.006335763	11.78543222	18.60144191
MD01-2513	7	255A	0.006411969	12.82477072	20.0013
MD01-2514	8	255A	0.005927469	11.56087315	19.50389475
MD01-2515	9	255A	0.005710447	10.08621623	17.66274231
MD01-2516	10	255A	0.004867307	9.859900105	20.25740184
MD01-2517	11	255A	0.006955931	12.73304655	18.30531008
MD01-2518	13	255A	0.005808324	11.81014614	20.33313982
MD01-2519	15	255A	0.006346275	10.71815667	16.88889299
MD01-2520	16	255A	0.003947655	8.006102274	20.28065217
MD01-2521	18	255A	0.00524204	9.060646129	17.28458025
MD01-2522	19	255A	0.004353827	10.41314306	23.91721852
MD01-2523	20	255A	0.007280967	12.04413023	16.54193858
MD01-2524	22	255A	0.004539086	12.73879281	28.06466525
MD01-2525	23	255A	0.006067675	11.08511411	18.26913

Appendix A

MD01-2526	25	255A	0.005587344	11.62711809	20.80974036
MD01-2527	2	260	0.00706093	13.69341044	19.39321064
MD01-2528	6	260	0.009085807	16.03545178	17.64890217
MD01-2529	7	260	0.006175583	11.55124362	18.7047
MD01-2530	10	260	0.006734646	11.39081947	16.91376067
MD01-2531	12	260	0.007552743	13.19890411	17.4756433
MD01-2532	1	270	0.005033049	11.1239841	22.10187786
MD01-2533	2	270	0.006142355	11.0983618	18.06857849
MD01-2534	4	270	0.005525632	10.17942695	18.42219517
MD01-2535	6	270	0.005390157	11.04985545	20.500062
MD01-2536	12	270	0.0062007	11.84815057	19.10776154
MD01-2537	13	270	0.004982757	9.843928347	19.75598842
MD01-2538	14	270	0.007495155	12.96387486	17.29634094
MD01-2539	15	270	0.005663766	9.58798254	16.92863333
MD01-2540	16	270	0.006492057	11.27136133	17.36177143
MD01-2541	18	270	0.006636125	11.52137438	17.3616
MD01-2542	19	270	0.00580377	12.07966017	20.81347009
MD01-2543	20	270	0.004570421	12.96596062	28.36929419
MD01-2544	21	270	0.00430191	10.29886648	23.94022041
MD01-2545	22	270	0.005325172	10.24370176	19.23637906
MD01-2546	23	270	0.006750418	11.61889798	17.21211556
MD01-2547	24	270	0.004742345	9.108809861	19.20739765
MD01-2548	2	270A	0.004471864	9.39192652	21.00226207
MD01-2549	3	270A	0.004735258	12.8014979	27.034425
MD01-2550	5	270A	0.00474043	8.987404554	18.95904797
MD01-2551	6	270A	0.005837535	10.27299287	17.59817019
MD01-2552	7	270A	0.004966977	10.82279654	21.789504
MD01-2553	8	270A	0.00575171	10.10606579	17.57053993
MD01-2554	10	270A	0.005857413	8.6593736	14.78361553
MD01-2555	11	270A	0.005458558	10.3145667	18.89613987
MD01-2556	12	270A	0.005966258	10.82855822	18.14966389
MD01-2557	13	270A	0.005536869	11.63037291	21.005325
MD01-2558	14	270A	0.004681169	9.672965983	20.6635703
Sagami Bay	1		0.004518096	9.923997549	21.9649988
Sagami Bay	2		0.004279749	7.588114801	17.73028125
Sagami Bay	3		0.00440102	6.671156104	15.15820465
Sagami Bay	4		0.004866284	9.121435952	18.74415172
Sagami Bay	5		0.006475341	11.38412303	17.58073177
Sagami Bay	6		0.005352761	8.640833302	16.14275816
Sagami Bay	7		0.004697551	8.488726302	18.07053655

Appendix A

Sagami Bay	8	0.004769347	7.800942811	16.35641548
Sagami Bay	9	0.00393816	8.835638085	22.43595634
Sagami Bay	10	0.005293493	9.347045857	17.65761386
Sagami Bay	11	0.00450254	8.285347782	18.40149681
Sagami Bay	13	0.004353588	8.06483253	18.5245646
Sagami Bay	14	0.004922879	10.12298511	20.5631417
Sagami Bay	15	0.005738649	10.54777177	18.38023611
Sagami Bay	16	0.004994214	10.20766099	20.43897429
Sagami Bay	18	0.005705394	9.957066731	17.45202313
Sagami Bay	19	0.003665006	6.83279216	18.64333245
Sagami Bay	20	0.005196146	7.822334337	15.05410929
Sagami Bay	21	0.005413495	8.271690437	15.279759
Sagami Bay	22	0.005461342	9.57084016	17.52470323
Sagami Bay	23	0.005371709	11.08597224	20.63770035
Sagami Bay	24	0.00413461	8.483665062	20.51865826
Sagami Bay	25	0.004790564	9.612818498	20.06615056
Sagami Bay	26	0.005585128	11.1378073	19.9419
Sagami Bay	27	0.005039066	8.816858491	17.49700787
Sagami Bay	28	0.004923601	8.526748518	17.31811304
Sagami Bay	30	0.005216426	8.103345324	15.53428664
Sagami Bay	31	0.004016713	7.186330052	17.8910711
Sagami Bay	32	0.005667804	9.357641675	16.51017248
Sagami Bay	33	0.005916046	12.88816825	21.78510469
Sagami Bay	34	0.004814342	10.26126876	21.31395945
Sagami Bay	35	0.005151831	7.436052516	14.433804
Sagami Bay	36	0.004337275	9.316280365	21.47956974
Sagami Bay	37	0.005768838	10.5269465	18.24794847
Sagami Bay	38	0.004650581	11.29292783	24.28283047
Sagami Bay	39	0.004621219	8.264555903	17.88392872
Sagami Bay	40	0.005915132	8.587620102	14.51805331
SO206-43-MUC	8	0.006096832	10.8587368	17.81045752
SO206-43-MUC	54	0.006214803	9.934571434	15.98533724
SO206-43-MUC	3	0.005035054	8.073453155	16.03449114
SO206-43-MUC	4	0.003920322	8.556346154	21.82562027
SO206-43-MUC	5	0.006091351	9.700665935	15.9253119
SO206-43-MUC	6	0.005997052	11.75874265	19.60753729
SO206-43-MUC	7	0.004594413	8.879705481	19.3271816
SO206-43-MUC	8	0.004793451	9.112244304	19.00977978
SO206-43-MUC	9	0.006252589	11.0702148	17.70501009
SO206-43-MUC	10	0.005580758	10.8402246	19.42428589

Appendix A

SO206-43-MUC	11		0.006546426	11.10844432	16.96871545
SO206-43-MUC	15		0.004579008	5.973745115	13.04593836
SO206-43-MUC	16		0.006533646	8.127561242	12.43955013
SO206-43-MUC	17		0.003783559	6.619087058	17.49434211
SO206-43-MUC	18		0.006908463	9.184796447	13.29499286
SO206-43-MUC	19		0.006533501	8.165308422	12.49760115
SO206-43-MUC	20		0.006253553	7.842738429	12.54125172
SO206-43-MUC	21		0.006002601	9.061502651	15.09596
SO206-43-MUC	22		0.006106737	7.751812598	12.69387077
SO206-43-MUC	23		0.004781521	9.046895138	18.92053731
SO206-43-MUC	24		0.00316853	6.959218031	21.96355472
SO206-43-MUC	26		0.008221517	10.03732086	12.20859955
SO206-43-MUC	27		0.007607455	11.04997011	14.52518571
SO206-43-MUC	28		0.008328474	10.9701786	13.17189584
SO206-43-MUC	32		0.005292474	9.278234053	17.53099615
SO206-43-MUC	36		0.005272616	9.066445646	17.19534502
SO206-43-MUC	43		0.006237596	10.0207349	16.06506
SO206-43-MUC	2		0.004989715	9.532215433	19.10372694
SO206-43-MUC	3		0.006688254	10.26617902	15.34956484
SO206-43-MUC	4		0.00547514	9.383219693	17.13786194
SO206-43-MUC	5		0.008140118	10.99881177	13.51185782
SO206-43-MUC	8		0.004195158	8.370064868	19.95172731
SO206-43-MUC	10		0.005272299	8.553083364	16.22268353
SO206-43-MUC	11		0.005094135	10.67864608	20.9626289
SO206-43-MUC	13		0.007778844	11.11411891	14.28762283
SO206-43-MUC	14		0.00614429	9.876771547	16.07471703
SO206-43-MUC	16		0.006652695	11.45995097	17.22602861
SO206-43-MUC	17		0.006731839	10.58401159	15.72231913
SO206-43-MUC	19		0.007184654	11.21521814	15.60996217

**Supplementary Table ST9.** Data of Inter-species comparison of pore parameters and pore density vs  $[\text{NO}_3^-]_{\text{BW}}$  calibration in the core-top samples.

\*From Glock et al. (2011), and the others from this PhD project.

Species	Location	$[\text{NO}_3^-]_{\text{BW}}$ ( $\mu\text{M}$ )	Water depth (m)	Avg. pore density ( $\text{P}/\mu\text{m}^2$ )	SD ( $\text{P}/\mu\text{m}^2$ )	SEM ( $\text{P}/\mu\text{m}^2$ )
<i>B. spissa</i> *	Peru	18.3	114	0.0155	0.00158	0.00039
<i>B. spissa</i> *	Peru	34.02	465	0.0069	0.00103	0.00016
<i>B. spissa</i> *	Peru	40.1	640	0.0052	0.00089	0.00014
<i>B. spissa</i> *	Peru	40.75	928	0.0053	0.00103	0.00019
<i>B. spissa</i> *	Peru	38.84	579	0.0057	0.00095	0.00012
<i>B. spissa</i> *	Peru	40.98	698	0.0049	0.00086	0.00043
<i>B. spissa</i> *	Peru	40.82	878	0.0053	0.00088	0.00021
<i>B. spissa</i> *	Peru	36.08	513	0.0062	0.00081	0.00017
<i>B. spissa</i>	Costa Rica	39.11	568	0.0059	0.00123	0.00020
<i>B. spissa</i>	Sagami Bay	42.2	1500	0.0050	0.00063	0.00010
<i>B. subadvena</i>	Costa Rica	39.11	568	0.0056	0.00095	0.00017
<i>B. subadvena</i>	Sagami Bay	42.2	1500	0.0049	0.00000	0.00000
<i>B. subadvena accumeata</i>	Costa Rica	39.11	568	0.0088	0.00018	0.00013
<i>B. argentea</i>	Costa Rica	39.11	568	0.0168	0.00219	0.00110

**Supplementary Table ST10.** Data of bottom-water oxygen, temperature, salinity, water depth of Peruvian OMZ, Costa Rica, and Sagami Bay with the average pore density of *B. spissa*

\* From Glock et al. (2011), and the others from this PhD project.

Species	Location	Water depth (m)	Salinity	Oxygen ( $\mu\text{mol}/\text{kg}$ )	Temperature ( $^{\circ}\text{C}$ )	Average pore density ( $\text{P}/\mu\text{m}^2$ )
<i>B. spissa</i> *	Peru	114	34.95	1.07	12.9822	0.0155
<i>B. spissa</i> *	Peru	465	34.64	2.42	8.12	0.0069
<i>B. spissa</i> *	Peru	640	34.56	8.17	6.7	0.0052
<i>B. spissa</i> *	Peru	928	34.56	36.78	4.76	0.0053
<i>B. spissa</i> *	Peru	579	34.55	3.695	7.21	0.0057
<i>B. spissa</i> *	Peru	698	34.57	12.55	6.68	0.0049
<i>B. spissa</i> *	Peru	878	34.53	34.23	5.7168	0.0053
<i>B. spissa</i> *	Peru	513	34.61	2.40	8.0514	0.0062
<i>B. spissa</i>	Costa Rica	568	34.69	9.53	7.47	0.0059
<i>B. spissa</i>	Sagami Bay	1410	34.50	56.4	2.3	0.0050
<i>B. subadvena</i>	Costa Rica	568	34.69	9.53	7.47	0.0056

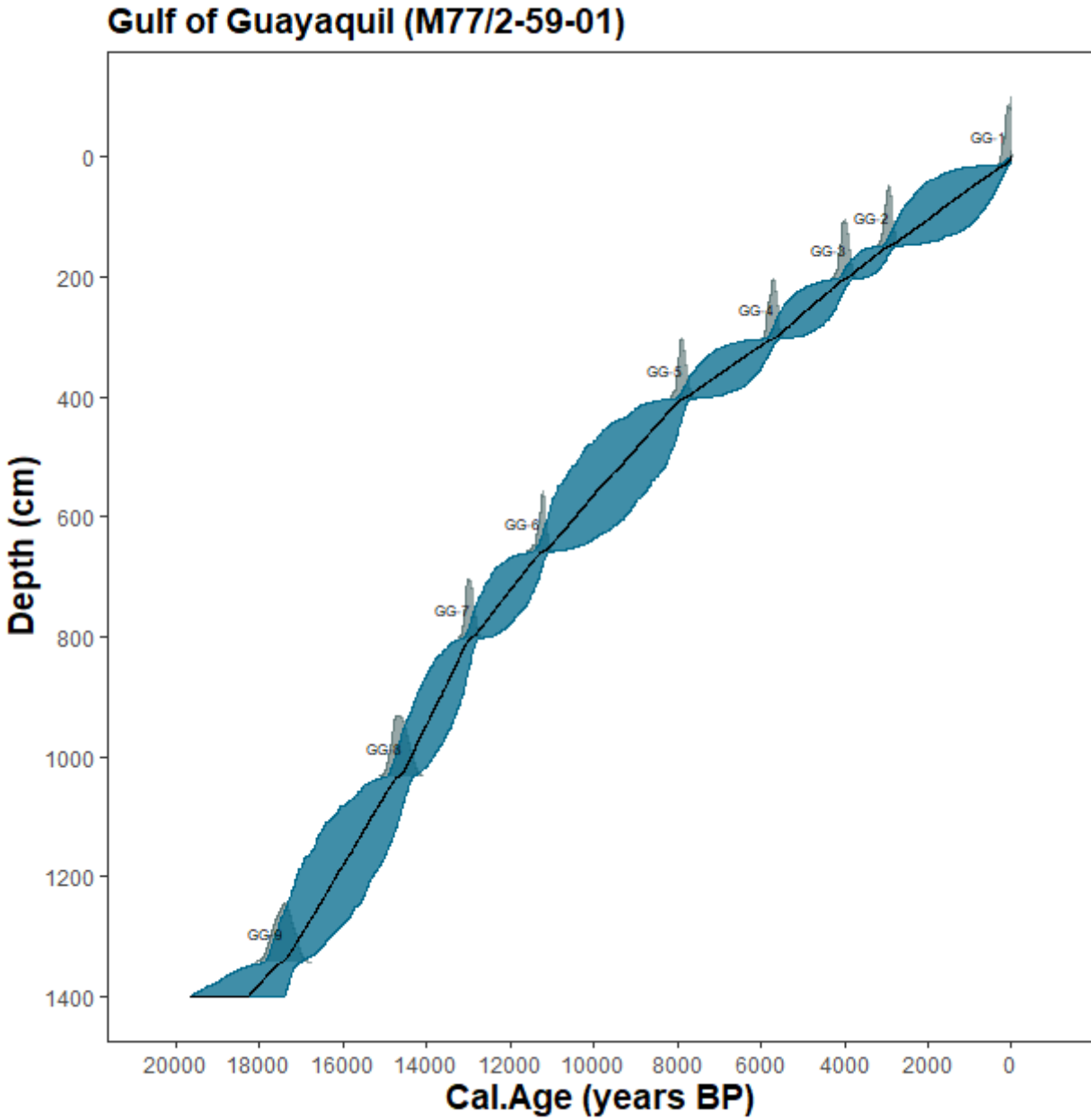
Appendix A

---

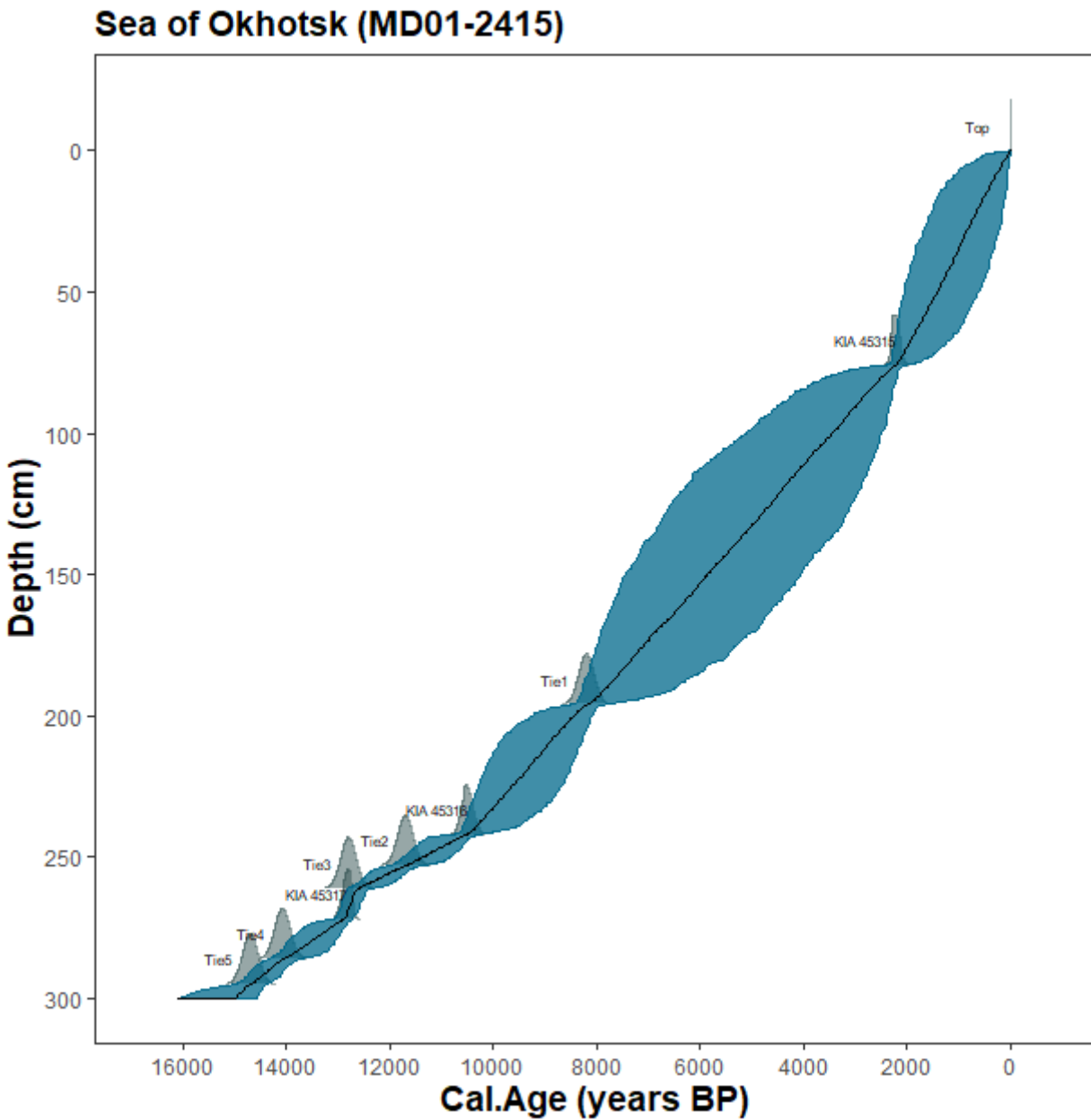
<i>B. subadvena</i>	Sagami Bay	1410	34.5	56.4	2.3	0.0049
<i>B. subadvena accumeata</i>	Costa Rica	568	34.69	9.53	7.47	0.00878
<i>B. argentea</i>	Costa Rica	568	34.69	9.53	7.47	0.0168

Appendix B

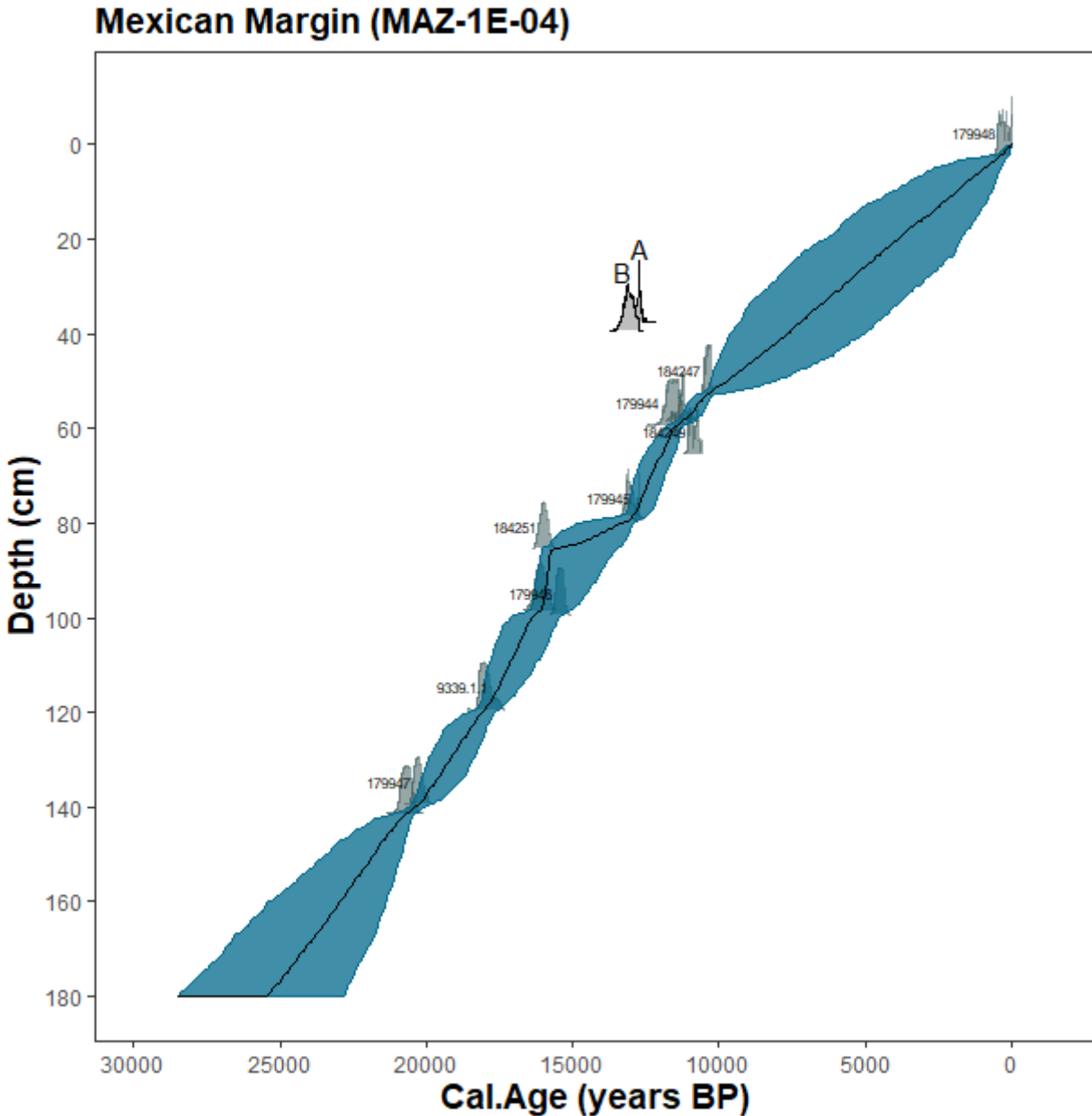
**Supplementary Figure SF1.** Age-depth model updated for core M77/2-59-01 from the Gulf of Guayaquil based on  $^{14}\text{C}$  dating and have been calibrated using Marine20. Error bands depict 95% confidence interval.



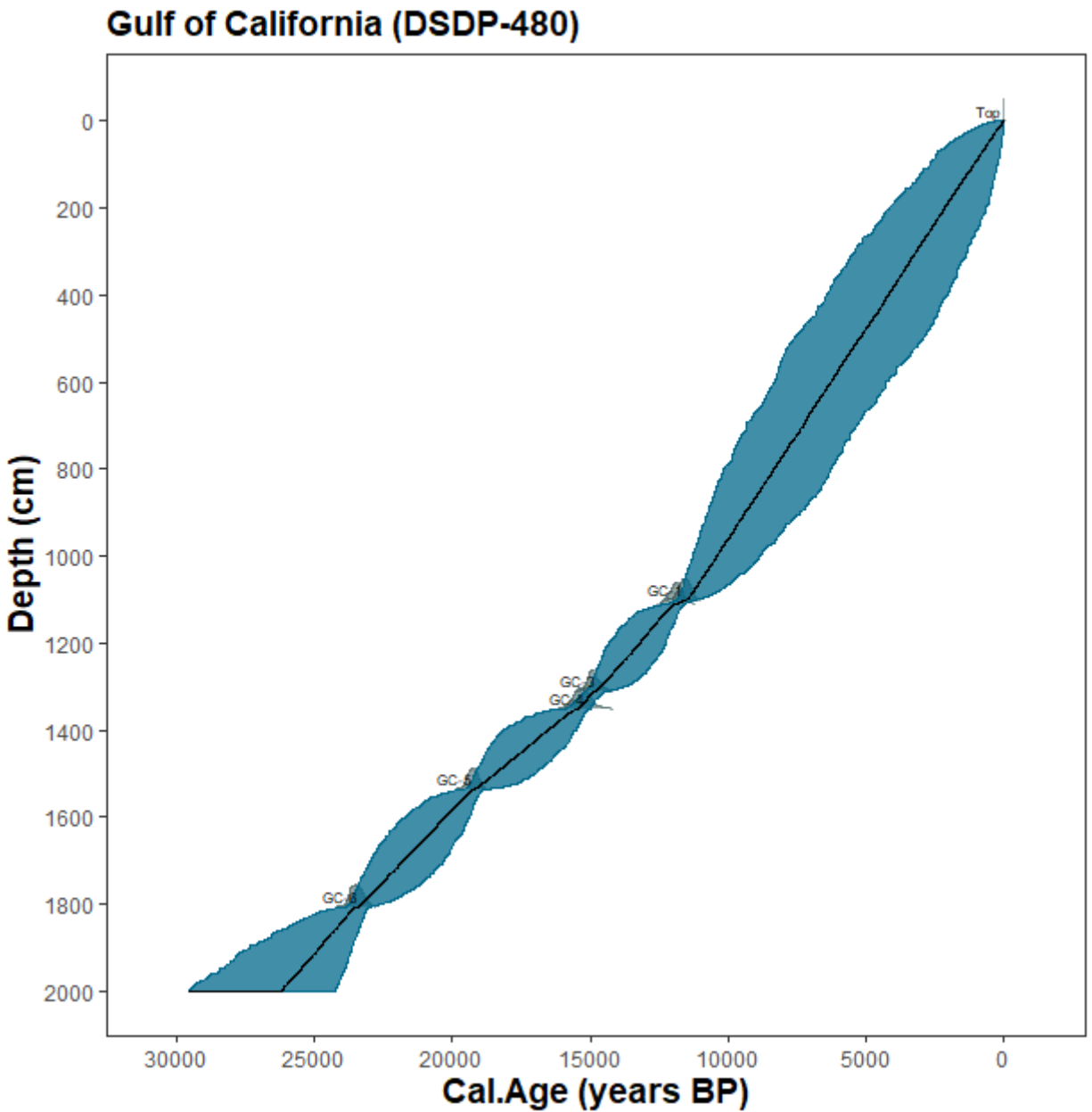
**Supplementary Figure SF2.** Age-depth model updated for core MD01-2415 from the Sea of Okhotsk based on  $^{14}\text{C}$  dating and have been calibrated using Marine20. Error bands depict 95% confidence interval.



**Supplementary Figure SF3.** Age-depth model completely developed in the framework of this PhD for core MAZ-1E-04 from the Mexican Margin based on  $^{14}\text{C}$  dating and have been calibrated using Intcal20. Error bands depict 95% confidence interval. In the radiocarbon data for this core, age reversals were observed for the top-part above sediment depth 52.5 cm onwards. This age reversal is shown in this age model. Points “A” and “B” in the figure depicts the age reversal.



**Supplementary Figure SF4.** Age-depth model updated for core DSDP-480 from the Gulf of California (Guaymas Basin) based on  $^{14}\text{C}$  dating and have been calibrated using Marine20. Error bands depict 95% confidence interval.



**Supplementary Table ST1.** Data of calculated ages, pore density (PD), reconstructed bottom-water nitrate ( $[\text{NO}_3^-]_{\text{BW}}$ ) in  $\mu\text{mol/mol}$ , sedimentary nitrogen isotope ( $\delta^{15}\text{N}_{\text{bulk}}$ ) of the Gulf of Guayaquil (GG), the Mexican Margin (Mex), the Sea of Okhotsk (Okh), and the Gulf of California (GoC) used in the Ph.D. project. SD is Standard deviation, SE is the Standard Error of the Mean

GG_Age (kyr BP)	GG_Mean PD	GG_SD of PD	GG_ $[\text{NO}_3^-]$ BW	$\delta^{15}\text{N}_{\text{bulk}}$ _GG (‰) from Mollier- Vogel et al. (2019)	GG_SD_ $[\text{NO}_3^-]_{\text{BW}}$	GG_SE_ $[\text{NO}_3^-]_{\text{BW}}$
0.189	0.0042	0.00064	44.465	3.549	3.074	0.505
1.152	0.0042	0.00057	44.576	4.208	2.857	0.469
1.363	0.0037	0.00065	46.482	4.353	3.023	0.497
1.469	0.0042	0.00070	44.323	4.428	3.274	0.538
1.786	0.0040	0.00080	45.138	4.211	3.579	0.588
1.998	0.0043	0.00068	44.155	4.126	3.222	0.529
3.161	0.0040	0.00059	45.034	4.384	2.910	0.478
3.931	0.0037	0.00052	46.199	4.172	2.636	0.433
4.651	0.0042	0.00084	44.624	3.916	3.743	0.615
5.340	0.0039	0.00066	45.621	4.369	3.090	0.508
6.052	0.0041	0.00062	44.788	4.663	3.003	0.493
6.921	0.0043	0.00092	44.135	4.513	4.042	0.664
7.791	0.0041	0.00070	44.692	4.506	3.260	0.536
8.429	0.0038	0.00099	45.827	4.640	4.221	0.694
8.929	0.0045	0.00058	43.297	5.589	2.965	0.487
9.428	0.0041	0.00078	44.828	5.388	3.525	0.579
9.928	0.0039	0.00078	45.466	5.500	3.492	0.574
10.427	0.0043	0.00072	44.120	5.221	3.333	0.547
10.927	0.0043	0.00045	44.164	5.185	2.531	0.416
11.428	0.0046	0.00088	42.959	5.186	3.914	0.644
11.935	0.0047	0.00091	42.676	5.195	4.046	0.665
12.443	0.0042	0.00061	44.501	5.363	2.987	0.491
12.950	0.0039	0.00045	45.954	5.289	2.433	0.400
13.305	0.0040	0.00050	45.518	5.832	2.608	0.429
13.569	0.0042	0.00096	44.486	5.428	4.162	0.684
13.834	0.0044	0.00059	43.983	5.427	2.923	0.481
14.098	0.0041	0.00071	45.038	5.886	3.280	0.539
14.362	0.0045	0.00083	43.301	5.382	3.754	0.617
14.626	0.0051	0.00096	41.034	5.183	4.252	0.699
15.033	0.0043	0.00109	44.155	5.032	4.628	0.761
15.459	0.0046	0.00126	42.922	5.095	5.265	0.865

Appendix B

15.885	0.0050	0.00122	41.387	4.907	5.179	0.851
16.312	0.0044	0.00088	43.772	4.971	3.905	0.642
16.738	0.0053	0.00104	40.510	4.940	4.576	0.752
17.165	0.0038	0.00049	46.322	4.351	2.515	0.413
17.591	0.0040	0.00074	45.311	4.570	3.370	0.554
18.017	0.0038	0.00074	46.226	4.400	3.328	0.547

Mex_Age (kyr BP)	Mex_Mean PD	Mex_SD- of PD	Mex__[NO <sub>3</sub> <sup>-</sup> ] <sub>BW</sub> (μmol/mol)	Mex_SD_ _[NO <sub>3</sub> <sup>-</sup> ] <sub>BW</sub>	Mex_SEM _[NO <sub>3</sub> <sup>-</sup> ] <sub>BW</sub>
2.139	0.005975	0.001290	37.722	5.532	1.154
3.634	0.005733	0.001000	38.663	4.502	0.939
5.101	0.005860	0.000790	38.171	3.827	0.798
8.201	0.005620	0.000900	39.104	4.135	0.862
9.170	0.005545	0.000900	39.396	4.122	0.859
10.473	0.005238	0.001010	40.592	4.447	0.927
11.085	0.005530	0.000900	39.454	4.121	0.859
11.781	0.005910	0.000880	37.976	4.122	0.860
12.219	0.004480	0.000690	43.547	3.270	0.682
12.525	0.004571	0.000670	43.191	3.212	0.670
12.887	0.004632	0.000890	42.952	3.941	0.822
14.291	0.004915	0.000830	41.853	3.800	0.792
15.261	0.005730	0.001000	38.675	4.495	0.937
15.514	0.005907	0.001140	37.986	4.993	1.041
15.793	0.005923	0.001060	37.925	4.740	0.988
16.556	0.005934	0.000900	37.882	4.194	0.875
16.961	0.005654	0.000670	38.973	3.434	0.716
17.424	0.005598	0.001040	39.189	4.594	0.958
17.884	0.005670	0.000870	38.909	4.067	0.848
18.584	0.005592	0.001020	39.212	4.544	0.947
19.094	0.005274	0.000650	40.452	3.300	0.688
19.577	0.005230	0.000980	40.623	4.360	0.909
20.581	0.005215	0.000910	40.681	4.113	0.858

Okh_Age (kyrs BP)	Okh_[NO <sub>3</sub> <sup>-</sup> ] <sub>BW</sub>	Okh_mean PD	Okh_SD of PD	Okh_SD _[NO <sub>3</sub> <sup>-</sup> ] <sub>BW</sub>	Okh_SE_[NO <sub>3</sub> <sup>-</sup> ] <sub>BW</sub>
4.911	44.085	0.00434	0.00025	2.069	0.624
5.836	41.980	0.00488	0.00046	2.683	0.809

6.723	39.689	0.00547	0.00089	4.079	1.230
9.164	41.496	0.00501	0.00086	3.907	1.178
9.383	42.209	0.00482	0.00081	3.725	1.123
9.594	41.111	0.00511	0.00104	4.529	1.365
9.999	41.380	0.00504	0.00072	3.455	1.042
10.833	37.474	0.00604	0.00092	4.265	1.286
11.895	38.826	0.00569	0.00088	4.101	1.236
12.404	32.474	0.00732	0.00111	5.112	1.541
12.819	38.828	0.00569	0.00088	4.095	1.235

GoC_Age (kyr BP)	GoC_ $[\text{NO}_3^-]_{\text{BW}}$ from PD	GoC_mean PD	GoC_SD of PD	GoC_SD _ $[\text{NO}_3^-]_{\text{BW}}$	GoC_SEM _ $[\text{NO}_3^-]_{\text{BW}}$
10.841	42.058	0.00486	0.00061	3.096	0.774
11.232	42.982	0.00462	0.00070	3.335	0.834
11.572	43.117	0.00459	0.00084	3.769	0.942
14.956	44.210	0.00431	0.00104	4.433	1.108
17.611	45.449	0.00399	0.00124	5.122	1.280
18.250	49.106	0.00305	0.00063	2.871	0.718
18.867	45.749	0.00391	0.00104	4.384	1.096
19.724	46.198	0.00380	0.00051	2.606	0.651
19.992	44.842	0.00415	0.00078	3.528	0.882
20.532	46.520	0.00372	0.00118	4.894	1.223
21.861	44.573	0.00422	0.00058	2.867	0.717
22.126	47.222	0.00354	0.00110	4.583	1.146
22.631	46.310	0.00377	0.00089	3.832	0.958
23.122	45.998	0.00385	0.00048	2.510	0.627
25.334	41.412	0.00503	0.00060	3.087	0.772
25.988	44.770	0.00417	0.00089	3.883	0.971

## Continuation of Supplementary Table ST1

Bulk nitrogen ( $\delta^{15}\text{N}_{\text{bulk}}$ ) from Sea of Okhotsk (Okh)		
Depth (cm)	$\delta^{15}\text{N}_{\text{bulk\_Okh}}$ (‰)	Cal. Age (kyrs BP)
155	7.562	6.056
160	7.107	6.281
165	7.383	6.502
170	7.519	6.723
175	7.648	6.935

180	7.723	7.169
185	7.727	7.412
190	7.743	7.678
195	8.273	8.014
235	9.409	10.023
240	9.441	10.288
245	9.171	10.833
250	9.430	11.286
255	9.213	11.895
265	8.573	12.710
270	8.258	12.819
301	8.390	15.060
305	8.281	15.237
310	8.144	15.449

Bulk nitrogen ( $\delta^{15}\text{N}_{\text{bulk}}$ ) from Gulf of California (GoC)		
Depth (cm)	Age calculated	$\delta^{15}\text{N}_{\text{bulk\_GoC}}$ (‰)
2	0.053	10.089
35.5	0.502	10.353
68.5	0.841	10.440
98.5	1.146	10.554
134.5	1.504	9.849
152	1.683	10.802
218.5	2.389	10.559
251.5	2.710	11.349
302	3.218	10.603
335.5	3.552	10.075
368.5	3.886	11.621
477	4.975	9.929
509.5	5.317	10.255
543.5	5.674	11.334
575.5	6.011	10.013
609.5	6.346	10.957
627.5	6.526	10.260
660.5	6.861	10.966
691.5	7.174	10.747
726.5	7.522	10.805
759.5	7.849	10.617
777	8.022	9.181
810.5	8.369	10.527
843.5	8.703	9.777

952.5	9.786	11.884
1018.5	10.481	12.466
1051.5	10.841	11.613
1084.5	11.232	11.441
1102	11.572	11.612
1135.5	12.391	12.977
1168.5	12.830	12.756
1201.5	13.263	12.383
1234.5	13.683	11.875
1255.5	13.936	12.697
1318.5	14.956	10.720
1427	17.031	10.806
1460.5	17.611	9.050
1495.5	18.250	9.149
1526.5	18.867	9.447
1559.5	19.724	9.117
1577	19.992	9.225
1614.5	20.539	9.441
1643.5	20.954	6.436
1673.5	21.373	8.409
1707.5	21.861	8.450
1727	22.126	8.886
1762.5	22.631	8.837
1794.5	23.122	9.335
1826.5	23.872	8.287
1902	24.885	8.551
1935.5	25.321	8.884
1968.5	25.736	6.881
1998.5	26.115	9.261
2034.5	26.139	8.184

**Supplementary Table ST2.** Radiocarbon data used for updating the age-depth model for core M77/2-59-01 from the Gulf of Guayaquil. SD is Standard deviation. Bchron package in RStudio is used for updating the age model.

Depth (cm)	Radiocarbon age ( $^{14}\text{C}$ yr)	SD ( $^{14}\text{C}$ yr)	Ages (Radiocarbon age -Delta R = 200)
13	830	25	630
148	3490	30	3290
203	4325	45	4125
303	5725	50	5525
403	7815	65	7615
658	10470	50	10270
803	11855	60	11655
1033	13140	70	12940
1344	15270	150	15070

**Supplementary Table ST3.** Radiocarbon data used for updating the age-depth model for core MD01-2415 from the Sea of Okhotsk. Data from Bubenschikowa et al. (2015). Bchron package in RStudio is used for updating the age model.

##	id	ages	ageSds	position	thickness	calCurves	
##1	Top	0	1	0	0	normal	core-top
##2	KIA 45315	2689	25	76	1	marine20	planktic radiocarbon age
##3	Tie1	8200	150	196	1	normal	$\delta^{18}\text{O}$ age tie point
##4	KIA 45316	9749	50	242	1	marine20	planktic radiocarbon age
##5	Tie2	11700	150	253	1	normal	$\delta^{18}\text{O}$ age tie point
##6	Tie3	12800	150	261	1	normal	$\delta^{18}\text{O}$ age tie point
##7	KIA 45317	11504	55	272	1	marine20	planktic radiocarbon age
##8	Tie4	14080	150	286	1	normal	$\delta^{18}\text{O}$ age tie point
##9	Tie5	14700	150	295	1	normal	$\delta^{18}\text{O}$ age tie point

**Supplementary Table ST4.** Radiocarbon data used for developing the age-depth model for core MAZ-1E-04 from the Mexican Margin.

AWI nr.	Sample	Depth (cm)	Age (y)	±(y)	MRA	MRA corrected	Calibrated Age (years BP)
179948	9/1/2022	2.5	260	110	737	0	262.3
184245	MAZ01_E04_37_38P, Mixed planktics	37.5	11,300	90	531	10,769	7,098.5
179943	9/1/2022	39.5	11,800	180	611	11,189	7,456.3
184247	MAZ01_E04_52_53P, <i>T. sacculifer</i>	52.5	9,730	50	522	9,208	10,109.3
9336.1.1	MAZ-1 E-04_58-59 cm, <i>G. ruber</i>	58.5	10,367	101	546	9,821	11,085.3
179944	9/1/2022	59.5	10,600	110	542	10,058	11,354.9
184249	MAZ01_E04_65_66P, <i>T. sacculifer</i>	65.5	10,150	50	634	9,516	11,924.4
9337.1.1	MAZ-1 E-04_78-79 cm, <i>G. ruber</i>	78.5	11,783	109	611	11,172	12,886.7
179945	8/29/2022	79.5	11,350	65	538	10,812	13138.032
184251	MAZ01_E04_85_86P, Mixed planktics	85.5	13,850	85	548	13,302	14831.645
9338.1.1	MAZ-1 E-04_98-99 cm, <i>G. ruber</i>	98.5	13,993	124	620	13,373	15793.264
179946	8/29/2022	99.5	13,550	70	643	12,907	16008.247
9339.1.1	MAZ-1 E-04_119-120 cm, <i>G. ruber</i>	119.5	15,384	136	680	14,704	17883.543
179947	8/29/2022	139.5	17,650	110	877	16,773	20149.511
9340.1.2	MAZ-1 E-04_141-142 cm. <i>G. ruber</i>	141.5	18,064	159	936	17,128	20581.484

**Supplementary Table ST5.** Radiocarbon data used for updating the age-depth model for core DSDP-480 from the Gulf of California. Data from Keigwin & Jones (1990).

Sediment Depth [m]	Age dated [ka] (Accelerator Mass Spectrometer...)	Age dated std dev [ $\pm$ ] (Age, $^{14}\text{C}$ conventional)	Age dated (reservoir correction 301 year...)	Age dated [ka] (reservoir correction 301 year...)
10.51	10.8	0.09	10499	10.499
10.81	11	0.11	10699	10.699
11.01	10.8	0.12	10499	10.499
11.11	11	0.13	10699	10.699
13.11	13.4	0.11	13099	13.099
13.51	13.7	0.21	13399	13.399
15.36	17	0.13	16699	16.699
18.06	20.6	0.18	20299	20.299

## Appendix C

**Supplementary Table ST1:** The Mn/Ca ratios of cleaned and uncleaned specimens of *B. spissa* and *B. subadvena* using LA-ICP-MS from different ODZs used in the PhD thesis.

## A) Gulf of Guayaquil

Sample number	Avg_ uncleaned	STDEV- uncleaned	SE-uncleaned	Avg_ cleaned	STDEV- cleaned	SE-cleaned
SN1	32.258	16.091	2.937	na	na	na
SN2	60.925	11.655	6.729	na	na	na
SN3	34.470	17.126	2.937	na	na	na
SN4	45.115	20.756	5.359	na	na	na
SN5	37.595	14.651	4.229	na	na	na
SN6	32.340	29.175	8.091	18.734	3.700	2.616
SN7	108.598	218.382	58.365	85.037	13.264	6.632
SN8	66.836	34.941	6.603	191.908	6.794	4.804
SN9	50.985	14.148	4.266	37.468	2.895	1.671
SN10	71.150	15.347	4.430	na	na	na
SN11	73.1472	28.456	10.755	54.360	27.062	13.531
SN12	63.0954	9.085	3.0283	75.428	3.945	2.789
SN13	164.164	241.436	72.795	215.310	150.991	75.495
SN14	81.147	26.667	6.885	128.522	4.460	3.154
SN15	76.224	75.0123	20.047	28.762	9.347	6.609
SN16	117.721	100.545	25.960	54.433	21.569	15.251
SN17	165.463	322.166	83.183	na	na	na
SN18	98.929	88.309	23.601	na	na	na

## B) Mexican Margin

Sample number	Avg_ uncleaned	STDEV- uncleaned	SE-uncleaned	Avg_ cleaned	STDEV- cleaned	SE-cleaned
SN1	429.748	281.912	72.789	1353.800	251.868	178.097
SN2	279.064	142.213	41.0535	na	na	na
SN3	183.386	99.615	28.756	na	na	na
SN4	453.305	246.263	87.067	554.695	17.791	12.580
SN5	378.882	141.301	36.483	250.928	91.627	64.790
SN6	301.742	240.093	61.991	481.594	163.678	66.821
SN7	328.311	328.871	84.914	na	na	na
SN8	253.962	151.846	43.834	na	na	na
SN9	224.124	62.712	18.103	na	na	na
SN10	176.247	78.336	22.613	102.231	5.956	4.211
SN11	152.729	33.356	8.090	101.0733	23.901	11.950
SN12	88.156	53.305	13.763	131.617	68.639	34.319

**C) Gulf of California**

Sample number	Avg_uncleaned	STDEV-uncleaned	SE-uncleaned	Avg_cleaned	STDEV-cleaned	SE-cleaned
SN1	82.958	24.648	6.587	41.467	9.300	5.369
SN2	53.235	22.154	5.920	35.231	10.243	5.914
SN3	77.391	25.189	4.847	30.734	4.307	2.486
SN4	71.740	17.721	2.837	na	na	na
SN5	84.443	22.311	7.437	40.458	1.638	0.945
SN6	83.764	23.256	9.494	52.850	11.169	6.448

**Supplementary Table ST2:** The Mn/Ca ratios of bulk (crushed) foraminifera samples measured from Q-ICP-MS.

**A) Gulf of Guayaquil (GG)**

GG_Age (kyr BP)	GG_Bulk_Mn/Ca ( $\mu\text{mol/mol}$ )
1.998351852	20.840
3.931681818	54.811
5.340775	33.992
6.92185	92.213
8.429205882	52.354
8.928735294	126.711
9.927794118	37.3310
11.93546552	80.7289
12.44263793	69.5199
12.94981034	88.2664
13.30516304	83.3245
13.56942391	62.6032
13.83368478	66.6668
14.09794565	86.8762
15.03258871	130.484
15.8853629	111.142
16.31175	67.1478
17.16452419	242.000
17.59091129	150.585
18.01729839	250.267

**B) Mexican Margin (Mex)**

Mex_Age (kyr BP)	Mex_Bulk_Mn/Ca ( $\mu\text{mol/mol}$ )
3.633933	261.915
11.085279	291.739
11.780522	232.012
12.218735	200.531
12.525089	172.258
12.88665	221.887
14.290616	200.692
15.514477	138.573
16.96142	179.754
17.883543	124.674
19.093561	96.6505
20.581484	77.8854

**C) Gulf of California (GOC)**

GOC_Age (kyr BP)	Bulk_Mn/Ca samples ( $\mu\text{mol/mol}$ )
10.84138	31.708
11.232	36.751
11.57239	30.431
14.95569	36.532
20.53177	45.362
23.12232	43.518

**Supplementary Table ST3:** The average Mn/Ca ratios from individual foraminiferal specimens using LA-ICP-MS.

**A) Gulf of Guayaquil**

Depth (cm)	Age (kyr BP)	Average Mn/Ca ( $\mu\text{mol/mol}$ )	STDEV Mn/Ca
93	1.998351852	32.258	16.091
188	3.931681818	60.925	11.655
268	5.340775	34.470	17.126
348	6.92185	45.115	20.756
428	8.429205882	36.086	15.046
468	8.928735294	30.526	27.450
548	9.927794118	58.781	29.653
708	11.93546552	75.174	46.316
748	12.44263793	48.088	13.726
788	12.94981034	71.150	15.347
828	13.30516304	66.315	28.203
868	13.56942391	65.337	9.6165
908	13.83368478	130.96	123.52
948	14.09794565	86.721	29.513
1068	15.03258871	72.938	73.434
1148	15.8853629	110.27	96.522
1188	16.31175	84.412	75.208
1348	18.01729839	98.929	88.309

**B) Mexican Margin**

Depth (cm)	Age (kyr BP)	average Mn/Ca ( $\mu\text{mol/mol}$ )	STDEV Mn/Ca
18.5	3.633933	538.460	409.490
58.5	11.08528	279.064	142.213
63.5	11.78052	183.386	99.615
68.5	12.21874	473.583	221.430
73.5	12.52509	363.829	140.715
78.5	12.88665	353.128	232.337
83.5	14.29062	269.696	246.934
93.5	15.51448	253.962	151.846
108.5	16.96142	224.124	62.7123
119.5	17.88354	165.673	76.9263
129.5	19.09356	142.890	37.5209
141.5	20.58148	97.3063	57.6771

**C) Sea of Okhotsk**

Depth (cm)	Age (kyr BP)	average Mn/Ca ( $\mu\text{mol/mol}$ )	STDEV Mn/Ca
220	9.382628	1288.304	319.974
245	10.833117	5197.550	2393.022
270	12.818883	6188.798	2659.181

**D) Gulf of California**

Depth (cm)	Age (kyr BP)	average Mn/Ca ( $\mu\text{mol/mol}$ )	STDEV Mn/Ca
10.515	10.841384	75.636	27.753
10.845	11.231995	50.058	21.492
11.02	11.572385	72.725	27.799
13.185	14.955692	71.740	17.721
16.145	20.531769	73.447	27.536
17.93	23.122318	73.459	24.660

## Appendix D

1. Experimental set-up used for measuring  $\delta^{15}\text{N}_{\text{FB}}$  in benthic foraminifera, *B. spissa* applying the denitrifier method.



The figure shows the a) Bacterial cell (*Pseudomonas chlororaphis*) concentrate in 20ml headspace vials. The foraminiferal samples ( $\text{NO}_3^-$ ) are injected into the bacterial vials. These are incubated overnight to allow complete conversion of  $\text{NO}_3^-$  to  $\text{N}_2\text{O}$  (10 min for *P. chlororaphis*). The sample vials are stored upside down to reduce any loss of  $\text{N}_2\text{O}$  b) Extraction and isotopic analysis of  $\text{N}_2\text{O}$  using an isotope ratio mass spectrometer. The detailed methodology of denitrifier method is explained in Sigman et al. (2001). The pictures were taken from the Max Planck Institute for Chemistry, Mainz, Germany.

2. Preliminary data of  $\delta^{15}\text{N}_{\text{FB}}$  of *B. spissa* using denitrifier method from the Mexican Margin core MAZ-1E-04. The  $\delta^{15}\text{N}_{\text{FB}}$  of planktic foraminifera, *Globigerinoides ruber* from the same core is also measured using the denitrifier method. However, these are results of an experimental trial and indeed more samples are needed, and this can be considered as a future project.

Core	Depth (cm)	Species	Type	Number of individuals	Total N in bacterial vial	$\delta^{15}\text{N}$ final
MAZ-1E-04	108-109	<i>B. spissa</i>	Benthic	215	1.0372	13.86
	108-109	<i>G. ruber</i>	Planktic	300	5.8363	8.58
	98-99	<i>B. spissa</i>	Benthic	418	2.9261	16.69
	98-99	<i>G. ruber</i>	Planktic	329	4.8648	8.45
	119-120	<i>B. spissa</i>	Benthic	278	1.3279	13.79
	119-120	<i>G. ruber</i>	Planktic	300	5.0880	8.79
Additional depth	88-89	<i>B. spissa</i>	Benthic	186	2.3898	17.48
	103-104	<i>B. spissa</i>		127	0.88907	13.48
	93-94	<i>B. spissa</i>		300	1.5661	16.54

## **Contribution to publications**

### **Peer-reviewed publications**

A deep-learning automated image recognition method for measuring pore patterns in closely related bolivinids and calibration for quantitative nitrate paleo-reconstructions

Field work: 0%

Laboratory pre-treatment: 80%

Data acquisition: 90%

Evaluation and interpretation: 80%

Publication authoring and composition: 80%

### **Prepared for publication in peer-reviewed journals**

Quantitative reconstruction of deglacial bottom-water nitrate in marginal Pacific seas using the pore density of denitrifying benthic foraminifera

Field work: 0%

Laboratory pre-treatment: 100%

Data acquisition: 100%

Evaluation and interpretation: 80%

Publication authoring and composition: 80%

Reconstruction of redox conditions in the Oxygen Deficient Zones in the marginal seas of the Pacific Ocean using benthic foraminiferal Mn/Ca

Field work: 0%

Laboratory pre-treatment: 100%

Data acquisition: 100%

Evaluation and interpretation: 80%

Publication authoring and composition: 90%

### **Declaration upon oath**

I hereby declare and affirm that this doctoral dissertation is my own work and that I have not used any aids and sources other than those indicated. If electronic resources based on generative artificial intelligence (gAI) were used in the course of writing this dissertation, I confirm that my own work was the main and value-adding contribution and that complete documentation of all resources used is available in accordance with good scientific practice. I am responsible for any erroneous or distorted content, incorrect references, violations of data protection and copyright law or plagiarism that may have been generated by the gAI.

### **Eidesstattliche Versicherung**

Hiermit erkläre ich an Eides statt, dass ich die vorliegende Dissertationsschrift selbst verfasst und keine anderen als die angegebenen Quellen und Hilfsmittel benutzt habe. Sofern im Zuge der Erstellung der vorliegenden Dissertationsschrift generative Künstliche Intelligenz (gKI) basierte elektronische Hilfsmittel verwendet wurden, versichere ich, dass meine eigene Leistung im Vordergrund stand und dass eine vollständige Dokumentation aller verwendeten Hilfsmittel gemäß der Guten wissenschaftlichen Praxis vorliegt. Ich trage die Verantwortung für eventuell durch die gKI generierte fehlerhafte oder verzerrte Inhalte, fehlerhafte Referenzen, Verstöße gegen das Datenschutz- und Urheberrecht oder Plagiate.

Hamburg, 30th September 2024

A handwritten signature in blue ink, consisting of stylized, overlapping loops and lines.

Signature:

Anjaly Govindankutty Menon

